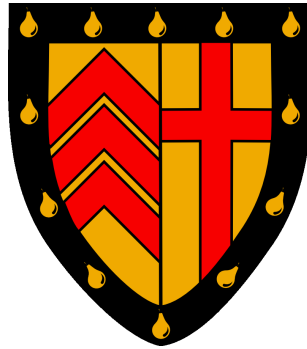


Optoelectronic processes in polyfluorene ambipolar transistors



Matthew J. Bird

Clare College

University of Cambridge

A dissertation submitted for the
degree of Doctor of Philosophy

November 2010

Declaration

This thesis describes work undertaken at the Cavendish Laboratory of the University of Cambridge.

Except where specific reference is made to the involvement of others, the work presented herein is my own and contains nothing which is the result of collaboration. This dissertation has not been submitted in whole or in part for the award of a degree at this, or any other University and does not exceed 60,000 words in length.

Matthew J. Bird

Clare College, October 2010

Captain Janeway: “Wouldn’t a polaron modulator be able to do that?”

Chief Engineer Torres: “Unfortunately, nobody in the Alliance has one”

July 2377

Contents

1	Introduction	1
2	Background	5
2.1	Conjugated Polymers	6
2.1.1	Electronic Structure	6
2.1.2	Hückel Theory	8
2.1.3	Quantum chemical calculations	12
2.1.4	Neutral excitations	14
2.1.5	Charge carriers	17
2.1.6	Electroabsorption	20
2.2	Charge transport models	21
2.2.1	Multiple Trap and Release/Mobility edge model	21
2.2.2	Hopping models	23
2.2.3	Polaronic Hopping Models	24
2.2.4	Disorder Hopping Models	26
2.2.5	Applicability of various models	29
2.2.6	Injection of charges into organic semiconductors	30
2.2.7	Trapping and chemical reactions	31
2.2.8	Transport at interfaces	34
2.3	Device physics	35
2.3.1	Hole/Electron only devices	35
2.3.2	Diodes	36
2.3.3	MIS diodes	38
2.3.4	Unipolar transistors	42
2.3.5	Ambipolar and light-emitting transistors	45
3	Materials and Experimental methods	49
3.1	Materials	50

3.1.1	Semiconducting Polymers	50
3.1.2	Dielectrics	52
3.1.3	PEDOT:PSS	53
3.2	Device fabrication	54
3.2.1	Substrate Preparation	54
3.2.2	Electrode Preparation	54
3.2.3	Film Preparation	55
3.2.4	Device structures	55
3.3	General device characterisation	61
3.3.1	Electrical characterisation	61
3.3.2	Impedance Spectroscopy	61
3.3.3	Profilometry	61
3.4	Photocurrent measurements	62
3.4.1	Time-correlated single photon counting	62
3.4.2	Photovoltaics Rig	62
3.4.3	Vacuum measurements	65
3.4.4	Scanning Kelvin Probe Microscopy	65
3.5	Device imaging and optical measurements	65
3.5.1	Fluorescence Microscopy	65
3.5.2	UV-VIS spectra	65
3.5.3	Photoluminescence spectra	66
4	Charge Modulation Spectroscopy technique	69
4.1	Introduction	70
4.2	Experimental setup	71
4.3	Calculating the cross section of charge-carriers	74
4.4	In situ electrical characterisation	77
4.4.1	Measuring admittance and impedance	77
4.4.2	Modelling a series RC device	79
4.4.3	Modelling a transistor	80
4.4.4	The importance of patterning the gate electrode	88
4.4.5	Applying a drain voltage during measurements	89
4.5	Summary	90
5	Optimising ambipolar transistors for charge modulation spectroscopy	91
5.1	Introduction	92

5.2	Reducing device thickness	95
5.2.1	Cross-linked PMMA	95
5.2.2	High molecular weight PMMA	97
5.3	Increasing mobility	98
5.4	Reducing contact resistance	100
5.4.1	Improving hole injection	103
5.4.2	Semiconductor thickness	105
5.4.3	Injecting electrons into lower electron affinity polymers	106
5.4.4	Leakage and contact resistance	107
5.5	Effect of the gate electrode	108
5.5.1	Varying gold gate thickness	108
5.5.2	Aluminium gate	109
5.6	Field induced changes in interference	110
5.6.1	Modulation spectra with no semiconductor	110
5.6.2	Modulation spectra with semiconductor	112
5.6.3	Theoretical model	112
5.6.4	Electrostriction	115
5.6.5	Electroabsorption modification of interference	117
5.6.6	Predicting extrinsic CMS effect from the transmission spectra	119
5.6.7	Linear field-dependent extrinsic effect	122
5.7	Optimum device structures	123
5.7.1	Thin or thick electrodes	123
5.7.2	Non-reflecting gate electrode - PEDOT:PSS	126
5.8	Summary	133
6	Charge absorption in polyfluorenes	137
6.1	Introduction	138
6.2	F8BT CMS	142
6.2.1	Typical optical and electrical data	142
6.2.2	Gate voltage dependence of the charge-induced absorptions	143
6.2.3	Electroabsorption	146
6.2.4	Frequency response	147
6.2.5	Accuracy of technique	147
6.2.6	Separating charge absorption from electroabsorption	149
6.2.7	Using a drain voltage to improve signal to noise	149
6.2.8	Analysis of charge-induced spectra	152

6.2.9	Comparison with chemical doping	155
6.2.10	Bias stress and the effect of light	158
6.3	F8 CMS	162
6.3.1	Gate voltage dependence of charge-induced absorptions	164
6.3.2	Frequency response	166
6.3.3	Obtaining corrected spectra	166
6.3.4	Analysis of charge-induced spectra	168
6.3.5	Comparison with charge-induced absorptions from pulse radiolysis	171
6.3.6	Bias stress and the effect of light	174
6.4	Summary	175
7	Exciton-polaron interactions in polyfluorenes	179
7.1	Introduction	180
7.2	Photocurrent in aligned polyfluorenes	185
7.3	Electric field and photocurrent	190
7.3.1	Electric field in planar diodes	193
7.3.2	Exciton lifetime measurements under applied fields	194
7.3.3	Gold/Chromium single layer devices	197
7.3.4	Gold/Aluminium single layer and bilayer devices	199
7.4	Quantifying charge-induced photoluminescence quenching	204
7.5	Using charge-induced photoluminescence quenching to visualise device operation	211
7.6	Implications of charge-induced photoluminescence quenching for electrically pumped lasing	216
7.7	Summary	217
8	Conclusions and outlook	221
8.1	Conclusions and further work	222
A	Supporting measurements	225
B	Equipment characterisation	229
C	Code	233

Chapter 1

Introduction

Common sense tells us that plastics do not conduct electricity as exemplified by their ubiquitous use as insulators in electrical applications. However, over the last few decades a new field of physics has emerged in which the remarkable electrical and optical properties of a certain class of plastics, conjugated polymers, have been revealed. The first discovery of conducting polymers can be traced back to a series of papers by Weiss et al.¹⁻³ from 1963 who studied the melanin polymer polypyrrole. Though not for electrical conduction, melanins were exploited by nature for dissipating UV radiation into heat through a process called internal conversion and thus providing some protection in skin against ionisation of DNA molecules under intense sunlight. Weiss however discovered that these polymers become highly conducting when doped with Iodine and we will see that it is the unique bonding structure in conjugated polymers that accounts for both the conductivity and optical properties.

Weiss' discovery was mostly overlooked at the time and it was not until high conductivity in doped polyacetylene was discovered in 1977 by Heeger et al.⁴, rewarded by the Nobel Prize for Chemistry in 2000,⁵ that the field took off. Notable landmarks along the way were the first polymer field-effect transistors^{6,7} (FETs), the discovery of light emission under application of an electrical bias (electroluminescence),⁸ and homopolymer,⁹ bilayer¹⁰ and polymer blend¹¹⁻¹³ photovoltaics. Conjugated polymers form part of a larger field of research called *Organic Electronics* which incorporates other carbon based systems with π conjugation including small molecules and oligomers, carbon nanotubes,¹⁴ fullerenes,¹⁵ and more recently graphene.¹⁶⁻¹⁸ The unique combination of electronic and mechanical properties coupled with the ease of processing large areas at low temperatures has already led to the successful commercialisation of many organic electronic products¹⁹ including televisions, e-readers and solar panels.

Whilst much has been learnt over the last few decades, there is still much to be understood in terms of the nature of the charge species on a conjugated polymer. In contrast to inorganic crystalline semiconductors where charges reside in a continuum (band) of delocalised states extending over many lattice constants,^{20,21} a charge on a conjugated polymer is typically localised to a segment of the chain due to a combination of disorder,^{22,23} weak intermolecular electronic interactions, and strong interactions with local structural deformations (phonons).²⁴ Whilst quantum chemical calculations can provide some information about the nature of the wavefunction of the charged polymer, there are few experimental probes that can determine exactly what is going on. A charged polymer will in general have different electro-magnetic absorptions to a neutral polymer. Such differences include changes in microwave,^{25,26} tera-hertz²⁷ and infra-red absorption²⁸ due to the change in conductivity; additional changes in IR absorption due to changes

in bond lengths²⁹; and changes in near-IR and visible absorptions due to new electronic transitions.³⁰ In this work we focus on the latter of these techniques making use of FETs to measure the absorptions from a known quantity of field-induced mobile charges. In particular due to the recent general demonstration of negative (n-type) charge transport in transistors³¹ followed quickly by ambipolar (n- and p-type) transistors³² we are able to compare for the first time both the positive (hole) and negative (electron) charge-induced absorptions on the same polymer without using chemical doping. Two polymers are studied in this thesis including a simple hydrocarbon-only polymer, poly(9,9-di-n-octylfluorene) (F8),^{33,34} which is expected to have similar electron and hole wavefunctions, and a related co-polymer, poly(9,9-di-n-octylfluorene-alt- benzothiadiazole) (F8BT),^{35,36} in which the BT unit is believed to localise the electron wavefunction.³⁷ A number of other interesting effects were elucidated by this charge modulation spectroscopy (CMS) technique including charge-induced quenching of photoluminescence (fluorescence) and the related phenomena of photoconductivity. A new technique for imaging device operation and charge trapping is derived from these results and possible implications for electrically pumped lasing discussed. The remainder of this thesis is organised as follows:

Chapter 2 provides a theoretical background to the concepts that are important in this work including the quantum mechanical basis for the semiconducting properties of conjugated polymers, excited states, charge transport models and device physics.

Chapter 3 covers the experimental methods used in the fabrication and testing of devices in this work.

Chapter 4 describes the charge modulation spectroscopy technique in detail and the new methods developed in this thesis to improve the accuracy of the obtained spectra.

Chapter 5 looks at the challenges of measuring charge absorptions in top-gate ambipolar transistors and traces the development of device structures and measurement techniques required to achieve this difficult measurement.

Chapter 6 includes the measured charge-induced absorptions in F8 and F8BT along with quantum chemical analysis. Other interesting results that arose during this experiment including charge trapping, detrapping, fluorescence quenching and electroabsorption are also highlighted.

Chapter 7 follows on from Chapter 6 to look in detail at charge-induced fluorescence quenching in F8BT and a technique to image device operation is developed. An associated photocurrent effect in a number of polyfluorenes is investigated particularly with regards to alignment and annealing conditions of the polymer film and the implications for lateral bilayer solar cells are discussed.

Chapter 8 provides conclusions and proposes future directions for this research.

Chapter 2

Background

2.1 Conjugated Polymers

Conjugated polymers are a particular class of polymer where the number of bonds that the carbon atoms of the polymer backbone make with their neighbours results in there being electronic states whose wavefunctions extend over many monomer repeat units. These extended states can have electrons added to or removed from without the polymer becoming structurally unstable thus allowing the polymer to be a medium for charge transport. An electron can be removed from the highest occupied molecular orbital (HOMO) to form a positive charge carrier known as a hole, or added to the lowest unoccupied molecular orbital (LUMO) to form a negative charge carrier known simply as an electron. The energy gap between these two delocalised states is typically of the order of a few electron volts allowing the absorption and emission of light at visible and infra red wavelengths depending on the polymer. To understand the mathematical reason for these properties we start by looking at the only system that can be solved exactly with quantum mechanics, the hydrogen atom, and follow the series of approximations that can be made until we arrive at the modern state-of-the-art methods used to calculate the electronic states in complex conjugated polymer systems.

2.1.1 Electronic Structure

Solving the following time-independent Schrödinger equation for an electron and proton reveals a set of states, φ , in which the negatively charged electron can reside or, in classical terminology, orbit around the heavier positively charged proton

$$-\frac{\hbar^2}{2\mu}\nabla^2\varphi - \frac{e^2}{4\pi\epsilon_0 r}\varphi = E\varphi \quad (2.1)$$

where $\mu = m_p m_e / (m_p + m_e)$ is the reduced mass constructed from the electron mass, m_e , and the proton mass, m_p , r is the separation between the proton and electron and E is the energy of the state φ .

Electron states are uniquely identified by three integer quantum numbers representing their quantised energy, n , angular momentum, l ($0 \leq l < n$) and projection of angular momentum onto the z axis, m_l ($-l \leq m_l \leq l$); any given combination defines a unique spatial wavefunction. Convention from the field of chemistry assigns a number (1,2,3 etc) to represent n , a letter to represent l ($s, p, d, f..$) and a subscript letter or letters to represent m_l (e.g. $p_x, d_{xy}, d_{x^2-y^2}$).

For relatively small atoms such as carbon, rather than solving the massively more complex Schrödinger equation for a multi-electron system we can use the one-electron

states from the hydrogen atom as a reasonable approximation to the solution. As fermions, only one electron can be in each quantum state, but owing to a fourth quantum label, spin ($+\frac{1}{2}$ or $-\frac{1}{2}$) two electrons of opposite spin can share the same spatial wavefunction. The hydrogen-like states are therefore filled up from the lowest energy with two electrons in each with some additional rules concerning spin in partially filled degenerate states (Hund's rules). It is as a result of the enforced spatial separation of the wavefunctions that the electron-electron interactions do not drastically alter the electronic states in some multi-electron atoms. We can thus label the electronic configuration of carbon which has six electrons as $1s^2 2s^2 2p^2$ where the superscript denotes the number of electrons (m_l and spin are not labelled here but implicitly represented by the maximum number of electrons for a given l). Carbon has four electrons in the outermost (valence) orbitals and can form stable molecules by bonding with between one and four neighbouring atoms. The bond geometries can be estimated by hybridising the energetically similar 2s and 2p orbitals in various ways. With four neighbouring atoms hybrid theory gives four sp^3 bonds with the large lobes equally spaced in three dimensions making a tetragonal structure. These can form a bond, for example, with another carbon sp^3 orbital or a 1s orbital in hydrogen as seen in diamond or methane respectively. These bonds, invariant upon rotation around the bond axis, are called σ bonds and electrons in these bonds are confined to the region between atoms.

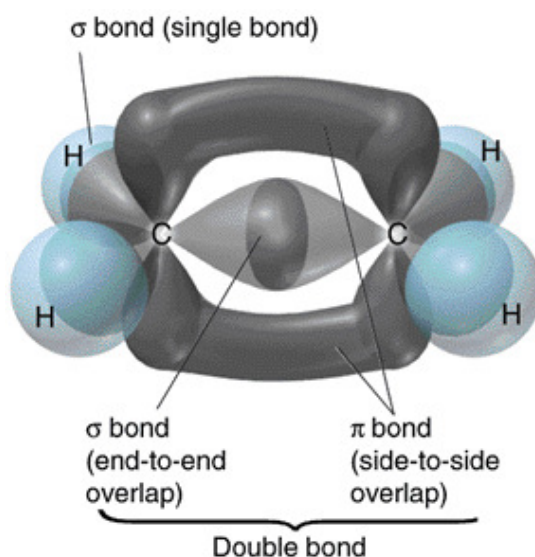


Figure 2.1: Ethene (taken from reference. ³⁸)

With 3 neighbouring atoms, the 2s, $2p_x$ and $2p_y$ orbitals become three equally spaced in-plane sp^2 σ bonds leaving the p_z out of plane which can form an additional bond with

an adjacent carbon p_z orbital making it a double bond as in ethene (figure 2.1). This extra bond which lies above and below the molecular axis is known as a π bond and can interact with π bonds on adjacent carbon atoms to form a delocalised molecular orbital.

2.1.2 Hückel Theory

The energy and shape of these molecular orbitals (MOs) can be predicted to some extent with Hückel theory. Hückel theory derives from the more general Linear Combination of Atomic Orbitals (LCAO) method (also referred to as tight-binding when used in crystalline solids), but only involves p_z orbitals and nearest neighbour interactions. The method uses n identical p_z orbitals as a set of basis states to construct n molecular orbitals. For the simple case of ethene ($n=2$) we can construct two molecular orbitals from two p_z orbitals of the form:

$$\Phi_a = c_a(1)\phi_1 + c_a(2)\phi_2 \quad (2.2)$$

where Φ_a is a molecular orbital indexed with label a , $c_a(1)$ is its coefficient for one p_z orbital, ϕ_1 , and $c_a(2)$ is its coefficient for the other p_z orbital, ϕ_2 . These molecular orbitals must satisfy the Schrödinger equation:

$$H|\Phi_a\rangle = E_a|\Phi_a\rangle \quad (2.3)$$

where H is the Hamiltonian and E_a is the energy of the a th MO. Taking the inner product with ϕ_1 and ϕ_2 gives two equations that can be written in matrix form.

$$\begin{pmatrix} \langle \phi_1|H|\phi_1\rangle - E_a \langle \phi_1|\phi_1\rangle & \langle \phi_1|H|\phi_2\rangle - E_a \langle \phi_1|\phi_2\rangle \\ \langle \phi_2|H|\phi_1\rangle - E_a \langle \phi_2|\phi_1\rangle & \langle \phi_2|H|\phi_2\rangle - E_a \langle \phi_2|\phi_2\rangle \end{pmatrix} \begin{pmatrix} c_a(1) \\ c_a(2) \end{pmatrix} = 0 \quad (2.4)$$

Using the results that $\langle \phi_i|H|\phi_i\rangle = \varepsilon$, $\langle \phi_i|H|\phi_j\rangle = t$ and $\langle \phi_i|\phi_j\rangle = \delta_{ij}$ we find that these equations are solved if the following determinant is equal to zero:

$$\begin{vmatrix} \varepsilon - E_a & t \\ t & \varepsilon - E_a \end{vmatrix} = 0 \quad (2.5)$$

Note that ε ($\varepsilon < 0$) is the energy of an electron in the atomic p_z orbital and t ($t < 0$) is the interaction energy between the two adjacent p_z orbitals. By solving the resulting quadratic equation and requiring that the Φ_a are normalised we get two molecular orbitals which we label π and π^*

$$\Phi_\pi = \frac{\phi_1 + \phi_2}{\sqrt{2}}, \quad E_\pi = \varepsilon + t \quad (2.6)$$

$$\Phi_{\pi^*} = \frac{\phi_1 - \phi_2}{\sqrt{2}}, \quad E_{\pi^*} = \varepsilon - t \quad (2.7)$$

whose energies indicate a HOMO-LUMO energy gap of $2t$. The $*$ indicates that the MO is anti-bonding as there is less electron density between the atoms as compared to non-interacting atomic orbitals leading to a repulsive force. This explains why, in the case of σ MOs based on $1s$ AOs, dihydrogen is stable but dihelium with 2 electrons in the σ and two electrons in the σ^* MO is not. Stability can be predicted by the *bond order* which is the number of electrons in bonding minus the number in anti-bonding orbitals all divided by two and has to be greater than zero for a molecule to exist.

For a more general system with N p_z orbitals we construct the molecular orbitals as:

$$\Phi_a = \sum_m^N c_a(m) \phi_m \quad (2.8)$$

Just as before, we end up with a determinant which must equal zero. In this case it is for a cyclic molecule as we have included the hopping terms in the corners.

$$\begin{vmatrix} \varepsilon - E_a & t & & & t \\ t & \varepsilon - E_a & t & & \\ & & t & \ddots & t \\ & & & t & \varepsilon - E_a & t \\ t & & & & t & \varepsilon - E_a \end{vmatrix} = 0 \quad (2.9)$$

The roots of the polynomial from this determinant give the energy levels:

$$E_a = \varepsilon + 2t \cos\left(\frac{2a\pi}{N}\right) \quad (2.10)$$

In the case of a linear chain they are similar

$$E_a = \varepsilon + 2t \cos\left(\frac{2a\pi}{N+1}\right) \quad (2.11)$$

To calculate the coefficients, visualise and label the orbitals without solving the difficult secular determinant, the tools of group theory are typically used which uses the symmetry of the molecule to construct symmetry molecular orbitals. The basic theory for this technique is to find which irreducible symmetry representations for the molecular symmetry group can be formed with the atomic orbitals as a basis. A technique can then be used to construct these molecular orbitals which due to their symmetry cause all but blocks along the diagonal of the secular matrix to be zero. Benzene, for example, belongs to the symmetry group D_{6h} . The six p_z orbitals form a set and the characters of this set

can be determined by applying the D_{6h} symmetry operations on the p_z orbitals e.g. the E operation leaves all six in the same place giving a character 6, or the $3\sigma_v$ mirrors the p_z orbitals in a plane perpendicular to the molecule containing two carbon atoms leaving only 2 in the same place with same sign giving character 2. The characters for the p_z set can then be constructed from the subset of irreducible representations A_{2u} , B_{2g} , E_{1g} and E_{2u} (the order of E representations is two). Either by inspection, or using the projector operator the LCAO coefficients can be determined using these representations such that each molecular orbital possesses a different symmetry and as a result form an orthonormal set (see figure 2.2).

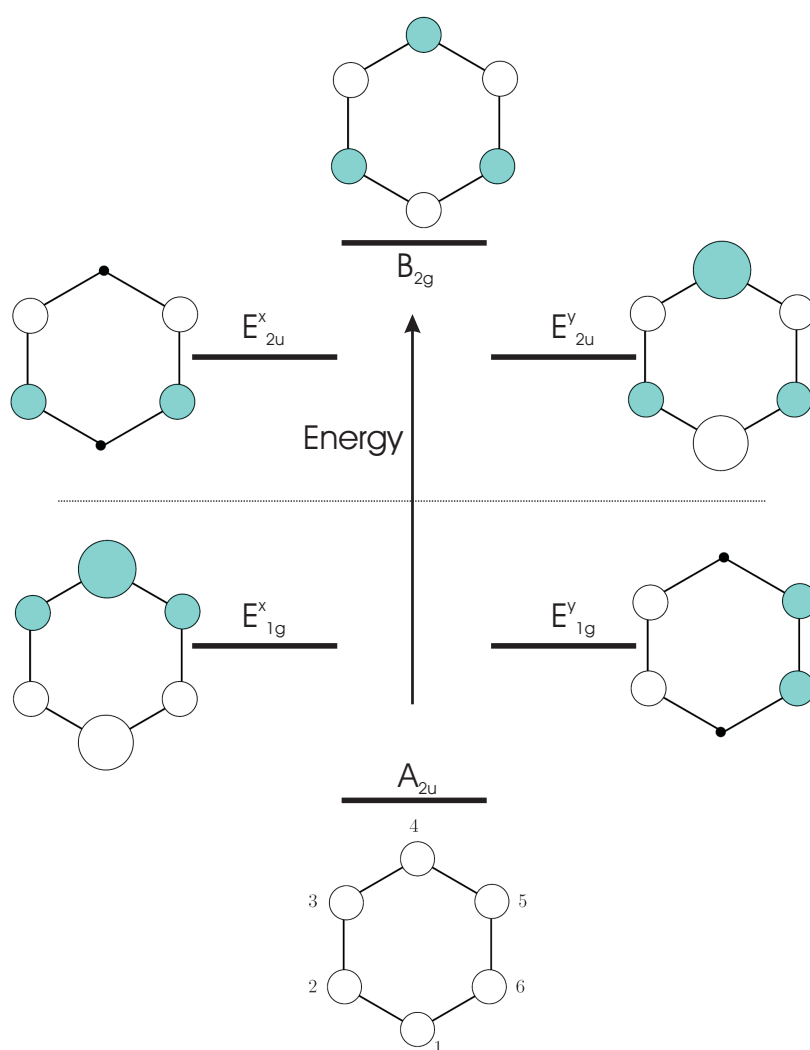


Figure 2.2: Benzene molecular orbitals (adapted from reference³⁹). The circles represent the top lobe of the p_z orbital, the colour and size represents the sign and size of the LCAO coefficients.

The expectation value of the energy of these states can then be found by using the symmetry MOs in terms of ε and t . The symmetry labels also help in identifying allowed optical transitions in some cases, without the need for complex quantum chemical analysis although does not provide the weighting of each transition. For more detail on group theory and molecular orbitals see Cotton.⁴⁰

The final part of this one-electron picture that follows step by step from the exact solution to the hydrogen atom is to look at the effect of polymerisation. In an ideal one dimensional conjugated chain of carbon atoms (trans-polyacetylene), a continuum of energy states is formed between $\varepsilon + t$ and $\varepsilon - t$. The consequence of this would be a metal as this continuum of states is only half full. Peierls⁴¹ showed however that this situation is unstable with respect to a change to a conformation with alternate single and double bonds of different lengths. In the language of band theory this is because the unit cell doubles from the original interatomic distance, a , thus halving the band gap to be at the fermi surface, $\pi/2a$, and so slightly lowering the total energy of the system as shown by figure 2.3.

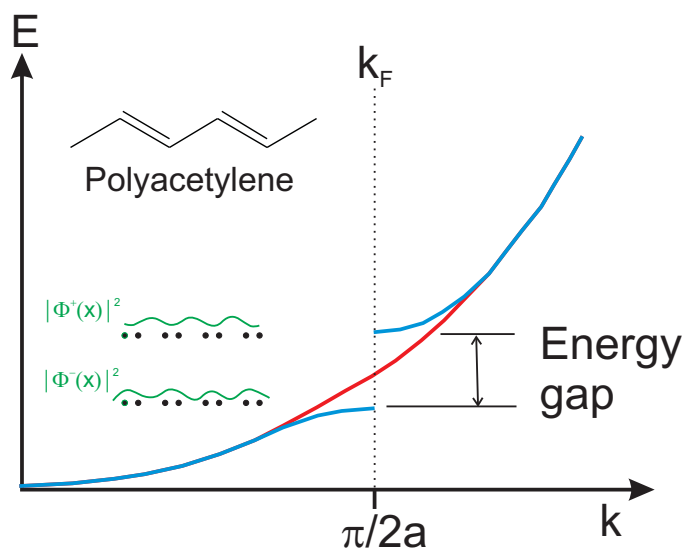


Figure 2.3: Energy, E , vs wavenumber, k , of the electronic states for an infinite one dimensional chain of equally spaced atoms (red line) showing the energy gap opened up by the Peierls distortion at the Fermi surface (blue line) resulting in a lowering in energy of the system.

The effect of this instability is that a gap is created causing trans-polyacetylene (inset figure 2.3) to behave as a semiconductor. Most polymers however, do not rely solely on this intrinsic electron-phonon coupling to produce an energy gap; the stereochemistry in most

hydrocarbon conjugated polymers including cis-polyacetylene and poly-phenylenes result in extrinsic dimerisation as well as intrinsic and hence an energy gap. Going from one repeat unit to many, this energy gap reduces although in practice the conjugation length is limited to around 5-10 repeat units due to kinks, twists or impurities. Typical energy gaps in conjugated polymers range from 1-3eV making them useful for optoelectronic applications in the visible and near infra-red. Copolymerisation with an electron-accepting monomer is often used to reduce the energy gap further if required.

It is important to note here why this electronic structure provides the basis of organic semiconductors. We have shown that conjugated systems have delocalised π molecular orbitals which result in an electronic energy gap, between the HOMO and LUMO. The nature of these bonds are different to σ bonds in that whilst coupled strongly to the lattice, are not responsible for holding the molecule together. An electron can be added or removed to an orbital without the polymer becoming unstable.

2.1.3 Quantum chemical calculations

Before dealing with the nature of excited states, charged states and charge transport we complete this step by step description of the electronic structure with the most modern techniques for calculating wavefunctions and energies accurately.

Hartree approximation

Hückel theory neglects electron-electron interactions which must be considered when aiming for an accurate description of molecular orbitals. As a first attempt, these interactions are added by introducing a new term in the Hamiltonian which represents the Coulomb repulsion between the i th electron and the average electron density of all the others. Through variational methods, a ground state wavefunction, expressed as the product over an orthonormal set of wavefunctions can be determined iteratively using this Hamiltonian. This method of using a product of wavefunctions does not take into account the spin of the electrons as the overall wavefunction is not symmetric under exchange of two electrons as it must for fermions. It turns out that this is important because even though the Hamiltonian is spin-independent, correlations between electrons resulting from Fermi statistics indirectly effect their interaction energy.

Hartree-Fock Theory

Fermi statistics can be guaranteed by representing the ground state wavefunction as a Slater determinant comprised of an orthonormal set of wavefunctions. This constraint modifies the energy of the system due to the effect it has on the total electron-electron Coulomb interaction. This correction to the Hartree energy, as put forward by Fock, is known as the exchange energy. It is short range and is only non-zero between electrons with parallel spins. This method falls short however as the system cannot always be exactly described by a Slater determinant and there are other electron correlations that modify the total energy. In common nomenclature, whilst the exchange energy is a correlation effect, it is the difference between the Hartree-Fock solution and the exact solution to the non-relativistic Schrodinger equation within the Born-Oppenheimer Approximation that is defined as the correlation energy. This method is typically used as a starting point to establish molecular geometries and ground states wavefunctions and is used in modern quantum chemistry calculations to calculate ground state geometries and the single electron wavefunctions for neutral or charged polymers. There are many variations of this semi-empirical quantum chemistry method including INDO (Intermediate Neglect of Differential Overlap), MNDO (Modified Neglect of Differential Overlap) and AM1 (Austin Model 1).

Post Hartree-Fock (Configuration Interaction)

By not including electron correlation terms, Hückel and Hartree-Fock fail to accurately predict optical transitions. For example, polyacetylene is falsely predicted to photoluminesce as the transition from the lowest excited state, as calculated with Hartree-Fock, to the ground state is symmetry-allowed. A Post-Hartree-Fock method known as Configuration Interaction (CI) includes correlation effects and predicts that the lowest excited state is a different one with the wrong symmetry for radiative transitions.⁴² CI therefore forms the basis of modern techniques for calculating optical transitions in conjugated polymers. It works by writing the excited state as a linear combination of configurations including all the electrons in the occupied levels (Hartree-Fock determinant), one electron promoted from an occupied to an unoccupied level, two electrons promoted from occupied to unoccupied levels and so on. The number of electrons included before the calculation is truncated defines the size of the CI-space. The number of orbitals used for the transitions is also truncated and will typically be just a few of the highest occupied molecular levels and the lowest unoccupied levels. The variational method is then used to minimise this excited state energy by varying the coefficients of the configuration state functions.

By including all these configurations, electron correlations are included. The resulting optical transitions can therefore not be thought of, in general, as an electron being promoted from one level to another within the one electron picture, but as a combination of configurations in which one or more electrons are promoted between a number of different states.

Density Functional Theory

Whilst not featured in this thesis, another notable method for the accurate description of quantum systems that include electron correlation terms is Density Functional Theory. This makes use of the remarkable fact that all the properties of an n -body electron system can be deduced simply by the 3 dimensional electron density. Properties such as kinetic energy are functions of this electron density function and known as functionals. The functionals for kinetic energy and electron-electron interactions are completely universal so the electron density function is only determined by the external potential e.g. from ions. By knowing this potential you can thus calculate the ground state density by using it as a variable to minimise the energy. With accurate functionals for the exchange and correlation interactions (using Local Density Approximations such as the Generalised Gradient Approximation), this method can be accurate and efficient in solving previously intractable many body problems. The reason why this very powerful technique is not used for calculating optical properties of conjugated polymers because it does not deal with excited states.

2.1.4 Neutral excitations

A conjugated polymer can access neutral excited states through the absorption of a photon of light. In inorganic semiconductors, such an absorption at room temperature would result in an electron in the conduction band and a hole in the valence band⁴³. The mutual coulombic attraction is largely screened by a large dielectric constant and at room temperatures the charges can escape easily so free charges are the result of excitation. At low temperatures the electron and hole can form a hydrogen-like state but with an average separation of a number of lattice constant⁴⁴. This quasiparticle is referred to as a Wannier exciton⁴⁵ and explains why the absorption edge can be approximately 0.01eV below the band gap energy at low temperature in inorganic semiconductors. The relative dielectric constant is typically much lower in conjugated polymers (2-3) meaning that absorption typically leads to strongly bound electron and hole pairs known as Frenkel excitons⁴⁴. Whilst there has been much debate over the years about the nature of the

primary excited species in conjugated polymers it seems that either immediately or soon after the absorption of a photon, an exciton is formed. The minimum energy loss when extracting charges in solar cells following the creation of an exciton is around 0.6eV which is made up of 0.1eV to create a charge transfer state and 0.5eV to separate this state to free charges⁴⁶. This indicates that the exciton has a binding energy of around 0.6eV. The onset of absorption is hence lower than the energy gap as calculated from the difference between the single electron HOMO and LUMO states.

For each electronic state, a conjugated polymer also has a number of vibrational states. When excitation occurs from the ground state, the electronic transition occurs much faster than the time for the nuclei to move due to the large difference in masses. Under this Born-Oppenheimer Approximation the nuclei will find themselves in a configuration that is a vibrational excited state of the excited electronic state. The polymer quickly relaxes in a few picoseconds to the vibrational ground state and the exciton itself can diffuse up to around 5-10nm onto other polymer units during its lifetime of around 1ns before decaying. One possible decay route is the emission of a photon in a process known as fluorescence. The combination of vibrational relaxation and migration to potentially lower energy sites causes the emission to be at lower energy than the absorption and this difference is called the Stokes shift as shown in figure 2.4.

As implied above the exciton is a quasi-particle and is not simply an electron in the LUMO and a hole in the HOMO. It is more appropriate to represent the excited states on an energy diagram as in figure 2.5. In this figure we can see all the possible excitations and decays together in terms of energy and spin state. The ground state S_0 is a spin singlet state ($S=0$) and due to optical transition rules, only singlet excitons can be formed through the absorption of photons. Absorption to the triplet state is shown with dashed lines to indicate that it is a forbidden or very weakly allowed transition. After rapid internal conversion to the lowest energy singlet exciton state the exciton can either decay radiatively, non-radiatively or, through inter-system crossing, can become the lower energy $S=1$ triplet state which decays non-radiatively with a long lifetime or radiatively if the energy is transferred to added phosphorescent compounds. The excited states can also be further excited optically to higher lying states with the triplet, for example, inducing one sub energy gap absorption. Singlet absorption and stimulated emission can also occur when probing an excited polymer.

Non-radiative processes other than the formation of triplets can be caused by extrinsic effects such as charge separation at hetero-interfaces,⁴⁸ electrodes⁴⁹ and defects⁵⁰ or energy transfer of the exciton to a non radiative molecule.⁵¹ Intrinsic non-radiative decay can occur by transfer of energy to intramolecular vibrational modes known as

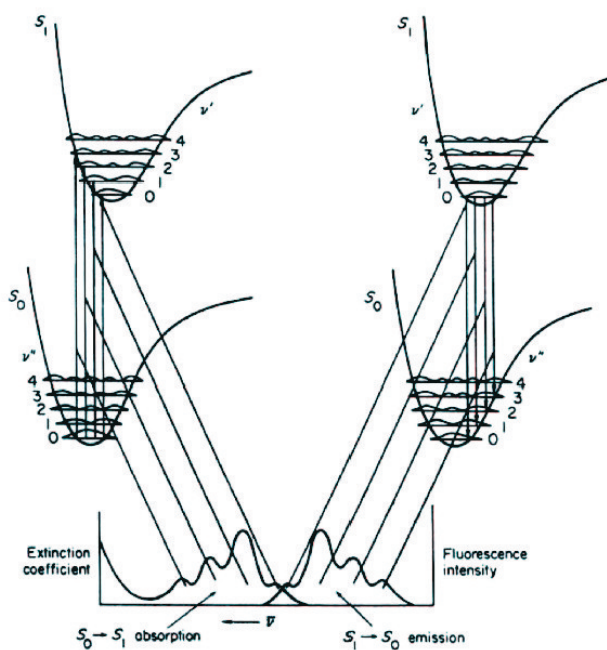


Figure 2.4: Schematic absorption and emission profiles for a conjugated polymer showing the Stokes shift between the two and the transitions involving vibrational levels within the electronic state (from reference²⁴).

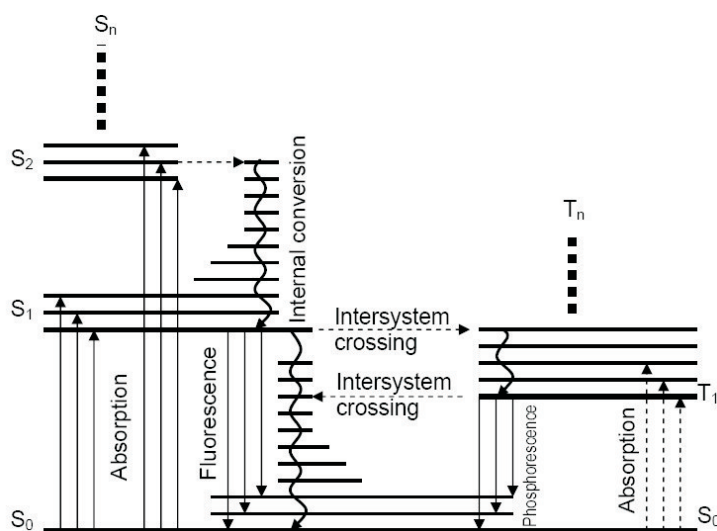


Figure 2.5: Energy diagram showing the excited states of a conjugated polymer (from reference⁴⁷).

phonons (heat).⁵² Such non-radiative effects limit the photoluminescence efficiency although efficiencies around 70% or more are obtainable in some conjugated polymers. Photoluminescence can also be quenched in the presence of other excitations or charges as in singlet-triplet⁵³ and singlet-singlet⁵⁴ annihilation or exciton-charge annihilation.³⁰ In general the photoluminescence (PL) efficiency is given by the following relationship between the radiative decay rate, k_r and the sum of non radiative decay rates k_{nr}^i .

$$\text{PL efficiency} = \frac{k_r}{k_r + \sum_i k_{nr}^i} \quad (2.12)$$

Electroluminescence

Excitons can also be formed from electrically injected electrons and holes. This process is described by Langevin recombination^{55,56} which states that once within a Coulomb radius, r_c , an electron and hole will be captured in their mutual field as they have insufficient thermal energy, kT , to escape. This capture radius is given by

$$r_c = \frac{e^2}{4\pi\epsilon\epsilon_0 kT} \quad (2.13)$$

The rate of bimolecular recombination is the product of the charge concentrations and the Langevin recombination rate β_L :

$$\beta_L = \frac{e(\mu_p + \mu_n)}{\epsilon\epsilon_0} \quad (2.14)$$

If one assumed that the ratio of formation of singlets and triplets are given by statistical considerations, the injected charges with random spin states would be expected to produce a 25% yield of singlet excitons. However, reports of higher yields of singlet excitons have led to speculation that the recombination cross section is spin-dependent.⁵⁷

2.1.5 Charge carriers

Early attempts to understand the nature of the charge species responsible for the conductivity in doped trans-polyacetylene⁴ identified a state between two degenerate regions of conjugated polymer with opposite senses of bond alternation. The domain wall between two regions of different bond alternations should exhibit dispersionless transport along the chain and is therefore known as a soliton. Being occupied by an unpaired electron in a neutral polymer, this single mid-gap electronic state has spin $\frac{1}{2}$ but no charge. It was suggested⁵⁸ that an electron could be added or removed from this state resulting in a spinless charge carrier.

Fesser, Bishop and Campbell⁵⁹ took this idea further and extended it to the more general case of polymers with a non-degenerate ground state including cis-polyacetylene and the vast majority of conjugated polymers. The presence of a charge on a polymer and the associated lattice distortion is termed a polaron (spin $\frac{1}{2}$) and is associated with the creation of two new electronic states in the energy gap spaced symmetrically about the midgap. In this model these states are produced by a pair of kinks between the low energy and high energy bond alternation schemes of which one contains the extra charge.

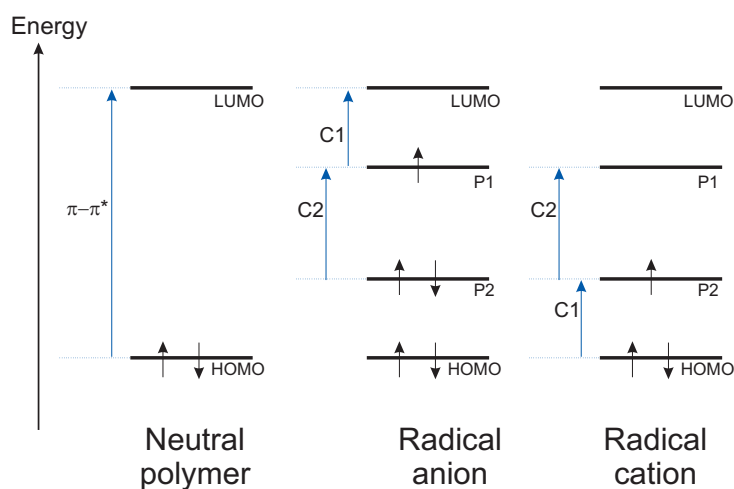


Figure 2.6: Schematic diagram showing the single electron states on the neutral and charged polymer. Optical transitions are indicative and the energy is not necessarily equal to the level spacing.

Since these original attempts to characterise the charge carrier, the field has moved towards quantum chemistry where the charge is regarded as a radical cation (+ve) or anion (-ve). A charge will typically extend over a few repeat units, alter the bond lengths to relax to the lowest energy configuration and in doing so induce two new electronic states in the energy gap as in the FBC model. With quantum chemical calculations, the chain is more realistically regarded as being made up of a series of finite conjugation segments rather than the infinite one-dimensional chains supposed in the original models. Figure 2.6 shows the two new states P1 and P2 inside the original HOMO-LUMO energy gap induced by adding or removing a charge from the neutral polymer. Ultimately the optical transitions are calculated under the CI method and do not necessarily correspond to these one-electron states however the energies will be similar to those marked on the diagram for symmetry-allowed transitions.

Förster Resonance Energy Transfer

Now that we have seen in figures 2.5 and 2.6 how singlets, triplets and charges can induce new absorptions we can understand the mechanism for energy transfer from singlet excitons to these species which can cause reduced fluorescence efficiency. This same mechanisms may also account for singlet exciton diffusion between chromophores of the same polymer and is called Förster Resonance Energy Transfer (FRET). FRET relies on dipole-dipole interactions between the excited donor state and the acceptor state. In this model, dipoles are assumed to be points which is not entirely valid in conjugated polymers as the intermolecular spacing is not large compared to the dipole length. Better line-dipole approximations exist but the point dipole method is commonly used. As dipole fields fall off with distance, r , as r^{-3} and the induced dipole on a nearby molecule also scales as r^{-3} the FRET rate, k_{FRET} , drops off as

$$k_{FRET} = \frac{1}{\tau} \left(\frac{R_0}{r} \right)^6 \quad (2.15)$$

where τ is the exciton lifetime and R_0 is the Förster radius. The Förster radius is given by

$$R_0^6 = \frac{9(\ln 10)\phi_0\kappa^2 J}{128\pi^5 n^4 N_A} \quad (2.16)$$

where n is the refractive index, κ is the dipole orientation factor (typically 2/3), ϕ_0 is the PL efficiency in the absence of any acceptors, N_A is Avogadro's number and J is the spectral overlap integral of the normalised donor emission spectra, $f_D(\lambda)$, and the acceptor molar extinction coefficient, $\epsilon_A(\lambda)$, given by

$$J = \int f_D(\lambda)\epsilon_A(\lambda)\lambda^4 d\lambda \quad (2.17)$$

where λ is wavelength. Note that although the spectra are involved no actual emission and absorption of a photon occurs.

Due to the short range of FRET, a reduction in the PL efficiency due to interactions with other photo-generated species is typically only observed with high intensity illumination and referred to as exciton-exciton annihilation. Charge carriers can also be produced following exciton-exciton annihilation and then exciton-charge quenching can be observed. The introduction of energy acceptors, either narrow energy gap molecules or charges through doping or electrical injection, can result in PL quenching at low light intensities. The sixth power means that the FRET rate changes dramatically around R_0 meaning that a diffusion-limited model can often be used where FRET occurs with a 100% probability within R_0 and 0% outside.

2.1.6 Electroabsorption

Electroabsorption is the effect by which the absorption of a polymer can shift in energy due to the presence of an applied field. Without the presence of an electric field, a polymer has an absorption spectra, $\alpha(E)$, corresponding to transitions between a set of orthonormal states, ψ_i with Eigenenergies E_i that are the solution to the Hamiltonian, H_0 . By applying an electric field the Hamiltonian is modified and hence the energy of these states. To find the change in absorption at a particular energy, E_0 , due to the perturbing field, a Taylor expansion can be done about this point with $\Delta E(\mathbf{F})$ being calculated from perturbation theory (where \mathbf{F} is the field).

$$\alpha(E) = \alpha(E_0) + \frac{\partial\alpha(E)}{\partial E}\Delta E + \frac{1}{2}\frac{\partial^2\alpha(E)}{\partial E^2}\Delta E^2 + \dots \quad (2.18)$$

The ΔE terms can be found by considering the change in the Hamiltonian due to the effect of an electric field on the energy of a charge/dipole distribution:

$$H = H_0 + \Delta H \quad (2.19)$$

$$\Delta H = \mathbf{m}\cdot\mathbf{F} - \mu\cdot\mathbf{F} = \mathbf{m}\cdot\mathbf{F} - e\mathbf{r}\cdot\mathbf{F} \quad (2.20)$$

where \mathbf{m} is the permanent dipole moment of the excited state and μ is the non-permanent transition dipole moment operator between the excited state and other states. Applying perturbation theory (first and second order) to this operator we get the shifts in energy of state E_i due to the electric field:

$$\Delta E_i^{(1)} = \langle \psi_i | \Delta H | \psi_i \rangle = \mathbf{m}\cdot\mathbf{F} \langle \psi_i | \psi_i \rangle + \langle \psi_i | e\mathbf{r}\cdot\mathbf{F} | \psi_i \rangle \quad (2.21)$$

$$\Delta E_i^{(2)} = \sum_{i \neq j} \frac{|\langle \psi_i | \Delta H | \psi_j \rangle|^2}{E_i - E_j} = \mathbf{m}\cdot\mathbf{F} \sum_{i \neq j} \frac{|\langle \psi_i | \psi_j \rangle|^2}{E_i - E_j} + \sum_{i \neq j} \frac{|\langle \psi_i | e\mathbf{r}\cdot\mathbf{F} | \psi_j \rangle|^2}{E_i - E_j} \quad (2.22)$$

Conventionally we say that the field is constant over the absorbing species and so the second term in the first order energy shift vanishes because $\mathbf{r}\cdot\mathbf{F}$ is thus an odd function. The first term in the second order shift also vanishes due to the orthogonality of the basis states. Putting first order shifts into the Taylor expansion gives:

$$\Delta\alpha_{LSE}(E) = \frac{\partial\alpha(E)}{\partial E}\mathbf{m}\cdot\mathbf{F} + \frac{1}{2}\frac{\partial^2\alpha(E)}{\partial E^2}|\mathbf{m}\cdot\mathbf{F}|^2 \quad (2.23)$$

which reduces to

$$\Delta\alpha_{LSE}(E) = \frac{1}{2}\frac{\partial^2\alpha(E)}{\partial E^2}|\mathbf{m}\cdot\mathbf{F}|^2 \quad (2.24)$$

for an isotropic distribution of permanent dipoles. Putting the second order shifts into the Taylor expansion gives:

$$\Delta\alpha_{QSE}(E) = \frac{d\alpha(E)}{dE} \sum_{i \neq j} \frac{|\mu_{ij} \cdot \mathbf{F}|^2}{E_i - E_j} + \frac{1}{2} \frac{\partial^2 \alpha(E)}{\partial E^2} \left(\sum_{i \neq j} \frac{|\mu_{ij} \cdot \mathbf{F}|^2}{E_i - E_j} \right)^2 \quad (2.25)$$

where $\mu_{ij} \cdot \mathbf{F} = \langle \psi_i | e \mathbf{r} \cdot \mathbf{F} | \psi_j \rangle$. This reduces to

$$\Delta\alpha_{QSE}(E) = \frac{d\alpha(E)}{dE} \sum_{i \neq j} \frac{|\mu_{ij} \cdot \mathbf{F}|^2}{E_i - E_j} \quad (2.26)$$

as the second term is negligible. As well as the shifts in the eigenstates of the system, there can also be a transfer of oscillator strength to previously forbidden transitions. Including this term (which has a negative contribution following the neutral absorption) we get the total change of absorption due to a perturbing electric field as⁶⁰:

$$\Delta\alpha(E) = c\alpha(E) + \frac{d\alpha(E)}{dE} \sum_{i \neq j} \frac{|\mu_{ij} \cdot \mathbf{F}|^2}{E_i - E_j} + \frac{1}{2} \frac{\partial^2 \alpha(E)}{\partial E^2} |\mathbf{m} \cdot \mathbf{F}|^2 \quad (2.27)$$

where $c < 0$.

2.2 Charge transport models

Armed with a quantum chemical understanding of the nature of the charge carrier on a single conjugated polymer the challenge is to understand how this self-localised species gives rise to conductivity on a macroscopic scale. This conductivity has experimentally been determined to, in general, increase with temperature,⁶¹ charge density⁶² and electric field⁶³ and a successful model must reflect this.

A unified description of charge transport that can account for the observed behaviour in all conjugated polymer systems is difficult to come by as the dominant mechanism limiting charge transport depends on the relative importance of the following three parameters: polaron binding energy (electron-phonon interactions), inter-chain electronic coupling and disorder. The wide variety of chemical structures and their associated packing arrangements can cause these values to vary significantly.

In the following sections, a few of the most commonly used charge transport models are discussed which are also summarised in recent reviews by Tessler⁶⁴ and Coropceanu.⁶⁵

2.2.1 Multiple Trap and Release/Mobility edge model

We have seen above that conjugated polymers can behave as semiconductors in that there is an energy gap between occupied and unoccupied molecular orbitals and these orbitals

can support neutral or charged excitations without breaking any bonds. In crystalline inorganic semiconductors this energy gap is between two band edges that represent a continuum of delocalised states. This accessibility of empty states with higher momentum means that upon application of an electric field charge carriers start to accelerate or in momentum space (k -space) the fermi surface starts shifting by Δk . At some point this increase in k reaches an equilibrium with scattering processes limiting the velocity of carriers resulting in a simple linear relationship between velocity and electric field. The constant of proportionality, mobility, μ , is limited at low temperatures by the impurity scattering time τ_i and at high temperatures by the phonon scattering time τ_{ph} .

For organic materials with strong inter-molecular electronic coupling due to close, ordered packing and weak self-localisation due to low polaron binding energy, one might assume that a similar situation with delocalised carriers could occur. However, even the most ordered conjugated polymers have many defects including boundaries between crystalline regions, packing defects and unintended impurities. It was shown by Mott and Twose⁶⁶ that defects in inorganic crystalline solids can lead to localised electronic states in the forbidden energy gap and an intuitive model where a temperature-dependent fraction of carriers are trapped in these immobile states with the remainder being unaffected has been applied successfully to amorphous silicon⁶⁷. A number of people have also applied this multiple trap and release (MTR) model to semicrystalline polymer systems as it often can fit the experimental data very well with an Arrhenius thermally activated mobility of the form

$$\mu \propto \exp\left(\frac{\varepsilon_T}{k_B T}\right) \quad (2.28)$$

where ε_T is the energy of the trap level below the mobility edge, or a characteristic trap energy for an energetic distribution of traps.

It is difficult to see how this model can truly apply to the majority of polymer systems as it requires a uniform distribution of traps in space combined with delocalised electronic states. This may be conceivable in molecular single crystals with randomly positioned packing defects or impurities that act as traps however in the vast majority of cases for semicrystalline polymers it is the grain boundaries between crystalline regions that likely dominate transport. Grain boundaries may include some trap states but unlike the MTR model this means they are not uniformly distributed and are more likely to hold up the transport rather than simply modulate the density of mobile charges. These grain boundaries have also been modelled as tunnelling barriers which, if dominant, can lead to temperature independent mobility which does not rule out that the MTR model could

apply in the crystalline regions, just that it is not the limiting mechanism.

The most commonly used charge transport models consider that all transport is limited by hopping between localised states without invoking delocalisation over multiple polymer segments. These hopping models are more apt for the low-mobility disordered conjugated polymers studied in this thesis.

2.2.2 Hopping models

Conduction arising from localised states was considered independently by Anderson,²² Mott⁶⁸ and Conwell⁶⁹ for the case of lightly-doped inorganic semiconductors at low temperatures. This form of transport, also known as *impurity conduction*, occurs when there is insufficient thermal energy to ionise the dopants to produce free carriers. As explained by Mott and Twose⁶⁶, the localised states are electrons (holes) bound to positively (negatively) charged impurities in enlarged hydrogen-like states. Localisation occurs when fluctuations in site energy exceed the *resonance energy* between the wavefunctions of adjacent donors and acceptors which prevents the formation of an extended *impurity band*. The phonon-assisted tunnelling of Miller and Abrahams⁷⁰ is the version of this model that is often applied to disordered organic semiconductors however due to higher electron-phonon coupling in these systems, polaron effects may also effect the hopping mechanism and this forms the basis of another set of hopping models.

Any hopping model first must consider the simple rate equation which expresses the temporal evolution of the probability, $f_i(t)$, that a charge is on site i when it has the option to hop to a site j with a rate W_{ij} or indeed from site j with a rate W_{ji} .

$$\frac{\partial}{\partial t} f_i(t) = \sum_{j \neq i} \kappa_{ji} f_j(t) [1 - f_i(t)] - \sum_{j \neq i} \kappa_{ij} f_i(t) [1 - f_j(t)] - \lambda_i f_i(t) \quad (2.29)$$

The expressions $f_j(t)[1 - f_i(t)]$ and $f_i(t)[1 - f_j(t)]$ ensure that hopping only occurs when the donor and acceptor site are occupied and unoccupied respectively although this can normally be assumed to be always the case at low charge densities. The decay rate λ_i expresses the rate of loss of charges through trapping or recombination.

It is clear from the master equation 2.29 that, given it can be solved, the hopping rates are the most fundamental properties of a given system. As alluded to above, there are two popular expressions for hopping rates known as the semi-classical Marcus expression⁷¹ and the Miller-Abrahams rate⁷⁰ with the former being based on polaronic effects and the latter on disorder. In the following two sections we will see how these rates have been applied, what predictions they give and how successful they have been.

2.2.3 Polaronic Hopping Models

The concept of polaron transport was first considered by Fröhlich in 1950⁷² for the case of an electron travelling in an ionic crystal. An electron would, he surmised, induce a displacement of nearby ions creating a potential well for the electron. However, unlike previous models, including that of Landau⁷³, that predicted self-trapping in this well, Fröhlich showed that the charge plus distortion, or polaron quasi-particle, was able to travel through the lattice much like a free electron and is now known as a Fröhlich polaron. This concept was extended by Holstein^{74,75} who considered small polarons where the reorganisation of nuclei only affects those within a distance of approximately one lattice constant. Holstein treated electronic coupling to nearby sites, measured by the electron transfer integral, J , as a perturbation which is valid in the case of weak coupling regime. Two types of charge transfer processes in which the total number of phonons were conserved or not during electron transfer were noted and labelled diagonal or non-diagonal respectively. The diagonal transitions correspond to coherent electron transfer (tunnelling) within a narrow polaron band and dominates transport at low temperatures. Coherent transfer is disrupted by phonon scattering and so the conduction would be predicted to reduce with increasing temperature. The non-diagonal transitions correspond to decoherent electron hopping which is a thermally (phonon) activated random diffusion processes and dominates transport at higher temperatures. In this hopping mechanism, the interaction of an electron-phonon with an optical phonon of energy $\hbar\omega_0$ gives rise to an electron transfer rate, κ , which is given by the following expression

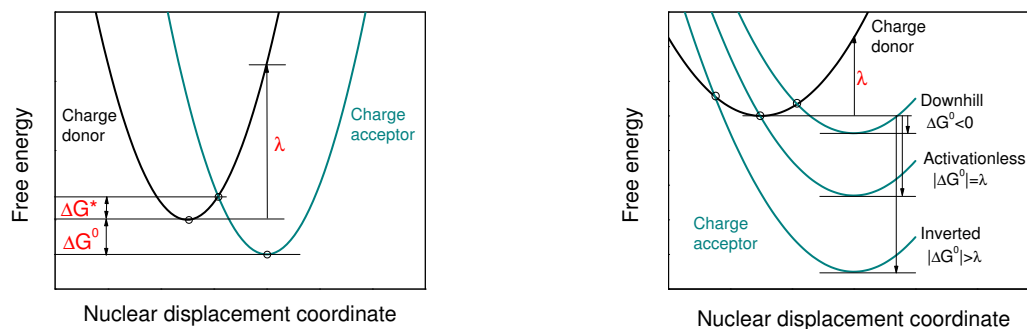
$$\kappa = \frac{J^2}{\hbar^2\omega_0} \sqrt{\frac{\pi}{g^2 \operatorname{csch}\left(\frac{\hbar\omega_0}{2k_B T}\right)}} \exp\left[-2g^2 \tanh\left(\frac{\hbar\omega_0}{4k_B T}\right)\right] \quad (2.30)$$

where $g^2 = E_{pol}/\hbar\omega_0$ is a measure of the strength of electron-phonon coupling in the system as characterised by a polaron binding energy E_{pol} . Electron transfer occurs when optical phonons in the system couple to nuclear motion and put the donor molecule in a configuration where the energy is equal to that of a neighbouring acceptor. This process is known as non-adiabatic hopping because J is small and so the neighbouring electronic states do not mix.

A similar expression for the non-adiabatic transfer rate is given by semi-classical Marcus theory⁷⁶ which derives from the field of chemistry and considers electron transfer between radicals in solution. In this case not only the reorganisation energy, $\lambda = 2E_{pol}$, but the difference in donor and acceptor site energies, as characterised by a difference in free energy, ΔG^0 , are included, but is otherwise identical to the classical limit of the

Holstein model.

$$\kappa_{ij} = \frac{J^2}{\hbar} \sqrt{\frac{\pi}{\lambda k_B T}} \exp \left[-\frac{-(\lambda + \Delta G^0)^2}{4\lambda k_B T} \right] \quad (2.31)$$



(a) Normal Marcus regime.

(b) As figure 2.7(a) but with activationless and inverted charge transfer regimes.

Figure 2.7: Free energy curves for acceptor and donor species involved in charge transfer within the semi-classical Marcus Theory picture. λ represents the reorganisation energy, ΔG^* the energy barrier and ΔG^0 the total change in free energy.

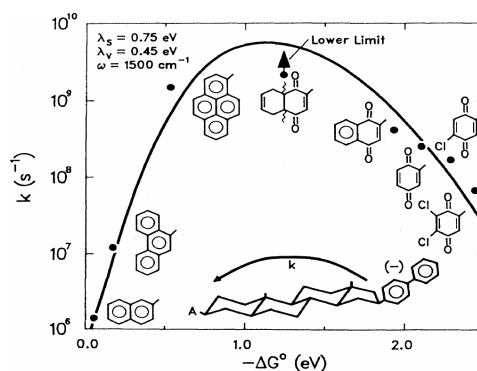


Figure 2.8: Experimental evidence for the inverted Marcus regime from reference⁷⁷

Experiments by Miller et al.⁷⁷ confirmed the presence of the so called inverted Marcus regime⁷¹ whereby as the driving force for electron transfer is increased, a maximum rate is obtained corresponding to activationless transfer before again requiring energy to reach a favourable configuration (see figure 2.8).

For the case of large electronic coupling (adiabatic hopping), the donor and acceptor states mix leading to a gap at the crossing point of energy $2J$. This can lower the activation energy for electron transfer to $\lambda/4 - J$ and when there is very strong coupling the barrier can be completely removed.

Whilst polaron models reveal the mechanism behind band-like to thermally activated hopping in idealised organic semiconductors, the majority of conjugated polymers contain significant static disorder and many models neglect polaronic effects completely believing disorder to be the limiting factor.

2.2.4 Disorder Hopping Models

In many conjugated polymers disorder is significant. Disorder is characterised as being *diagonal* or *off-diagonal* where these terms originate from the matrix describing the energy of the two sites. Diagonal terms represent the energy of a particular site which can vary due to the influence of nearby static dipoles and variations in conjugation length as observed by the Gaussian broadening observed in absorption spectra. Off-diagonal terms represent the interaction between neighbouring sites which can vary due to differences in inter-molecular spacing and orientation. The Miller-Abrahams hopping rate,⁷⁰ κ_{ij}^{MA} , mentioned above is given by

$$\kappa_{ij}^{MA} = \nu_0 \exp(-2\alpha r_{ij}) \times \begin{cases} \exp(-E_{ij}/k_B T) & E_{ij} > 0 \\ 1 & E_{ij} < 0 \end{cases} \quad (2.32)$$

where α is the inverse localisation length, r_{ij} is the inter-site spacing, E_{ij} is the difference in site energy and ν_0 is the hopping attempt frequency or typical phonon frequency. Note that unlike the Marcus expression for polaron hopping, the rate becomes constant for all downhill hops and does not include polaronic effects. The Miller-Abrahams rate appears in a number of models with various density of states functions and both analytical and computational methods of calculating the overall conductivity from the jump rate. A few of these disorder models are explored next.

Variable Range Hopping - Mott

In what is referred to as the Variable Range Hopping (VRH) model, Mott took the Miller-Abrahams rates but related the energy difference, E_{ij} , from equation 2.32 to the distance between sites, R , assuming a uniform density of states, ρ around the Fermi energy.

$$E_{ij} \sim \frac{3}{4\pi R^3 \rho} \quad (2.33)$$

For low barrier hops, there are less nearby sites to hop to but for higher energy hops there are more nearby sites. By optimising the expression for hopping rate with this constraint Mott showed that hopping occurs in an energy band, $\Delta\varepsilon$, of width⁶⁴

$$\Delta\varepsilon = \frac{(8\alpha k_B T)^{3/4}}{\frac{4}{3}(\pi\rho)^{0.25}} \quad (2.34)$$

Using the optimised hopping rate, the following power law temperature dependence of the mobility is obtained

$$\mu_{VRH} \propto \exp \left[- \left(\frac{T_0}{T} \right)^{\frac{1}{n+1}} \right] \quad (2.35)$$

where n is the dimensionality of the system and can be between 1 and 3 for conjugated polymers and T_0 is a constant that characterises the disorder. This simple intuitive model does not have any field or charge density dependence but has been used to fit the temperature dependence of mobility in conjugated polymer systems.

Hopping in exponential DOS using analytical percolation - Vissenberg and Matters

A popular model that addresses the charge density dependence of mobility that has been observed in conjugated polymers⁶² is the Vissenberg-Matters model.⁷⁸ The Vissenberg-Matters method is based on the percolation approach⁷⁹ where Miller-Abrahams hopping rates are converted to resistors that form a network. Only resistors that have a conductance above a critical value, G_c , are counted and conduction is dependent on there being a percolation path through the network. The density of states takes the following exponential form

$$g(\epsilon) = \frac{N_t}{k_B T_0} \exp \left(\frac{\epsilon}{k_B T_0} \right) \quad (-\infty < \epsilon \leq 0) \quad (2.36)$$

where N_t is the number of states per unit volume and T_0 is related to the width of the exponential distribution. The conductivity, σ , is then given by

$$\sigma = \sigma_0 \left(\frac{\delta}{\Gamma(1 - T/T_0)\Gamma(1 + T/T_0)} \frac{\pi T_0^3 N_t}{\phi[2\alpha T]} \right)^{\frac{T_0}{T}} \quad (2.37)$$

where Γ is the gamma function and ϕ is the ratio of conduction paths to hopping sites and usually 2.8 in three-dimensional amorphous systems.⁸⁰ With a conductivity that increases

with charge density it is possible to explain the increase in mobility, μ , with gate voltage, V_g , observed in many transistors and an expression for this mobility is

$$\mu = \frac{\sigma_0}{e} \left(\frac{\pi(T_0/T)^3}{(2\alpha)^3 \phi \Gamma(1 - T/T_0) \Gamma(1 + T/T_0)} \right)^{T_0/T} \times \left(\frac{(C_i V_G)^2}{2k_B T_0 \epsilon_{sc}} \right)^{T_0/T-1} \quad (2.38)$$

where C_i is the dielectric capacitance per unit area (see section on transistors), ϵ_{sc} is the semiconductor dielectric constant and all other constants have the same meanings as above in this section. The temperature dependence of the mobility comes out as being Arrhenius-like as in the MTR model and the model has successfully been applied to experimental transistor curves.⁸¹

Hopping in Gaussian DOS using Monte Carlo - Bässler

Analytical approaches to hopping in a Gaussian density of states have been attempted by Arkhipov⁸² using the effective transport energy approach but here we see a computational method for solving this problem. Bässler numerically creates a landscape of sites with a Gaussian spread of energetic and positional disorder with widths σ and Σ respectively. A charge is introduced to a site and the Miller-Abrahams jump rates are then applied to allow the charge to move under the influence of a field, F , which has the effect of lowering the energy of the sites in the direction of the field. A Monte-Carlo approach is then used to repeat the process over and over again until macroscopic properties of the system converge. It is noted that regardless of the initial energy of the carrier, the distribution of carriers after a time is centered at an energy $\langle \epsilon_\infty \rangle = -\sigma/k_B T$ as shown in figure 2.9. Note that this is possible because the calculation is done for single carriers which is to say it is the low density limit and filling of the states with Fermi statistics does not apply.

An expression for the field and temperature dependence of the mobility is given by

$$\mu = \mu_0 \exp \left[- \left(\frac{2\sigma}{k_B T} \right)^2 \right] \times \begin{cases} \exp \left(C \left[\left(\frac{\sigma}{k_B T} \right)^2 - \Sigma^2 \right] \sqrt{F} \right) & \Sigma \geq 1.5 \\ \exp \left(C \left[\left(\frac{\sigma}{k_B T} \right)^2 - 2.25 \right] \sqrt{F} \right) & \Sigma < 1.5 \end{cases} \quad (2.39)$$

where C is a constant that depends on the site spacing. The \sqrt{F} dependence of mobility bears a resemblance to the generic fitting equation⁸³ with a Poole-Frenkel field dependence commonly used to fit temperature and field dependence of mobility. In the low field limit the Bässler model leads to a non-Arrhenius temperature dependence of the form

$$\mu = \mu_0 \exp \left(- \frac{T}{T_0} \right)^2 \quad (2.40)$$

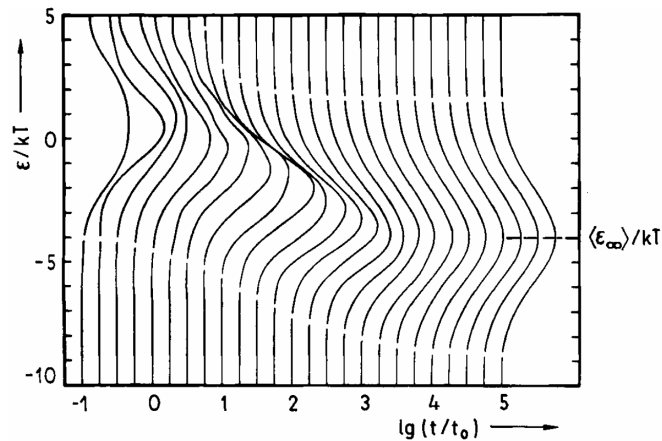


Figure 2.9: Temporal evolution of the distribution of charge carrier energies in a Gaussian DOS as calculated with the Bässler Gaussian Disorder model and assuming low enough charge densities to ignore Fermi statistics.

which is fairly difficult to distinguish from Arrhenius behaviour in the limited temperature ranges available for conjugated polymers.⁸⁴ The Bässler model does not deal with field dependence very well at low fields although this problem was overcome by introducing correlations in site energy in the Correlated Disorder Model (CDM). The CDM mobility for an average site spacing, a , is given by the empirical formula⁸⁵

$$\mu = \mu_0 \exp \left[- \left(\frac{3\sigma}{5k_B T} \right)^2 \right] \exp \left[C_0 \left(\left(\frac{\sigma}{k_B T} \right)^{3/2} - \Gamma \right) \sqrt{\frac{eaF}{\sigma}} \right] \quad (2.41)$$

where $C_0 = 0.78$ and $\Gamma = 2$.

2.2.5 Applicability of various models

It is clear that any complete model that can be applied to any conjugated polymer system should include both disorder and polaron effects although it is believed that disorder completely dominates in amorphous polymers with mobilities of less than 10^{-2} cm²/Vs. The disorder models have shown some success at explaining the temperature and field dependence of mobility although do not contain the physics to describe polaronic effects which may be significant in high mobility semicrystalline conjugated polymers. On the other hand, polaron models alone give unreasonable large activation energies for transport.⁸⁴ In terms of combining both effects, Bässler et al. suggested that, in the low field

limit, the activation energy is simply the sum of the disorder and polaron contributions.⁸⁶ Correlated disorder has also been introduced into the small polaron model by Parris et al.⁸⁷ which uses reasonable values of activation energy (50-500meV) and transfer integrals (1-20meV) to fit experimental temperature and field-dependent data. Fishchuck et al.⁸⁸ have used a Marcus hopping rate in a disorder model in a similar way and noted recently⁸⁹ that polaron effects can explain why some materials show a smaller dependence of mobility on charge density than others.

Despite the great advances in both the ability to calculate polaron energies, transfer integrals and to combine them with disorder to predict measurable parameters many would agree that the field is not yet at the stage where a theoretician could tell a chemist exactly how to design a polymer that would give the best transistor or solar cell performance. With the ability to synthesise new materials on a weekly basis it is currently the chemists and experimentalists who with a combination of intuition and luck are making leaps in this area.

2.2.6 Injection of charges into organic semiconductors

Making electrical contact to inorganic semiconductors is well understood and can be achieved either through matching the work function, ϕ , of the metal to the conduction/valence band of the semiconductor or through high doping of the region around the contact; the latter causing a minimal region of band bending which creates a sufficiently narrow energy barrier for tunnelling. In organic electronics doping of the contacts is not so straightforward, although it has been observed for both electron⁹⁰ and hole injection.⁹¹ Work function matching is therefore the most common technique used and relies on either careful selection of the electrode, or modification of its surface. Relying on the natural work function does not give an adequate range of stable and easy-to-deposit metals that give ohmic injection to any arbitrary polymer. Some popular electrode metals include gold ($\phi = 5.3\text{eV}$),⁹² aluminium ($\phi = 4.3\text{eV}$),⁹³ silver ($\phi = 4.1 - 4.5\text{eV}$),⁹⁴ chromium ($\phi = 4.58\text{eV}$)⁹⁵ and calcium ($\phi = 3.0\text{eV}$)⁹⁶ although transparent conducting oxide indium tin oxide (ITO $\phi = 4.6\text{eV}$)⁹⁷ and the conducting polymer PEDOT:PSS ($\phi = 5.2\text{eV}$)⁹⁸ are also common. These values for metal work function are typically measured in high vacuum on atomically clean surfaces and depend on which crystallographic plane is measured. In reality, the actual work function will depend on the processing conditions, for example gold can exhibit a work function of 4.7eV after exposure to atmosphere⁹⁹ and aluminium can have its work function reduced to 4.1eV.¹⁰⁰

Work function modification can be achieved with self-assembled monolayers (SAMs)

on gold or silver electrodes^{101,102} or thin transition metal oxide layers¹⁰³ such as molybdenum trioxide (MoO_3)¹⁰⁴. The SAM method can extend the range of the gold work function over many eV as investigated recently by Rissner et al.¹⁰⁵ who studied, with computational DFT techniques, biphenyl with various docking and head groups. Pyridine docking group gave rise to the largest work function decrease, followed by the isocyanide and the thiolate. For the head, cyano and fluoro groups could take the work function up to 8eV or alternatively it could be decreased to around 1eV with dimethyl-amine or amine groups.

With an accurate measure of the actual work function and the HOMO and LUMO levels of the semiconductor, one might expect that the injection barrier could be predicted to be the energy difference and would thus follow the Mott-Schottky law. If the work function does not lie in the energy gap, the injection barrier should be independent of work function in behaviour described as Fermi level pinning caused by the formation of an interface dipole. In practice however the slope of injection barrier vs work function is typically less than one. Departure from the Schottky-Mott limit has been attributed to a number of effects including charge transfer to or from the metal, image charges, chemical interaction, interface states, the pillow effect and permanent interface dipoles. For a review of the issue of charge injection including descriptions of these effects see Shen et al.¹⁰⁶, Ishii et al.¹⁰⁷ and Kahn et al.¹⁰⁸

In some devices such as top gate, bottom contact transistors, injection can also be limited by transport through the bulk of the semiconductor between the electrodes and the highly conductive accumulation layer. Although the distance that charges have to travel through the bulk is only a few tens of nanometres, the low number of free carriers in this region has been shown to provide the dominant contribution to contact resistance. This was observed by Richards et al.¹⁰⁹ where, through the use of four-point probe measurements, both the injection and collection resistance at the source and drain respectively were found to be identical.

2.2.7 Trapping and chemical reactions

So far we have just considered charge transfer between conjugated segments of a polymer with various densities of states. It has been observed in numerous examples however that charges can become trapped in conjugated polymer devices causing unwanted effects such as threshold voltage shifts in transistors or a reduction in current in light emitting diodes. Trapping in devices is often referred to as bias stress as it occurs during device operation. There is still much debate as to whether the trapping of charges is due to intrinsic structural defects¹¹⁰, impurities¹¹¹ or bipolaron formation¹¹² in the semiconductor

or extrinsic factors such as water and oxygen or, in the case of transistors, trap states in the dielectric¹¹³ or mobile ions from the substrate¹¹⁴. There is a recent review into this field by Sirringhaus¹¹⁵ and a few key concepts are outlined here.

A key result relating to trapping by extrinsic effects comes from the story of n-type (electron) transport in organic materials. It was long believed that only hole transport was possible in a large number of cases, even when measured in inert conditions however Chua et al.³¹ noted that it was hydroxyl groups on the surface of the commonly used SiO₂ dielectric that trapped electrons. By replacing the SiO₂ with a dielectric lacking these trapping groups Chua showed that electron transport was fairly ubiquitous in conjugated polymers under inert conditions. In the more general case, in atmospheric conditions, a negatively charged polymer (radical anion) is susceptible to oxidation by a number of atmospheric species including oxygen and water as noted by de Leeuw et al.¹¹⁶

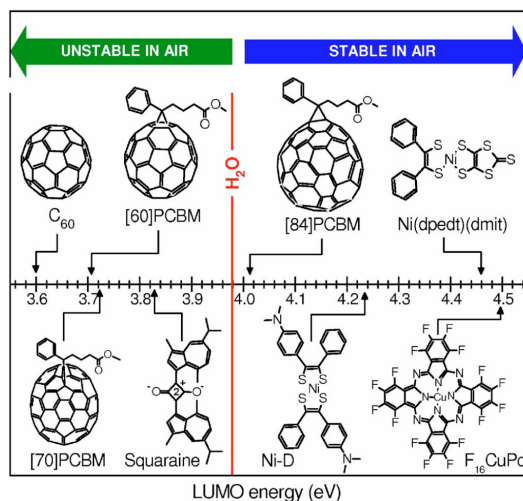
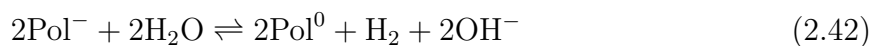


Figure 2.10: Diagram showing the stability of anions of various organic molecules in air from.¹¹⁷

Figure 2.10 shows the LUMO energy for a range of different small molecules and the redox potential for water. It is only molecules or polymers with a LUMO level lower than 4eV¹¹⁷ that are able to carry an excess electron in the presence of water without losing it to water to form negative hydroxyl groups and hydrogen molecules as shown in equation 2.42 where Pol represents the polymer.



The requirement for a deep LUMO level is achieved through the incorporation of

electron-withdrawing groups such as cyano, perfluoroalkyl or diimide.¹¹⁸ As a large number of conjugated polymers have a LUMO level higher than 4eV electron transport is typically only observed when devices are characterised in an inert environment such as in vacuum or nitrogen. The active layer in a solar cell is typically buried beneath 100nm of aluminium with a glass cover slip bound on with resin which allows measurement in air. For transistors, it has recently been observed that fluorinated dielectrics can reduce the effect of exposure to atmosphere.¹¹⁹

Whatever the nature of the trapped charges, they often either partially or totally detrapp if left in a dark inert atmosphere to recover. Salleo et al.¹²⁰ observed that the degree to which total detrapping occurred in P3HT transistors depended on the duration of initial device operation allowing the allocation of long-lived *deep traps* and short-lived *shallow traps*. Recovery has shown to be expedited with illumination^{121,122} at wavelengths where the semiconductor absorbs.

Calhoun et al.¹²³ recently investigated the effect of charge trapping in the dielectric layer in p-type tetracene single crystal transistors. It was noticed that positive charge trapping simply increased the magnitude of the negative turn on voltage required for hole accumulation. On the other hand negative charge trapping shifted the turn on voltage the other way and reduced the mobility of the holes due to the coulombic potential wells produced by the oppositely charged trapped electrons in the adjacent layer. The implication for ambipolar transistors where both hole and electron operation can lead to trapping could mean both threshold shifts and a reduction in mobility may be expected.

In terms of the energetics of traps, a state in pentacene related to water¹²⁴ has been analysed by Pernstich et al.¹²⁵ who suggest that the step-like current increase in the subthreshold region of the p-type transistor, induced by negative bias stress, can be modelled by hole traps at a discrete energy level. This kind of trap is neutral when empty and positively charged when occupied by a trapped hole. On the other hand, Scheinert et al.¹²⁶ used the concept of bulk acceptor states, also at a discrete energy, which are negative when empty and neutral when occupied by a hole to explain the positive turn on voltage and subthreshold behaviour in regioregular poly(3-dodecylthiophene). This behaviour is common in thiophenes where chemical changes can occur in a film simply by exposure to atmosphere and effects have been seen in the dark with oxygen¹²⁷, with wet nitrogen (no mention of lighting conditions)¹²⁸, in air in the dark¹²⁹ and with dry oxygen (enhanced by light and bias).¹³⁰ Reactions involving oxygen are believed to be with the optically excited (via inter-system crossing) triplet state in P3HT resulting in radical cations and O_2^- and has been seen to be reversible¹³¹. Despite the various conclusions about the cause, the result is trapped negative charges that can stabilise mobile holes

to maintain charge neutrality giving the film an intrinsic conductivity. To turn off this conductivity, the film must be depleted by applying positive gate voltages indicating that the negatively charged species indeed behaves much like a conventional acceptor state.

2.2.8 Transport at interfaces

In transistors, charge transport occurs in a region around 1-2nm thick in the semiconductor at the interface with the insulator making the nature of this interface very important. It was noticed by Veres et al.²³ in transistors with a polytriarylamine (PTAA) or polyfluorene copolymer (F8T2) as the semiconductor that the mobility depended on the dielectric constant of the insulator layer. The model used to explain this behaviour was that the static disorder at the interface due to randomly orientated dipoles in the dielectric broadens the density of states in the semiconductor which reduces mobility as would be predicted in disorder models. An attempt to quantify this model was made by Richards et al.¹³² who used a Vissenberg-Matters charge transport model combined with analytical expressions for dipole-induced disorder broadening to predict the mobility in PTAA. In this paper, the same concept was used to explain the *reduction* in mobility with gate voltage as a higher fraction of the charge becomes nearer to the disordered interface region. Martinelli et al.¹³³ took this further and used quantum chemical and force-field calculations to numerically compute disorder broadening in pentacene with polystyrene (PS) and polymethyl methacrylate (PMMA) dielectrics. The result was a reduction in mobility by 12 times with PMMA as compared to PS due to the polar bonds in the carbonyl groups in PMMA. This increase in mobility exceeds the reduction in accumulated charge due to the lower dielectric constant (for a given dielectric thickness and gate voltage) meaning that a low dielectric constant insulator without polar groups can be the dielectric of choice to give higher currents.¹³⁴

A similar effect has been observed in single crystal organic semiconductors with highly polarisable dielectrics where it is believed that Fröhlich polarons⁷² occur with the charge being coupled to a polarisation cloud in the dielectric. The Fröhlich polaron causes localisation of charge carriers resulting in a transition from metallic-like to insulating-like mobility as measured by the temperature dependence.¹³⁵ This is not expected in low mobility amorphous conjugated polymers where semiconductor disorder already causes localisation and the dielectric disorder model is expected to dominate. Recently it has been suggested,¹³⁶ in ordered polymers such as pBTTT, that alkyl side chains can provide protection from energetic disorder at interfaces by providing a spacing of around 0.3nm between the charge transport and the dielectric.

Modification of the interface in bottom gate transistors by self-assembled monolayers (SAMs) can play an important role in both the electronic and morphological behaviour of the semiconductor. Pernstich et al.¹³⁷ were able to tune the turn on voltage of pentacene and rubrene transistor by the application of SAMs with various functional groups. Equally, some of the most ordered semiconducting polymers¹³⁸ are often fabricated on substrates treated with SAMs such as octyltrichlorosilane (OTS) to give the best ordering and hence charge transport properties.

2.3 Device physics

2.3.1 Hole/Electron only devices

One of the most basic devices to measure charge transport in conjugated polymers is a hole-only or electron-only device where the polymer is in between two electrodes whose work functions are matched to the HOMO or LUMO respectively. Typically undoped and with energy gaps too large to allow thermal promotion of electrons from the HOMO to LUMO states, these polymers have little or no intrinsic conductivity; conduction occurring mostly through injection from the contacts. In the case of a unipolar co-facial or sandwich structure with ohmic contacts, no traps, field-independent mobility and dielectric constant, ϵ_r , the current can be derived from Poisson's equation to be

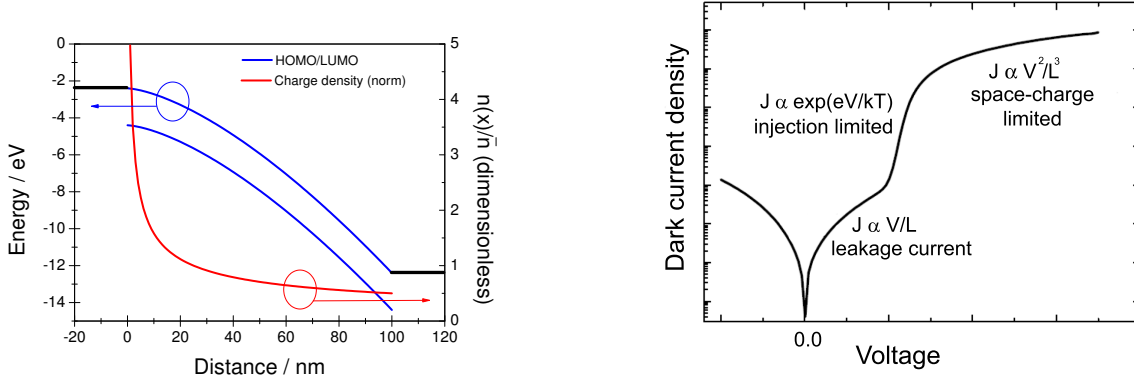
$$J = \frac{9}{8} \mu \epsilon_0 \epsilon_r \frac{V^2}{L^3} \quad (2.43)$$

Equation 2.43 is known as the Mott-Gurney equation for space-charge limited current (SCLC) which is an analogue of Child's law for the vacuum diode. There are some remarkable properties of this type of transport including field, $F(x)$, potential, $\phi(x)$, and charge density, $n(x)$, profiles that are independent of the polymer mobility and dielectric constant:

$$\frac{F(x)}{\bar{F}} = \frac{3}{2} \left(\frac{x}{L}\right)^{1/2}, \quad \frac{\phi(x)}{\phi} = \left(\frac{x}{L}\right)^{3/2}, \quad \frac{n(x)}{\bar{n}} = \frac{1}{2} \left(\frac{L}{x}\right)^{1/2} \quad (2.44)$$

where \bar{F} is the average field, ϕ is the applied potential and \bar{n} is the spatially-averaged charge density. Figure 2.11(a) shows the energy levels in an electron-only device exhibiting SCLC where it can be seen that the build up of charge density in the device flattens the potential in the polymer and thus reduces the field near the injecting electrode. In a realistic device, the current may be limited by leakage at low voltages and non-ohmic

injection at intermediate voltages before entering the SCLC regime as shown in figure 2.11(b).



(a) Energy diagram of an electron-only device under forward bias.

(b) Current vs voltage plot for a hole/electron-only device (adapted from reference⁴⁷).

Figure 2.11: Illustration of the potential, charge density and current-voltage characteristic of single carrier devices with ohmic contact.

In a lateral or co-planar device it has been predicted that SCLC is modified to the following equation¹³⁹ which has a different dependence on inter-electrode spacing L .

$$J = \frac{2\mu\epsilon_0\epsilon_r}{\pi} \frac{V^2}{L^2} \quad (2.45)$$

Some modelling predicts that due to the geometry of the electrodes in the co-planar case (flat and thin), the sharp edges of the electrodes may enhance the field due to the blade effect.¹⁴⁰ In this scenario and in the more general cases of devices with contact resistance, field-dependent mobility and trapping it becomes hard to find an analytical solution and numerical methods are typically used to fit data. An improved expression for the total current in the case of a field-dependent mobility is given by:¹⁴¹

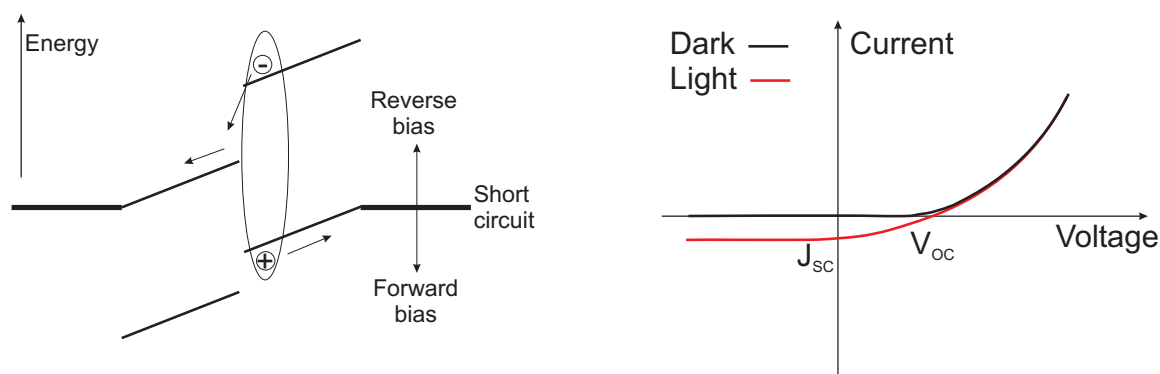
$$J = \frac{9}{8}\epsilon_0\epsilon_r\mu_0 \exp\left(0.891\gamma\sqrt{\frac{V}{L}}\right) \frac{V^2}{L^3} \quad (2.46)$$

2.3.2 Diodes

A diode is a two terminal electronic component that only conducts significant current in one direction. In organic electronics this is usually achieved by controlling the injection barriers from the contacts such that injection is only possible in one biasing direction (see

figure 2.11). The most common diode configuration is the co-facial or sandwich structure where a polymer is coated onto a pre-existing electrode and then a second electrode is deposited on top of that allowing inter-electrode distances of less than 100nm. For light-emitting diodes and photovoltaics the first electrode is usually transparent Indium-Tin Oxide (ITO) coated with a thin layer of the conducting polymer PEDOT:PSS. The PEDOT:PSS gives a smoother homogenous surface and higher work function compared to bare ITO for lower dark current and improved hole injection. A thick layer of aluminium is commonly used for the top electrode as it has a low work function, reflects nearly all of the light that would otherwise be wasted and helps to encapsulate the device to protect it from atmospheric species that lead to polymer degradation. Diodes can be driven with large forward bias to emit light as injected electrons and holes recombine or, under illumination, can generate a current as photo-excitation leads to charge generation. Both of these types of device have received further development to increase efficiency. Light emitting diodes (OLEDs) typically consist of an emissive layer in-between electron-transporting and hole-transporting layers¹⁴² to improve injection, balance mobilities and keep the excitons further from the electrodes to prevent quenching of the luminescence. Phosphorescent materials have also been added to OLEDs to harvest light from the weakly emitting triplet exciton states¹⁴³ and the main obstacle to 100% efficiency of light emission is now the outcoupling of light. Photovoltaics (OPVs) are characterised by light absorption leading to exciton formation, exciton diffusion, exciton dissociation, charge separation and charge collection. Efficiencies have been improved by having a heterojunction between two different polymers within the device either as a bilayer¹⁰ or blend.^{11–13} The heterojunction, as shown in figure 2.12(a), provides the energy drop required to make it favourable for the strongly bound electron-hole exciton to be sufficiently spatially separated to escape their mutual coulombic attraction. This picture is of course oversimplified and the precise energetics of charge generation in bulk conjugated polymers and heterojunctions is still a matter of vigorous debate although this picture qualitatively explains why heterojunctions vastly improve OPV efficiency.

Co-planar or lateral structures have also been demonstrated^{140,144–146} although the distance between electrodes and the metals available are limited by the resolution and method of patterning. Whilst the sandwich structure can be fabricated entirely in an inert environment, lateral structures with small channel lengths usually require photolithography which can typically only define features down to around 2 μm and exposes the electrodes to solvents and atmosphere. Electron-beam lithography and inkjet printing can get down to smaller channel lengths, comparable to that of sandwich structures at the cost of longer fabrication times.



(a) Energy diagram showing an exciton and the HOMO/LUMO levels of a heterojunction in an OPV where the dark lines represent the work functions of the contacts.

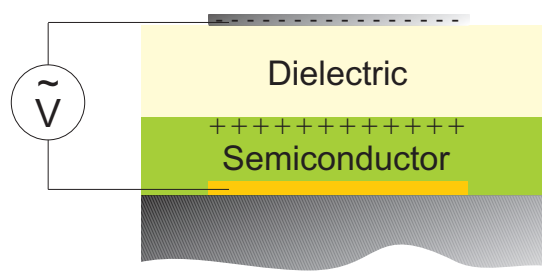
(b) Typical current vs voltage characteristics of an OPV in the dark and under illumination with the open-circuit voltage and short-circuit current labelled.

Figure 2.12: Energy diagram and current-voltage characteristics of a typical bilayer OPV device.

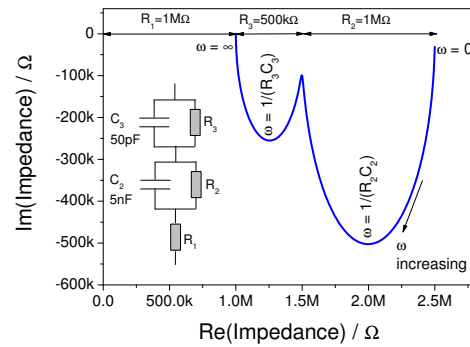
2.3.3 MIS diodes

Another two terminal device that has been demonstrated with conjugated polymers is the Metal-Insulator-Semiconductor diode as shown in figure 2.13(a). The structure is similar to those described above except an insulating dielectric material separates the semiconductor from one of the electrodes which will be referred to here as the gate electrode. In this thesis, the term MIS diode will apply to this structure to be consistent with that used elsewhere⁴³, although the author notes that MIS structure or MIS capacitor is equally valid. The application of a bias across the device induces an accumulation layer of field-induced charges at the semiconductor-insulator interface. With enough time these charges would spread out to cover the whole area below the gate electrode. The amount of charge that can be accumulated for a given voltage is determined by the capacitance of the insulator which can be measured by integrating the current flowing onto the device as the gate voltage is increased in a Quasi-Static Capacitance vs Voltage (QSCV) sweep. QSCV is inherently noisy as it is essentially a DC measurement and it is complicated by the presence of any significant leakage current between electrodes or elsewhere. Capacitance or, more generally, impedance measurements are therefore measured with a small signal modulation which reduces noise and provides information about the phase of the current going to the device which can distinguish between capacitive and leakage currents. With a sinusoidal applied voltage, resistive current has the same phase whereas capacitive

current leads by a phase factor of $\pi/2$. In the more general case there may be contributions from resistance, capacitance and inductance from numerous components resulting in a more complicated relationship between the phase and amplitude of the current and the voltage which is given by the impedance. Taking impedance values over a range of frequencies and plotting the complex part against the real part gives a Cole-Cole plot. The semi-circular features in a Cole-Cole plot provides a method for extracting values for components in an equivalent circuit which can provide information relating to contact resistance, bulk resistance, leakage and the capacitance of the layers in the device. Figure 2.13(b) shows an example of how a Cole-Cole plot can, in some cases, very quickly suggest an equivalent circuit and reveal the values of the components. It is not always the case that an equivalent circuit is easy to find especially when the features in the Cole-Cole plot overlap and equivalent circuits can rapidly become complicated and unrealistic when trying to fit real device data over all frequencies.



(a) Diagram of an Metal-Insulator-Semiconductor (MIS) diode on a glass substrate.



(b) Cole-Cole plot showing the imaginary part of the impedance plotted against the real part for the circuit diagram shown.

Figure 2.13: MIS structure and Cole-Cole plot for a capacitor-resistor network.

MIS structures are typically studied as a function of the gate voltage. The behaviour of a doped inorganic semiconductor in this structure is well understood and shown in figure 2.14. A p-type semiconductor will accumulate a positive charge density at the interface with the dielectric upon the application of a negative gate bias. The measured capacitance in this hole accumulation regime is simply that of the insulator which, given per unit area, is:

$$C_i(Fcm^{-2}) = \frac{\epsilon_r \times 8.85 \times 10^{-7}(Fm^{-1} \times 10^5)}{d_{ins}(nm)} \quad (2.47)$$

For positive gate voltages, free positive charge carriers move away from the semiconductor/insulator interface creating a depleted region. As the depletion region increases with positive gate voltage the measured capacitance reduces as the boundary between conductive and non-conductive regions moves further into the semiconductor. The way in which the capacitance varies with gate voltage in this regime reveals the density of charge carriers in the bulk and is given through Mott-Schottky analysis as the gradient of a plot of $1/C^2$ against voltage, V :

$$N = \frac{2}{eA^2\epsilon_0\epsilon_{sc}} \left| \frac{d(1/C^2)}{dV} \right|^{-1} \quad (2.48)$$

At high frequencies (green line in figure 2.14) this process continues until the entire semiconductor is depleted and the measured capacitance reflects the series combination of insulator and semiconductor. However, at positive gate voltages an inversion layer appears at the semiconductor/insulator interface as the minority carriers start to accumulate. Whilst the inversion layer is conductive, the bulk only has a low concentration of minority carriers which are electrons in this case. The ability of the charge density at the interface to respond to the gate voltage modulation is dependent on the recombination-generation rates of the electrons and thus only as the frequency reduces does the capacitance start to increase due to inversion⁴³ (blue and red lines).

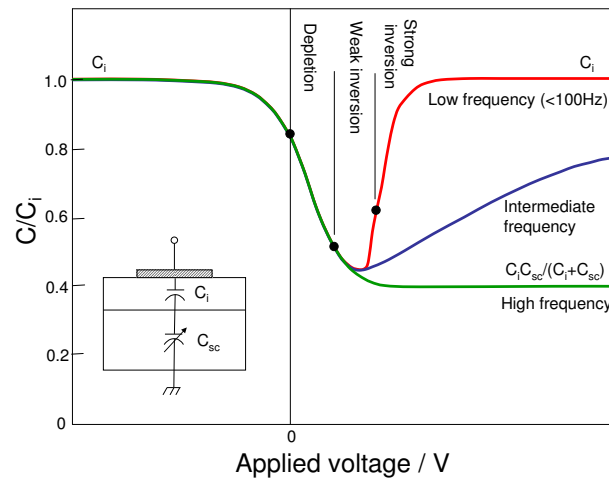


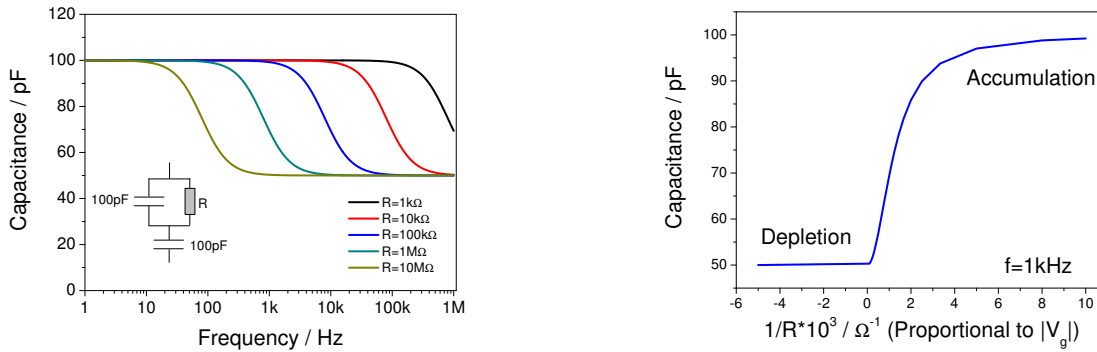
Figure 2.14: Capacitance as a function of voltage for a p-type inorganic semiconductor at high, intermediate and low frequencies. The inset shows the MIS structure with the insulator capacitance C_i and semiconductor capacitance C_{sc} .

Behaviour akin to that observed in doped inorganic semiconductors has been observed

in the polythiophene poly(3-hexylthiophene), P3HT, which is commonly unintentionally doped as explained above and has shown depletion of bulk carriers¹⁴⁷ and possible light-induced formation of an inversion layer.^{148,149} In the case of organic semiconductors with negligible intrinsic conductivity the increase in capacitance with gate voltage is commonly referred to as accumulation although, given the absence of bulk conductivity, it has some similarities with inversion. Ullah et al. recently showed that in C₆₀ MIS structures, the reduction in capacitance with gate voltage when coming out of accumulation was not due to depletion but reduced injection.¹⁵⁰ This idea of injection limiting capacitance fits in with Richards et al. who noted that contact resistance in such structures is gate voltage dependent as it is limited by bulk transport.¹⁰⁹

Perhaps the simplest circuit diagram to describe the fundamental processes in an organic MIS diode with a gate-voltage dependent contact resistance is given in the inset to figure 2.15(a). In this case, the dielectric constant and thickness of the semiconductor and insulator are assumed to be identical so that the two layers have the same capacitance for clarity. The resistor, R , represents the resistance of the bulk of the semiconductor and the capacitance of the entire structure is plotted against frequency for a range of different values of R . It can be seen that the capacitance at high frequencies is the series combination of insulator and semiconductor but at lower frequencies, charges can be injected into the semiconductor at a sufficient rate to follow the driving voltage modulation and the capacitance of the insulator alone is measured. By choosing a particular frequency and converting the resistance to something that is proportional to gate voltage we can see in figure 2.15(b) how something similar to the behaviour of bulk depletion occurs in a plot of capacitance against gate voltage.

MIS structures must be fabricated with care as charges will tend to spread further than the region of the bottom contact and will spread out over the whole gate region, or in the case of a modulated gate voltage, the charges can reach a distance of approximately $\sqrt{\pi^2\mu|V_g|/\omega}$ as given by the time constant for charging a channel when the gate voltage goes from zero to V_g given by Bürgi¹²¹ (the factor of π^2 was found experimentally and has been ignored elsewhere¹⁵¹). At 100Hz, with a modulation of 10 Volts, charges in a material with a mobility of $10^{-3} - 10^{-2}\text{cm}^2/\text{Vs}$ can spread hundreds of microns. Charge spreading can thus lead to erroneous interpretation of capacitance data for devices of comparable dimensions as the frequency-dependent spreading increases the capacitance.¹⁵⁰



(a) Apparent capacitance of the given circuit diagram as a function of frequency for various values of R .

(b) Apparent capacitance taken from figure 2.15(a) at 1kHz plotted against the inverse of R .

Figure 2.15: Frequency and gate voltage dependence of the apparent capacitance of a simple circuit to model accumulation in an undoped semiconductor where injection is limited by bulk resistance.

2.3.4 Unipolar transistors

A transistor is a three terminal electronic switch where the voltage on the gate electrode, V_g , controls the conductivity of the channel in the semiconductor between the source and drain electrodes. It could be thought of as a MIS diode where the electrode for the semiconductor is split in two forming a gap between the two electrodes (called source and drain) of length, L and width W .

Typically the source is grounded and a voltage, V_{sd} , is applied to the drain relative to the source. In the absence of doping, the current in the off state is determined by the intrinsic conductivity of the bulk of the semiconductor which is very low as there is not enough thermal energy at room temperature to promote charges from the HOMO to LUMO states. As the gate voltage increases, the charge density at the interface and hence the conductivity of the channel increases. To calculate the current flowing through the device a series of simplifications are made. Firstly it is assumed that the potential is the same throughout the whole width of the channel reducing it to a two dimensional problem. The Poisson equation and drift-diffusion equation should then be solved for this two-dimensional problem, however it can be simplified by assuming that the electric field perpendicular to the interface is much larger than the lateral field between source and drain electrodes. With this Gradual Channel Approximation⁴³, the charge density can be

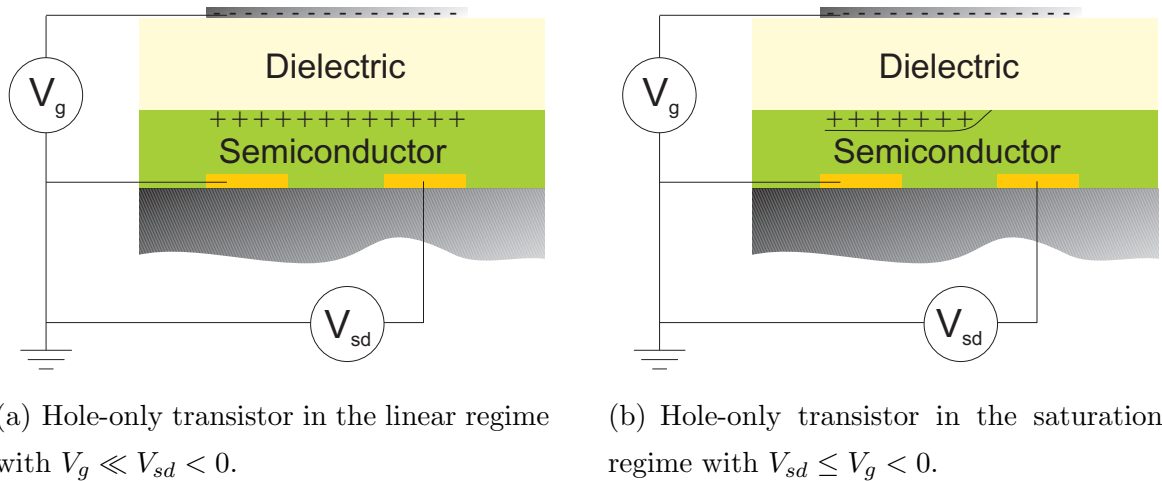


Figure 2.16: Unipolar hole-only transistors operating in the linear and saturation regimes.

calculated as

$$Q(x) = C_i(V_g - V(x)) \quad (2.49)$$

where $V(x)$ is the semiconductor potential as a function of distance along the channel with $V(x = 0) = 0$ at the source and $V(x = L) = V_{sd}$ at the drain assuming negligible potential drops due to contact resistance. With the applied drain voltage, the current through the device, neglecting diffusion, is then given by

$$I_d = W \mu C_i \frac{dV}{dx} \quad (2.50)$$

where the derivative gives the local lateral electric field. Integrating equation 2.50 assuming a constant mobility and neglecting the term in V_{ds}^2 which is valid if $V_{ds} \ll V_g$ we get the current in the linear regime to be

$$I_{lin} = \frac{W}{L} \mu C_i (V_g - V_t) V_{sd} \quad (2.51)$$

where V_t is the threshold voltage. The threshold voltage is a fitting parameter which is affected by the capacitance of the dielectric, the contact resistance¹⁵² and density of states in the semiconductor. In this linear regime, the current depends linearly on both the gate voltage and drain voltage. The mobility in this regime, μ_{lin} , is related to the slope of a plot of current against gate voltage, referred to as the *Transfer Characteristics*, by the following equation.

$$\mu_{lin} = \frac{dI_{lin}}{dV_g} \frac{L}{C_i V_{sd} W} \quad (2.52)$$

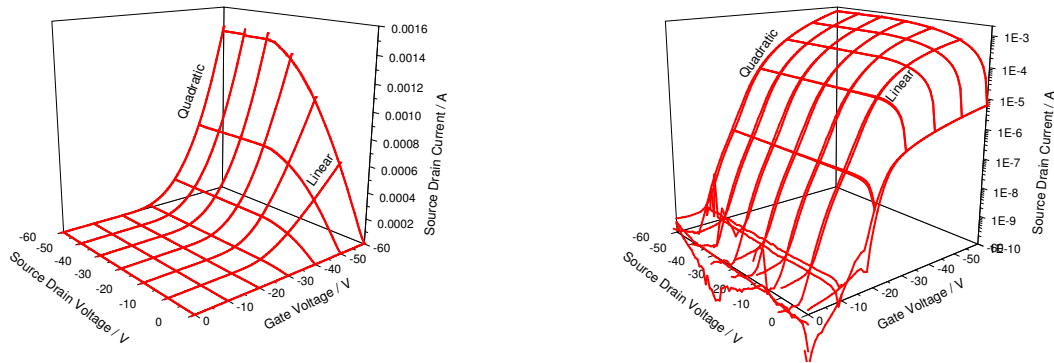
If the drain voltage is comparable to or bigger than the gate voltage, the region near the drain is effectively depleted of carriers and the accumulation layer has a *pinch-off* point which causes the drain current to saturate. This is best observed in a plot of current against drain voltage which is commonly referred to as the *Output Characteristics*. In this regime the current is independent of drain voltage but has a quadratic dependence on gate voltage and is given by

$$I_{sat} \approx \frac{W}{2L} \mu C_i (V_g - V_t)^2 \quad (2.53)$$

The current in the saturation regime depends quadratically on the gate voltage and is independent of drain voltage. The mobility in the saturation regime can be calculated from the slope of a plot of the square-root of current against gate voltage by

$$\mu_{sat} = \left(\frac{d\sqrt{I_{sat}}}{dV_g} \right)^2 \frac{2L}{C_i W} \quad (2.54)$$

Figure 2.17 shows the transfer and output characteristics of a pentacene transistor plotted in three dimensions on both linear and logarithmic scales to show how they relate. Output characteristics are typically studied on a linear scale where it can be seen clearly if the current saturates and if there are injection problems which result in sublinear characteristics at low drain voltages. Transfer characteristics are typically shown on a logarithmic scale where the on:off ratio, subthreshold slope and turn on voltage can be seen clearly.



(a) 3D plot showing source-drain current on a linear scale as a function of V_g and V_{sd} . (b) Same as 2.17(a) but with current on a log scale.

Figure 2.17: Combined transfer and output characteristics of a top contact (Au) bottom gate p-type pentacene transistor with a BCB/SiO₂ dielectric fabricated by author.

It is quite common that the saturation mobility will be higher than the linear mobility due to non-ohmic charge injection or field-dependent mobility. The mobility is also often a function of gate voltage and in some cases increases whilst in other cases reduces which has been attributed to filling of the density of states and disorder at the dielectric interface respectively. Saturation of the channel may not occur if the dimensions of the transistor are inappropriate. Such effects can be seen in very short channel devices, where the dielectric thickness must be reduced to remain less than a quarter of the channel length for the saturation regime to exist.

Unipolar transistors, in the case of undoped polymer semiconductors, can either transport holes or electrons depending on whether charges can be injected from the electrode and whether they are able to get through the device without being trapped which depends on the dielectric being used and the inherent stability of radicals on the polymer as noted above. Despite the absence of doping, certain materials have become known as n or p-type although it would be more appropriate to say that it is easier to fabricate electron only or hole only transistors from these materials. Materials more suitable for electron-only transistors¹¹⁸ have deep LUMO levels which give good ambient stability and easy electron injection from commonly used metals. Equally, materials more suitable for hole transport have the HOMO energy matched to the injecting electrode. For an early review on organic transistors see Dimitrakopoulos et al.¹⁵³

2.3.5 Ambipolar and light-emitting transistors

Ambipolar transistors are capable of both p-type and n-type operation and a regime in which electrons and holes are simultaneously injected to later recombine at some point in the channel as shown in figure 2.18.

For ambipolar operation there are three main requirements relating to injection, stability of charge species and trapping at the dielectric interface. Ambipolar transistors have been fabricated using bilayers, blends and one component polymers and have been reviewed recently by Zaumseil.¹⁵⁴ The equation for the current in the ambipolar regime has been derived assuming two saturated channels in series with a constant current and is given by

$$|I_d| = \frac{WC_i}{2L} [\mu_e(V_g - V_t^e)^2 + \mu_h(V_{ds} - (V_g - V_t^h))^2] \quad (2.55)$$

The transfer and output characteristics for typical ambipolar transistors are shown in figure 2.19.

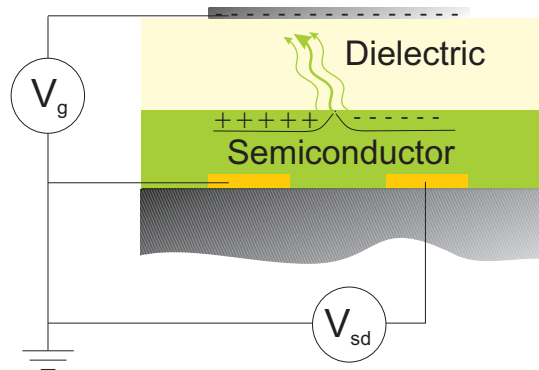
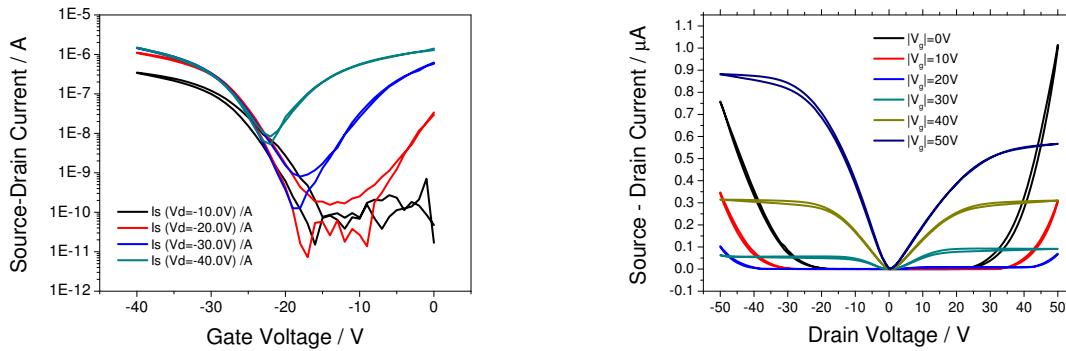


Figure 2.18: Ambipolar transistor in the ambipolar regime with $V_{ds} < V_g < 0$ showing the light emission from the recombination zone where electrons and holes meet.



(a) Transfer characteristics of top gate F8BT device B3-2a with PMMA dielectric.

(b) Output characteristics of top gate F8BT device B17-6b with PMMA dielectric (V_d is < 0 for traces on left side and > 0 on right side).

Figure 2.19: Examples of transfer and output sweeps for ambipolar transistors.

The position of the recombination zone in the channel, x_0 , can then be derived as

$$x_0 = \frac{L(V_g - V_t^e)^2}{(V_g - V_t^e)^2 + \frac{\mu_h}{\mu_e}(V_{ds} - (V_g - V_t^h))^2} \quad (2.56)$$

where V_t^e , μ_e , V_t^h and μ_h are the threshold voltages and mobilities for electron and hole transport respectively. It is clear from equation 2.56 that for the recombination zone to be in the channel and not from the edge of one electrode, balanced mobilities and low threshold voltages are required.

Figure 2.20 gives a summary of the different regimes that are seen for both unipolar and ambipolar transistors for both signs of drain voltage as a function of the entire range of gate voltages. When using a positive drain voltage instead of negative the characteristics are shifted into the positive gate voltage region and the injecting electrode is switched which is important to know when testing devices with different metals for the source and drain.

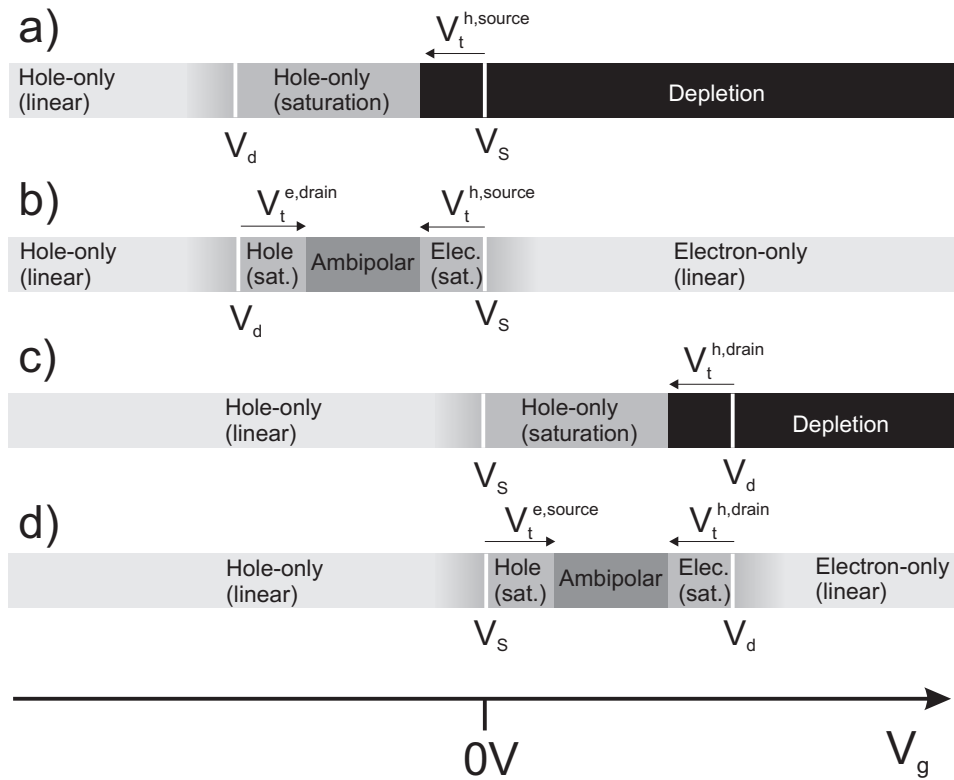


Figure 2.20: Schematic diagram of regimes of unipolar and ambipolar transistor operation as a function of gate voltage, V_g , for a) Hole-only device with $V_d < V_s = 0$, b) Ambipolar device with $V_d < V_s = 0$, c) Hole-only device with $V_d > V_s = 0$, d) Ambipolar device with $V_d > V_s = 0$. Threshold voltages for both electron and hole injection from both source and drain are included.

Chapter 3

Materials and Experimental methods

3.1 Materials

3.1.1 Semiconducting Polymers

The semiconducting polymers featured in this work were provided by Cambridge Display Technology Ltd (F8, F8BT and PFB) and Dow Chemical Company (F8T2) with the latter now being supplied by Sumitomo Chemical Company. Polymers were used as supplied and without further purification. The chemical structures of the semiconducting polymers are shown in figure 3.1 with the polymer properties including the number average molecular weight, M_n , peak molecular weight, M_p , and the luminescence efficiency, η , given in the caption where available.

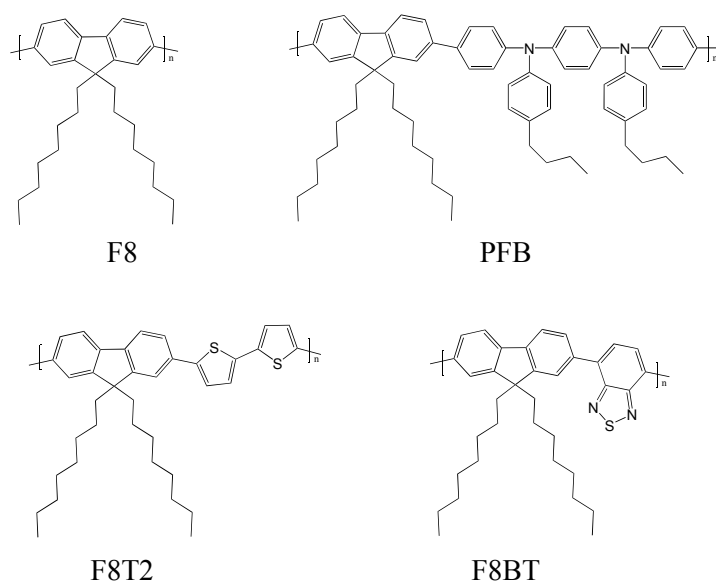


Figure 3.1: Semiconducting polymers: **F8** (poly(9,9-dioctyl-fluorene), $M_n=112K$, $M_p=274K$, $\eta=52\%$), **PFB** (poly(9,9-dioctylfluorene-co-bis-N,N-(4-butylphenyl)-bis-N,N-phenyl-1,4-phenylenediamine), $M_n=60K$, $M_p=135K$, $\eta=27\%$), **F8T2** (poly(9,9-dioctyl-fluorene-co-bithiophene)), and **F8BT** (poly(9,9-dioctyl-fluorene-co-benzothiadiazole), $M_n=112K$, $M_p=163K$, $\eta=82\%$).

The HOMO and LUMO levels of these polymers are typically measured using cyclic voltammetry where a thin film of polymer is applied to a working electrode in an electrolyte solution. The voltage on the working electrode is ramped up and down in cycles with the current being measured by a counter electrode and voltage by a reference elec-

trode. At a particular potential, charge transfer will occur to the polymer as it is either oxidised or reduced and the onset rather than the peak potential is recorded.¹⁵⁵ A value is typically added to these redox potentials, depending on the reference electrode used, to convert to HOMO and LUMO energy levels which are relative to vacuum.¹⁵⁶ Ambiguity persists with these values derived from cyclic voltammetry as often only one of the processes, typically oxidation, is reversible and sometimes the energy gap, as measured optically, is added to estimate the LUMO level. In a case where both have been measured reversibly,¹⁵⁵ the energy gap is larger than the onset of the optical gap by $\sim 0.7\text{eV}$ which is associated with the exciton binding energy. The approximate energy levels for the polymers used in this thesis, as measured by cyclic voltammetry, are shown in figure 3.2. The HOMO levels have been averaged from a number of reported values^{32,155,157–163} and a range of LUMO levels is given allowing for an exciton binding energy of 0.3eV - 0.7eV in addition to the onset of optical absorption as taken from measurements in figure 3.3.

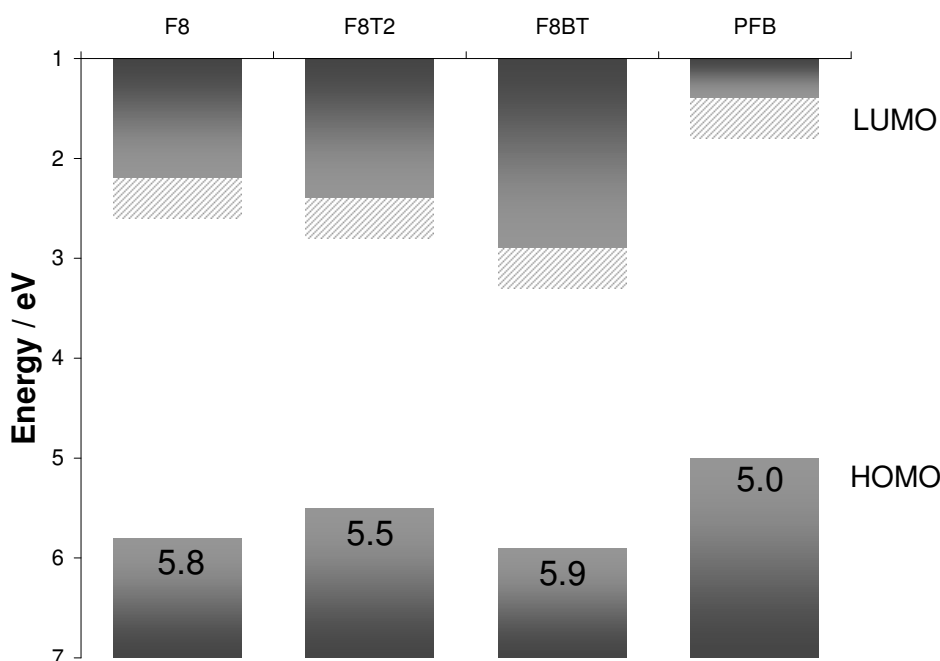
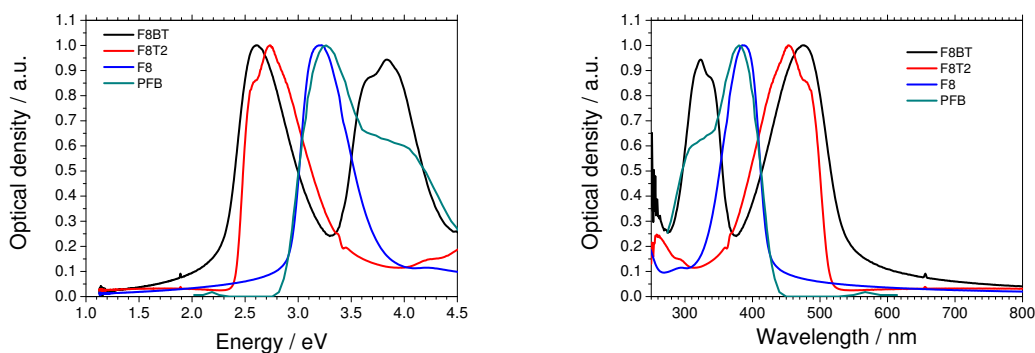


Figure 3.2: HOMO and LUMO levels for the semiconducting polymers used in this thesis. HOMO levels are averaged over 3-4 independently reported cyclic voltammetry measurements^{32,155,157–163} and LUMO levels estimated by adding the energy of the onset of optical absorption from 3.3 and an exciton binding energy of 0.3eV - 0.7eV giving semi-shaded region.

The polymers were weighed in ambient conditions in a cleanroom before being transferred to a nitrogen glovebox ($<1\text{ppm H}_2\text{O, O}_2$). Solutions were then dissolved in anhydrous xylene (Sigma-Aldrich) at $70\text{--}80^\circ\text{C}$ for approximately 10 minutes or until solutions



(a) Semiconductor Optical Density as a function of energy (b) As 3.3(a) but versus wavelength

Figure 3.3: Optical density of the semiconducting polymers used in this work (PFB data from¹⁶⁴).

became clear. F8T2 required longer, typically 100°C for around an hour to dissolve completely and would precipitate out of solution after several hours at room temperature so would be used immediately. Fresh polymer solutions were always made for each device run for consistency. Typical concentrations ranged from 4-12g/l which would give film thicknesses in the range of 25-100nm. Solutions were filtered through 0.2 μ m PTFE filters into a cleaned (rinsed in acetone/IPA) glass vial before deposition using cleaned glass pipettes.

3.1.2 Dielectrics

The dielectrics featured in this work, shown in figure 3.4, were purchased from Sigma-Aldrich (PIB, PCHE, PS), Polymer Source Inc. (PMMA), Asahi Glass Ltd (CYTOP) and the Dow Chemical Company (BCB). CYTOP was purchased, pre-dissolved, in a fluorosolvent and was further diluted in the same solvent as required. BCB was diluted further from its purchased 30 wt% to 5% with mesitylene in air before being transferred to the glovebox. Apart from CYTOP and BCB, dielectrics came in solid form and were weighed out in air but dissolved in the glovebox. PIB was dissolved in octane, PCHE in cyclohexane and PS and PMMA were both dissolved in n-butyl acetate (all solvents were anhydrous and purchased from Sigma-Aldrich). Temperatures up to 80°C were required to dissolve most dielectrics and typically left overnight in the glovebox to dissolve. Before spin coating, dielectric solutions were filtered, hot, through a PTFE filter into a pre-cleaned vial. The pore size of the filter depended on the molecular weight and concentration of

the polymer and solution with molecular weight of around 500k and concentrations much over 40g/l needing a $1\mu\text{m}$ filter whereas $0.45\mu\text{m}$ could be used in most other cases.

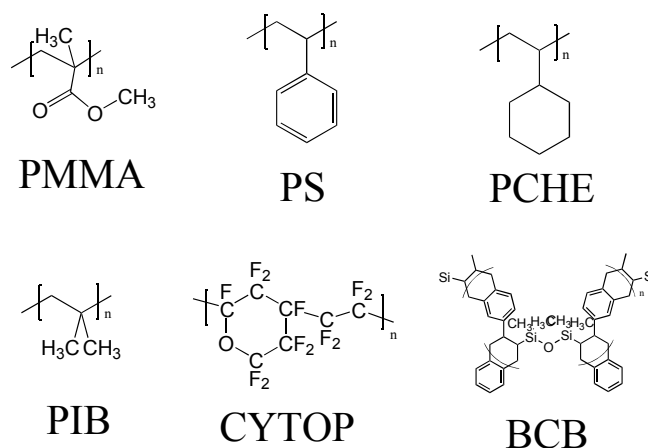


Figure 3.4: Dielectrics: **PMMA** (poly(methyl methacrylate)), **PS** (polystyrene), **PCHE** (poly(cyclohexylethylene)), **PIB** (poly(isobutylene)), **CYTOP** (poly(perfluorobutenylvinylether)), **BCB** (cross-linked B-staged divinylsiloxane-bis-benzocyclopentene resin)

3.1.3 PEDOT:PSS

PEDOT:PSS, as shown in figure 3.5, was purchased as Baytron PH (now Clevios PH) which is an aqueous dispersion of the two polymers with a ratio of 1:2.5 and solid content of 1.2-1.4%. For the requirements in this thesis, the PEDOT:PSS was not filtered or diluted and used as delivered. PEDOT:PSS provides high conductivity of up to 10 S/cm although in the final film this will be dependent on the residual water content which reduces conductivity.

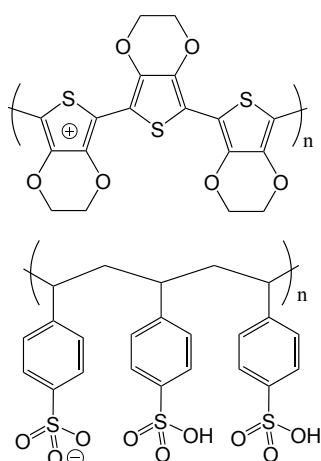


Figure 3.5: Chemical structure of PEDOT:PSS which is an aqueous dispersion of poly(3,4-ethylene dioxythiophene) (top) and poly(styrenesulfonate) (bottom) in a ratio of 1:2.5

3.2 Device fabrication

3.2.1 Substrate Preparation

Devices were prepared on Corning 1737F 0.7mm thick glass substrates. Typical substrates were cut to size 13mm x 20mm and then sonicated sequentially in de-ionised water, acetone and iso-propanol for 10 minutes each before being dried in a stream of nitrogen. The cleaned substrates were then treated with oxygen plasma (250W, 10 minutes) to remove any residual organic material and make the surface more hydrophilic and suitable for spin coating. All processing was carried out in a cleanroom under laminar flow.

3.2.2 Electrode Preparation

Source-drain contacts with a channel length of 40 μ m or less were prepared with a two layer photolithography process. Firstly filtered (0.45 μ m) LOR 5B was spin-coated for 30s at 4000rpm onto a substrate and then annealed in air for five minutes at 190°C. A layer of S1813 was then spin-coated with the same spin recipe but annealed for 2 minutes at 120°C. The films were then exposed to UV light through a patterned photomask using a Karl Süss MJB3 mask aligner for 12-20 seconds depending on the lamp life before being developed for 30 seconds in MF319 developer. To remove any residual resist from the exposed areas the developed samples were given a short oxygen plasma treatment (150W, 1 minute). A thin (0.7nm) adhesion layer of chromium was thermally evaporated from

a tungsten basket onto the patterned substrates followed by various thicknesses of gold evaporated at a rate of $0.5\text{\AA}/\text{s}$ from an alumina coated tungsten basket. Electrodes were typically deposited at a pressure of 2×10^{-6} mbar. The substrates were then left in NMP for a least an hour before being rinsed and sonicated again in NMP, Acetone and IPA and dried again in nitrogen. Finally another oxygen plasma treatment was performed (250W, 10mins). In the case of platinum electrodes the deposition was done by sputter coating from a platinum target using Ar plasma at a process pressure of 5×10^{-4} and RF power of 50W. Evaporation rates were typically higher with this process $\sim 1\text{nm}/\text{s}$. For metal gate electrodes, the devices were pumped down over night to 2×10^{-7} mbar and then either gold or aluminium was evaporated. For aluminium either a tantalum source or TiB_2 crucible was used and at a higher rate of $1\text{\AA}/\text{s}$ was required for obtaining conductivity in thin films ($\sim 5\text{nm}$). PEDOT:PSS gate electrodes were prepared by pre-evaporating less than 1nm of aluminium onto the dielectric surface and then spin-coating the PEDOT:PSS in air before annealing briefly in air at 100°C and then returning to the glovebox for a further anneal at 120°C for 1 hour.

3.2.3 Film Preparation

Spin-coating of semiconductors was carried out for 45 seconds at 1000rpm followed by 1 second at 4000rpm to remove any solution from the corners of the substrate. Coated substrates were typically annealed over the polymer melting temperature for 20 minutes before being quenched on a metal surface. For the most commonly used PMMA dielectric, a solution of 40g/l was spun at 1000rpm for 45 seconds to give a thickness of 450nm. Substrates were then annealed for 20 minutes at 80°C before the gate electrode deposition. At no point were the solutions or films exposed to air during fabrication or testing. For bottom gate device with BCB dielectric, BCB was spin coated at 2000rpm onto a silicon substrate with a 300nm thermally grown oxide on the surface. The substrates were subsequently annealed at 290°C for 10 seconds to cross-link the BCB and then quenched on a metal surface.

3.2.4 Device structures

With the basic techniques of film and electrode deposition described above, a number of device structures can be fabricated. A number of additional tricks that were required in this thesis and the structures in which they were employed are outlined below.

Top gate, bottom contact transistor

The top gate, bottom contact transistor is the most commonly used in this thesis and has been shown schematically already in figure 2.16. For standard transistor measurements photolithography is used to define the source and drain electrodes and a metallic gate stripe that covered both the two transistors and pads on one substrate at the same time was used.

For the spectroscopic measurements in this thesis it is necessary to have an interdigitated electrode structure with a short channel length ($\sim 40\mu\text{m}$) so that the charges can be modulated in the largest area possible particularly if the mobility is low. It is also desirable to be able to have bottom contacts of any desired metal which is limited if using photolithography. Two further desired requirements are that each device has its own patterned gate electrode and that the gate electrode is the conducting polymer PEDOT:PSS. To meet all these requirements, and avoid time-consuming inkjet printing of PEDOT:PSS, a new technique for fabricating top gate, bottom contact transistors was developed as shown in figure 3.6 where nine devices could be made at a time in one day.

The key to this technique is a substrate holder in which the substrates are spring loaded into position so can be removed and replaced with identical relative positions. With the substrate positions guaranteed, a set of shadow masks were fabricated with features on each mask that align with the others. The first stage is to evaporate contacts to the transistor which must have a chromium adhesion layer so that contact can be made to the gold upper layer later without scratching it off. The actual source-drain electrodes with $40\mu\text{m}$ spacing are evaporated with the next mask and no adhesion layer to ensure good electrical contact with the first gold layer. Two steps are required for this type of short channel interdigitated pattern due to the fragility of the shadow mask. After spin coating the semiconductor and dielectric, a third mask is used to pattern the gate electrode area and a 1nm layer of aluminium (oxidised and non-conducting) is evaporated. The final step is to spin coat PEDOT:PSS over the entire device and it only wets the patterned area. An additional step of covering up the area above the source-drain electrodes and evaporating gold over the rest of the pattern had to be inserted as the PEDOT:PSS did not remain on the narrow interconnects between the gate and the pad.

Asymmetric electrodes

For ambipolar transistors it is common to have different metals for the source and drain electrodes. Two-stage photolithography can be used to make different electrodes however this is not compatible with reactive low work function metals and is both difficult and

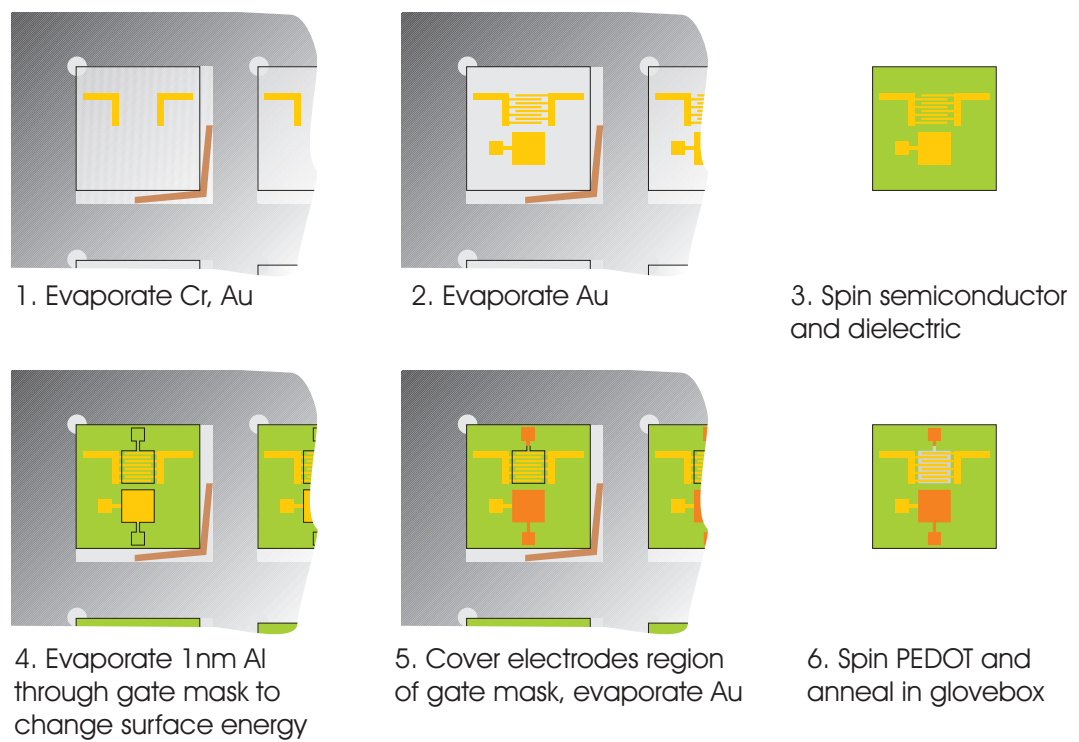
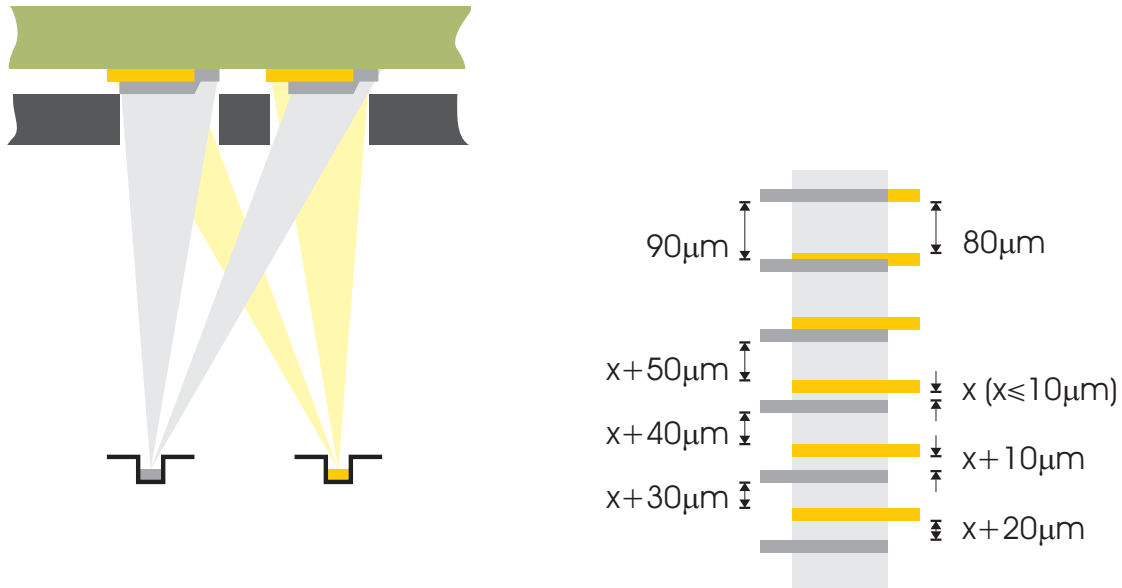


Figure 3.6: Procedure for making $40\mu\text{m}$ channel length devices with a patterned PEDOT gate without inkjet printing.

time-consuming. Due to the finite thickness of shadow masks it is inevitable that if two different metals are evaporated from two different sources there will be imperfect overlap of the two metals leading to a channel where the edges of the source and drain are different as shown in figure 3.7(a).



(a) Angled evaporation technique relying on the thickness of the shadow mask to produce an overlap of electrodes.

(b) 'Vernier' technique where subsequent evaporations through masks with lines of different spacing produces a range of channel lengths.

Figure 3.7: Methods for patterning different metal source and drain electrodes.

This technique has been used successfully to make light-emitting ambipolar transistors using semiconductors with smaller electron affinities. However, ambiguity can remain about where the charges are being injected from, what the channel length is and if rectification is desired, running the device in reverse bias just gives an identical device with a longer channel length.

To create distinct electrodes with channel lengths comparable to that achieved through photolithography a technique was developed based on the principle of a Vernier calliper. Two masks with lines of electrodes of different spacing were fabricated. When the second set of lines are evaporated on the first, the difference in spacing ensures that some electrodes will overlap but there has to be a set of channels of increasing length with distinct

electrodes as shown in figure 3.7(b).

Aligned polymer devices

The semiconducting polymers F8, F8BT and F8T2 can be aligned when annealed above their melting temperatures whilst in contact with an alignment layer. Polyimide (PI) is a polymer which, when rubbed with a cloth, forms an alignment layer. Polyimide (PI2525, HD Microsystems) is added to NMP (1-methyl-2-pyrrolidinone) in a ratio of 1:7 and heated at 100°C until fully mixed. The PI solution is spin-coated at 2000rpm for 4 minutes and dried at 110°C before being transferred to the glove box and annealed at 165°C for 1 hour and then 300°C for 3 hours. The PI-coated substrates can be sonicated in DI water, Acetone and IPA before any further steps. Electrodes are deposited onto the PI and then the substrate is rubbed with a cloth in a RM-50 rubbing machine (E.H.C. Co. Ltd) where the cylinder wrapped in cloth is rotating at 1200rpm as the substrate passes once under at 2.2mm/s. Polymers with a number average molar mass, M_n , of around 100k proved to be easily aligned when annealed above the melting temperature (270-290°C) for 20 minutes and then quenched on a metal surface. The procedure for alignment is shown in figure 3.8.

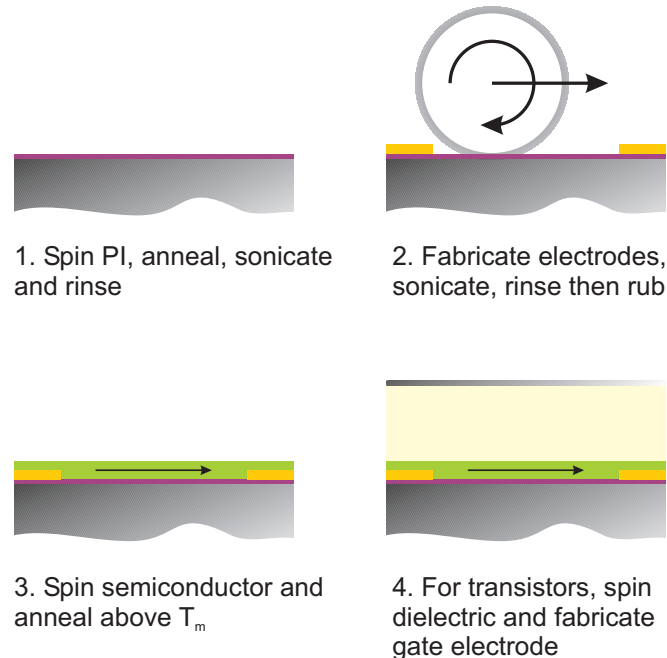


Figure 3.8: Procedure for devices with aligned semiconductor

The fact that the electrodes are deposited prior to rubbing, which is performed in air, puts some restrictions on the metals that can be used for electrodes. To avoid exposure of

the contacts to air, by bringing out of the glove box following metal evaporation, the PI would have to be rubbed first. As can be seen in figure 3.9, rubbing before the electrode deposition leaves areas around the electrodes where the polymer is not aligned. The unaligned region extends approximately $20\mu\text{m}$ around the electrodes and could be due to melting of the PI as the hot metal lands on the surface. For channel lengths of around $60\mu\text{m}$ or more there will still be a region of aligned polymer in the channel where the recombination zone can be viewed in the aligned polymer. Mobility measurements for such partially aligned devices can not be used for quantitative measurements of mobility in aligned polymers.

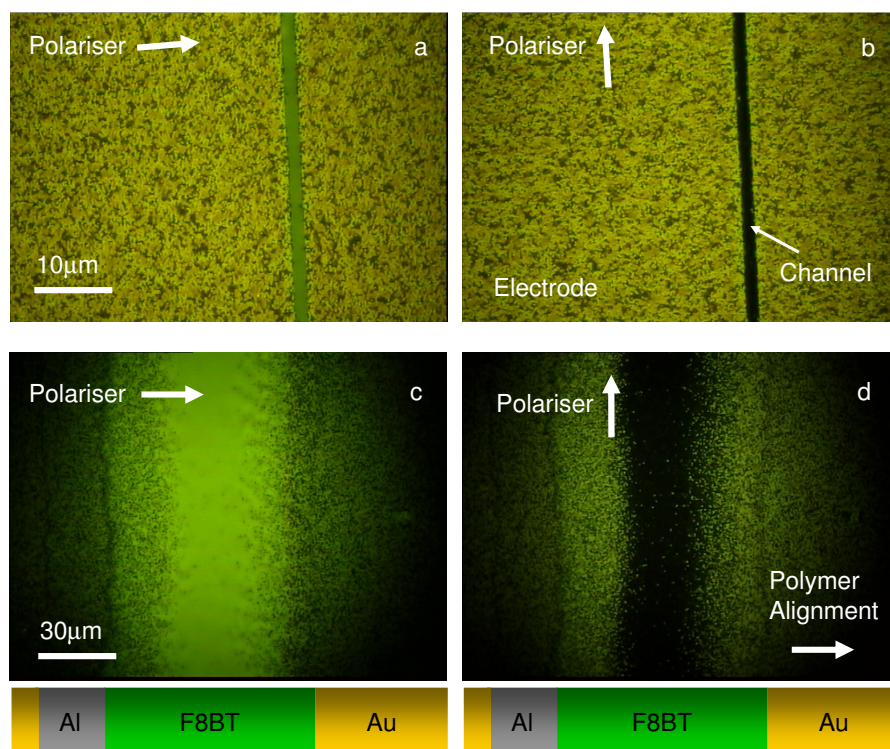


Figure 3.9: Polarised (analyser) fluorescence images of aligned F8BT devices. Figures a) and b) show that alignment is possible even with $2\mu\text{m}$ channels if rubbing is done after electrode deposition. Note the lack of alignment on the electrodes themselves. Figures c) and d) show the extent of the lack of alignment extending about $20\mu\text{m}$ around the electrodes when the electrodes are deposited after rubbing.

Planar photodiodes

Planar photodiodes are similar to transistors except without a dielectric or gate electrode and can have either top or bottom contacts. Devices in this work were fabricated using either pre-fabricated photolithographically defined gold and chromium electrodes as used elsewhere,¹⁴⁰ photolithographically defined gold electrodes on PI-coated glass substrates or shadow mask patterned electrodes as either top or bottom contacts using the technique in figure 3.7(b). When investigating alignment, the PI was rubbed after electrode deposition for the gold bottom contact devices.

3.3 General device characterisation

3.3.1 Electrical characterisation

Transistor characterisation was performed in a glovebox under dry Nitrogen atmosphere ($O_2 < 2\text{ppm}$). Electrical connection was made to the devices with probes which were connected via approximately 2m of coaxial cable to a switch box. The switch box connects the signal lines to the central lines of triaxial cables whose inner shield is left floating in the box, and outer shield shares a common ground with the coaxial cables. The triaxial cables are then connected to an Agilent Semiconductor Parameter Analyser 4155B which, prompted by a custom Labview program, performs programmed voltage sweeps while simultaneously measuring the current on up to four probes. Current leakage from the switch box is 50pA at 50V.

3.3.2 Impedance Spectroscopy

Impedance measurements, when performed in the glovebox as in the previous paragraph, were carried out with a Hewlett-Packard HP4192A Impedance Analyser. The combination of low frequency electrical noise, limited voltage range of $\pm 35\text{V}$, small capacitance and high contact resistance of the devices used means that this method could only be used accurately for measuring the capacitance of the dielectric and semiconductor in series in depletion. In combination with the known dielectric constants and film thicknesses, this could be used to confirm the dielectric capacitance.

3.3.3 Profilometry

Film thicknesses were measured by scraping a trench in the film with a cocktail stick and then measuring the height profile with a Sloan Dektak Surface Profiler (Model IIA).

A number of measurements on different areas of the film were averaged to reduce and quantify the uncertainty of the final value.

3.4 Photocurrent measurements

3.4.1 Time-correlated single photon counting

The lifetime of radiative exciton decay in F8BT devices was measured by counting photons emitted after exciting the sample, mounted in air, with laser pulses at 470nm. The setup for TCSPC is shown in figure 3.10 and essentially synchronises an electronic timing circuit with a laser pulse. When a photon that has been emitted from the F8BT, following excitation, arrives at the detector, the timing circuit stops and the interval recorded. This process is repeated being careful to insure that the frequency of detecting events is much less than the repeat frequency of the laser so that all the time intervals have equal chance of being sampled. The result of the measurement is a histogram of time intervals usually showing an exponential or bi-exponential decay.

3.4.2 Photovoltaics Rig

The efficiency of converting incident radiative photons to current, known as the external quantum efficiency, EQE, is measured using the photovoltaics rig as shown in figure 3.11. Incident light was first measured with a calibrated photodiode (Hamamatsu S8746-01) in the sample position and simultaneously at a Si photodiode that receives 10% of the light from the monochromator. Next, with a sample in place, the Si-photodiode voltage can then be used to assess the incident number of photons arriving at the sample whilst electrical measurements are being performed. This compensates for any fluctuations in the lamp intensity. For this experiment, the custom Labview routines for calculating EQE were not appropriate as a larger voltage was required which needed a different voltage source. The Labview routine for calibrating the photodiode was however performed first and then the appropriate scaling factor was taken so that the Si-photodiode voltage could be related to the number of photons incident on the sample at the single wavelength that was used. Measurements were performed in dark ambient conditions and the spot size of 1mm^2 was approximately the same size as the device area.

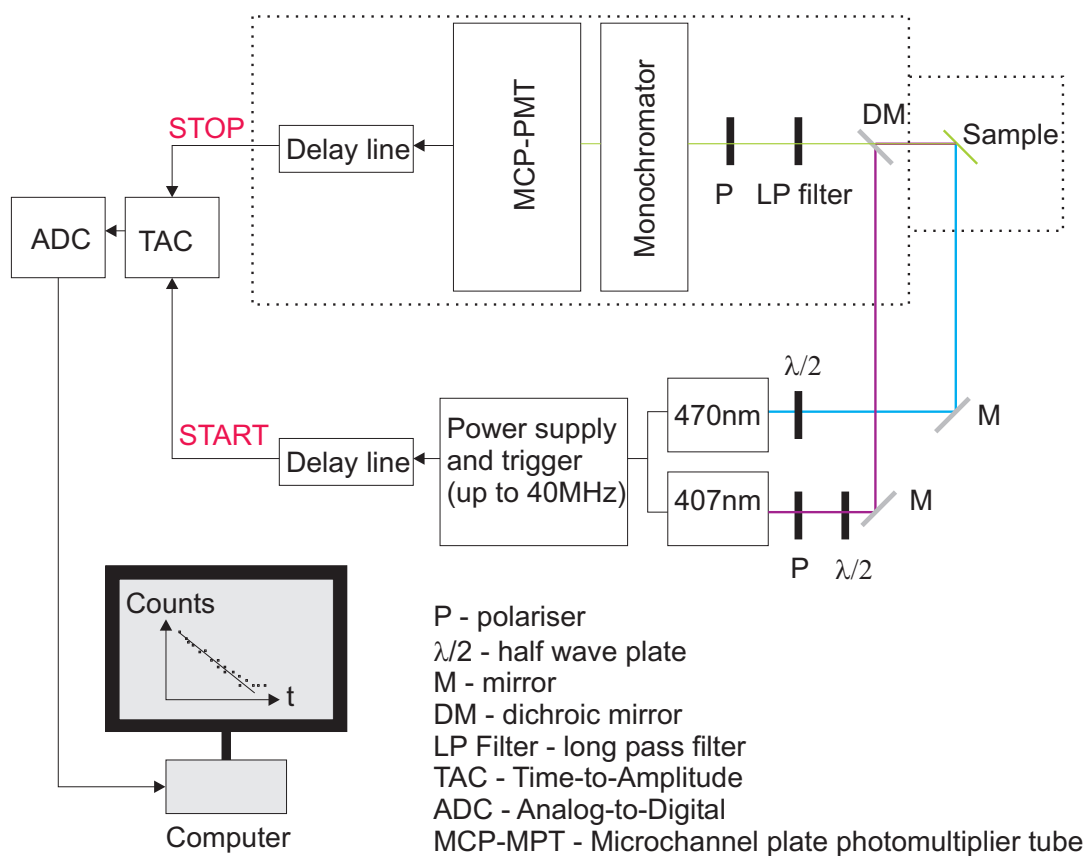


Figure 3.10: Schematic diagram of the time-correlated single photon counting (TCSPC) setup.

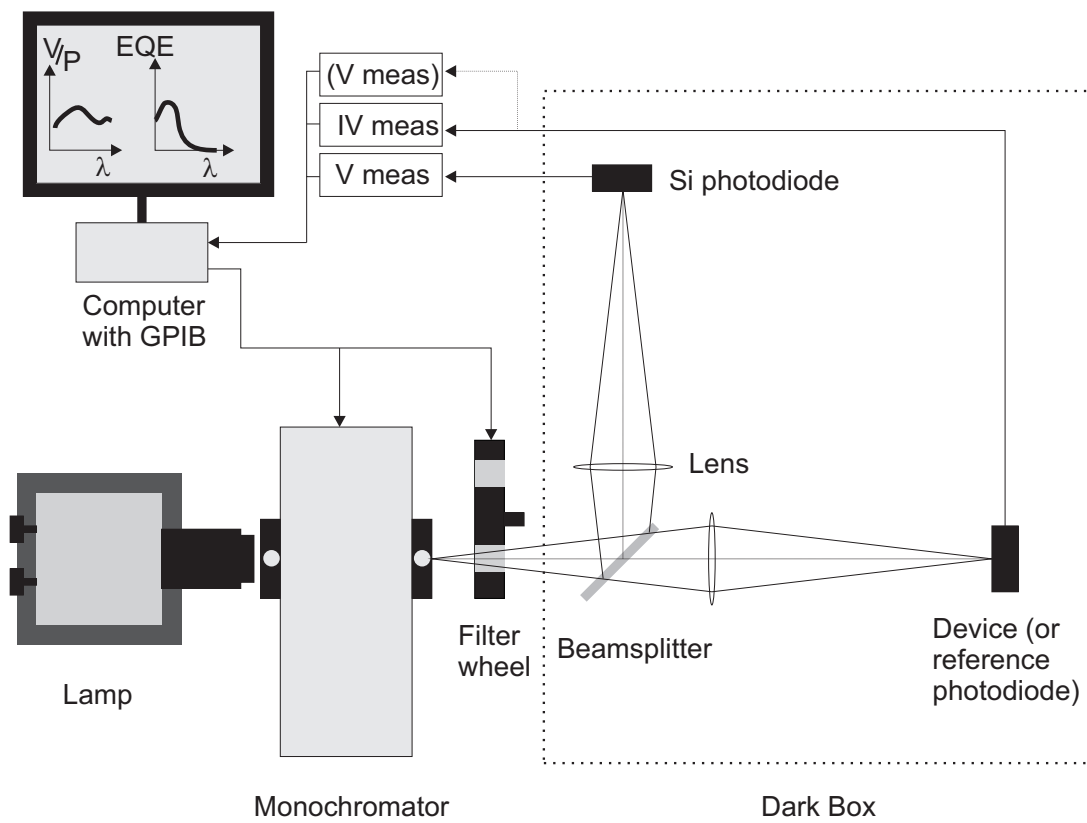


Figure 3.11: Schematic diagram of the EQE setup.

3.4.3 Vacuum measurements

Photocurrent in vacuum was measured using a Desert Cryogenics TTP4 probe station and a pressure of $<10^{-5}$ mbar. Unfocussed, yet high intensity white light was shone on the devices from outside of the chamber from a Schott Ace light source¹⁶⁵. Electrical measurements were made with an Agilent Semiconductor Parameter Analyzer (SPA) model number 4155C with tri-axial shielding all the way up to the probes. Devices also experienced brief exposure to air and some white light during the loading process.

3.4.4 Scanning Kelvin Probe Microscopy

Devices for Scanning Kelvin Probe Microscopy, SKPM, were made as described above using photolithography to define a $10\mu\text{m}$ channel length but then cut after fabrication to be approximately $10\text{mm} \times 5\text{mm}$ so that they could be mounted. The devices were exposed to air after fabrication for this cutting and mounting process. Electrical connections were made with silver dag before being transferred into ultra-high vacuum. The SKPM was a commercial Omicron beam deflection scanning force microscope with a conducting tip and operating in non-contact mode. A schematic of the method of operation is given in figure 3.12. The voltage of the tip is used to give the potential of the surface of the device whilst simultaneously giving height information.

3.5 Device imaging and optical measurements

3.5.1 Fluorescence Microscopy

Fluorescence microscopy was performed with an Olympus BX60 microscope in reflection mode. As shown in figure 3.13, the sample is illuminated with light from an ultraviolet source and only the fluorescence is passed back through the cube to be observed or saved as an image or video. A polariser was also used at the last stage before observing the image to see the degree of polymer alignment in particular devices. For measurements of operating devices, a small enclosed sample holder with a window on the top that could be flushed with nitrogen was used to reduce exposure of the device to atmosphere.

3.5.2 UV-VIS spectra

Absorption spectra, unless otherwise stated were carried out in air with an HP 845x Visible-UV System Spectrometer. A blank spectrum was taken with a glass substrate before measuring any spin-coated film on identical glass substrates.

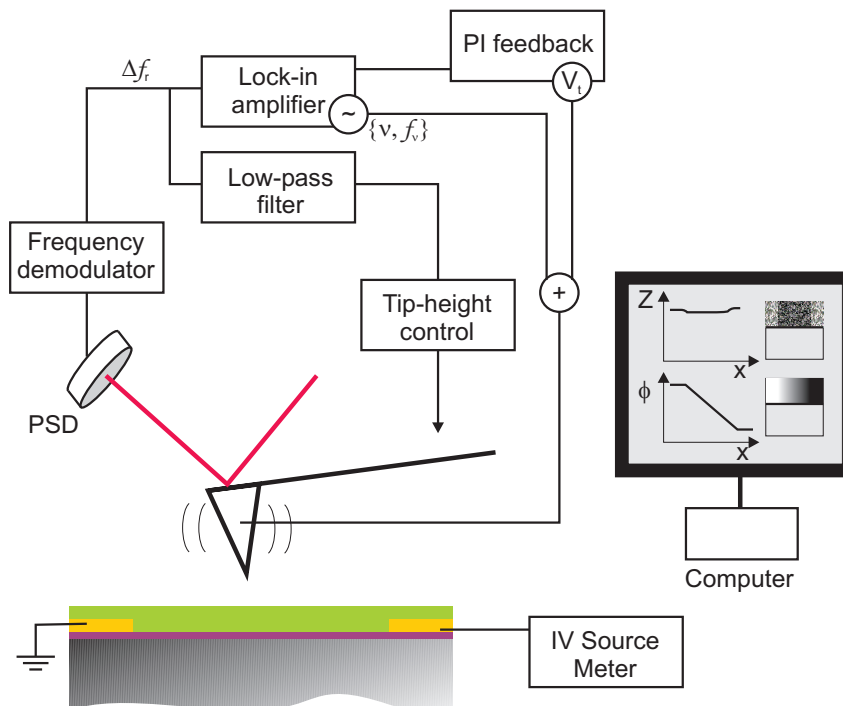


Figure 3.12: Schematic diagram of the SKPM setup.

3.5.3 Photoluminescence spectra

Photoluminescence spectra were measured with a Varian Cary Eclipse Fluorescence spectrophotometer in air. Following an absorption spectra, the excitation wavelength would be chosen to coincide with the peak in absorption. The sensitivity was then adjusted to maximise the detected fluorescence signal without saturating the detector.

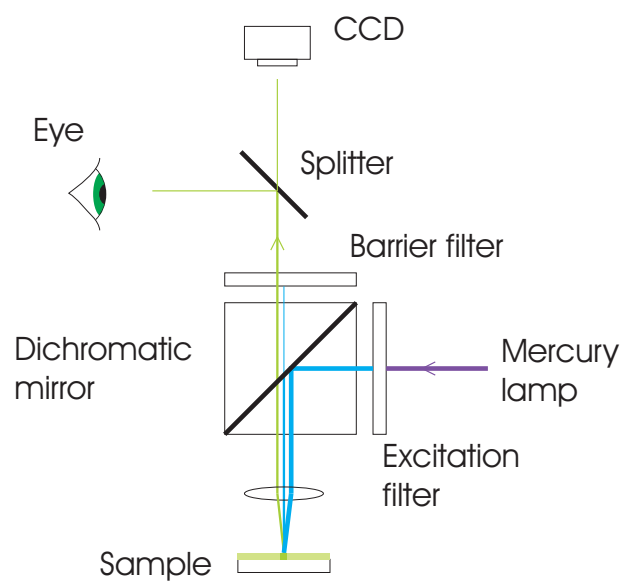


Figure 3.13: Schematic diagram of PL microscopy setup.

Chapter 4

Charge Modulation Spectroscopy technique

4.1 Introduction

In this chapter, the experimental technique of charge modulation spectroscopy (CMS) is explained in depth. Whilst this technique has been used before, the particular challenges arising in this work from the need to compare electron and hole spectra for the same polymer required new methods of taking and analysing data. This challenge could be expressed as the need for highly accurate and reproducible data for making subtle conclusions coupled with the highly non-ideal performance of the ambipolar transistors necessary for this particular experiment. The new techniques and theory developed in this chapter not only make these measurements possible in the worst case scenarios but also offer an improved standardised method that can be applied to other materials particularly where extreme accuracy is required. The introduction of simultaneous electrical and optical measurements during CMS, new constraints placed on device design and the removal of some pre-existing systematic errors summarises the advances outlined in the chapter.

Charge modulation spectroscopy is a method to measure the absorption spectra of charged conjugated polymers in a thin film by electrically injecting charges with a transistor configuration. The relatively low proportion of charged polymer segments that it is possible to accumulate by capacitive coupling to a gate electrode means that the absorption is very small with the fractional change in transmission being in the range $10^{-5} - 10^{-4}$. A way to measure such a small change in transmission is to modulate the number of charge carriers at a particular frequency, f , and selectively measure only changes in transmission at this frequency. This process has to be repeated for each wavelength of light in the range required. The difference with this modulation technique compared to using an extremely sensitive spectrophotometer is an improved sensitivity and the ability to measure only mobile charges. The faster measurements and ability to measure immobile charges with a spectrophotometer mean that the two techniques can be considered complimentary.

To select changes in transmission due to the modulated charge density, the output of the detector is connected to a lock-in amplifier to attenuate noise at all other frequencies and measure the signal. Noise still exists at the same frequency as the modulation although this reduces at higher frequencies as the noise is characterised by a $1/f$ dependence. A lock-in amplifier not only demodulates the transmitted intensity to measure the root-mean-square (RMS) amplitude but records the phase relative to the applied gate voltage modulation. A lag between the gate voltage modulation and the charge density it is driving can originate from contact or channel resistance and thus provides further information about the transistor under examination. The amplitude and phase of the

change in transmission at each wavelength can equally be expressed by its X and Y components with the positive X axis being in phase with the trigger to the lock-in and the Y axis being a quarter of a period, $1/(4f)$ seconds, ahead.

The absorption is typically measured as the change in transmission, ΔT , divided by the total transmission, T , which eliminates the need to calibrate the detector or know the lamp emission profile. This normalised quantity, $\Delta T/T$ is directly proportional to the density of charges and the absorptivity of the charged polymer at a given wavelength, the latter being the sought after quantity. The density of charges has in the past been estimated by the areal capacitance of the dielectric in the transistor and the gate voltage modulation. Large resistance from the channel or contacts, device degradation during the lengthy scan and the assumptions made in calculating the capacitance can introduce errors in this technique. The new experimental setup outlined below adds the ability to simultaneously measure the number of charges being modulated on the device during the modulation scan.

4.2 Experimental setup

The experimental setup for charge modulation spectroscopy is shown in figure 4.1. The light source was a halogen lamp powered by a constant current source set to 8.45 amps consuming an electrical power in the range of 75-100 Watts depending on the state of the bulb. The computer-controlled double grating monochromator selects a particular wavelength in the range of 2500nm ($\sim 0.5\text{eV}$) to 440nm ($\sim 2.8\text{eV}$) and the filter wheel blocks higher harmonic frequencies that also make it through. Slits on the entrance and exit to the monochromator can increase the wavelength resolution at the cost of intensity and an optimised slit width of 3mm was used leading to a resolution of around 10nm (see appendix B.1 and B.2 for a full optical characterisation of the setup). The light is focussed onto the device which is housed in a cryostat under a vacuum of 10^{-6} - 10^{-5} mbar achieved with a diffusion pump. The transmitted light is collimated and then focussed onto a silicon photodetector (built by the electronics workshop, characterised in appendix B.5 and B.6) or a liquid nitrogen-cooled InAs infra-red (IR) detector depending on the wavelength range. The amplified signal from the detector is measured by a lock-in amplifier (SRS 830) and transferred to the computer which controls the whole process through a Labview program.

For measuring the simple transmission of light through the device, T , in what is called the background scan, the beam is chopped with a chopper wheel that is now at a point before the sample where it is focussed down to a small spot. This insures that no visible

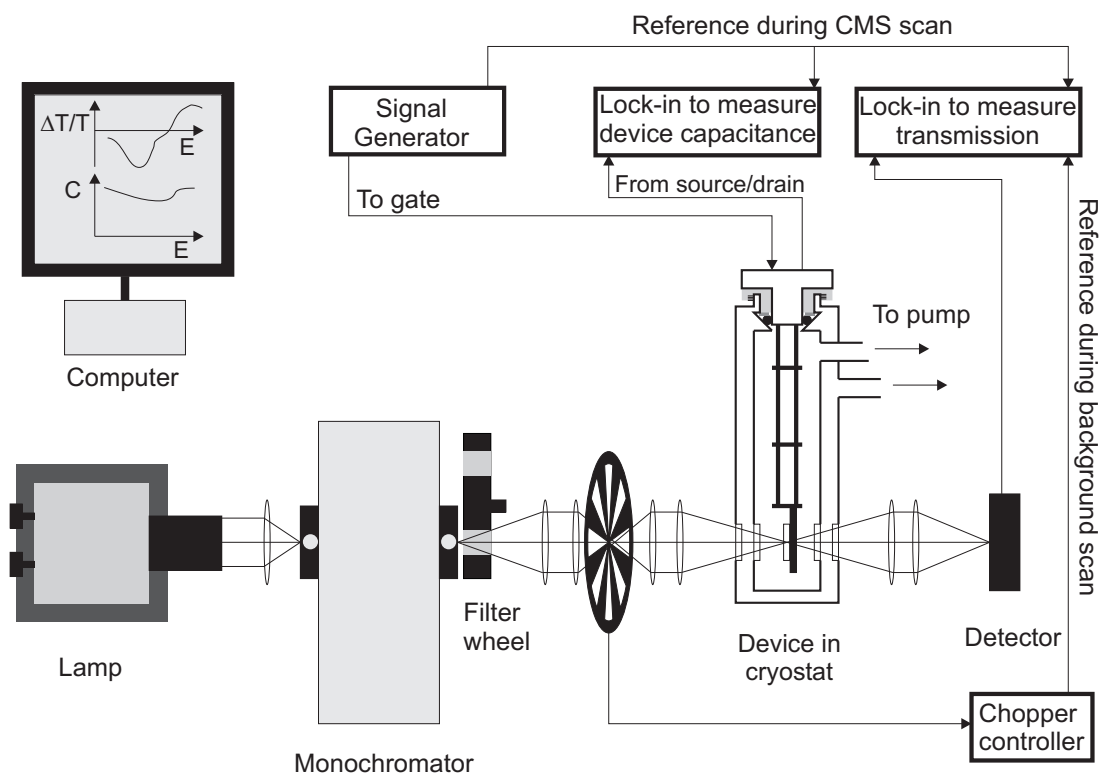


Figure 4.1: New charge modulation spectroscopy setup.

light or IR radiation from the room is modulated and measured by the detector and that the waveform of the detected light is as close to a square wave as possible for correct interpretation. The reference from the chopper wheel is connected to the lock-in for this measurement and fine adjustments of the lamp mirror and sample position are used to maximise the transmitted light without saturating the detector. The light in the room is also turned off for all measurements to avoid saturating the detector and to reduce noise. For this background scan the light was chopped at a frequency of $\sim 400\text{Hz}$ and the lock-in had a time constant of 300ms with a sample time of 2 seconds. As the waveform of the chopped light is a square wave, the measured RMS amplitude of the background transmission T was divided by $4/\pi$ which is the fourier component of a square wave at the fundamental frequency.

For the standard modulation scan to measure ΔT , the source and drain contacts of the transistor were shorted together and grounded. The gate voltage was modulated by a Keithley 3390 Waveform/Function Generator with output set to high impedance followed by a custom built amplifier which multiplied the waveform by -20 and whose frequency response is given in appendix B.3 and B.4. The amplification stage effectively shifts the phase of the signal relative the reference so that the lock-in is triggered when the signal voltage is on a downwards zero crossing. Figure 4.2(a) shows the amplified waveform consisting of a DC and AC component which was typically modulated at 37Hz. For hole accumulation a negative DC component is typically required whereas a positive component is needed for electron accumulation. At the point in the voltage cycle when the magnitude of the voltage is largest, the most charges are accumulated and the transmission is minimised at wavelengths where charges absorb. Equally, at wavelengths where the material used to absorb, the transmission is maximised when the maximum number of charges are present as the absorption is bleached. Figure 4.2(a) gives examples of this time-dependent $\Delta T/T$ for both charge absorption and bleaching associated with hole accumulation for the general case where there may be a phase delay between the applied voltage and accumulation of charges due to contact or channel resistance. By studying figure 4.2(a) or the phasor versions given in figure 4.2(c) and 4.2(d) the changes in transmission as a function of the light energy in figure 4.2(b) can be easily interpreted. Electro-absorption effects, as outlined in section 2.1.6, are due to the field and so typically are exactly in phase with the applied voltage and hence only show up in the X channel meaning that the Y channel often gives a spectra that is free from these effects albeit with a smaller signal. The charge absorption will only be entirely in the X channel if the frequency of modulation is low enough for the given RC charging time of the transistor which reduces with increasing gate voltage. For large contact resistance devices the charge

absorption will always be somewhere between the X and Y channels and the magnitude of the signal will also be reduced as shown schematically in figures 4.2(c) and 4.2(d). Whilst this data can be 'rotated' so that the charge absorption is all in the same channel, all $\Delta T/T$ plots in this thesis, unless otherwise stated, retain this unrotated convention to help elucidate the origin of various spectral features with different phase.

It is important to note that these phasor diagrams are correct for hole and electron accumulation regimes rather than specific gate voltage regimes meaning that a doped sample which still shows hole accumulation with positive gate voltages will have the same phase of $\Delta T/T$ as it did with a negative gate voltage. Opposite charge species will always be 180 degrees out of phase with each other as is clear in figure 4.2(b) which is a consequence of the phase of the trigger relative to the applied voltage.

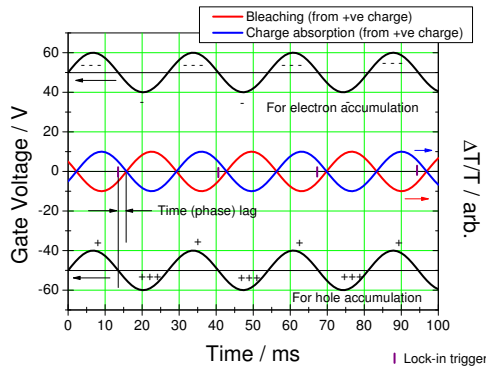
A reasonable signal to noise ratio was achieved with a time constant of 1 second and a sample time of 2 seconds. Despite it being the RMS amplitude of ΔT being measured, no adjustments were made to convert to peak to peak amplitude as the background transmission scan also contains this factor of $1/(2\sqrt{2})$ so it cancels out. Simultaneous electrical measurements on the device were added by measuring the current going onto the source and drain with another lock-in amplifier as explained fully in section 4.4.

Devices were loaded onto the sample holder in air under yellow lights and transferred to the CMS laboratory in darkness. No electrical measurements were performed until the device had been under vacuum at least over night to avoid irreversible charge trapping due to moisture or oxygen in the film. Figure 4.3 shows a device in situ in the sample holder. The transistor is lined up with a small hole such that the hole is smaller than the device to ensure that the light is being modulated by the same amount across the entire area of the device.

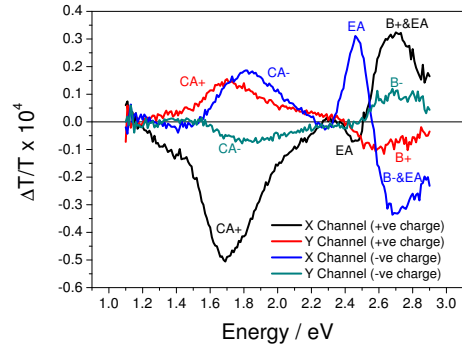
4.3 Calculating the cross section of charge-carriers

The Beer-Lambert law describes how the intensity, I , of light propagating through a medium drops off logarithmically with distance with a decay constant known as the absorption coefficient, α . The absorption coefficient is expressed as a product of cross section, σ (cm^2), and number density of absorbing units, n (cm^{-3}), if using base e or molar absorptivity, ε ($\text{M}^{-1}\text{cm}^{-1}$), and molar concentration, c , (M), if using base 10 as shown in equation 4.1.

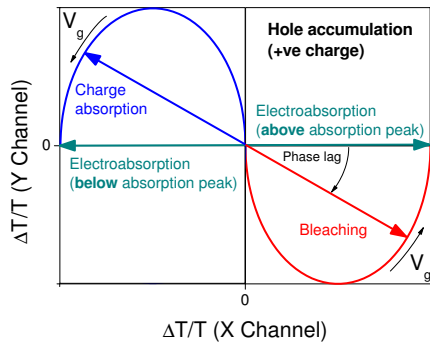
$$I = I_0 \exp(-\sigma n L) = I_0 \cdot 10^{-\varepsilon c L} \quad (4.1)$$



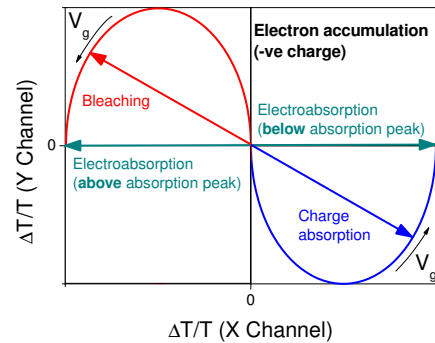
(a) Time domain representation of applied gate voltages with the response of $\Delta T/T$ given for hole accumulation with 37Hz modulation



(b) Unrotated X and Y channels of $\Delta T/T$ for both hole and electron accumulation for an F8BT transistor (absorption peak 2.6eV) with processes labelled (colours not significant)



(c) Phasor diagram for hole accumulation



(d) Phasor diagram for electron accumulation

Figure 4.2: Diagrams to explain the phase and amplitude of the change in transmission through an ambipolar transistor due to bleaching, B, charge absorption, CA, and electroabsorption, EA, processes relative to the trigger from the signal generator which supplies the gate voltage modulation.

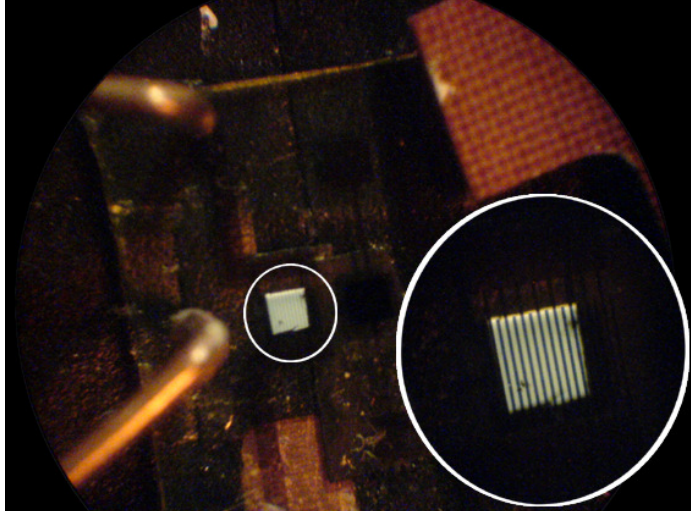


Figure 4.3: Transistor in situ in sample holder.

The absorbance, A , in the two cases has a different definition

$$A = \sigma nL = -\ln\left(\frac{I}{I_0}\right), \quad A' = \varepsilon cL = -\log_{10}\left(\frac{I}{I_0}\right) \quad (4.2)$$

and the absorption coefficient, α is given by

$$\alpha = \sigma n, \quad \alpha' = \varepsilon c \quad (4.3)$$

The relationship between the absorption coefficients is given by

$$\alpha = \alpha' \ln(10) \quad (4.4)$$

In this thesis, from here on, the absorption of charged polymers is expressed in terms of cross sections but in order to relate this to similar measurements¹⁶⁶ using molar absorptivity, the following relationship is required.

$$10^{-3}\varepsilon (M^{-1}cm^{-1}) = \frac{N_A\sigma}{\ln(10) \times 10^6} \quad (4.5)$$

In a transistor, the charged semiconducting polymer segments are in a narrow region within a few nanometers of the interface with the dielectric. The number of charges per unit area, n_{areal} , can be calculated from the capacitance per unit area, C_i , and the voltage applied to the gate, V_g , according to

$$n_{areal} = \frac{C_i V_g}{e} \quad (4.6)$$

From equations 4.6 and 4.2 the thickness of the accumulation layer cancels out and the absorbance from the accumulation layer, A_{acc} , becomes

$$A_{acc} = \frac{C_i V_g \sigma}{e} \quad (4.7)$$

During the CMS experiment the gate voltage is modulated by an amount ΔV_g and the fractional change in transmitted intensity, $\Delta T/T$, is recorded. By considering how a small change in voltage relates to a small change in transmission, the relationship between the two can be shown to be

$$\frac{\Delta T}{T} = -\frac{C_i \sigma}{e} |\Delta V_g| \quad (4.8)$$

The sign here is correct for charge absorptions but would be the opposite for the bleaching of an existing absorption by the presence of a charge. Equation 4.8 is an idealised relationship for a transistor with a constant, gate voltage-independent capacitance and assumes that the charges on the device are in phase with the applied voltage modulation. Such an idealised relationship would exist for a transistor with low contact resistance, high mobility and operating in full accumulation. In reality for the devices in this thesis none of those approximations are correct and the number of charges on the device needs to be measured directly as will be explained in the next section.

4.4 In situ electrical characterisation

4.4.1 Measuring admittance and impedance

An improvised impedance analyser was put together to measure the capacitance of devices during the CMS experiment. The arrangement of the hardware is shown in figure 4.1, but the simplified circuit model is shown in figure 4.4.

The following derivation shows how to establish the impedance, \mathbf{Z} , or admittance, $\mathbf{Y} = \frac{1}{\mathbf{Z}}$, of a device by measuring \mathbf{V}_{out} when knowing \mathbf{V}_{in} and then using \mathbf{Z} or \mathbf{Y} with an appropriate circuit model to establish the capacitance of the device. Note that bold terms indicate that the value is complex.

For $|\mathbf{Z}| \gg r$ (valid at frequencies $\omega \ll 100\text{MHz}$ (for $C=100\text{pF}$) and gate leakage $I_g \ll 100\text{mA}$) then $|\mathbf{V}_{in}| \gg |\mathbf{V}_{out}|$. With conservation of current, this leads to:

$$\frac{\mathbf{V}_{out}}{r} = \frac{(\mathbf{V}_{in} - \mathbf{V}_{out})}{\mathbf{Z}} \approx \frac{\mathbf{V}_{in}}{\mathbf{Z}} \quad (4.9)$$

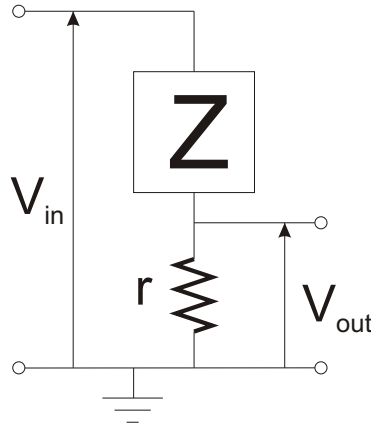


Figure 4.4: Schematic of improvised impedance analyser.

As \mathbf{V}_{out} is measured by a lock-in amplifier referenced from \mathbf{V}_{in} , the common term $e^{i\omega t}$ that appears in both will cancel out in the expressions for the complex impedance and admittance. To achieve this in practice the lock-in had to be set to shift the phase of the trigger by 180 degrees to compensate for the amplifier which inverts the voltage being applied to the device as illustrated previously in figure 4.2(a). \mathbf{V}_{in} and \mathbf{V}_{out} can thus be redefined as the complex *amplitudes* of the time varying voltages which is what the lock in is actually measuring. However because the reference to the lock in is set up to be exactly in phase with \mathbf{V}_{in} , there is no phase constant meaning that it is real so $\mathbf{V}_{\text{in}} = V_{\text{in}}$. The following expressions can then be obtained:

$$\mathbf{Z}(V_{\text{in}}, \mathbf{V}_{\text{out}}) = \frac{rV_{\text{in}}}{\mathbf{V}_{\text{out}}} = \frac{rV_{\text{in}}X_{\text{out}}}{X_{\text{out}}^2 + Y_{\text{out}}^2} - i \frac{rV_{\text{in}}Y_{\text{out}}}{X_{\text{out}}^2 + Y_{\text{out}}^2} \quad (4.10)$$

$$\mathbf{Y}(V_{\text{in}}, \mathbf{V}_{\text{out}}) = \frac{\mathbf{V}_{\text{out}}}{rV_{\text{in}}} = \frac{X_{\text{out}}}{rV_{\text{in}}} + i \frac{Y_{\text{out}}}{rV_{\text{in}}} \quad (4.11)$$

where $\mathbf{V}_{\text{out}} = X_{\text{out}} + iY_{\text{out}}$ has been used as this is the form in which the lock-in amplifier outputs the complex amplitude.

In the simple case of a parallel resistor-capacitor circuit a simple relationship exists between the admittance, \mathbf{Y} and the resistance, R_p , and capacitance, C_p , where the subscript, p , indicates that these components are arranged in the parallel formation:

$$\mathbf{Y} = \frac{1}{R_p} + i\omega C_p \quad (4.12)$$

This means that in terms of the actual RMS amplitude measurements made, the resistance and capacitance can be extracted from the X and Y channels, $X_{\text{out}}^{\text{RMS}}$ and $Y_{\text{out}}^{\text{RMS}}$

respectively.

$$C_p(f) = \frac{2\sqrt{2}Y_{out}^{RMS}}{2\pi frV_{in}^{p-p}} \quad (4.13)$$

$$R_p = \frac{rV_{in}^{p-p}}{2\sqrt{2}X_{out}^{RMS}} \quad (4.14)$$

In the case of a series circuit model, with resistance (R_s and capacitance C_s), the impedance is more appropriate:

$$\mathbf{Z} = R_s + \frac{1}{i\omega C_s} \quad (4.15)$$

So again, in terms of measured quantities:

$$C_s(f) = \frac{2\sqrt{2}(X_{out}^2 + Y_{out}^2)}{2\pi frV_{in}^{p-p}Y_{out}} \quad (4.16)$$

$$R_s = \frac{rV_{in}^{p-p}X_{out}}{2\sqrt{2}(X_{out}^2 + Y_{out}^2)} \quad (4.17)$$

4.4.2 Modelling a series RC device

The unrealistic case of an MIS diode in full accumulation with low leakage but a significant resistance from the electrodes, can be modelled as a series RC circuit and is a starting point to illustrate how to correlate the phase of charges and change in transmission. By analysing the amplitude and phase of the voltage between the resistor and capacitor, \mathbf{V}' , the magnitude and phase of the charge, \mathbf{Q} , in the accumulation layer can be found. We obtain the following result:

$$\mathbf{Q} = \mathbf{V}'C_s = \left(\frac{V_{in}^{p-p}}{1 + i\omega R_s C_s} \right) C_s \quad (4.18)$$

The concept of complex charge has been introduced here which is simply to say that the magnitude and phase of the charges on the device is related to the applied voltage by a phase factor. It should then be expected that the modulus, real and imaginary parts of \mathbf{Q} relate directly to modulus, real and imaginary parts of $\Delta T/T$ i.e. the R, X and Y channels. It turns out that if the parallel circuit model is used to extract the device capacitance, the value obtained is incorrect by the same factor as the real part of \mathbf{V}' , which is to say that the X channel of $\Delta T/T$ scales with C_p . In fact all the terms for \mathbf{Q} can be constructed in terms of C_s and C_p :

$$|\mathbf{V}'|C_s = V\sqrt{C_s C_p} = \frac{eA}{\sigma} \left(\frac{\Delta T}{T} \right)_R \quad (4.19)$$

$$Re(\mathbf{V}')C_s = VC_p = \frac{eA}{\sigma} \left(\frac{\Delta T}{T} \right)_X \quad (4.20)$$

$$Im(\mathbf{V}')C_s = -VC_p \sqrt{\frac{C_s}{C_p} - 1} = \frac{eA}{\sigma} \left(\frac{\Delta T}{T} \right)_Y \quad (4.21)$$

where A here is the area of the capacitor. It is useful to be able to calculate σ independently from the different $\Delta T/T$ channels as the Y channel is often completely free of electro-absorption effects as illustrated in figure 4.2(b).

A different but mathematically equivalent way to obtain the cross sections is to not ever use circuit models but simply measure the number of charges going to the device:

$$\mathbf{Q}^{p-p} = \frac{2\sqrt{2}\mathbf{V}_{out}^{RMS}}{i2\pi fr} \quad (4.22)$$

V_{out} here is, in general, complex as it is not in phase with V_{in} which is what everything is measured relative to. The 'complex' charge on the device can then be explicitly obtained which can again be related to $\Delta T/T$.

$$|\mathbf{Q}| = \frac{2\sqrt{2}R_{out}^{RMS}}{2\pi fr} = \frac{eA}{\sigma} \left(\frac{\Delta T}{T} \right)_R \quad (4.23)$$

$$Re(\mathbf{Q}) = \frac{2\sqrt{2}Y_{out}^{RMS}}{2\pi fr} = \frac{eA}{\sigma} \left(\frac{\Delta T}{T} \right)_X \quad (4.24)$$

$$Im(\mathbf{Q}) = -\frac{2\sqrt{2}X_{out}^{RMS}}{2\pi fr} = \frac{eA}{\sigma} \left(\frac{\Delta T}{T} \right)_Y \quad (4.25)$$

4.4.3 Modelling a transistor

In the more complex scenario where the dominant series resistance is from contact or bulk resistance, the capacitance of the semiconductor layer complicates the measurement. When the semiconductor layer is thin it is especially hard to say whether the charges are being modulated on the source and drain contacts or at the accumulation layer or any combination of those two extremes even though the total number of them can be electrically measured. Using a transistor structure with a very thin semiconductor layer relative to the dielectric offers a better way to measure the number of charges in the semiconductor as charges spreading into the channel increases the capacitance significantly whilst charges moving to and from the metal to the dielectric interface lead to a negligible 2%-4% increase in capacitance. The possibility can be considered that any *increase* in

capacitance tells us how many charges are in the semiconductor channel; the validity of which is now analysed.

The charging and discharging of a transistor channel at a given gate modulation frequency could be limited by the injection of charges into the semiconductor due to contact resistance or by the conductivity of the channel which is determined by the mobility and gate voltage. A circuit model to describe contact resistance is connected to a circuit model to describe a transistor channel in figure 4.5. This represents the simplest model that demonstrates the range of behaviours that could occur in various transistors. It is similar to that reported by Miyadera et al.¹⁵¹ except for R_2 is in parallel with C_{ins} here instead of series. When R_2 is in series with C_{ins} , unless R_2 is much smaller than R_1 the high frequency response is different if the capacitance is extracted via the series, $1/Im(\omega\mathbf{Z})$, or parallel, $Im(\mathbf{Y}/\omega)$, methods which was not observed experimentally. If R_2 were much smaller than R_1 in the Miyadera model then the phase and amplitude of the voltage at the point connected to the channel does not tend to $-\pi$ and zero respectively at high frequency as has been observed experimentally.¹⁶⁷

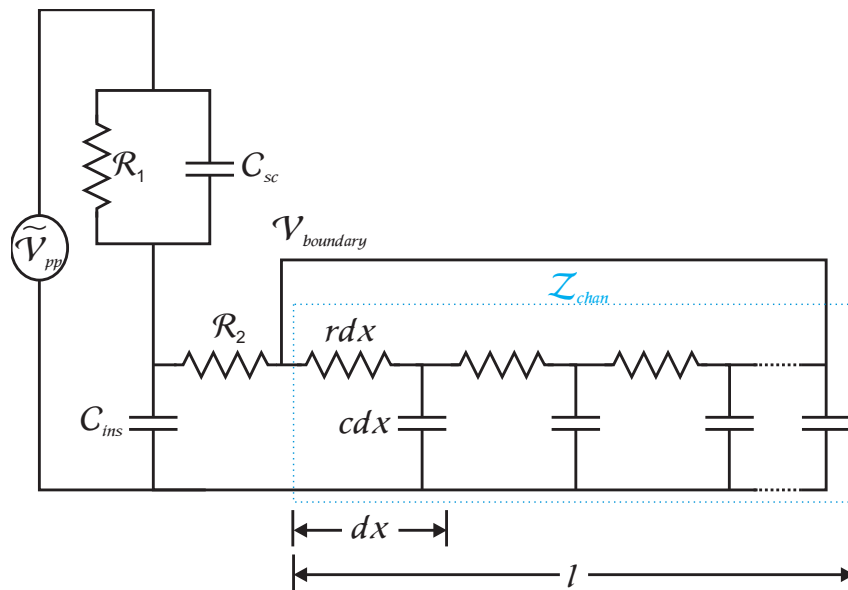


Figure 4.5: Circuit model for transistor. The highlighted area represents the channel.

The equations to describe the voltage, \mathbf{V} , and current \mathbf{I} , in the channel region are given by

$$\frac{d\mathbf{V}}{dx} = r\mathbf{I}, \quad \frac{d\mathbf{I}}{dx} = i\omega c\mathbf{V} \quad (4.26)$$

$$\frac{d^2\mathbf{V}}{dx^2} = i\omega r c \mathbf{V}, \quad \frac{d^2\mathbf{I}}{dx^2} = i\omega r c \mathbf{I} \quad (4.27)$$

where r is the impedance per unit length (x) of the channel (in this case only resistive) and $i\omega c$ is the admittance per unit length (in this case only capacitive). The general solution for the voltage in the channel as a function of position is given by¹⁶⁸

$$\mathbf{V}(x) = V_1 \exp(-\sqrt{i\omega r c} x) + V_2 \exp(\sqrt{i\omega r c} x) \quad (4.28)$$

This solution has been used to fit the amplitude and phase of charges in the channel in a transistor measured by changes in the thickness of the device¹⁶⁷ however the complex pre-factors, V_1 and V_2 , were just used as fitting parameters. In this work the form of these pre-factors is sought by using the voltage at the point $V_{boundary}$ in figure 4.5 as the boundary condition.

$$\mathbf{V}(x=0, x=l) = \frac{V_{pp}}{\left[1 + \left(i\omega C_{ins} + \frac{1}{R_2 + \mathbf{Z}_{chan}}\right) / \left(\frac{1}{R_1} + i\omega C_{sc}\right)\right] \left[1 + \frac{R_2}{\mathbf{Z}_{chan}}\right]} \quad (4.29)$$

The impedance of the channel, \mathbf{Z}_{chan} , is given by this continued fraction

$$\mathbf{Z}_{chan} = r dx + \frac{1}{i\omega c dx + \frac{1}{r dx + \frac{1}{i\omega c dx}}}}}}}}}} = \sqrt{\frac{r}{i\omega c}} \quad (l \rightarrow \infty) \quad (4.30)$$

This is given in the case of three RC repeat units. The dependence on the channel length, l , is subtle and related to the number of iterations of this fraction through the interval dx

$$dx = \frac{l}{\text{number of RC units}} \quad (\text{number of RC units} \rightarrow \infty) \quad (4.31)$$

In the absence of an obvious analytical solution to the finite channel length case this can be solved computationally and is found to converge to three significant figures with 1000 iterations.

The general solution for the given boundary conditions is

$$\mathbf{V}(x, \omega) = \frac{V_{pp} [\exp(-\sqrt{i\omega rc}x) + \exp(\sqrt{i\omega rc}(x-l))] / [1 + \exp(-\sqrt{i\omega rc}l)]}{\left[1 + \left(i\omega C_{ins} + \frac{1}{R_2 + \mathbf{Z}_{chan}}\right) / \left(\frac{1}{R_1} + i\omega C_{sc}\right)\right] \left[1 + \frac{R_2}{\mathbf{Z}_{chan}}\right]} \quad (4.32)$$

The channel resistance per unit length, r , the channel capacitance per unit length, c , the capacitance across the semiconductor above the contacts, C_{sc} , and the capacitance across the insulator above the contacts, C_{ins} are given by

$$r = \frac{d_{ins}}{W\mu\epsilon\epsilon_0(V_g - V_t)}, \quad c = \frac{\epsilon\epsilon_0 W}{d}, \quad C_{sc} = \frac{\epsilon\epsilon_0 A_c}{d_{sc}}, \quad C_{ins} = \frac{\epsilon\epsilon_0 A_c}{d_{ins}} \quad (4.33)$$

It has been shown that in the top gate transistor structures used in this thesis that the contact resistance varies with the gate voltage in the following way¹⁶⁹:

$$R_c = \frac{A}{V_g - V_t} + r_c \quad (4.34)$$

where A is a constant representing the gate voltage dependence of the bulk conductivity and r_c is a constant representing an injection barrier between the metal and semiconductor. Figure 4.6(a) shows equation 4.32 plotted in a $40\mu\text{m}$ channel for a series of different frequencies with a low contact resistance. At high frequencies, the decay of the amplitude of the modulated voltage drops off exponentially into the channel from each electrode. Figure 4.6(b) shows an identical scenario but with the contact resistance being 1000 times larger which reduces the voltage under the contacts and looks similar to experimental observations.¹⁶⁷

What is required is knowledge of how the measured phase and amplitude of the charge going to the device, \mathbf{Q}_{dev} , relates to the total phase and amplitude of all the charge in the channel, \mathbf{Q}_{ch} . This is equivalent to saying how does the electrical measurement of the entire device relate to the optical measurement of $\Delta T/T$ in the channel. To compute this, the overall impedance of the device, \mathbf{Z}_{dev} , is needed which is given by

$$\mathbf{Z}_{dev} = \left[\frac{1}{\frac{1}{R_1} + i\omega C_{sc}} + \frac{1}{i\omega C_{ins} + \frac{1}{R_2 + \mathbf{Z}_{chan}}} \right] \quad (4.35)$$

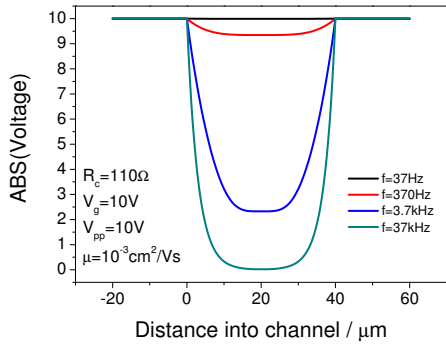
The complex values for the charge in the channel and that measured going to the device are then given by

$$\mathbf{Q}_{ch} = c \int_0^l \mathbf{V}(x, \omega) dx \quad (4.36)$$

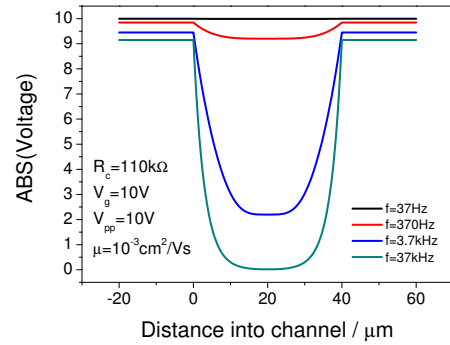
$$\mathbf{Q}_{dev} = \frac{V_{pp}}{\mathbf{Z}_{dev}i\omega} \quad (4.37)$$

Figure 4.6(c) shows the real and imaginary parts of the total charge in the channel, \mathbf{Q}_{ch} , and that going to the whole device, \mathbf{Q}_{dev} , as a function of gate voltage for moderate and high contact resistance cases. The contact resistance is gate voltage dependent according to equation 4.34 and is always less than the total channel resistance in the moderate case and always greater in the high case. The modulation frequency is such that the channel should fully accumulate with voltages greater than around 10V where the channel resistance is around 310M Ω . This figure illustrates very clearly how, in a low contact resistance case, the number of charges in the device and channel rapidly saturates and becomes in phase with the gate voltage even when the mobility is only 10⁻³cm²/Vs. The low contact resistance case therefore shows that the channel fully accumulates and in this regime the charges are in phase with the applied voltage. This means that both the X channel or modulus of $\Delta T/T$ corresponds to the amount of charges predicted by the areal capacitance and gate voltage modulation so equation 4.8 is valid. In the case of high contact resistance, the channel may never fully accumulate and the phase of the charges both going to the device and in the channel reflects a lag behind the applied voltage. In this case, the applied peak to peak voltage and capacitance per unit area can thus never be used to determine the number of charges being modulated in the channel as this will always underestimate the cross section measurement by an amount depending on the contact resistance. The measured amplitude and phase of the charges going to the device does however relate to the amplitude and phase of the charges in the channel and hence $\Delta T/T$. To see this correlation more clearly, figure 4.6(d) plots the real against imaginary parts of the charge going to the device and and the charge in the channel.

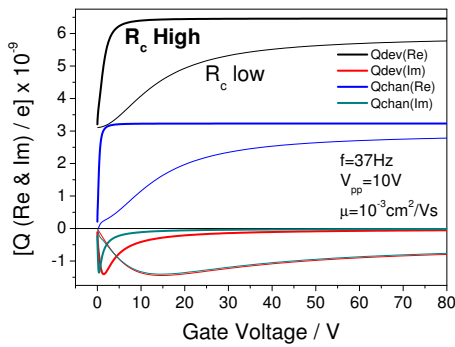
Given that in high contact resistance devices the traditional method of calculating cross sections can never work, there are two methods to use the in-situ electrically measured charging of the device to correct this. Figure 4.6(d) has been replotted as figure 4.7(a) to illustrate the two methods to calculate the number of charges in the channel. The number of charges in the channel has been labelled $\Delta T/T$ as this is what it proportional to in amplitude and phase. In the first method, the modulus of the charge going to the device in depletion is recorded and vectorially subtracted from the modulus in accumulation in order to establish the increase in charge going to the device. If the semiconductor is sufficiently thin, and the combination of modulation frequency and channel resistance is such that the channel should accumulate fully then the increase in charge going to the device corresponds well to the number of charges in the channel and hence $\Delta T/T$. As



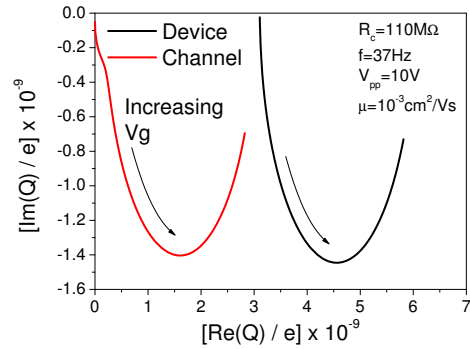
(a) Modulus of the complex voltage in a low contact resistance device for various frequencies of modulation. Channel resistance is $31\text{M}\Omega$



(b) As 4.6(a) but with moderate contact resistance showing incomplete accumulation above contacts



(c) Real and Imaginary parts of the complex charge (scaled to number of charges) in the channel and device as a function of gate voltage for a moderate ($A=1\text{M}\Omega$, $r_c=10\text{k}\Omega$, thick lines) and high ($A=1\text{G}\Omega$, $r_c=10\text{M}\Omega$, thin lines) contact resistance



(d) Real vs Imaginary parts of high contact resistance case from 4.6(c) showing similarity between the complex charge in the channel and that going to the device

Figure 4.6: Plots from equations 4.32, 4.36 and 4.37 applied to a top gate bottom contact transistor with a channel length of $40\mu\text{m}$, width of $2\mu\text{m}$, dielectric and semiconductor thickness of 500nm and 20nm respectively with both having a relative dielectric constant of 3.65. Contact resistance, R_c , equals both R_1 and R_2 and uses the form from 4.34 in plots 4.6(c) and 4.6(d). Code for calculation given in appendix C.

it is the number of charges per unit area that is required, the area corresponding to the extra charge is the area of the channel and any region where the gate is patterned near the source and drain electrodes (within a distance that is accessible to the charges given their mobility). The equations representing Method 1 are given here where \mathbf{Q}_{dev} , X_{dep} , and Y_{dep} represent the depletion values of these quantities where charges are simply being modulated on the source and drain electrodes without entering the semiconductor.

$$|\mathbf{Q}_{dev} - \mathbf{Q}_{dep}| = \frac{2\sqrt{2}\sqrt{(X_{out}^{RMS} - X_{dep})^2 + (Y_{out}^{RMS} - Y_{dep})^2}}{2\pi fr} = \frac{eA_{chan}}{\sigma} \left(\frac{\Delta T}{T} \right)_R \quad (4.38)$$

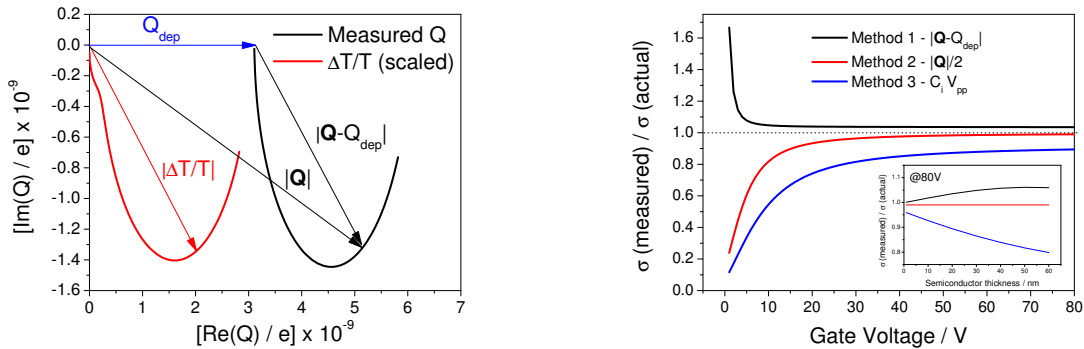
$$Re(\mathbf{Q}_{dev} - \mathbf{Q}_{dep}) = \frac{2\sqrt{2}(Y_{out}^{RMS} - Y_{dep})}{2\pi fr} = \frac{eA_{chan}}{\sigma} \left(\frac{\Delta T}{T} \right)_X \quad (4.39)$$

$$Im(\mathbf{Q}_{dev} - \mathbf{Q}_{dep}) = -\frac{2\sqrt{2}(X_{out}^{RMS} - X_{dep})}{2\pi fr} = \frac{eA_{chan}}{\sigma} \left(\frac{\Delta T}{T} \right)_Y \quad (4.40)$$

Note that using the modulus has the best signal to noise ratio and is relatively insensitive to any systematic phase errors in either of the measurements which would rotate the red or black lines in 4.7(a) about the origin affecting the X and Y channel amplitudes. However sometimes it is more useful to use the X channel as it retains the sign of the spectra. According to the circuit model, this method fails when the channel resistance or frequency is high enough such that the channel would not fully accumulate even in the absence of contact resistance as illustrated for very low gate voltages in figure 4.7(b). The inset shows the effect of the semiconductor thickness on the validity of the cross section when extracted by this method illustrating that the error is not very significant if the semiconductor is sufficiently thin.

The second method is to use the unchanged modulus of the electrical measurement, $|\mathbf{Q}|$ and divide this by two or whatever the ratio of the channel to electrode area is to get the number of charges in the channel. In practice, this is done implicitly by using equation 4.23 with A corresponding to the entire area of the gate which is equivalent to saying that all the charges in the semiconductor have spread out evenly across the gate area. This method does not perform well for very large contact resistances such as 100M Ω or more when modulating at 37Hz but is independent of the semiconductor thickness and becomes exactly correct when the contact resistance is around 10M Ω or less. Method 2 together with the traditional Method 3, where no electrical measurements are made in situ, are also shown in figure 4.7(b).

To summarise these methods, regardless of contact resistance, all three fail to enable the accurate measurement of cross section when the channel conductivity itself is not



(a) Visualisation of the vectors used to correlate the measured charge and the actual charge in the channel.

(b) Ratio of estimated number of charges in channel to actual number and hence error in σ for three methods described in text.

Figure 4.7: Illustration of the three methods to calculate the number of charges in the channel in order to compute the cross section of absorption, σ .

high enough at a given frequency to enable complete charging and discharging. This critical frequency, ω_c has already been alluded to in the background section and is given approximately by

$$\omega_c = \frac{\pi^2 \mu |V_g - V_t|}{L^2} \quad (4.41)$$

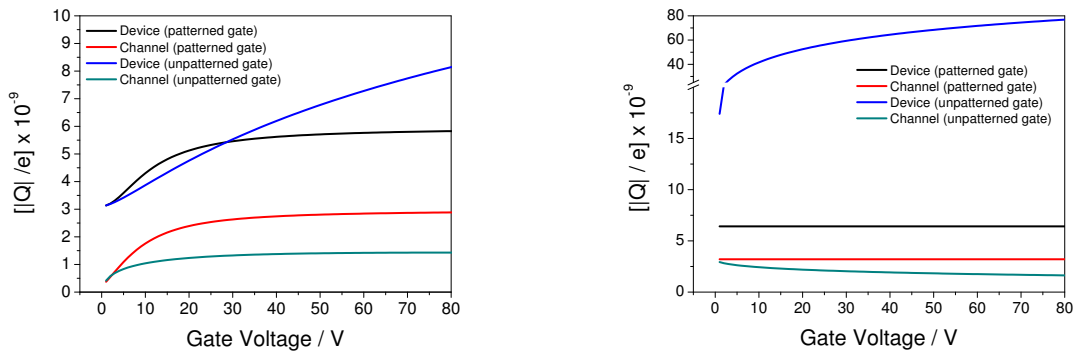
where L is the channel length. At frequencies below 100Hz and for typical channel lengths, this criteria is easily met with a reasonable gate voltage. According to the model, Methods 1 and 2 work in this regime to compensate for the effect of contact resistance. Method 1 can cope with any contact resistance but has a systematic error related to the semiconductor thickness whereas Method 2 only becomes accurate for intermediate contact resistances and is independent of semiconductor thickness. Conveniently Method 1 and 2 form an upper and lower limit for the cross section when contact resistance dominates. The traditional Method 3 performs least well when contact resistance is involved and the areal capacitance is typically measured at a different time on a different part of the sample or based on film thickness measurements which can both introduce errors.

Since the electrical measurement is performed simultaneously with the optical measurement, any changes in channel or contact resistance that occur with time will be automatically adjusted for. In a two hour long scan, trapping in the channel or in the vicinity of the electrodes can often reduce the amount of charge that can be modulated in a polymer transistor. Without being corrected by this new technique, device degradation

would cause the extracted cross section to reduce in the scanning direction thus reducing the accuracy and reproducibility.

4.4.4 The importance of patterning the gate electrode

A subtle yet significant effect comes into play if the gate electrode extends over a larger area than the source and drain electrodes when contact resistance is taken into account. Up until now all the modelling has assumed that the gate only covers the channel and electrodes but if it covers a larger area then charges will spread out to the same area given enough time. The value of the area that is required in the equations for methods 1 and 2 then becomes ambiguous and the measured capacitance will tend to continue to increase with gate voltage as the distance to which charges can spread increases with the square root of gate voltage. In a situation where the injection of charges is slowed by contact resistance, charges will tend to spread out thinly over a large area rather than fully accumulate in the channel. Figure 4.6(c) shows the high, gate-voltage dependent contact resistance case from figure 4.6(c) replotted and repeated with an infinite gate area using the infinite channel length limit of equation 4.30 to calculate the boundary values of the channel and in calculating the device impedance. As expected, the number of charges going to the device continues to increase with gate voltage and the number of charges in the channel never reaches the same level as when the gate is finite.



(a) As figure 4.6(c) but repeated for the case of an unpatterned gate electrode of infinite extent.

(b) As 4.8(a) but with a fixed contact resistance of $1\text{M}\Omega$ and mobility of $10^{-1}\text{cm}^2/\text{Vs}$.

Figure 4.8: Two simulated examples of how the combination of contact resistance and an unpatterned gate electrode will lead to an overestimate of the number of charges being measured and a reduction in the number of charges in the channel.

The effect is even more pronounced in figure 4.8(b) where the mobility is 100 times higher and a constant contact resistance of $1\text{M}\Omega$ is used. The number of charges in the channel clearly decreases with gate voltage and the measured number of charges going to the device increases significantly. Care must be taken to avoid this artifact if looking for subtle effects with CMS such as gate-voltage dependent changes in cross section.

4.4.5 Applying a drain voltage during measurements

One final new electrical technique employed in this thesis is to perform the CMS experiment whilst applying a voltage on the drain relative to the grounded source. A drain voltage can enable accumulation to be reached at lower gate voltages because transistor conductivity is drain voltage dependent in some top gate transistors as observed by suppressed current at low drain voltages on output scans.

When a drain voltage is applied and the current is measured on the source, not only the charging current is modulated by the gate but also the source-drain current due to the change in conductivity. In order to isolate the charging current from the source-drain current, the experiment must be performed when measuring the source current and then the drain current with the results added together. The source-drain current cancels out leaving only the charging current. Rather than measure all wavelengths and then reconnect the source and drain, a Labview program was written to take two measurements at each wavelength and choosing a drain and gate voltage such that both situations were equivalent only the label of source and drain are switched. The input of the program is simply two gate voltages, V_g^1 and V_g^2 . The applied voltages for the two scans are then

$$V_s = 0V, \quad V_g = V_g^1, \quad V_d = V_g^1 - V_g^2 \quad (4.42)$$

$$V_s = 0V, \quad V_g = V_g^2, \quad V_d = V_g^2 - V_g^1 \quad (4.43)$$

A simple example with $V_g^1 = -50V$ and $V_g^2 = -45V$ would give $V_s = 0V$, $V_g = -50V$ and $V_d = -5V$ for the first scan and then $V_s = 0V$, $V_g = -45V$ and $V_d = +5V$ for the second. The two $\Delta T/T$ spectra will be identical and can be averaged to reduce error and then the individual X and Y components of the currents from each scan are added together to give the X and Y components of the charging current.

This method can be used to get a higher quality spectra as the device will be further into accumulation with more charges being modulated however the accuracy of the cross section is sacrificed as the area that is being charged becomes ambiguous.

4.5 Summary

To summarise, the existing CMS setup was modified to increase the accuracy and allow for the measurement of the optical cross section of charge-induced absorptions when measured on devices that are hampered by large contact resistance. This was done by adding simultaneous electrical measurements of the charge on the device to compliment the optical measurement of $\Delta T/T$. In order for the electrical measurements to be correlated to the number and phase of the charges in the channel a transistor structure with a thin semiconductor layer, patterned gate and low leakage current was shown to be necessary through the use of an equivalent circuit model. This technique can also be extended to the case where a drain voltage is required to help the device get into accumulation to improve the size of the measured change in absorption. The magnitude of the cross section with this drain-voltage technique should be scaled to the case with no drain voltage as the area where charges are becomes ambiguous with a drain field.

Chapter 5

Optimising ambipolar transistors for charge modulation spectroscopy

5.1 Introduction

In the previous chapter the problem of simultaneously measuring the number of charges being modulated in a device and the associated change in transmission through the device was solved leading to a more accurate method for determining the cross section of polarons. The focus of this chapter is the device structure itself and understanding and eliminating processes that can lead to an absorption spectra for the polaron that contains device-dependent artifacts. The novel measurement being attempted in this work is to record the polaron absorption spectra for both the hole and the electron on the same polymer to understand fundamental differences or similarities between their respective wavefunctions. The possibility to do this measurement has come about due to the recent advances in single component ambipolar transistors,³² however it will turn out that some features of these devices render them highly susceptible to spectral artifacts and constraints on the successful fabrication of the devices make these hard to overcome. The process of identifying the origin of these artifacts, developing analytical descriptions of them and using this to fabricate optimised device structure to obtain artifact-free spectra is chronicled in this chapter.

Measuring the optical absorption of films whose thickness is comparable to the wavelength the incident light is notoriously difficult due to the same interference effects that produce the familiar colours when a film of oil lies on the surface of water. The origin of these wavelength-dependent modulations in reflectance or transmittance is from multiply-reflected light waves interfering either constructively or destructively with each other. Reflections occur at any interface between media with different refractive indices such as the oil/water and oil/air boundaries in this example. In devices, the interfaces between the different polymer layers, the substrate and air or any metallic layers will result in reflections. Interference effects disappear as the layer becomes thinner than $\lambda_{min}/4n$ where λ_{min} is the shortest incident wavelength and n is the refractive index of the layer. Also, the fringes become so closely spaced that they blur out if the film is significantly thicker than the longest incident wavelength. The wavelengths of interest for polaron absorptions are between 400nm and 3000nm but the range of polymeric dielectric thicknesses in transistors that can accumulate a large enough number of charges over a reasonable area with sensible voltages but not suffer from electrical breakdown is in the range of 200nm to 1000nm. Coupled with a refractive index of around 1.5 in these polymer layers, these facts mean interference effects are unavoidable as the entire device would need to be less than around 70nm.

Interference effects do not necessarily have to cause a problem in the CMS experi-

ment as it is the normalised quantity $\Delta T/T$ that is being measured so any wavelength-dependent intensity modulations due to the device thickness might be expected to cancel out, however there are two effects that must be considered. Firstly, if any property of the device changes with the gate voltage modulation, the interference and thus the transmitted intensity could change giving the appearance of an absorption or bleach. Secondly, the multiple reflections can cause a standing wave effect in which the intensity of the electric field can modulate through the thickness of the film. This can have the effect of reducing the absorption at particular wavelengths, particularly if an absorbing layer is in a narrow region in a thicker layered structure. These effects will be henceforth referred to as interference and standing wave filtering respectively for brevity.

The standing wave effect might modulate the magnitude of the spectrum but could never cause the sign or phase of $\Delta T/T$ to change. The result of this would be a normal looking spectra with a charge absorption and neutral absorption bleach, but there would be a wavelength dependent modulation distorting the shape. The spectra would change from device to device or if the device were rotated. Changes in the reflection and transmission coefficients of the device could however cause the sign of $\Delta T/T$ to change and this process may or may not be in phases with the charge absorption depending on whether it is the field or charges causing it. A spectrum with no familiar bleaching and sub energy gap absorption features could result if the interference changes dominate. These changes in the interference spectrum could originate from any of three mechanisms:

1. A charged polymer has new absorptions which, via the Kramers-Kronig relations, will have a different refractive index function compared to the neutral polymer.
2. The electrostatic force across the device could change the thickness in a process known as electrostriction.
3. A shift in the absorption of the dielectric or semiconductor with electric field (electroabsorption) will have an effect on the bulk dielectric constant at the wavelengths being probed, again via the Kramers-Kronig relations.

All of the effects listed above could be large when interference is observed in the regular transmission spectra of the device and in reality this can never be completely removed. However, the effects can be minimised and a number of strategies have been employed in the past to this effect for CMS. Brown⁶⁰ worked with an MIS diode structure for measuring P3HT and made the devices as thin as possible ($\sim 150\text{nm}$) using a SiO_2 dielectric. Deng¹⁷⁰ made F8T2 transistors with thick dielectrics ($>500\text{nm}$) but replaced all the metal electrodes with PEDOT:PSS to reduce reflections. Zhao¹⁷¹ used thin metal

electrodes and transistor structures but kept the dielectric thickness to $\sim 200\text{nm}$ which was aided by cross-linking to improve performance. Of these methods, the only one that is immediately completely compatible with ambipolar transistors is the latter one as SiO_2 is not a suitable dielectric for electron transport³¹ and the high annealing temperatures required for stable electron transport are incompatible with PEDOT:PSS source-drain electrodes. Stable ambipolar transistor with F8BT can be made successfully with $\sim 20\text{nm}$ thick gold bottom contacts covered with a layer of F8BT annealed at 290°C , which is over its melting temperature, topped with a PMMA dielectric and a metallic gate. The increase in performance with annealing over the melting temperature is at odds with the performance of F8BT in photovoltaics¹⁷² and may be related to morphology or thickness of the film on the contacts.^{173,174} Initial attempts using conventional F8BT ambipolar transistors, only differing to the architecture successfully used by Zhao for P3HT by having a dielectric that was twice as thick, gave unrecognisable CMS spectra (see fig 5.1). Whilst the Y channel resembles a charge absorption spectra, the X channel contains some features that are in phase with the applied voltage but resemble a sub energy gap bleach which is not physically possible owing to the lack of existing neutral absorptions in that region. As mentioned above, this points to a change in the interference due to the applied field being the origin of the artifact.

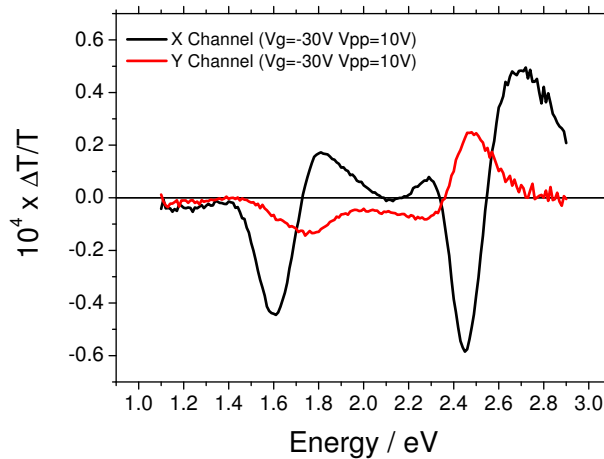


Figure 5.1: Charge modulation spectra for a typical F8BT ambipolar transistor with $\sim 20\text{nm}$ thick gold source drain electrodes, $\sim 30\text{nm}$ thick F8BT, $\sim 500\text{nm}$ thick PMMA and a gold metal gate electrode. Note, the X channel is exactly in phase with applied voltage modulation.

There are a number of differences between the P3HT and F8BT cases including a

thicker dielectric, lower mobility, higher contact resistance, less stability and higher photoluminescence efficiency. This chapter begins with the most obvious first step of reducing the device thickness.

5.2 Reducing device thickness

In the ambipolar light-emitting biasing regime, a transistor consists of two saturated channels in series and so the current is proportional to $(V_{gs}^2 + V_{gd}^2)/l$ as seen in equation 2.55, where l is the dielectric thickness. Typically these devices are made to maximise the current and hence light emission. Making the dielectric thicker means less charge density but, by the same factor, higher breakdown voltages. Due to the squared dependence of current on the voltage across the dielectric, the maximum intensity of light emission therefore scales linearly with dielectric thickness for a given channel length. The same light emission could be maintained in thinner devices by scaling the channel length with the dielectric thickness, but thinner dielectrics are generally avoided due to the higher probability of spin coating defects. F8BT transistors are therefore typically fabricated with dielectric thicknesses of $\sim 400\text{nm}$ - 500nm which enables 100V (SPA maximum) between either electrode and the gate to be repeatedly applied without danger of breakdown. For CMS, a transistor design with $40\mu\text{m}$ channel length is used due to its high ratio of channel to electrode area ($\sim 1:1$). The following attempts to make the dielectric thinner with this relatively long channel length therefore result in transistor characteristics that look different to F8BT transistors optimised for light-emission.

5.2.1 Cross-linked PMMA

The first attempt at reducing the dielectric thickness was to use a cross-linker which has been shown to increase the yield in thin layers.¹⁷⁵ Low molecular weight PMMA (120 kgmol^{-1}) was used at concentrations of 40-45mg/ml and 1,6-bis(trichlorosilyl)hexane (Acro Organics), was added to the solution (0.7 volume percent) before filtering. Films had to be spun in air for the cross-linking to be effective. Resulting dielectric thicknesses were around 200nm.

As shown in figure 5.2 acceptable leakage currents were obtained at the voltages required for accumulation however the spin-coating in air seemed to have a negative effect on the device performance with current degradation occurring after subsequent scans. The CMS spectra was measured on one of these devices as shown in figure 5.3(a). Comparing the spectra to the absorption of F8BT and also the first derivative of the absorption in

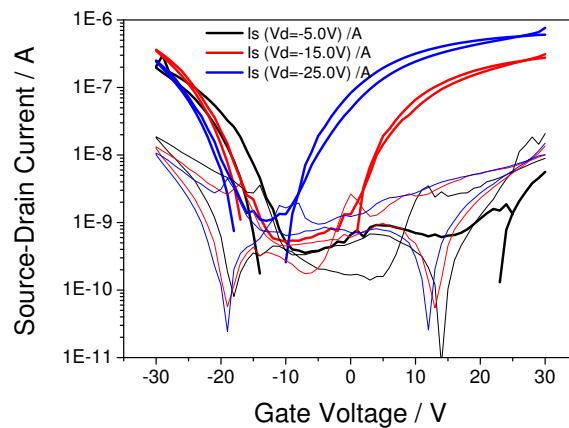
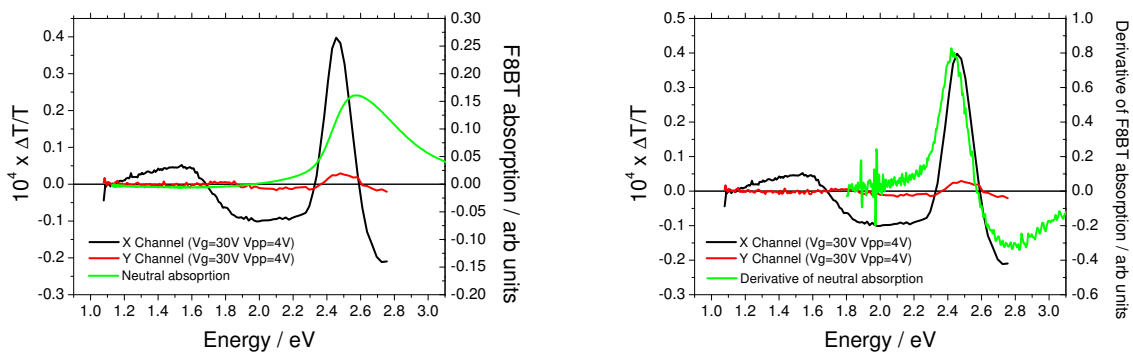


Figure 5.2: Transfer characteristics of a typical F8BT transistor with a 200nm cross-linked PMMA dielectric. Thinner lines show leakage current.

figure 5.3(b), the large feature can clearly be seen to be caused by electroabsorption. As mentioned above, there should be no change of sign of the signal in the sub-gap region as there is no absorption there that can be bleached. This feature is therefore an artifact and not caused by the absorption of charges.



(a) Modulation spectra compared to F8BT neutral absorption.

(b) Modulation spectra compared to the derivative of F8BT neutral absorption.

Figure 5.3: CMS spectra for F8BT transistor with cross-linked low Mw 200nm PMMA dielectric.

5.2.2 High molecular weight PMMA

The electroabsorption suggested that the device was not fully accumulated because the charges should screen the electric field from the semiconductor. This is possible if charges trap and shift the threshold for the accumulation of mobile charges to higher gate voltages. To avoid this possibility, a high molecular weight PMMA ($M_W = 1M$) was used which gave similar dielectric thicknesses, smoother films and more importantly, less hysteresis as it did not need to be spin coated in air. The device characteristics are shown in figure 5.4.

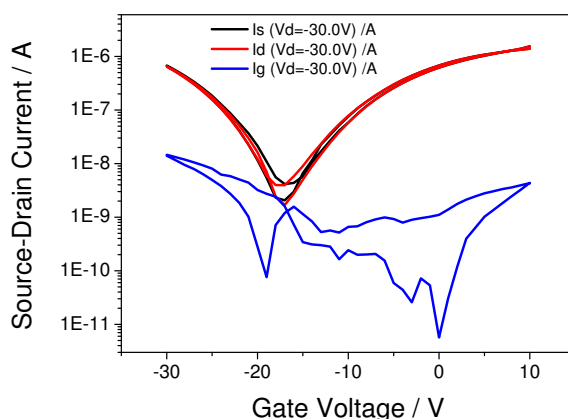


Figure 5.4: Transfer characteristics of a typical F8BT transistor with a 200nm high Mw PMMA dielectric.

The forward and backward sweep overlap very well indicating significantly reduced charge trapping. In fact, above 200nm, most molecular weights of PMMA perform well without cross-linking when the solutions are filtered, the cleaning steps are performed very carefully and the source-drain electrodes are not too thick ($\sim < 20nm$). As seen in figure 5.5 the spectrum was still unphysical despite being a stable device with the same dimensions as had successfully been used with P3HT. Again, the Y channel contains something recognisable as a CMS spectra, but the X channel includes some of this but with an added artifact and some electroabsorption.

In conclusion, the thinnest devices were made that could still achieve stable ambipolar behaviour in an identical device structure has had been successfully used with P3HT as the semiconductor and yet the CMS spectra was still far from correct with a strong electroabsorption signal persisting even when supposedly in accumulation. The next step was to try to increase the mobility of the charges in F8BT to be completely sure that

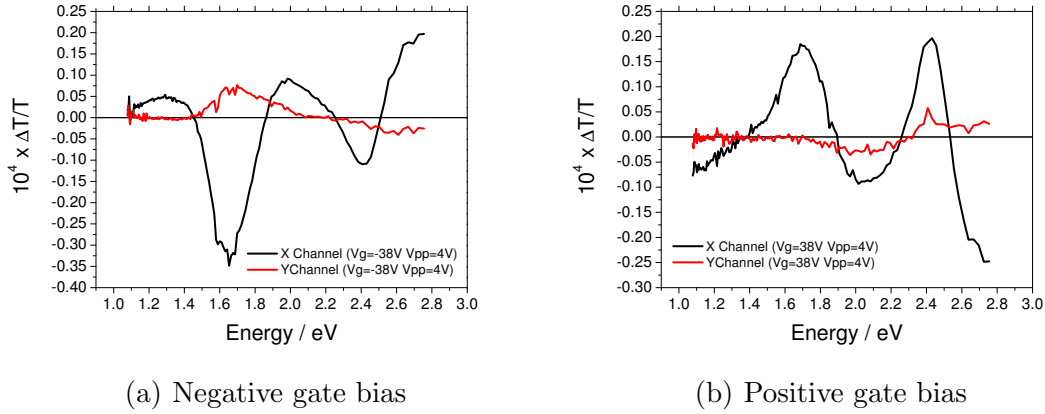


Figure 5.5: CMS spectra of F8BT device with $\sim 200\text{nm}$ thick high Mw PMMA dielectric.

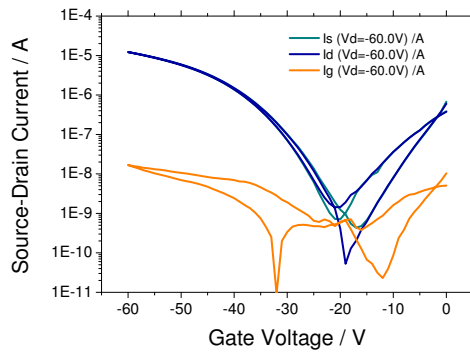
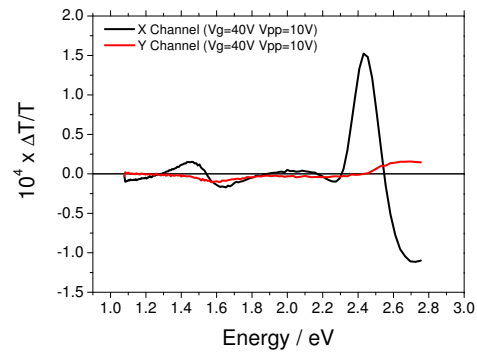
they could respond at the modulation frequency and screen the gate field to remove the electroabsorption.

5.3 Increasing mobility

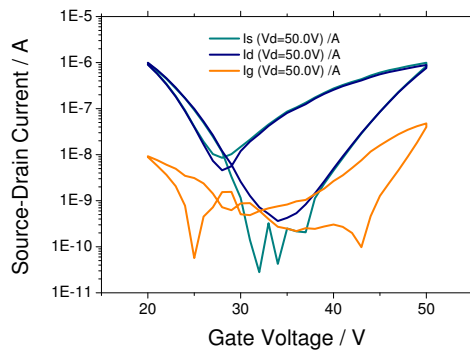
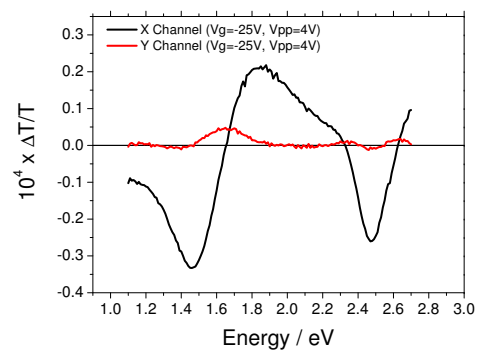
It has been reported that lower dielectric constants can increase FET mobility²³ so different dielectrics were used. The transfer characteristics of representative transistors from these different dielectrics are shown in figure 5.6. The device stability was never as good as when using PMMA but the new dielectrics did increase the mobility by up to an order of magnitude. However, the CMS spectra were not improved. The sub-band gap feature was different in each case although all show the common feature of electroabsorption. This is a clear indication that the gate voltage is not being screened and the device is not fully in accumulation.

By reducing the frequency to 6Hz (see figure 5.7), the emergence of a dominant charge absorption peak made it apparent that the charges are not moving fast enough to screen the gate field. The persistence of the electroabsorption signal at 2.4eV is a first indication that even if the channel is filling with charge, the field between the contacts and the gate is still being modulated suggesting that blocking this region from the experiment is a logical step forward.

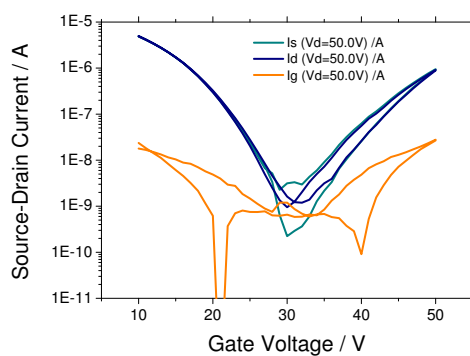
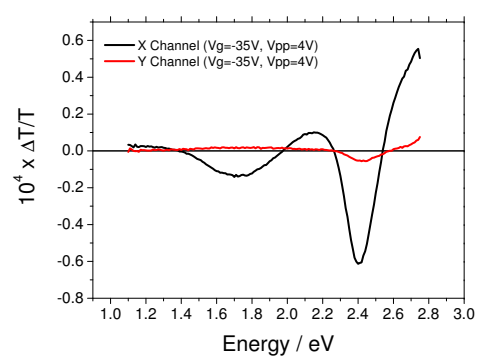
Bürigi et al.¹⁷⁶ showed that charging of a channel upon a step change in the channel potential proceeds according to the drift of charges in their self-induced field. Applying this model to a $40\mu\text{m}$ channel for F8BT with the measured saturation mobility of $10^{-3}\text{cm}^2/\text{Vs}$ predicts a time constant of $1.6\text{ms}/\text{V}$ which corresponds to a frequency of


 (a) CYTOP device characteristics ($\mu_h = 8 \times 10^{-3}$)


(b) CYTOP device CMS


 (c) PIB device characteristics ($\mu_h = 3 \times 10^{-3}$)


(d) PIB device CMS


 (e) PCHE device characteristics ($\mu_h = 1 \times 10^{-2}$)


(f) PCHE device CMS

Figure 5.6: Transfer characteristics and CMS spectra from F8BT devices with a variety of dielectrics which offer higher mobility transistors.

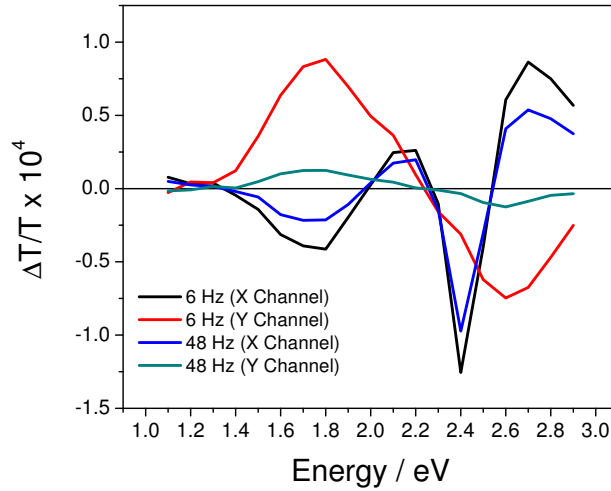


Figure 5.7: CMS spectra of an F8BT device with PCHE dielectric at 48Hz and 6Hz showing that charge accumulation becomes dominant at frequencies 3 orders of magnitude lower than expected from the mobility. Data has been rotated so that X channel contains all electroabsorption as the phase angle of the lock-in was unknown for this experiment.

$\sim 2\text{kHz}$. The model assumes ohmic contact and as shown in figure 5.8, F8BT transistors show non-ohmic behaviour and heavy current suppression at the kind of low drain voltages that are equivalent to the modulation voltage in CMS. By assuming that charging is limited by injection much more than the channel conductivity, we can crudely model the transistor as a series resistor and capacitor where the capacitive roll-off frequency gives us a massive contact resistance of $\geq 2\text{G}\Omega$.

Reducing the contact resistance and blocking the region between the contacts and gate then follows as the next logical step towards getting a sensible CMS spectra from F8BT ambipolar transistors.

5.4 Reducing contact resistance

At this stage with the issue of accumulation being limited by contact resistance, the simultaneous electrical and optical characterisation was added to the setup as explained in the previous chapter. Not only does this measurement help to identify and compensate for contact resistance effects, it can also correct for charge trapping during the scan which can reduce the number of charges being modulated with time. To illustrate the degree to which contact resistance dominates F8BT ambipolar transistors much more than other material

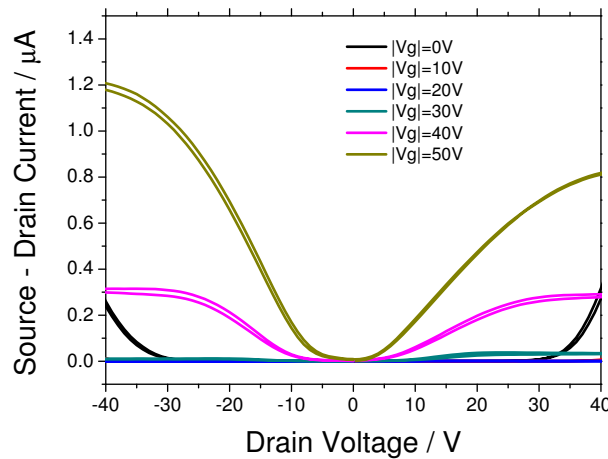
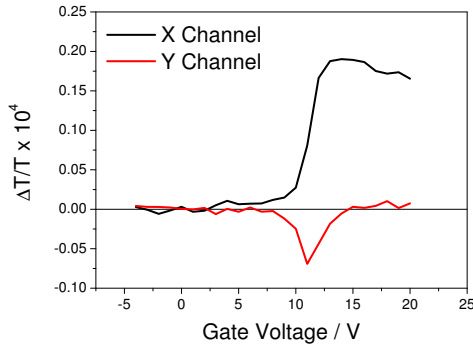


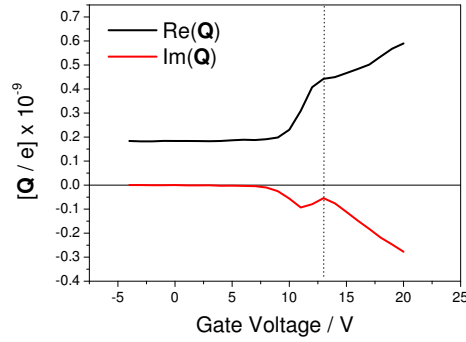
Figure 5.8: Output characteristics of an F8BT transistor showing heavy current suppression at low drain voltages. Gate voltages take the same sign as the drain voltage in that region.

systems, figure 5.9 shows the evolution of a spectral feature originating from charges in an F8BT transistor and contrasts this with a high mobility, low contact resistance N2200¹⁷⁷ transistor courtesy of Dr Mario Caironi.

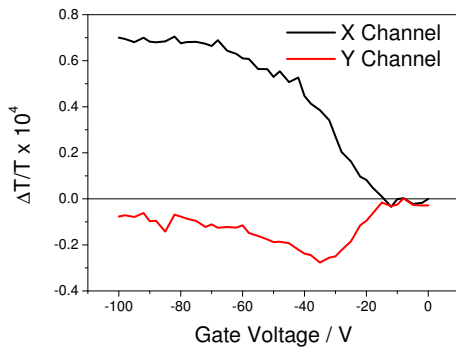
Whilst different dielectrics and dielectric thicknesses, were used, the capacitance of the N2200 and F8BT devices were very similar and yet the N2200 device goes from depletion to full accumulation in the space of around 5 volts on the gate. As the N2200 device is entering accumulation, the phase of $\Delta T/T$ in figure 5.9(a) rotates from the Y channel to being completely in the X channel indicating that the accumulation layer charge density is exactly in phase with the driving gate voltage. This behaviour is mirrored in the impedance data in figure 5.9(b) although due to the unpatterned gate and high mobility, the measured number of charges on the device continues to rise with gate voltage as described in the previous chapter. In stark contrast, the F8BT device does not fully reach accumulation even over a range of 80 volts and a phase lag remains between the gate modulation and charge modulation as seen in figure 5.9(c). Due to the patterned gate, the number of charges in figure 5.9(d) is clearly approaching a saturation value. As the mobility of the device is known to be high enough for accumulation even with just 10 volts of charges, this behaviour is completely due to a gate voltage-dependent contact resistance. Close inspection of all the data in figure 5.9 shows that not only is the gate voltage around 8 times larger in the F8BT device to achieve something close to full accumulation, but the change in transmission is only 3 times larger in the F8BT despite



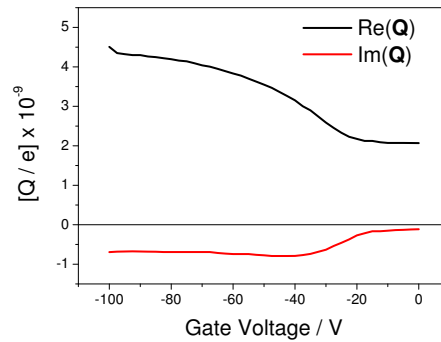
(a) $\Delta T/T$ at 1.5eV (827nm) of a polaron absorption in an N2200 device



(b) Simultaneous measurement of number of charges going to N2200 device



(c) $\Delta T/T$ at 2.60eV (477nm) of neutral absorption bleach in an F8BT device



(d) Simultaneous measurement of number of charges going to F8BT device

Figure 5.9: Comparison of $\Delta T/T$ at a single wavelength and the electrical measurements of the number of charges on the device for a high mobility, low contact resistance N2200 device (courtesy of Dr Mario Caironi) modulated with $V_{pp}=1V$ and an F8BT device with $V_{pp}=10V$. Both devices have very similar electrode areas and so from the factor of 10 difference in the number of charges accumulated, it can be inferred that the capacitance of the two devices are almost identical.

modulating 10 times as many charges than in the N2200. The combination of these two factors means that any artifacts that scale with gate voltage will be 20-30 times more significant relative the charge absorption in F8BT devices as compared to N2200 devices. This explains why artifacts dominate the spectra in F8BT devices but are hard to spot in high mobility, low contact resistance devices.

5.4.1 Improving hole injection

After showing that the lack of charge absorption features and the presence of electroabsorption was caused by incomplete accumulation, even at low frequencies, as a result of a large non-ohmic contact resistance, separate transistors were designed to be optimised for ohmic injection of either electrons or holes only. This has the disadvantage of introducing some error in the measurement of the *difference* between the hole and electron-induced absorption cross sections. Thiol-based self-assembled monolayers are typically used to modify the work function of gold electrodes to improve charge injection but due to the high annealing temperatures used to produce stable electron transport, this was not an option. Platinum has a work function of around 6.4eV which should provide better hole injection and electrodes were fabricated by sputtering and were patterned in the usual photolithographic process.

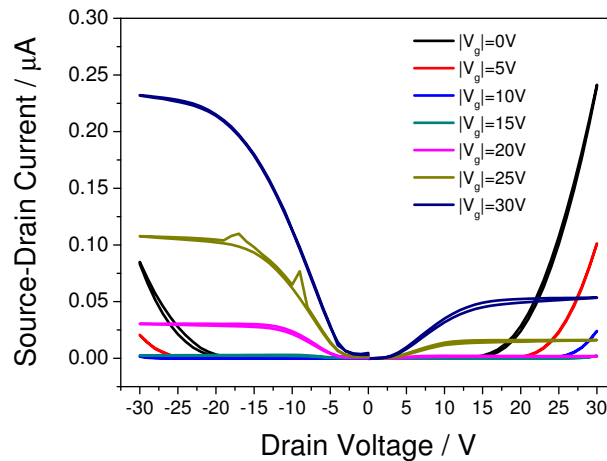


Figure 5.10: Output characteristics of an F8BT transistor with platinum source and drain electrodes.

The device characteristics shown in figure 5.10 reveal that despite the larger work-function, there is similar injection of both charge carriers as compared to when using gold electrodes. This result seems strange at first, but there have been many reports

of deviations from the Schottky-Mott rule in the relation between metal workfunction and injection barrier observed in organic conjugated materials deposited on top of electrodes^{178,179}. Predictable barrier heights are typically only observed in the case of metal evaporated on top of a polymer, or, in the case of small molecules, if the organic material is deposited on top of an atomically clean metal surface in high vacuum. Richards et al.¹⁰⁹ showed that in the case of top gate F8T2 transistors which have an injection barrier of $\sim 0.3\text{eV}$, contact resistance was dominated by bulk resistance which reached a minimum for film thicknesses of $\sim 30\text{nm}$ before increasing again as the film got thinner; this being attributed to bad coverage of the film over the edge of an electrode which was thicker. Schidleja al.¹⁸⁰ showed that modifying the work function of the injecting electrode affected the injection in F8BT top gate transistors where the barrier is much larger and that the current was dominated by a field-dependent relationship based on field-enhanced thermionic emission. Whatever the exact mechanism, it is clear that changing the electrode metal does not offer an obvious route to dramatically improving hole injection.

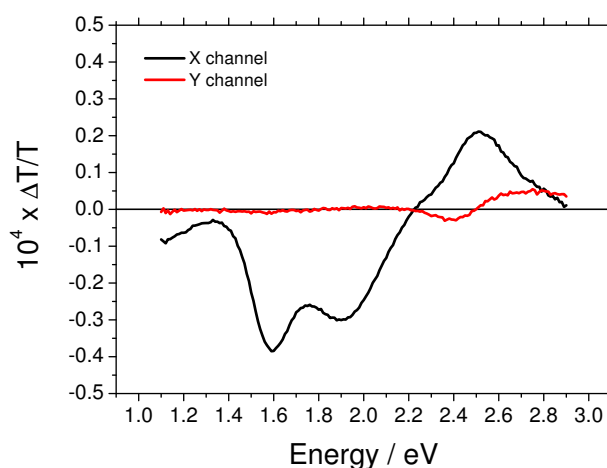


Figure 5.11: CMS spectra of an F8BT device with thick platinum source and drain electrodes rotated so that the charge absorption is completely in the X channel.

A fortunate consequence of the device with platinum electrodes was that the electrodes happened to be much thicker than conventional devices due to lack of correct sensor calibration during deposition. However, as can be seen by the spectra obtained with these thicker ($\sim 100\text{nm}$) platinum electrodes, in figure 5.11, the electroabsorption has been suppressed and practically everything is in phase showing clear charge absorption and bleaching of the neutral absorption. It is clear therefore that the electroabsorption and the sub energy gap artifact that is in phase with the applied voltage occurs more

strongly in the region between the source-drain electrodes and the gate electrode owing to the larger field and the enhanced interference effect due to two cofacial semi transparent yet reflecting metal surfaces.

5.4.2 Semiconductor thickness

Despite the platinum electrodes used in the device in fig 5.10 being much thicker than the F8BT film thickness, the device performed well at low drain voltages. This was investigated further and turned out to be related more to the thickness of the F8BT on top of the electrodes. Figure 5.12 shows output characteristics of two transistors with two different F8BT thicknesses. There appears to be a trend that thinner layers show almost linear behaviour at low drain voltages at the expense of lower currents at high drain voltages.

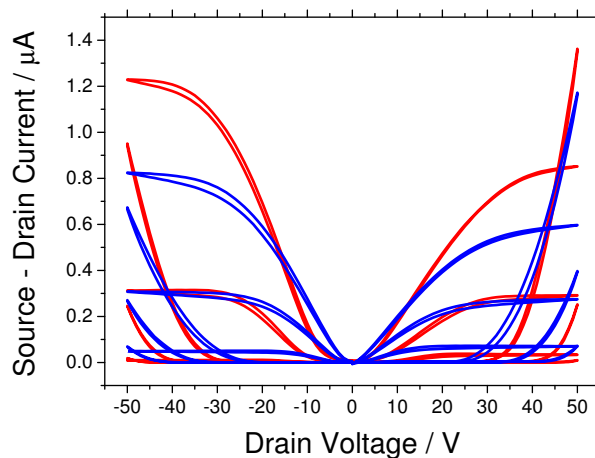
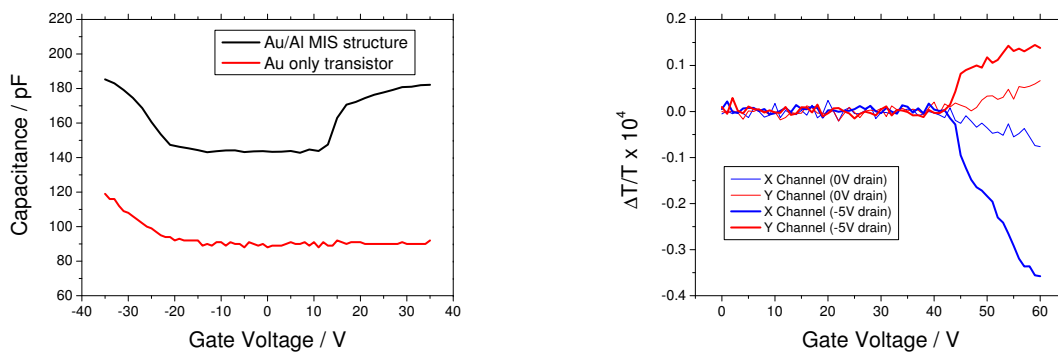


Figure 5.12: Output characteristics of indicative devices of two different F8BT thicknesses spun at 3000rpm (thin, blue) and 1500rpm (thick, red).

A further advantage of reducing the F8BT layer thickness other than reduced contact resistance is that the electroabsorption signal is reduced as it scales with the amount of absorption. The ultimate device would have ohmic injection and a semiconductor thickness of just a few nanometres to maximise the charge absorption to electroabsorption ratio.

5.4.3 Injecting electrons into lower electron affinity polymers

Whilst platinum failed to improve hole injection into F8BT, using aluminium as an electrode was more successful for injecting electrons into the polymers F8 and F8T2 where gold does not work well. Figure 5.13(a) shows capacitance measurements of an F8 transistor with gold electrodes and a second with aluminium stripes evaporated over the gold electrodes at right angles prior to semiconductor deposition. The capacitance shows electron accumulation is only observed with aluminium in the given range of gate voltages. Despite the small amount of electron accumulation when using gold electrodes when the source and drain are both grounded, it was found that this could be enhanced in F8 and F8T2 transistors using a small drain voltage as witnessed spectroscopically in figure 5.13(b). The modified CMS technique given in section 4.4.5 is required when using a drain voltage to exploit this effect.



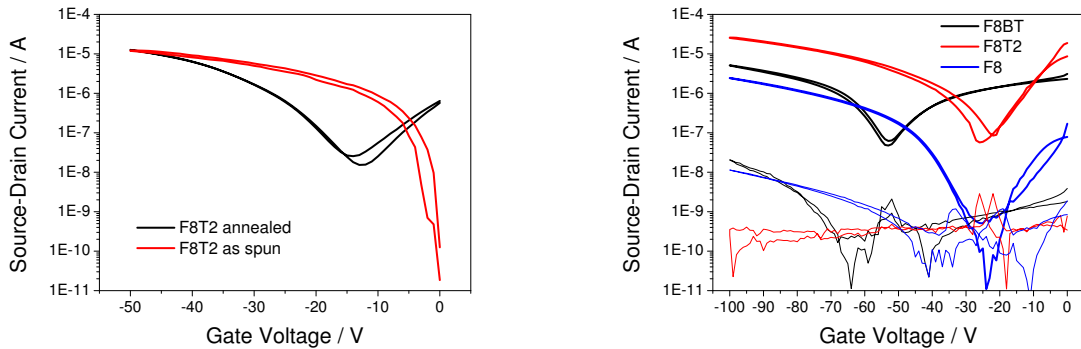
(a) Capacitance plot for gold-only and gold-aluminium contacts with the latter giving electron accumulation at low gate voltages.

(b) Effect of the drain voltage on increasing the amount of modulated charge as observed by $\Delta T/T$ for gold-only contacts.

Figure 5.13: Methods of improving electron injection into a lower electron affinity polymer, F8, through the use of aluminium as an injecting material or with the application of a drain voltage with gold-only electrodes.

Due to the requirement of having thick light-blocking electrodes, it is difficult to make devices with both gold and aluminium contacts without the leakage current becoming unacceptably high as the electrode height can be up to 200nm at overlapping points. As shown in figure 5.14(a), electron injection from gold contacts can become possible, although non-ideal, when the semiconductor is thin and annealed over its melting temperature. This improvement may have its origin in the improved contact between the polymer and the electrode¹⁷⁴. The exponential increase of current with gate voltage seen

in figure 5.14(b) for F8 and F8T2 shows that the injection likely follows a field dependent tunnelling mechanism which contrasts with the good injection into F8BT. This method of injecting electrons from gold is what is used for CMS measurements on F8 in this work.



(a) Transfer characteristics of as-spun and annealed F8T2 transistors with gold contacts.

(b) F8BT, F8T2 and F8 devices fabricated in identical fashions and all annealed over their melting temperatures. Thick lines represent source-drain current and thin lines are the leakage currents.

Figure 5.14: The extent to which electron transport can be observed with untreated gold source and drain electrodes and the need for annealing to observe this. The exponential increase in electron current with gate voltage for F8 and F8T2 suggests field-dependent injection from the gold contacts.

5.4.4 Leakage and contact resistance

When the current is being limited by a large contact resistance, there is the danger that charge can escape from the device through leakage paths in the insulator at a comparable rate to which it is entering. In this situation the effective capacitance is reduced. A program was written to simulate the electrical characteristics of various resistor and capacitor combinations. It can be seen in figure 5.15 that the leakage resistance must be bigger than the contact resistance by a factor of 100-1000 to achieve full accumulation. In typical devices, the leakage path through the dielectric has a resistance of 1G Ω or more corresponding to a leakage current that can increase by 10⁻⁸ amps over a range of 10 volts at large gate voltages. It is clear that this can be an issue in devices with contact resistances of this order. By measuring the capacitance directly during the experiment we can allow for this in the calculation of cross section even if it means that we never reach

full accumulation.

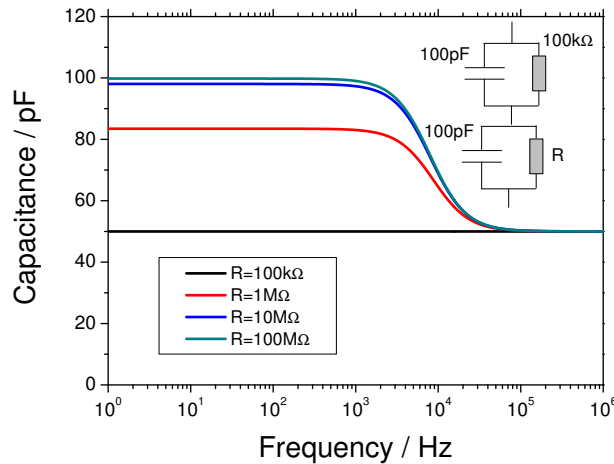


Figure 5.15: Computed capacitance for an MIS diode with gate leakage of resistance R .

5.5 Effect of the gate electrode

During the investigation into reducing contact resistance it became apparent that thick source and drain electrodes result in CMS spectra which show the expected bleaching and charge absorption and a much reduced electroabsorption signature. This difference is attributed to the thicker electrodes ($\sim 100\text{nm}$) blocking the light that would have been transmitted through the region where the gate overlaps the source and drain. In this region, not only is the field stronger, but interference effects are larger due to the metal-metal cavity. The origin of this effect is discussed at the end of this chapter, but in this section we concern ourselves with the question of whether this effect exists to a lesser extent in the channel region. To investigate the effect in the channel region, the thickness of the gold gate electrode was varied (changing the dielectric thickness is not so straightforward with thick source-drain electrodes as shorts are more likely below 400nm and filtering is more difficult at higher concentrations).

5.5.1 Varying gold gate thickness

In a series of devices made in different runs, the gold gate electrode was deposited with the following thicknesses: 8.5nm , 6.5nm , 5nm and 3.5nm . As the thickness reduced, the spectra did change by an amount that is not negligible as compared to the difference in

the hole and electron spectra. The thinnest electrode was as thin as it was possible to make before it was no longer conducting.

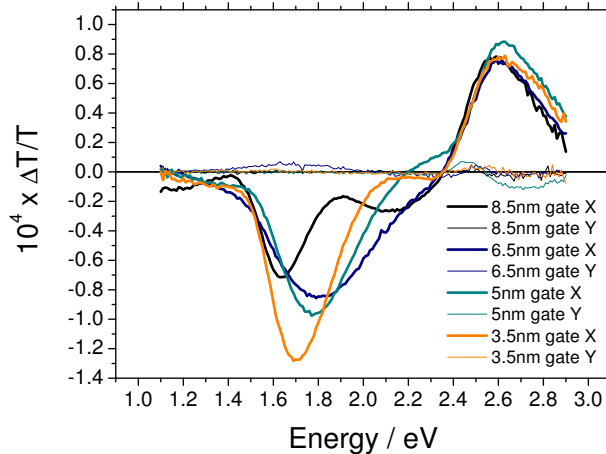


Figure 5.16: CMS spectra with different thickness gold gate electrodes.

It is interesting to note that the bleaching looks identical in all the devices. This observation could be consistent with the charges changing the refractive index of the accumulation layer in the vicinity of the charge absorption¹⁷⁰. One other explanation is that the F8BT absorption attenuates the amount of internal reflections that are possible at that wavelength which would reduce interference effects regardless of the mechanism. If this is the case, the addition of an optical density filter at some point in the device could have the same effect across all the wavelengths. One other contributing factor could be that the reflectivity of the gold drops rapidly in the unaffected region suggesting which means that artifacts will be reduced here. The reflectivity of gold layer should be the only thing that is different between the devices however, to check that the differences had nothing to do with any other properties of the gold, aluminium gates were attempted.

5.5.2 Aluminium gate

Aluminium was used as a gate electrode as, unlike gold, it has no plasmon absorptions in the visible region. In case shifts in the plasmon frequency with field were in any way related to variations in the spectra with different gold thicknesses, aluminium as a gate should eliminate this. As seen in figure 5.17, the main peak in the spectra matched that of the device with the thinnest gold gate electrode. However, there do still seem to be some differences, particularly in the peak energy of the bleaching perhaps confirming that

the identical bleaching in the gold case was due to the lower reflectivity in this region.

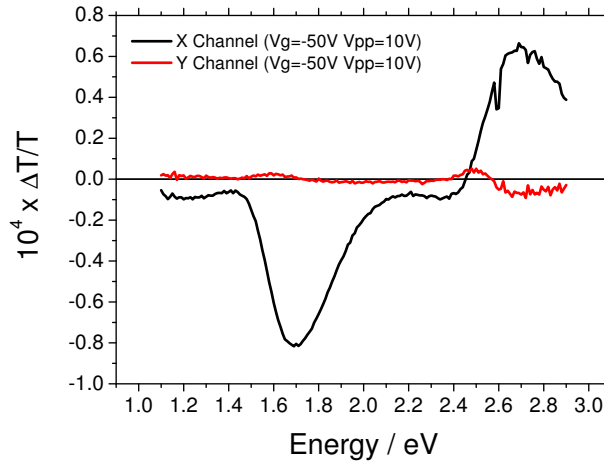


Figure 5.17: CMS spectra for F8BT transistor with an aluminium gate electrode.

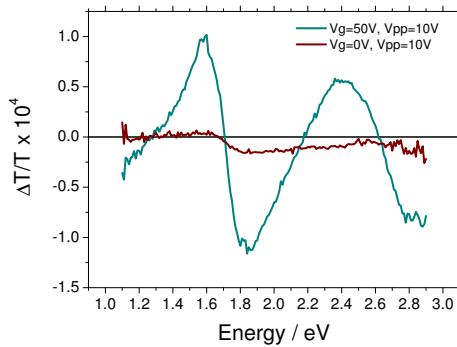
In conclusion, the results here shows that whilst thick source and drain electrodes and a thin semiconductor layer both remove the dominant artifact that was in phase with the voltage and reduces electroabsorption there is still some residual artifact occurring that is in phase with the charges themselves rather than the gate voltage. The possibility of it being some kind of filtering effect as mentioned at the beginning of the chapter seems to be discounted by the fact that the X channel of the "5nm gate" spectra in figure 5.16 changes sign below the energy gap. In the following section, the origin of the interference effects both above the source drain contacts and in the channel are addressed.

5.6 Field induced changes in interference

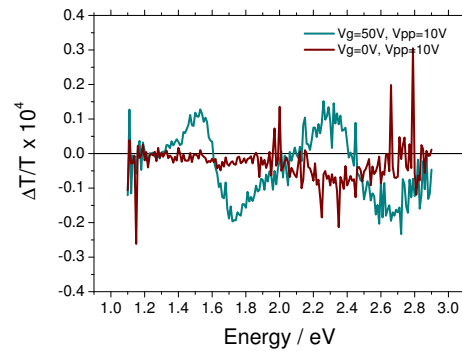
5.6.1 Modulation spectra with no semiconductor

As this chapter has shown, the dominant cause of extrinsic effects in CMS comes from the overlap region where there is a cavity with two semi-transparent cofacial planar metal layers. To look at these suspected field-induced effects, a metal-insulator-metal, MIM, capacitor was made with a 20nm thick gold layer and 6nm aluminium layer sandwiching a 450nm layer of PMMA. As can be seen in figure 5.18(a), despite the absence of semiconductor, there is a modulation of $\Delta T/T$ with $V_g = 50V$ and $V_{pp} = 10V$ and to a lesser extent in the transistor electrode configuration in figure 5.18(b).

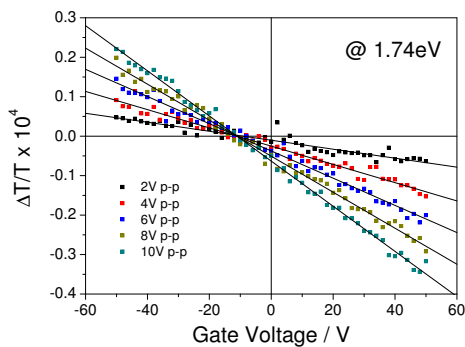
Figures 5.18(c) and 5.18(d) show the evolution of the signal at one wavelength as the



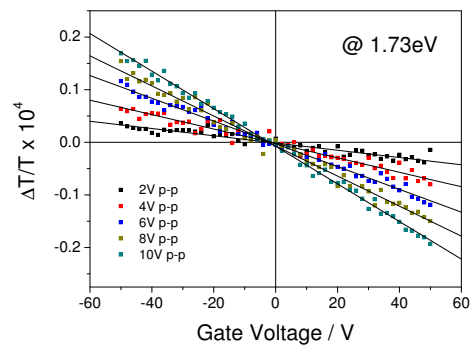
(a) Modulation spectra of MIM capacitor (no F8BT).



(b) Modulation spectra of transistor structure (no F8BT).



(c) Dependence of $\Delta T/T$ on V_g and V_{pp} in MIM capacitor (no F8BT).



(d) Dependence of $\Delta T/T$ on V_g and V_{pp} in transistor structure (no F8BT).

Figure 5.18: Modulation Spectra for MIM diode and transistor structure with no semiconductor (20nm gold/450nm PMMA/6nm aluminium).

gate voltage is varied revealing a linear dependence on both gate voltage and peak to peak voltage which means that the effect is quadratic in the field. The fact that it does not intercept 0V could mean that there is some fixed charge at one of the electrodes adding a constant voltage offset, however, in figure 5.18(a), the spectra at 0V looks different to the spectra at 50V indicating a different mechanism which would have to be linearly dependent on the field.

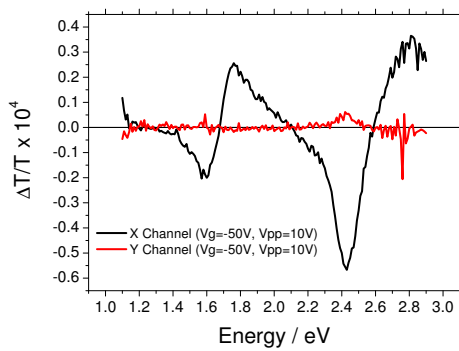
5.6.2 Modulation spectra with semiconductor

In the same batch as the devices in section 5.6.1, MIS diode and transistor structures with F8BT were also fabricated. The most noticeable difference is the presence of electroabsorption from the F8BT; this is responsible for the large peak at 2.42eV in the X channel which is in phase with the applied voltage. Tracking this feature as a function of gate voltage for the MIS diode shows that the magnitude increases with gate bias but quickly saturates as the accumulation layer forms and the field modulated across the semiconductor becomes independent of gate bias. This behaviour is different to the subgap feature in the MIS diode structure which behaves in the same way as the spectra in the previous section and continues to increase linearly with gate bias. An interesting and somewhat unexpected result is that there is absolutely no evidence of charge absorption in the MIS diode structure which corresponds well to the lack of any change in the capacitance. On the other hand, the transistor structure, whilst showing electroabsorption and interference effects in phase with the applied bias, the Y channel shows a component of the phase-delayed spectra resulting from charges. Electrical characterisation shows a corresponding increase in the capacitance. This could be explained by accumulated charge in the F8BT transistor above the contacts moving in the slight lateral field towards the centre of the channel facilitating a higher injecting field at the contacts to inject further charges.

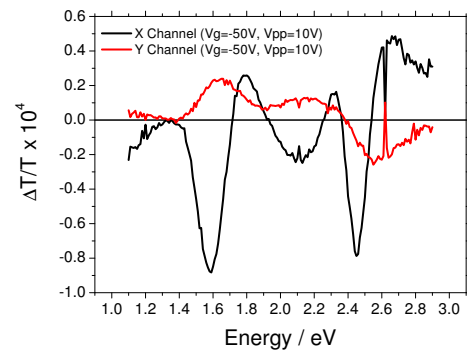
5.6.3 Theoretical model

This model was originally developed by Eldering et al.¹⁸¹ although has been derived again from first principles to be applied, at the end of this section, to a transistor structure. In doing so some differences were noted compared to the original paper.

Starting from the transmission at normal incidence through a piece of dielectric with reflectivity r and r' and transmission t and t' at the first and second interfaces we have



(a) Modulation spectra of MIS diode.



(b) Modulation spectra of transistor.

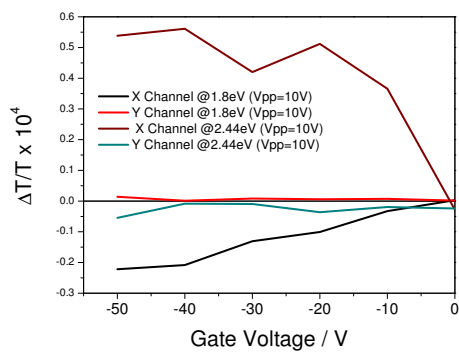
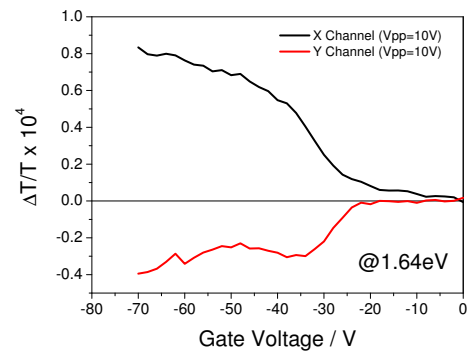

 (c) Dependence of $\Delta T/T$ on V_g in MIS diode.

 (d) Dependence of $\Delta T/T$ on V_g in transistor.

Figure 5.19: Modulation Spectra for MIS diode and transistor structure with F8BT but otherwise identical to figure 5.18.

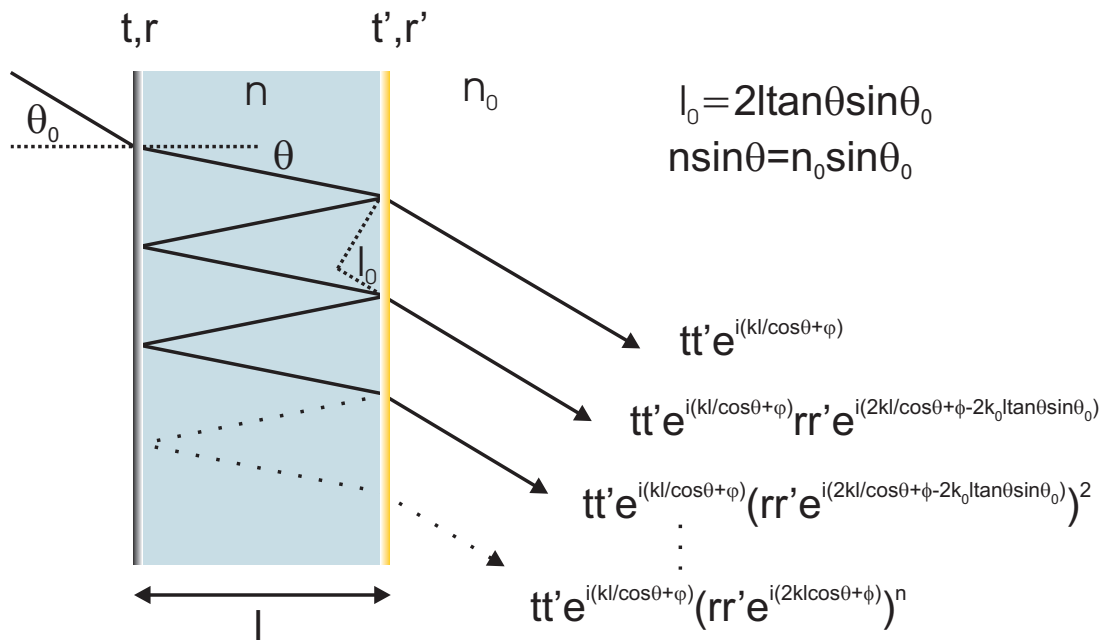


Figure 5.20: Phase and amplitude of transmitted light after multiple reflections in a Fabry-Perot etalon structure relative to phase and amplitude of incident light.

the amplitude of the transmitted light:

$$t_0 = tt' e^{i(kl+\psi)} \sum_{m=0}^{m=\infty} (rr' e^{i(2kl+2\pi+\phi)})^m = \frac{e^{i(kl+\psi)} tt'}{1 - rr' e^{i(2kl+\phi)}} \quad (5.1)$$

where k is the spatial frequency or wavevector of the light inside the dielectric and ψ and ϕ are any phase shifts introduced by transmission or reflection from the mirrors (without the metal layers there would be a π phase shift at each reflection giving the same result overall). The transmittance (intensity) of the light that has passed through the structure is then given by:

$$T = t_0 t_0^* = \frac{(tt')^2}{(1 - rr')^2} \frac{1}{1 + \frac{4rr'}{(1-rr')^2} \sin^2 \left(\frac{2\pi nl}{\lambda} + \phi \right)} \quad (5.2)$$

Substituting $F = \frac{4rr'}{(1-rr')^2}$ and $M = \frac{(tt')^2}{(1-rr')^2}$ we have a familiar looking equation for the Fabry Perot étalon:

$$T = \frac{M}{1 + F \sin^2 \left(\frac{2\pi nl}{\lambda} + \phi \right)} \quad (5.3)$$

To see how this transmission can be changed by small changes in the thickness we get:

$$dT = \left(\frac{dT}{dl} \right)_{n,\phi,M,F} dl = \frac{-2\pi n F M \sin \left(\frac{4\pi nl}{\lambda} + 2\phi \right)}{\lambda (1 + F \sin^2 \left(\frac{2\pi nl}{\lambda} + \phi \right))^2} dl \quad (5.4)$$

We can follow an identical process for changes in the refractive index. If we assume that these changes are independent and that the reflectivity, transmission and phase change of the metal layers do not change with field, we end up with:

$$\frac{dT}{T} = \frac{-2\pi nl F \sin \left(\frac{4\pi nl}{\lambda} + 2\phi \right)}{\lambda (1 + F \sin^2 \left(\frac{2\pi nl}{\lambda} + \phi \right))} \left(\frac{dl}{l} + \frac{dn}{n} \right) \quad (5.5)$$

This equation, whilst based on a simple model reveals some interesting facts about interference effects. Firstly, for a given fractional change in l or n , the amplitude of the effects scale linearly with $\frac{l}{\lambda}$. This follows the conventional wisdom that making devices thin relative to the wavelength you are studying reduces interference effects. However, we must also consider how $\frac{\Delta l}{l}$ and $\frac{\Delta n}{n}$ depend on the device thickness. Firstly we consider the mechanism for a change in the thickness of a device with applied field known as electrostriction.

5.6.4 Electrostriction

The force between two plates of a capacitor with thickness l , area A and a potential difference of V (assuming changes in l are small relative to l) can be obtained simply

by differentiating the energy stored on a capacitor per unit area, $\frac{CV^2}{2}$, with respect to thickness

$$F(t) = -\frac{\epsilon_0\epsilon_r V(t)^2 A}{2l^2} \quad (5.6)$$

The restoring force constant due to uniaxial stress can be expressed in terms of the Young's modulus as $\frac{YA}{l}$. Including damping, and with the substitution $\omega_0 = \sqrt{\frac{YA}{lm}}$, the displacement from equilibrium thickness $\Delta l = Re(z)$ satisfies this differential equation

$$\ddot{z} + 2\gamma\dot{z} + \omega_0^2 z = \frac{F(t)}{m} = -\frac{\epsilon_0\epsilon_r (|V_g| + \frac{V_{pp}}{2} e^{i\omega t})^2 A}{2ml^2} \quad (5.7)$$

Ignoring any terms at zero frequency and assuming steady state we will try the solution

$$z = \alpha e^{i\omega t} + \beta e^{i2\omega t} \quad (5.8)$$

$$\alpha e^{i\omega t} (-\omega^2 + 2i\gamma\omega + \omega_0^2) + \beta e^{i2\omega t} (-4\omega^2 + 4i\gamma\omega + \omega_0^2) = \frac{-\epsilon_0\epsilon_r A}{2ml^2} (|V_g|^2 + |V_g|V_{pp}e^{i\omega t} + \frac{V_{pp}^2}{4} e^{i2\omega t}) \quad (5.9)$$

Equating the (orthogonal) terms at ω and 2ω we get

$$z = -\frac{|V_g|V_{pp}\epsilon_0\epsilon_r A e^{i\omega t}}{2ml^2(\omega_0^2 - \omega^2 + 2i\gamma\omega)} - \frac{V_{pp}^2\epsilon_0\epsilon_r A e^{i2\omega t}}{8ml^2(\omega_0^2 - 4\omega^2 + 4i\gamma\omega)} \quad (5.10)$$

From the phase of the effect during the experiment ($\approx 0^\circ$), we can conclude that there is no significant damping term and ω_0 is far greater than frequencies used in the experiment so the contribution at the frequency ω is simply

$$\frac{\Delta l}{l} = -\frac{(|V_g| + \frac{\sigma l}{\epsilon_0\epsilon_r})V_{pp}\epsilon_0\epsilon_r}{2Yl^2} \quad (5.11)$$

where the possibility of fixed charge at the gate electrode interface has been introduced which would shift the effective V_g by a constant ($\sigma > 0$ for holes). At 2ω the expression is

$$\frac{\Delta l}{l} = -\frac{V_{pp}^2\epsilon_0\epsilon_r}{8Yl^2} \quad (5.12)$$

Thus assuming that electrostriction is the dominant mechanism, we have the final formula for a MIM capacitor structure

$$\frac{dT}{T} = \frac{\pi n F \sin(\frac{4\pi n l}{\lambda})}{Y \lambda (1 + F \sin^2(\frac{2\pi n l}{\lambda}))} \left(\frac{\epsilon_0\epsilon_r V_{pp} |V_g|}{l} + \sigma V_{pp} \right) \quad (5.13)$$

Note that when comparing this artifact to the charge spectra which also scales linearly with $\frac{\epsilon_r V_{pp}}{l}$, there is no relative change in magnitude of the artifact with different

dielectric thickness; only the period changes. This can be understood by remembering that the force between the plates is inversely proportional to the thickness *squared*. If $\frac{\Delta l}{l}$ had a linear inverse dependence on or been independent of l , the artifact would reduce in magnitude for thinner devices. This result therefore serves as a caveat to the commonly held statement that devices should be made thinner to avoid interference problems, although if the thickness is below $\sim \frac{\lambda}{40\pi n}$, the sine term becomes approximately equal to the argument and the equation does become independent of l so charge absorptions begin to dominate; this however requires currently unfeasible ambipolar devices of less than 2nm thickness if you want to go up to 3eV (413nm), or 53nm if you are in the IR up to 0.12eV (1000cm⁻¹). It should also be noted that this effect varies linearly with gate voltage whilst the charge absorptions vary with gate voltage in the same way as capacitance. In practice it is too difficult to separate the two because the capacitance is approximately linear in gate voltage up to full accumulation which cannot always be reached and the effect is too small to fit when the gate voltage is below the threshold. To reduce the size of this effect, a lower refractive index or stiffer dielectric could help but it is very clear that F or rather the reflectivity of the interfaces is the only thing that can reduce the electrostriction effect in any reasonably thick polymer device. It is the consequence of the large voltages, or rather fields, required to get to full accumulation due to contact resistance in the ambipolar transistors used in this thesis that electrostriction dominates the CMS spectra. As seen in figure 5.9, the gate voltage needs to be around ten times larger to approach accumulation in F8BT devices with a similar capacitance to a high mobility, low contact resistance N2200 device.

5.6.5 Electroabsorption modification of interference

Now, for completeness, we address the mechanism that could change the refractive index of the dielectric due to applied field. It is known that materials can exhibit a phenomena known as electroabsorption whereby upon application of an electric field, the energy at which it absorbs can shift. As we saw earlier, the relevant terms that come out of perturbation theory are

$$\Delta\alpha(E) = c\alpha(E) + \frac{d\alpha(E)}{dE} \sum_{i \neq j} \frac{|\mu_{ij} \cdot \mathbf{F}|^2}{E_i - E_j} + \frac{1}{2} \frac{\partial^2 \alpha(E)}{\partial E^2} |\mathbf{m} \cdot \mathbf{F}|^2 \quad (5.14)$$

A shift in the absorption will also cause a shift in the refractive index function as the real and imaginary parts of the dielectric function, $\epsilon = \epsilon_1 + i\epsilon_2 = (n + ik)^2$, are related

via the Kramers-Kronig relation

$$\epsilon_1(\omega) - 1 = \frac{1}{\pi} P \int_{-\infty}^{\infty} \frac{\epsilon_2(\omega')}{\omega' - \omega} d\omega' \quad (5.15)$$

$$\epsilon_2(\omega) = -\frac{1}{\pi} P \int_{-\infty}^{\infty} \frac{\epsilon_1(\omega') - 1}{\omega' - \omega} d\omega' \quad (5.16)$$

Even with the terms in equation 5.14, due to the nature of the relationship between the extinction coefficient, k , and the refractive index, n , it is not straightforward to find an analytical expression for $\frac{dn}{dk}$ to relate changes in one to changes in the other. The form and more importantly the sign of this effect can be approximated with two steps. Firstly, from the typical behaviour of n and k in the vicinity of an absorption as seen in figure 5.21, we make the crude assumption that, for small shifts, a translation in k from $k(E)$ to $k(E + \Delta E)$ corresponds to an identical translation in n .

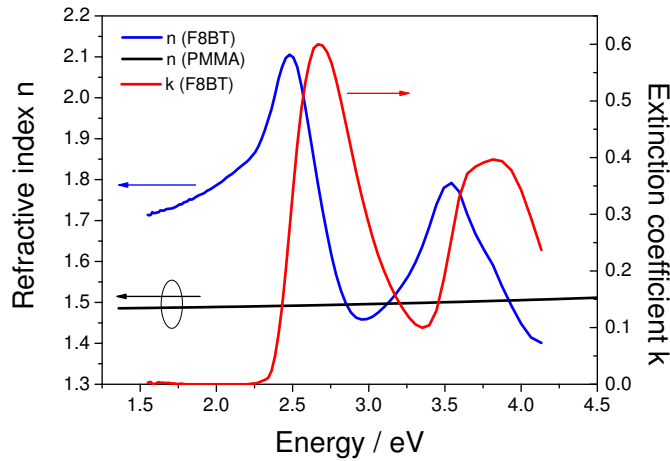


Figure 5.21: Refractive index, n , and extinction coefficient, k , for F8BT (measured by Dr Inchan Hwang) and PMMA taken from ¹⁷⁰ (k for PMMA is too small to be measured in this region).

Secondly we know that electroabsorption shifts k to lower energies which is equivalent to saying $\Delta E > 0$ and the voltage dependent $\Delta E(V)$ can be measured experimentally (at least for F8BT). Mathematically we can express this as:

$$\Delta n(E) = \left(\frac{dn}{dE} \right) \Delta E \quad (5.17)$$

Relating $\Delta E(V)$ to measurable quantities we get an expression for a small change dn in terms of the slope of n , the inverse of the derivative of transmission spectra, T ,

the electroabsorption spectra and the voltage, expressed in that order in the following equation.

$$dn = \left(\frac{dn}{dE} \right) \left(\frac{dE}{dT} \right) \left(\frac{dT}{dV} \right) dV \quad (5.18)$$

In region where we are interested, both n for PMMA and F8BT are always rising and the product of the second two derivatives is always positive. This can be summarised in the equation below where $\gamma(E)$ is an experimentally determined positive constant (valid at energies below absorptions).

$$dn = \gamma(E)V_{pp}|V_g| \quad (5.19)$$

We can then make an equivalent expression to equation 5.13 for the case when bulk refractive index changes with field cause the modulation in transmission with voltage.

$$\frac{dT}{T} = -\frac{2\pi\gamma(E)lF \sin\left(\frac{4\pi nl}{\lambda}\right)V_{pp}|V_g|}{\lambda(1 + F \sin^2\left(\frac{2\pi nl}{\lambda}\right))} \quad (5.20)$$

Since PMMA, which constitutes the bulk of the device, absorbs at a much higher energy than used in this experiment it is unlikely that the field will change n much as it is very flat in the region of interest. It is also clear from the equation that the sign of this effect is the opposite to electrostriction at sub gap energies. In the next section we will see how this proves that the effect is definitely electrostriction and not a change in the refractive index.

5.6.6 Predicting extrinsic CMS effect from the transmission spectra

It was expected that if the interference is changing with applied field then the expected modulation spectra should be similar to the derivative of the transmission spectra. Rewriting equation 5.3 in terms of photon energy, E , we can now see why $-\frac{1}{T} \left(\frac{dT}{dE} \right)$ is related to the measured $\frac{dT}{T}$ due to electrostriction.

$$\frac{dT}{T} = \frac{1}{T} \left(\frac{dT}{dE} \right) dE = \frac{-\frac{2\pi nlE}{hc} F \sin\left(\frac{4\pi nlE}{hc}\right)}{(1 + F \sin^2\left(\frac{2\pi nlE}{hc}\right))} \left(\frac{dE}{E} \right) \quad (5.21)$$

Here we have assumed that M , F and n are flat over a given range of wavelengths which will constitute the biggest error in this method although it is close enough to being true for the method to work. Combining with equation 5.13 we get

$$\left(\frac{dT}{T} \right)_{E,n} = -\frac{1}{T} \left(\frac{dT}{dE} \right)_{l,n} \left(\frac{\epsilon_0 \epsilon_r V_{pp} |V_g| E}{2l^2 Y} \right) \quad (5.22)$$

which turns out to be mathematically identical to an equation given by Matsui¹⁶⁷ apart from voltage and photon energy are the variables here instead of charge and wavelength.

To calculate the quantity $\frac{1}{T} \left(\frac{dT}{dE} \right)_{l,n}$, the following operation is performed on the transmission spectra with no sample in the cryostat T_{ns} and that with the sample T_s

$$\frac{T_{ns}}{T_s} \frac{d(T_s/T_{ns})}{dE} \quad (5.23)$$

Care must also be taken with the sign because depending on whether the gate voltage is positive or negative the phase of the transmission spectra will be 180 degrees rotated due to the way the reference from the signal generator is setup. The sign convention adopted here is explained in figure 4.2 meaning that equation 5.13 corresponds to negative gate voltages and needs the sign to be reversed for positive gate voltages.

Figures 5.22(a) and 5.22(b) shows the equation applied to the capacitor and transistor structures with no semiconductor using the value of Young's Modulus for PMMA of 3GPa. The only other input in the prediction is the transmission spectra with and without the sample in place, the voltages applied and the thickness of the film. The prediction fits well in large regions and where it does not fit it most likely in regions where the reflectivity of the surfaces is changing with wavelength. In the transistor electrode configuration with no semiconductor the prediction may be slightly lower because the channel region may not be changing thickness so much as there is no accumulation layer with charges so the field across the dielectric is much lower here.

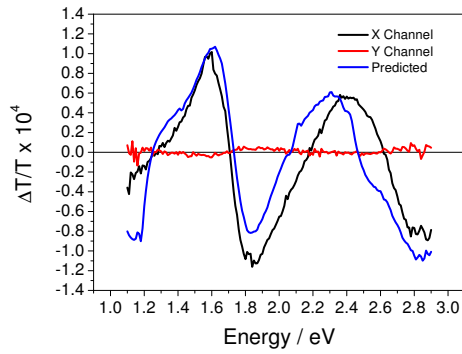
To simplify and visualise the point that the effect must be electrostriction and not some change in the refractive index, the equivalent equation to 5.22 would be

$$\left(\frac{dT}{T} \right)_{E,l} = \frac{1}{T} \left(\frac{dT}{dE} \right)_{l,n} \gamma(E) V_{pp} |V_g| E \quad (5.24)$$

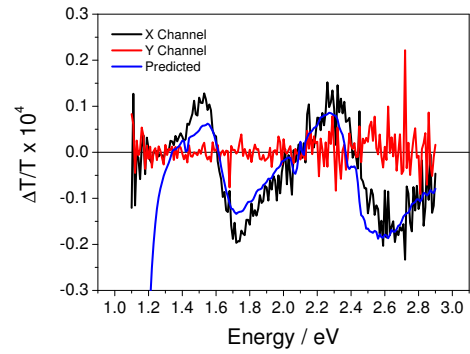
which is the same sign as electroabsorption where

$$\left(\frac{dT}{T} \right) \propto \left(\frac{dT}{dE} \right) V_{pp} |V_g| \quad (5.25)$$

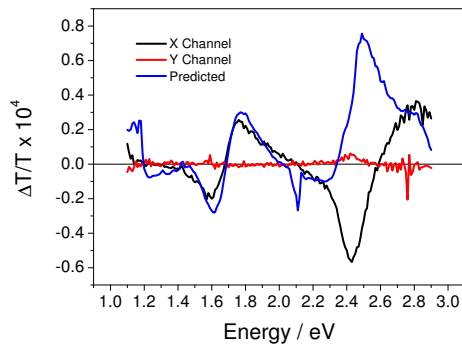
Figure 5.22(c) shows the model applied in an MIS diode with a layer of F8BT and shows the actual measured spectra for comparison. The prediction and measurement are only different in the region of electroabsorption which shows unambiguously that the electroabsorption and the electrostriction differ in sign with respect to the derivative of the transmission spectra. The fact that electroabsorption and refractive index modulation model would have the same sign applied to the derivative of the transmission spectra thus in turn gives clear proof that it can only be electrostriction that is the mechanism.



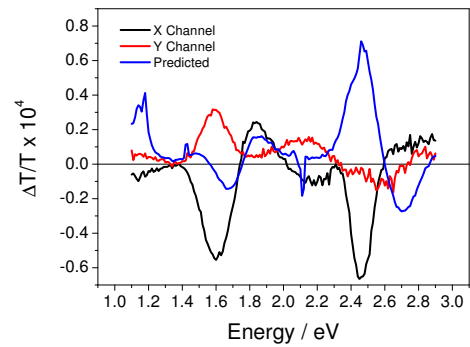
(a) Au(20nm)/PMMA(470nm)/Al(6nm) capacitor structure modulated at $V_g=+50\text{V}$, $V_{pp}=10\text{V}$



(b) Au(20nm)/PMMA(470nm)/Al(6nm) transistor structure modulated at $V_g=+30\text{V}$, $V_{pp}=10\text{V}$



(c) Au(20nm)/F8BT(30nm)/PMMA(470nm)/Al(6nm) capacitor structure modulated at $V_g=-50\text{V}$, $V_{pp}=10\text{V}$



(d) Au(20nm)/F8BT(30nm)/PMMA(470nm)/Al(6nm) transistor structure modulated at $V_g=-50\text{V}$, $V_{pp}=10\text{V}$

Figure 5.22: Modulation Spectra for capacitor and transistor structure with and without F8BT. Absolute value of voltage used in model and sign of prediction reversed in figures 5.22(a) and 5.22(b) as lock-in reference 180 degrees out of phase for positive gate voltages.

In figure 5.22(d) which is a regular F8BT transistor, there is a combination of charge absorption from the channel region and the electrostriction effect from the contacts. The charge absorption is notable by its different phase with a significant component in the Y channel whereas the electrostriction and electroabsorption are in the X channel.

In the previous section, by blocking the light in the source-drain electrode region by making them very thick, a spectra of charge absorption and bleaching was obtained where all features occurred in phase with each other. The question of whether electrostriction is responsible for the residual effect leading to differing spectra with different gate electrodes is a difficult one to answer. If the changes in thickness only occur when the charges are in the channel and hence there is a field across the dielectric then the process will be exactly in phase with the charge absorption and only appear in accumulation. If full accumulation could be reached and then the gate voltage increased further, the electrostriction component of the spectra would continue to change shape whilst the charge absorption part would stay constant due to its lack of dependence on gate voltage in full accumulation. As it is with F8BT, the regime cannot be reached and even if it were the changes would be small compared to the noise so it would be difficult to experimentally remove the electrostriction effect. The solution, it seems is to make the gate electrode from a non-metallic material such that the reflection at this interface can be reduced to the lowest possible values.

5.6.7 Linear field-dependent extrinsic effect

The electrostriction effect showed a dependence on the field squared as witnessed by the linear dependence on gate voltage for a fixed peak to peak voltage seen in figure 5.18(c). This plot also reveals that the intercept is not at zero. This could imply an amount of fixed charge injected into the dielectric as given by σ in equation 5.13. However, looking at the shape of the spectra at $V_g=0V$ in figure 5.23 shows that the shape is different to that of the electrostriction modulation in figure 5.18(a). The cause of this effect remains unknown with the only clue being that it has a linear dependence on voltage and a different spectral shape to an interference modulation. As this effect is independent of gate voltage, if it does not appear in depletion then it is not there for any gate voltage and so can be safely ignored in the devices used for measurements in this thesis.

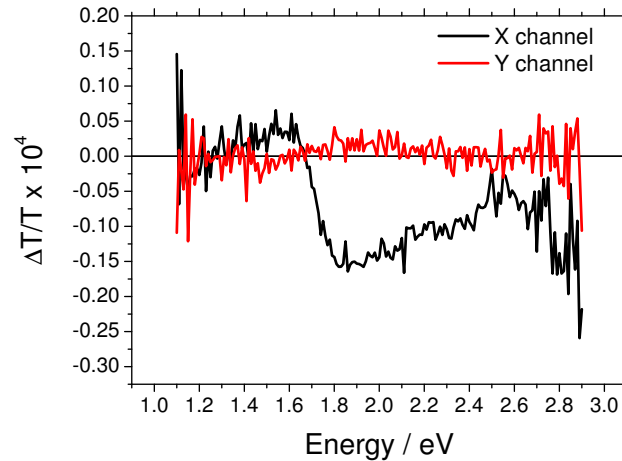


Figure 5.23: Au(20nm)/PMMA(470nm)/Al(6nm) capacitor structure modulated at $V_g = +50\text{V}$, $V_{pp} = 10\text{V}$.

5.7 Optimum device structures

In the previous section a picture has developed of how to make optimum devices for CMS particularly where high fields are required due to large contact resistance. A thin semiconductor layer will reduce contact resistance and electroabsorption, a patterned gate will give accurate electrical measurements and increase confidence in the charge density, low gate leakage will maximise charge density in accumulation, and avoiding reflecting surfaces will reduce undesirable electrostriction effects. In this section we take these concepts to derive the best device structure for CMS in ambipolar transistors featuring high contact resistance, although this knowledge can and should be applied to all materials where the same processes occur. The first question addressed is whether making the source-drain electrodes as thin as possible to reduce reflectivity and electrostriction would be preferable to making them as thick as possible to block light from that region altogether.

5.7.1 Thin or thick electrodes

It is clear from equation 5.13 that for an MIS diode structure, the optimum device have the lowest possible reflectivity and hence thickness of electrodes, however in a transistor structure, making the source drain electrodes thicker will mean relatively more light going through the channel region where there is only one metal reflecting surface. To find out if there is an optimum thickness of electrodes for a transistor structure we must add up

the two contributions appropriately:

$$\frac{\Delta T}{T} = \frac{\Delta T_1 + \Delta T_2}{T_1 + T_2} \quad (5.26)$$

where we have assumed for ease equal areas of electrode and channel. Using equations 5.3 and 5.4 we can construct $\Delta T/T$ for the entire device. To make it easier, the argument in the sine terms has been replaced with the term δ as we expect the same behaviour at any wavelength.

$$\frac{\Delta T_1 + \Delta T_2}{T_1 + T_2} = -\frac{\frac{M_1 \delta F_1 \sin(2\delta)}{(1+F_1 \sin^2(\delta))^2} + \frac{M_2 \delta F_2 \sin(2\delta)}{(1+F_2 \sin^2(\delta))^2}}{\frac{M_1}{1+F_1 \sin^2(\delta)} + \frac{M_2}{1+F_2 \sin^2(\delta)}} \left(\frac{dl}{l} + \frac{dn}{n} \right) \quad (5.27)$$

To simply further, lets assume that the channel region has no reflectivity at the glass/polymer interface i.e. $F_2 = 0$ and $M_2 = t^2$ where t is the transmission through the gate

$$\frac{\Delta T_1 + \Delta T_2}{T_1 + T_2} = -\frac{\delta F_1 M_1 \sin(2\delta)}{M_1(1 + F_1 \sin^2(\delta)) + t^2(1 + F_1 \sin^2(\delta))^2} \left(\frac{dl}{l} + \frac{dn}{n} \right) \quad (5.28)$$

setting $\delta = \frac{\pi}{4}$ for clarity and ignoring constant prefactors that do not effect the functional form of the equation gives

$$\frac{\Delta T_1 + \Delta T_2}{T_1 + T_2} \propto -\frac{\gamma F_1 M_1}{\gamma M_1(1 + F_1/2) + (1 - \gamma)t^2(1 + F_1/2)^2} \quad (5.29)$$

where γ is the fraction of area taken up by the source and drain electrodes. The equivalent for an MIS diode ($\gamma = 1$) would be

$$\frac{\Delta T}{T} \propto -\frac{F_1}{1 + (1 + F_1/2)} \quad (5.30)$$

When both are plotted (figure 5.24) you can see that for a transistor there are two optimal electrode thicknesses, very thin or very thick, whereas for an MIS diode, thin electrodes are always optimal.

In summary, if electrodes are made as thin as possible, whilst still conducting, a similar reduction in interference to that observed for very thick electrodes is achieved. There are two negative effects of this however; a different morphology of semiconductor on the electrodes may complicate the spectra and electroabsorption in the overlap region will almost certainly be unavoidable for materials with high contact resistance. In principle, electroabsorption can be removed due to the different phase but when the phase difference is small, this process adds a lot of noise to the spectra. In contrast, thicker electrodes should block the light from this problematic region and remove the interference. The problem with this is that gold needs to be very thick ($>100\text{nm}$) to block 99% of light across the entire spectrum. As a consequence, the dielectric must be very thick ($>500\text{nm}$)

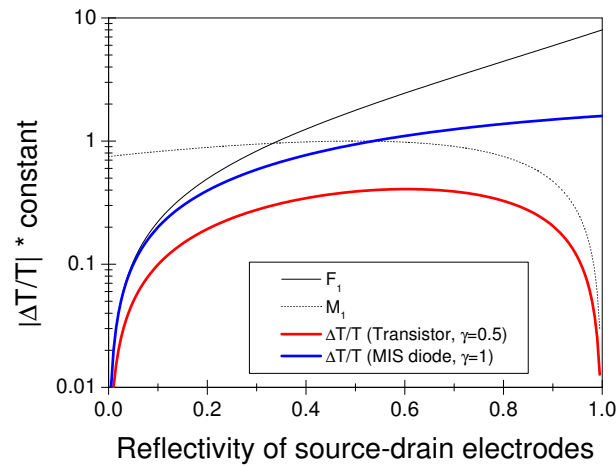


Figure 5.24: The functional form of the magnitude of the electrostriction effect as a function of reflectivity of the bottom electrode for MIS diode and transistor structures.

to prevent shorts or high leakage currents. The disadvantage of a thick dielectric is that if any interference effects are present they have a modulation, with photon energy, that can modify the shape of the spectra. Interference effects in thinner films may still be there with the same amplitude but are smeared out so are less likely to shift peaks or create new ones. Attempts were made to make thin devices whilst still blocking the light in this region by using thin source-drain electrodes but then evaporating them again through the same mask on top of the gate with 100nm of aluminium. Good alignment was achieved with a couple of devices and a spectra obtained from the best one is shown in figure 5.25. Whilst successful in some respects, the spectra still contains features that are not from charge absorption such as the bleaching-type peak at 2.2eV which is lower than the onset of absorption.

The blocking electrodes could be a possible future avenue for CMS devices but requires more development to increase the yield both due to damage to samples in the mask alignment step and the difficulty in getting alignment due to different parallax effects for the eye and evaporation source. Having thick, light-blocking electrodes that are sunk into the substrate and flush with its surface would be a very clean method to achieve this but were beyond the limits of existing in-house patterning techniques.

Regardless of the method used to block light above the source and drain electrodes, the channel region still shows interference artifacts and the ultimate solution to this, as stated above, is to reduce the reflectivity of the gate electrode which is the topic of the next section.

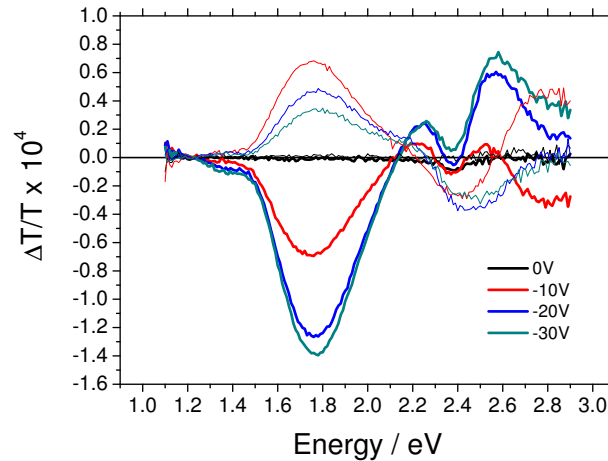


Figure 5.25: CMS spectra for an F8BT (30nm)/PMMA (350nm) transistor with aluminium gate (6nm) and light-blocking aluminium evaporated onto the gate to overlap with the gold (20nm) source and drain contacts.

5.7.2 Non-reflecting gate electrode - PEDOT:PSS

Whilst the thin transistor with blocking electrodes was close to a consistent device configuration, the process of alignment is difficult and results in a low yield. The structure also does not necessarily remove all artifacts as electrostriction will still be occurring to a lesser degree in the channel and it will not be removed completely by making the device thinner. Whilst every attempt was made to reduce the thickness of the metal gate electrode, it could not be made thin enough to remain suitably conductive and yet non-reflecting. High evaporation rates are needed to make very thin (<10nm) aluminium layers conductive and can be difficult to achieve due to the notorious problems of aluminium wetting evaporation crucibles when molten. Variations in the evaporated thickness across the shadow mask, the tooling factors (ratio of thickness on sample and measured at film thickness monitor), and the heating properties of various crucibles from which the metal evaporates make it close to impossible to consistently make metal electrodes that may be in an optimum thickness window of conducting but non-reflecting. Even when thin electrodes could be made, making a contact to it that lasts over the course of days of CMS measurements is also very difficult.

A more robust gate electrode material was required that was consistently non-reflecting and conductive enough for the purposes of CMS. An added requirement for accurate capacitance characterisation is to pattern the gate such that the charges are in a well defined region. PEDOT:PSS is a polymeric material consisting of poly(3,4- ethylene

dioxythiophene) and poly(styrenesulfonate) that is soluble in water and has a conductivity up to 10 S/cm in dry films. Zhuo et al.²⁸ recently showed that the charge carriers at the Fermi energy in PEDOT:PSS have Drude-like optical absorptions that are much different to the population average. It was therefore expected that at higher energies, away from this absorption, there should be no charge-induced absorptions arising from modulating the charge density in PEDOT:PSS. Inkjet printed PEDOT:PSS has been used before as both source, drain and gate electrodes for CMS devices.¹⁷⁰ Whilst unsuitable as source and drain electrodes for ambipolar devices due to the high annealing temperature required for the semiconductor film and the inability to inject electrons into low electron affinity polymers, PEDOT:PSS was used here as a gate electrode. With a combination of oxygen plasma treatment, heat during printing and optimisation of printing speed, the water-based PEDOT:PSS could wet the hydrophobic PMMA film. Aligning the gate was time consuming, not suited to high throughput and required an inkjet printer to be taken away from its primary use of fabricating narrow channel FETs with nano-particle inks. When using the same dielectric thickness as usual, 450nm, the majority of electrodes turned out to be shorted however, it was clear that electron transport was still possible even after this extreme processing. The spectra for this device is shown in figure 5.26.

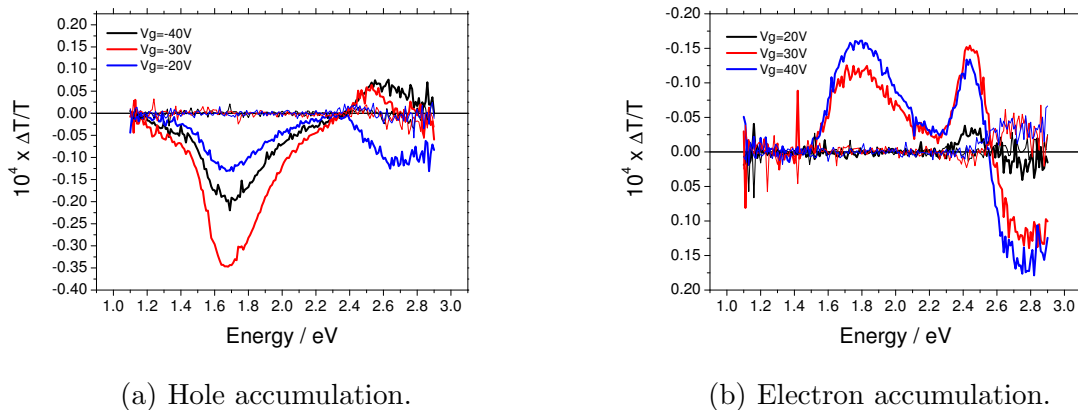


Figure 5.26: CMS spectra of F8BT/PMMA transistor with inkjet-printed PEDOT:PSS gate

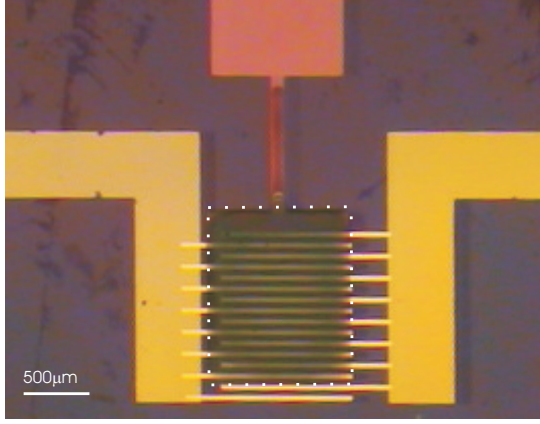
Notice that the peak position in figure 5.26(a) matches well to the devices with the thinnest gold gate electrodes and also the aluminium gate electrode device. The unusual behaviour in the bleaching region is coincidental and is not a feature of the PEDOT:PSS but due to the quenching of the luminescence from F8BT by the charge carriers. This is due to the fact that the detector picks up photoluminescence from the sample which gets

modulated significantly by a quenching mechanism with the modulated charge density. As the charges reduce the luminescence and hence the amount of light detected, it appears to be an absorption in the spectra with a shape that matches the neutral absorption profile thus inverting the bleach feature. This effect is more significant in thick F8BT films because whilst the transmitted light is heavily attenuated by the remainder of the F8BT layer, the luminescence from the accumulation layer passes straight through and so makes up a more significant fraction of the detected light. This interesting effect is investigated in the final chapter.

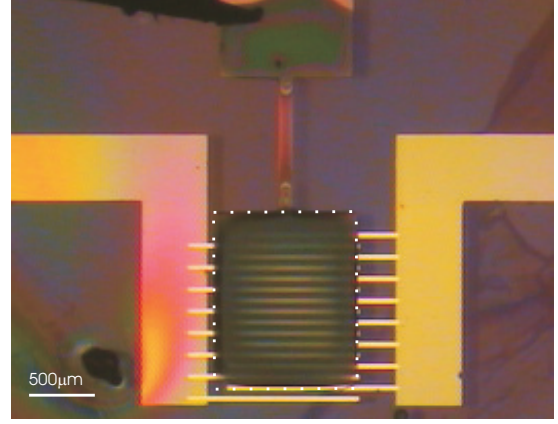
A number of methods to deposit a PEDOT:PSS gate in a more convenient way whilst retaining the patterning of the gate area were attempted before the development of the method described in figure 3.6. Images and transfer characteristics of two such devices that were used for CMS are shown in figure 5.27. The transfer characteristics show that the processing involved in the fabrication has not affected the ambipolar device performance with little sign of hysteresis being observed.

A feature that could be described as a low energy shoulder on the hole spectra from these devices in figure 5.26(a) at around 1.4eV does not appear in the electron spectra where in this region the spectra almost changes sign. A similar feature was noted in F8T2 hole absorption spectra when using PEDOT:PSS electrodes.¹⁷⁰ When the F8T2 was aligned, this feature was unaffected for different polarisations of incident light. To shed further light on this feature with the added benefit of having both electron and hole accumulation spectra to compare, aligned F8BT devices were made with the same patterned PEDOT:PSS gate electrode technique. Images of the devices and their transfer characteristics are shown in figure 5.28. Whilst the alignment increase the mobility, the thicker F8BT layer that is required to prevent dewetting on the polyimide layer is likely to have caused the hysteresis due to trapping in the bulk of F8BT.

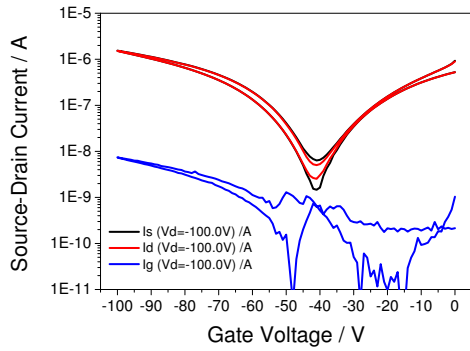
By performing CMS experiments with the incident light either unpolarised, polarised parallel, or perpendicular relative to the alignment direction of the F8BT an unpolarised feature can be seen that is believed to originate from the presence of PEDOT:PSS. When the light is polarised perpendicular to the F8BT alignment, only the PEDOT:PSS feature can be seen. When the light is unpolarised, the PEDOT:PSS feature and the F8BT absorption are both seen. When the light is polarised parallel to the alignment direction, the PEDOT:PSS feature is seen and the $\Delta T/T$ from the F8BT charge absorption is doubled in size relative to the unpolarised light case. This doubling is because there is half the amount of transmitted light but the same number of charge carriers that can absorb relative to the unpolarised light situation due to the dipole for absorption being orientated along the polymer chain. The PEDOT:PSS feature retains the same amplitude



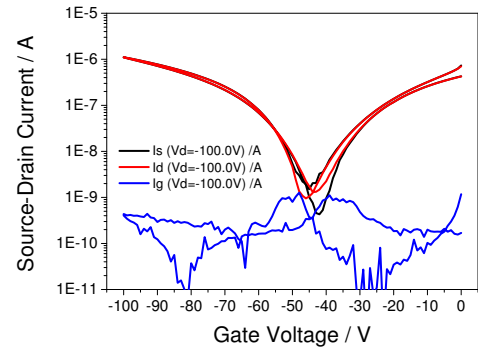
(a) Device B24-1a: Au(80nm) / F8BT(<20nm) / PMMA(500nm) / PE-DOT:PSS. $W=1.36\text{cm}$, $L=40\mu\text{m}$, $A_{gate} = 1.36 \times 10^{-2}\text{cm}^2$, $A_{electrodes} = 5.9 \times 10^{-3}\text{cm}^2$.



(b) Device B24-2a: Au(80nm) / F8BT(<20nm) / PMMA(500nm) / PE-DOT:PSS. $W=1.36\text{cm}$, $L=40\mu\text{m}$, $A_{gate} = 1.36 \times 10^{-2}\text{cm}^2$, $A_{electrodes} = 5.9 \times 10^{-3}\text{cm}^2$.

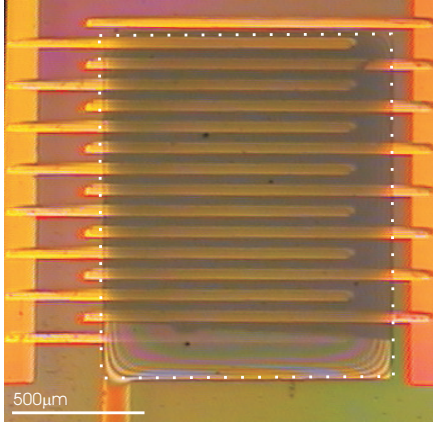


(c) Device B24-1a $\mu_h = 4.4 \times 10^{-4} \pm 1 \times 10^{-5}\text{cm}^2/\text{Vs}$, $\mu_e = 4.1 \times 10^{-4} \pm 1 \times 10^{-4}\text{cm}^2/\text{Vs}$.

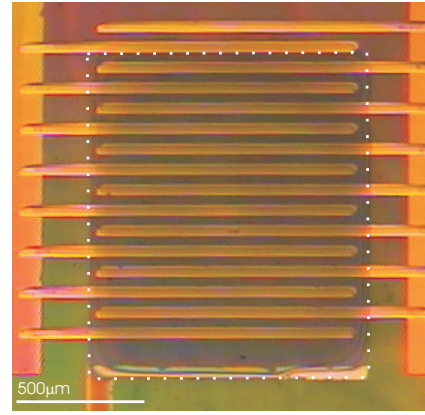


(d) Device B24-2a $\mu_h = 3.7 \times 10^{-4} \pm 2 \times 10^{-5}\text{cm}^2/\text{Vs}$, $\mu_e = 3.0 \times 10^{-4} \pm 4 \times 10^{-5}\text{cm}^2/\text{Vs}$.

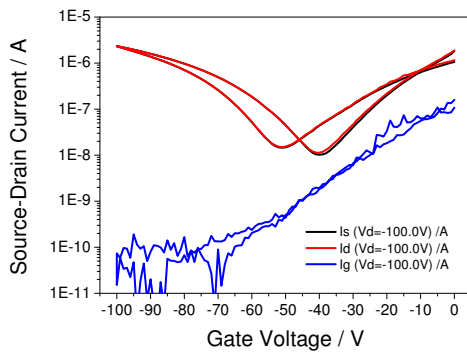
Figure 5.27: F8BT devices fabricated with the new technique to make patterned PE-DOT:PSS gate electrodes with a high throughput capability and minimal processing that can degrade performance. The dashed white squares indicate the region where the PE-DOT is patterned.



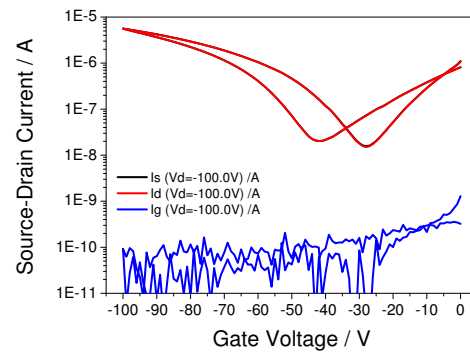
(a) Device B25-3b: Al(17nm) / Au(20nm) / F8BT(aligned)(60nm) / PMMA(750nm) / PEDOT:PSS. $W=1.34\text{cm}$, $L=40\mu\text{m}$, $A_{\text{gate}} = 1.44 \times 10^{-2}\text{cm}^2$, $A_{\text{electrodes}} = 6.1 \times 10^{-3}\text{cm}^2$



(b) Device B25-6b: Al(17nm) / Au(20nm) / F8BT(aligned)(60nm) / PMMA(750nm) / PEDOT:PSS. $W=1.42\text{cm}$, $L=40\mu\text{m}$, $A_{\text{gate}} = 1.40 \times 10^{-2}\text{cm}^2$, $A_{\text{electrodes}} = 5.9 \times 10^{-3}\text{cm}^2$



(c) Device B25-3b $\mu_h = 2.0 \times 10^{-3} \pm 2 \times 10^{-4}\text{cm}^2/\text{Vs}$, $\mu_e = 1.4 \times 10^{-3} \pm 8 \times 10^{-4}\text{cm}^2/\text{Vs}$



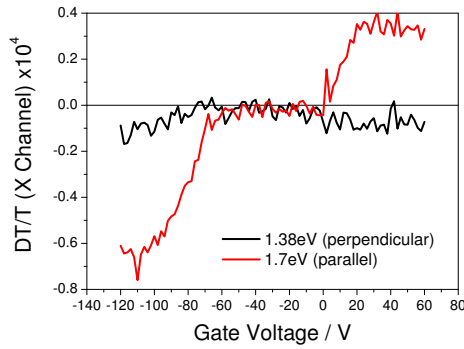
(d) Device B25-6b $\mu_h = 2.0 \times 10^{-3} \pm 5 \times 10^{-4}\text{cm}^2/\text{Vs}$, $\mu_e = 1.9 \times 10^{-3} \pm 1 \times 10^{-3}\text{cm}^2/\text{Vs}$

Figure 5.28: Aligned F8BT devices fabricated with the new technique. F8BT layers have to be thicker to prevent dewetting the polyimide alignment layer leading to less ideal transfer characteristics.

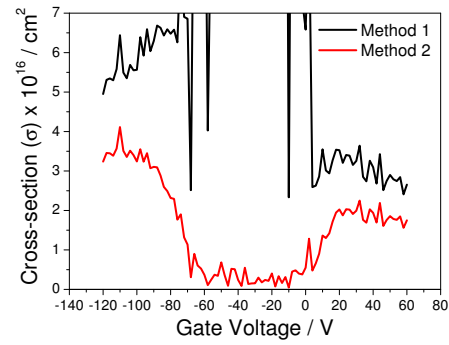
throughout as whatever causes it has no preferential direction so polarising the light halves both the transmitted light and the number of species that can absorb. Figures 5.29(c) and 5.29(d) show the cross sections of these absorptions for the various light polarisations in the case of hole accumulation and electron accumulation respectively. Note that the cross sections are calculated using Method 1 as described in the previous chapter. Due to the large contact resistance resulting from the thicker films needed for alignment, the two methods for calculating cross section do not converge as seen in figure 5.29(b). However, the *shape* of the F8BT spectra can be extracted as (Parallel-Perpendicular)/2 and is shown in figure 5.30(a). These spectra could then be scaled by comparing the unpolarised case with an unaligned thin layer F8BT device however the approach adopted here will be to obtain the PEDOT spectra and subtract it from the spectra of optimised, unaligned F8BT devices.

To further emphasise the fact that the shoulder feature does not originate from some unpolarised absorption in the F8BT, the sign of the absorption at 1.38eV can be seen in figure 5.29(a) to remain the same whether in hole or electron accumulation. For comparison, the sign of an F8BT charge absorption feature at 1.7eV reverses between hole and electron accumulation due to the relationship between trigger and waveform shown in figure 4.2. This is consistent with the feature originating from modulating the charge density in the doped PEDOT:PSS. The sign of the feature when accumulating holes in F8BT suggests it is an absorption from the neutral PEDOT which corresponds to the PEDOT:PSS film becoming more negatively charged. Conversely, when accumulating electrons in F8BT it is the same process occurring in reverse with an additional positive charge on the PEDOT bleaching a neutral absorption. At lower energies this feature changes sign indicating a region where the PEDOT radical cation absorbs. The fact that the feature only appears when F8BT is in accumulation can simply be put down to the fact that there will be a corresponding change in charge density in the PEDOT:PSS above the channel region only when charges flow into the F8BT channel. A control experiment with a PEDOT:PSS/PMMA/PEDOT:PSS structure will also not reveal this spectra as the two would cancel each other out.

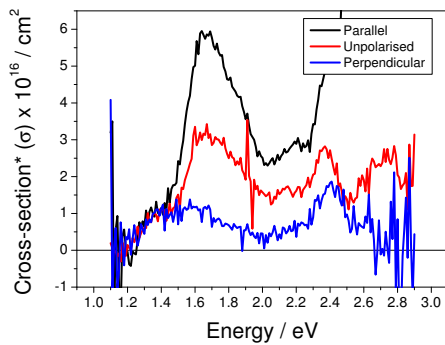
As a final piece of evidence to confirm that the feature is due to the doping and de-doping of PEDOT, the evolution of the PEDOT absorption spectra with doping level is shown in figure 5.30(c) as measured electrochemically.¹⁸² As the film is oxidised, the neutral absorption gets bleached and a sub-gap absorption appears. There is a region in between these two features where the absorption first increases and then reduces at even higher doping levels. As the PEDOT used in the CMS devices is doped with PSS it is not surprising that the change in transmission correlates very well to the difference



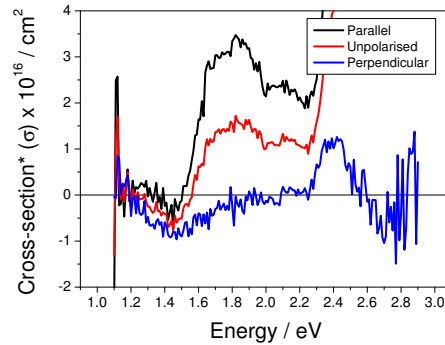
(a) $\Delta T/T$ as a function of gate voltage for two different spectral features originating from PEDOT and F8BT with the polarisation of incident light labelled.



(b) The two methods of cross section calculation applied to the absorption at 1.7eV illustrating the difficulty when using thick F8BT with large contact resistance.



(c) Cross section of hole absorptions on aligned F8BT device B25-6b with polarisation of incident light labelled.



(d) Cross section of electron absorptions on aligned F8BT device B25-6b with polarisation of incident light labelled.

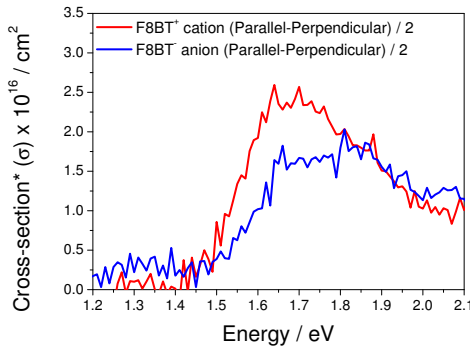
Figure 5.29: The evidence for the shoulder feature in the F8BT spectra arising from PEDOT charge absorptions. The same phase during hole and electron accumulation indicates it can not originate from the F8BT. Cross sections are calculated using the X channel rather than R channel of $\Delta T/T$ to preserve the changes of sign in the spectra in the sub gap region and then the sign of the entire spectrum is adjusted such that charge absorptions are positive for both electrons and holes. Using light polarised perpendicular to the F8BT alignment, the PEDOT spectra can be obtained. The thick layer of F8BT in this device introduces the photoluminescence quenching effect as described in the text rendering the spectra above 2.1eV void, although an electroabsorption feature can be seen at 2.4eV.

between the two most doped spectra in figure 5.30(c). To illustrate this more clearly, figure 5.30(d) shows the difference between the absorption of intermediate and highly doped PEDOT. The peak at 1.5eV and the change of sign at 1.2eV are consistent both in sign and energy with the explanation given above. The PEDOT spectra was obtained experimentally by measuring spectra in both hole and electron accumulation when the light was polarised perpendicular to the F8BT chains alignment. The resulting spectra, shown in figure 5.30(b), were almost identical and matched exactly if 15% of the cation and anion spectra were removed indicating that the alignment was not 100% perfect. The cation and anion spectra were obtained by using the difference between the spectra taken with parallel and perpendicular light which will obtain the correct *shape* of the spectra even if alignment is not perfect and as mentioned above the cross sections are not accurate for these devices.

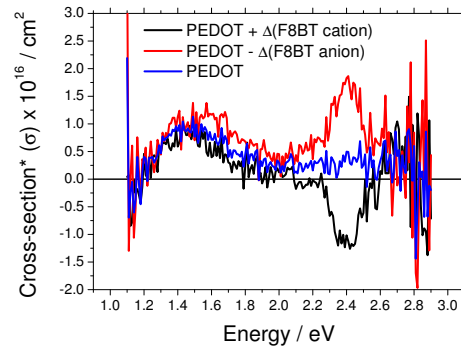
In conclusion, PEDOT:PSS can be successfully used as a gate electrode to remove spectral artifacts originating from interference effects. During the gate voltage modulation the charge density on the PEDOT will be modulated resulting in a small bleach and absorption feature showing up in the CMS spectra. As the PEDOT:PSS is not aligned, this feature can be isolated by using an aligned semiconductor with perpendicularly aligned incident light effectively making the charges on the semiconductor invisible. The known PEDOT spectra can then be subtracted from subsequent CMS measurements where aligning the polymer might not be possible.

5.8 Summary

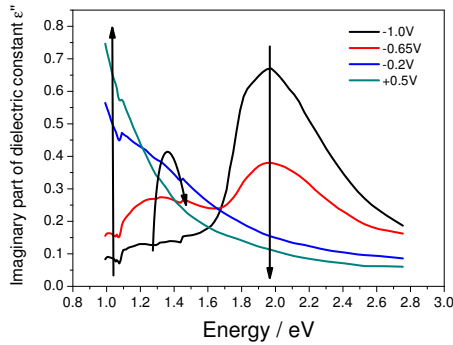
In summary, the reason why initial CMS measurements on F8BT ambipolar transistors resulted in incomprehensible charge-induced absorption spectra was a consequence of the large voltages required to accumulate a given number of charges owing to massive contact resistance. The fields produced by these large voltages were almost 10 times larger than needed for many other materials used in CMS where such artifacts have not dominated the spectra. Furthermore, the cross section for charge absorption in F8BT ambipolar transistors is around 3 times smaller than in some other materials that have been successfully used for CMS increasing the relative size of the artifact even more. The mechanism for the artifact is the modification of a pre-existing interference-induced modulation of the transmission by the changes in film thickness when a field is applied. This process, known as electrostriction, is most dominant in the region between the source-drain electrodes and the gate electrode. By blocking the light in this region the effect is reduced significantly with the added benefit of reducing the electroabsorption spectra



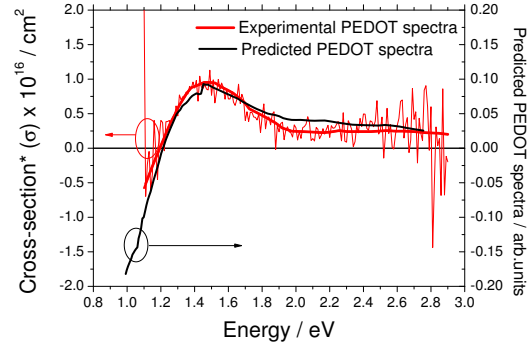
(a) F8BT cation and anion cross sections calculated using the difference between spectra taken with light polarised either parallel or perpendicular to the F8BT alignment. Cross section is calculated with Method 1 and is an over-estimate due to thickness of F8BT film.



(b) PEDOT spectra found using F8BT spectra in hole and electron accumulation with the light polarised perpendicular to the F8BT alignment. A small amount, $\Delta=0.15$, of the spectra from figure 5.30(a) is removed from each such that the two to coincide and can be averaged.



(c) Evolution of the PEDOT absorption with electrochemical doping.¹⁸² Arrows indicate development of spectra with increasing oxidation of PEDOT.



(d) Difference between the two spectra with the highest doping levels from figure 5.30(c) compared to the PEDOT spectra calculated experimentally in figure 5.30(b).

Figure 5.30: Analysis of the polarised CMS experiments on an aligned F8BT device B25-d6b (5.28(b)) used to extract the F8BT cation, anion and PEDOT spectra. Due to the thickness of the F8BT in this device the cross sections are inaccurate as the two methods for calculating them did not converge (Method 1 shown here). A comparison between the PEDOT spectra obtained experimentally and extracted from difference between electrochemically-doped PEDOT spectra is made to further justify PEDOT as being the origin of the unpolarised artifact.

that is highest in this region due to the high field. The electrostriction effect still appears to exist to some extent in the channel and the ultimate solution was found by reducing the reflectivity of the gate electrode by using the conducting polymer PEDOT:PSS. A new method of patterning PEDOT:PSS was developed to enable CMS devices to be routinely made with a patterned transparent gate electrode. Whilst it turned out that the PEDOT:PSS produced some charge-induced absorption and bleaching of its own, these could be isolated using aligned F8BT transistors to be removed from subsequent spectra. Simultaneous electrical measurements were added to the experimental setup to monitor and compensate for the large contact resistance effects which can limit the charge density that it is possible to accumulate. With the findings from this chapter it is now possible to take accurate, clean CMS spectra with ease.

Chapter 6

Charge absorption in polyfluorenes

6.1 Introduction

Since the discovery of conducting polymers¹⁻⁴ much theoretical and experimental effort has gone into trying to understand the nature of the charge carriers responsible for this conductivity. Early theoretical work using one-electron band-structure models⁵⁸ applied to polymers with two degenerate ground state bond configurations led to the concept of a charge existing in a spinless mid-gap soliton state. This concept was extended to the case of polymers with non-degenerate ground state configurations due to either intrinsic or extrinsic dimerisation-inducing factors leading to two new states in the energy gap⁵⁹. The combination of this charge and the associated localised structural distortion of the polymer chain was termed a polaron and possesses spin 1/2. There was much early debate about how to interpret the optical transitions associated with either polarons or the related doubly-charged distortion known as a bipolaron (spin zero).¹⁸³⁻¹⁸⁵ It was expected from the one-electron picture that three new sub gap transitions could be expected for the polaron and two new transitions for a bipolaron which should coincide with either the presence or absence of a signal from electron spin resonance experiments (ESR). These transitions were either between the localised states or between the band-like states and the localised states.

Cornil et al. advanced the early band models by considering conjugated polymers as being made up of short units that could be characterised as oligomers^{186,187} which was also found by others to be more appropriate.¹⁸⁵ Using quantum chemical calculations which include electron correlation effects and then calculating the allowed transitions they came to the conclusion that in general two absorptions should be expected in the polaron case and one in the bipolaron case. The current best method for calculating optical transitions is to first use semi-empirical Hartree-Fock methods to determine the ground state and charged state geometries. The charged state does, as with the continuum models, predict two energy gap states and the relaxation energy of the polaron can be calculated. The Configuration Interaction method is then used to calculate the optical transitions by including various configurations of electronic transitions between the one-electron states. In some simple cases, the resulting optimised transitions mostly have character of HOMO-P1 or P1-P2 which have historically been labelled the C1 and C2 transitions as shown on figure 2.6. However the general result is that the optimised transition energies will have significant contributions from a number of configurations. There are of course further transitions at higher energies between the polaronic levels and higher lying states.

In the case where there is good molecular packing, it is possible for the charge to spread over one or more adjacent polymer units. This results in a splitting of the P1 and P2 levels

and the symmetry of the new states opens up the possibility of new transitions known as C3 and C3' whilst C2 becomes symmetry forbidden. Experimental evidence for the new optical transitions associated with intermolecular electronic interactions was found in regio-regular P3HT.¹⁸⁸ As ordering improves, the emergence of delocalised polaron bands are expected and recent findings have shown that in single crystals, charge-induced absorptions can have Drude-like behaviour indicating delocalised band-like transport.¹⁸⁹ It has also been observed in heavily doped polymers that the charge carriers at the Fermi energy have different optical absorptions as compared to the bulk average which also resemble delocalised Drude-type behaviour.²⁸

Building on this previous work into polarons the work presented in this chapter investigates the differences between the positive and negative polaronic species on the same polymer. In the one dimensional band picture of conjugated polymers, the symmetry of the Hamiltonian means that there should be no difference between the optical transitions associated with positive and negative polarons which is referred to as charge-conjugation or particle-hole symmetry.¹⁹⁰ It has been suggested that this rule is universal and would also apply in the quantum chemical molecular orbital approach.¹⁸⁵ In both cases however this applies for hydrocarbon-only polymers and the rule is expected to be broken in the presence of heteroatoms in the polymer chain which would break the particle-hole symmetry. In this work, two model polyfluorene-based materials are used to investigate this symmetry-breaking for the first time which is now possible with ambipolar transistors. F8 is a hydrocarbon-only polymer which is expected to have symmetric electron and hole wavefunctions whilst F8BT contains a benzothiadiazole (BT) unit which is known to localise the electron wavefunction whilst the hole wavefunction remains more delocalised.³⁷ The comparison of the hole and electron-induced absorptions of these two polymers should provide evidence of this symmetry breaking which will be manifest in different optical absorptions.

Quantum chemical calculations were performed for F8 and F8BT by Dr. Vincent Lemaure from Jérôme Cornil's group at the Université de Mons-Hainaut. The electronic structure of F8 and F8BT was estimated at the Hartree-Fock semi-empirical MNDO level on the basis of the MNDO optimised geometry in the ground state. Figure 6.1 shows the energies and charge densities of the HOMO and LUMO states in the F8, BT and F8BT monomer units which confirms the point that the electron in the LUMO is localised on the BT unit.

By combining a number of repeat units, the distribution of the charge density of the positive (cation) and negative (anion) charged states in F8BT and F8 oligomers is shown in figure 6.2. The F8BT anion does indeed mostly reside on the BT unit although there

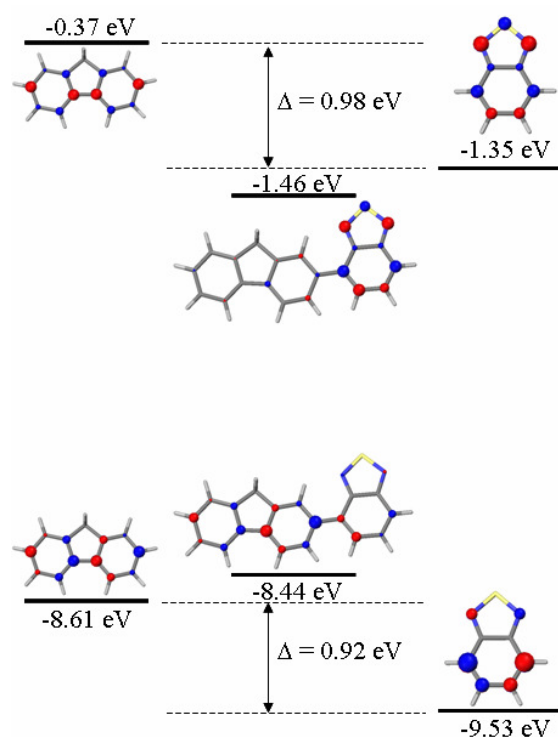


Figure 6.1: Energy diagram of the HOMO and LUMO states in F8, BT and F8BT monomers (calculated by Dr. Vincent Lemaury). Note the much larger energy gap in these monomer units as compared to longer oligomers or polymers. The energy gap is reduced when subsequent monomer units are added.

is still some electron density on the adjacent F8 units. The F8BT cation on the other hand is more delocalised and spreads uniformly over three repeat units. In contrast, the charge density of the F8 anion and cation are close to identical.

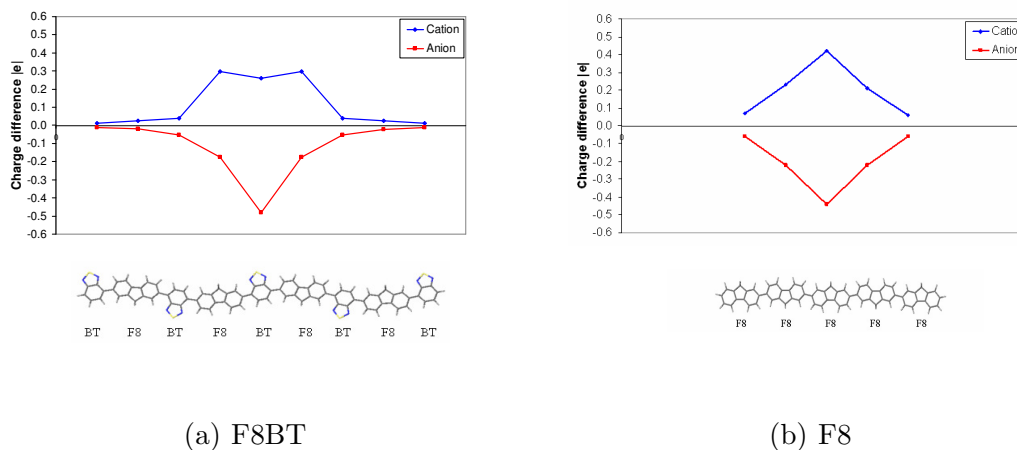


Figure 6.2: Comparison of the charge density of the wavefunctions for the anion and cation as a function of position along the oligomer (calculated by Dr. Vincent Lemaur).

Early time of flight (TOF) measurements indicated dispersionless transport of holes in F8 whilst no electron transport could be observed although this was attributed to trapping rather than any fundamental difference in the wavefunction.³⁴ Electron transport was observed in TOF measurements on F8BT¹⁹¹ and this electron transport was studied further in FETs as a function of molecular weight and annealing temperature by Donley et al.³⁶ where it was suggested that electron transport was dominated by interchain transport rather than intrachain due to the F8 barrier between the electron rich BT sites. Zaumseil et al.³² showed that electron and hole mobilities were balanced in polycrystalline F8BT ambipolar transistors. In aligned F8BT devices the anisotropy between transport in the direction of the chains and perpendicular to them showed similar ratios for both electrons and holes¹⁹² which could imply that intrachain transport was no different for the two species. However, these measurements do not reflect the microscopic charge transport along one chain or between two chains and inferences about the microscopic mobility from the light emission in these devices indicate a much larger mobility anisotropy.

Whilst electrical measurements of charge transport determine macroscopic properties and can be strongly influenced by extrinsic effects such as injection and trapping, optical measurements of the charge-induced absorptions provide a direct probe of the charge species. In this chapter, the methods described in the previous two chapters to measure charge-induced absorptions in ambipolar transistors are applied to F8BT and F8 devices.

The optical cross sections for the anion and cation are obtained in both cases in order to better understand the nature of the associated wavefunctions and electron-hole symmetry.

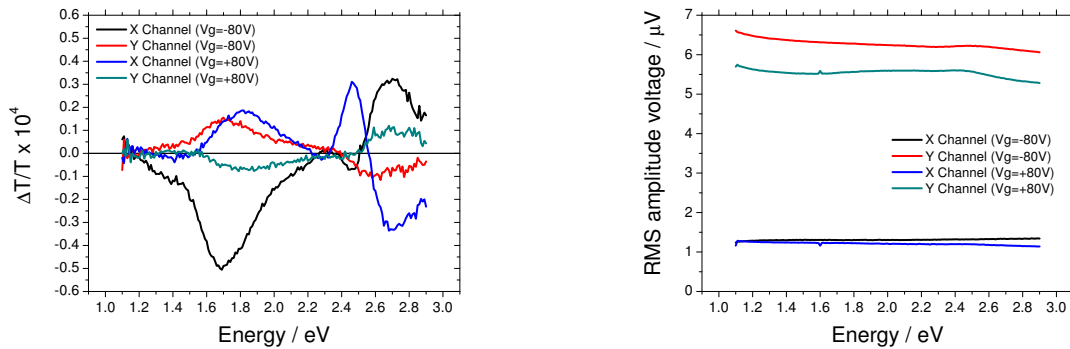
6.2 F8BT CMS

In the previous chapter, the a new patterning technique to make transistors with a PEDOT:PSS gate electrode that minimised reflection to remove electrostriction effects from CMS spectra was developed. In doing so, it was noticed that the PEDOT itself had both neutral and charged absorptions that were either bleached or induced when modulating the gate voltage and the spectra of this was extracted. The devices used for isolating the PEDOT and F8BT spectra were far from ideal as the thick F8BT films needed for alignment caused an increase in electroabsorption and luminescence quenching artifacts as well as significantly increasing contact resistance which made it impossible to fully accumulate the device resulting in noisy spectra with a large uncertainty when calculating the cross section of absorption. In this section F8BT transistors that were optimised for CMS by having a thin F8BT layer ($\leq 20\text{nm}$) although still containing the PEDOT artifact were studied and the known PEDOT spectra removed at the end to give clean, artifact-free accurate F8BT charge spectra.

6.2.1 Typical optical and electrical data

The typical $\Delta T/T$ spectra for an optimised F8BT device (B24-d1a, see figure 5.27(a)) showing both the X and Y channels from the lock-in amplifier for both electron and hole accumulation are shown in figure 6.3(a). By using figure 4.2 as a guide to understanding the phase and origin of the various features a number of observations can be made. Firstly, whilst predominantly in the X channel, both spectra contain a significant component in the Y channel indicating a phase lag due to a series contact resistance. However, looking at the region above 2.2eV shows that there is a feature in both the X channels that is not present in the Y channels which is due to electroabsorption and is much stronger for electron accumulation. In contrast the Y channels show only bleaching of the neutral absorption from F8BT. Secondly, between 1.1eV and 1.5eV there is an absorption for hole accumulation and what appears to be a slight bleaching for electron accumulation due to the bleaching of an absorption in doped PEDOT. The PEDOT bleach always has the same phase relative to the driving voltage, whereas the charge absorptions in F8BT change phase relative to the driving voltage depending on whether in hole or electron accumulation. The fact that the feature in this region is not equal and opposite indicates

that there is an absorption here from at least one of the charge species in F8BT. Finally, the peak energy and magnitude of the charge-induced absorptions around 1.7eV-1.8eV are different for electrons and holes although this data must be corrected for the number of charges being modulated and the effect of the PEDOT before an accurate comparison can be made.



(a) $\Delta T/T$ for both hole ($V_g = -80V$) and electron ($V_g = +80V$) accumulation showing both X and Y channels.

(b) Lock-in measurements used to determine number of charges being modulated on device.

Figure 6.3: Raw measurements of $\Delta T/T$ and the voltage across the 130 Ω resistor between the (shorted) source and drain contacts and ground. Scans performed with $V_{pp} = 10V$ and at 37Hz on F8BT device B24-d1a (5.27(a)).

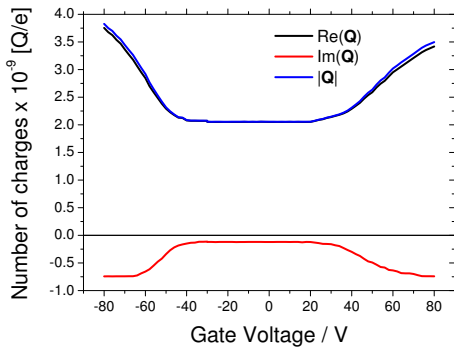
Figure 6.3(b) shows the voltage measured by a lock-in amplifier across a 130 Ω resistor connected between ground and the shorted source and drain contacts. The Y channel is 90 degrees in phase ahead of the X channel and so the positive value here is a measure of capacitive current leading the voltage modulation. As the scan takes approximately 2 hours and runs from low energy to high energy, the decay in the voltage with energy indicates the gradual trapping of charges reducing the amount of mobile charges that can be modulated around that particular gate voltage. The X channel corresponds to either leakage current which is in phase with the applied voltage or a lag in the capacitive current which rotates it into the X channel due to a series resistance which is the case here.

6.2.2 Gate voltage dependence of the charge-induced absorptions

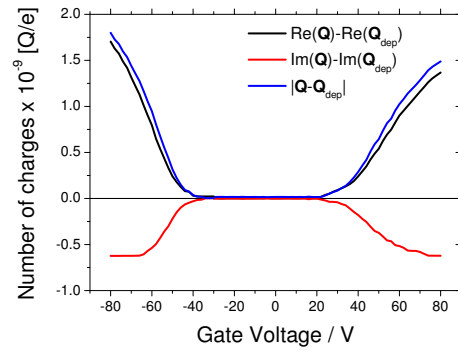
To calculate the cross section for charge absorption it is often helpful to look at one wavelength of light and study the evolution of an absorption with gate voltage as the

transistor goes from depletion to accumulation. Figure 6.4(a) shows the electrical measurements converted via equations 4.24, 4.25 and 4.23 to the real part, imaginary part and modulus of the complex charge on the device. The real part of the charge corresponds to the component of charges that are in phase with the applied voltage just like the X channel for the spectroscopic measurements whilst the imaginary part of the charge corresponds to the Y channel. In depletion it is the charge on the source and drain electrodes that is being measured electrically but as the device enters accumulation, charges begin spreading into the channel and the number of charges increases. In figure 6.4(b) the increase in charge relative to depletion is shown as calculated using equations 4.39, 4.40 and 4.38. In Method 1 for calculating the cross section of charges, this increase in charge and the difference between the area of the gate and the electrodes is used in combination with the appropriate X, Y or R channels of $\Delta T/T$ shown in figure 6.4(c) to calculate the cross section. In Method 2 for calculating the cross section, the total amount of charge from figure 6.4(a) and the total area of the gate is used and in Method 3 simply the capacitance per unit area of the dielectric and the peak to peak modulation voltage is used as in equation 4.8. The cross section as calculated by all three methods for the absorption at 734nm (1.69eV) is shown in figure 6.4(d). As was found in the modelling section 4.4.3, Method 1 and 2 correspond to an upper and lower limit of the cross section which converge as the device gets closer to full accumulation. Method 3 will also converge although only when full accumulation is reached.

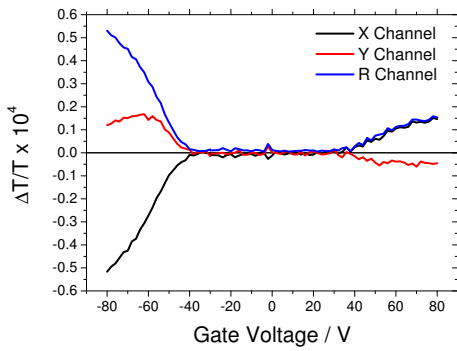
The shape of the spectra as a function of gate voltage was also studied in figures 6.4(e) and 6.4(f). In the case of a doped semiconductor, the shape could change as the device enters depletion due to the difference between modulating charges at the interface and in the bulk.¹³⁶ There may also be changes in the spectra as the charge density increases and the fermi energy rises through the density of states as it is only states around the fermi energy that are being probed.²⁸ Depending on the material system, bipolarons might be observed whereby two charges occupy the same structural deformation thus lowering the energy however this has not been observed in F8BT.¹⁹³ In order to fully characterise charge density effects it would be necessary to be able to modulate the charge density over a large range however, even at the largest densities achieved in these transistor of $\sim 4 \times 10^{18} \text{cm}^{-3}$ there is only one charge for a few hundred repeat units therefore significant changes are not expected to be seen. Indeed there is very little change observed here in F8BT apart from perhaps a slight blue shift in the hole absorption spectra. The main change in these spectra is due to a reduction of electroabsorption as the device enters accumulation.



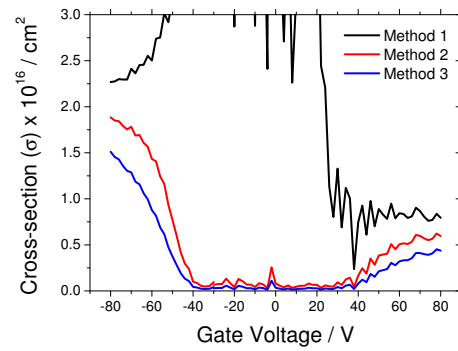
(a) Real and imaginary parts of charge measured on the device (scaled to number of charges).



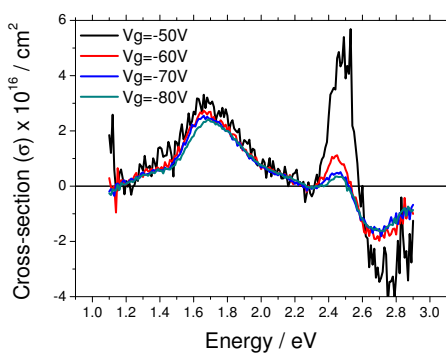
(b) Increase of charge relative to depletion (dep).



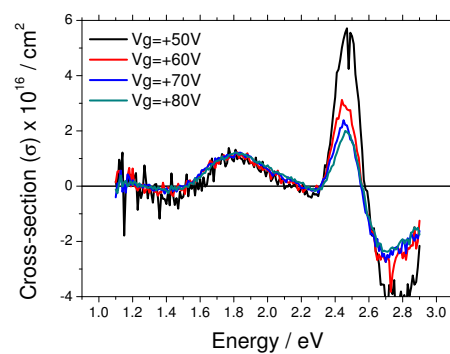
(c) $\Delta T/T$ at 734nm (1.69eV) measured simultaneously with electrical data.



(d) Cross sections at 734nm (1.69eV) calculated according to the three methods.



(e) Cross section spectrum for hole accumulation for various gate voltages using Method 1.

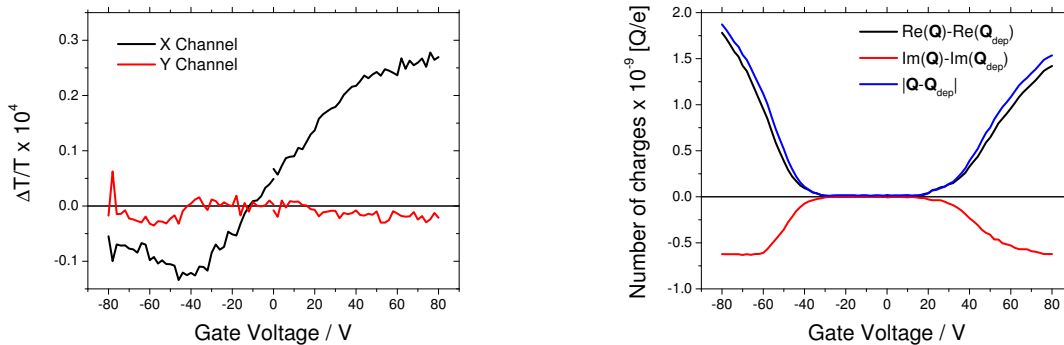


(f) Cross section spectrum for electron accumulation for various gate voltages using Method 1.

Figure 6.4: Illustration of the methods used to convert measured data to cross sections illustrating the effect of gate voltage for F8BT device B24-d1a (5.27(a)) using $V_{pp}=10V$ at 37Hz.

6.2.3 Electroabsorption

To illustrate the difference between a charge absorption feature and an electroabsorption feature, other than noting the difference in the X and Y channel in figure 6.3(a), the dependence of the feature at 2.43eV is shown as a function of gate voltage in figure 6.5(a). The feature at 2.43eV is entirely in the X channel and increases linearly when the device is in depletion as can be seen by comparing with the electrical measurements in figure 6.5(b). The fact that it does not cross the y-axis at zero indicates that there may be some trapped charge in the device resulting in a field even when the gate is at zero bias. The linear increase with gate voltage continues until the conductivity or contact resistance becomes such that charges can be modulated in the device at that frequency. When charges can respond to the applied gate voltage and reach the interface with the dielectric, the field across the F8BT can be partially or completely screened causing the electroabsorption to either disappear, reduce or increase more slowly with gate voltage. As the charges start entering the device, the bleaching feature starts appearing at this wavelength also. For a negative gate bias, the bleaching has a positive sign whereas for a positive gate bias it has a negative sign indicating that in this device the field can be screened more effectively in hole accumulation compared to electron accumulation which is attributed to lower contact resistance.



(a) $\Delta T/T$ at 510nm (2.43eV) where electroabsorption occurs.

(b) Electrical measurement of number of charges on the device.

Figure 6.5: Correlation between electroabsorption and measured charges in F8BT device B24-d1a (5.27(a)) using $V_{pp}=10V$ at 37Hz.

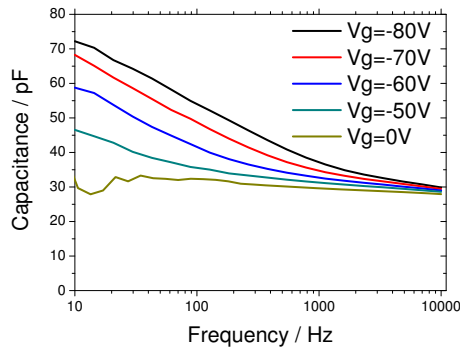
6.2.4 Frequency response

As CMS is only sensitive to a charge density that modulates at a given frequency, it could be that differences arise in the spectra as this frequency is changed. The frequency response of the capacitance of the F8BT device in hole accumulation is shown in figure 6.6(a) for various gate voltages. The continuing increase in capacitance as the frequency reduces even down to 10Hz indicates that the capacitance is severely limited by contact resistance and never reaches full accumulation. Figures 6.6(b) and 6.6(c) show the extra charge density being modulated on the device compared to depletion and $\Delta T/T$ measured at 2.6eV (bleaching) as a function of frequency for various gate voltages. Using this data, the cross section of the bleach as a function of frequency is calculated. Again, the two methods for calculating cross section converge as the charges become able to comfortably respond to the driving frequency. The apparent reduction at high frequencies is due to the small bandwidth of the detector amplifier as shown in appendix B.5.

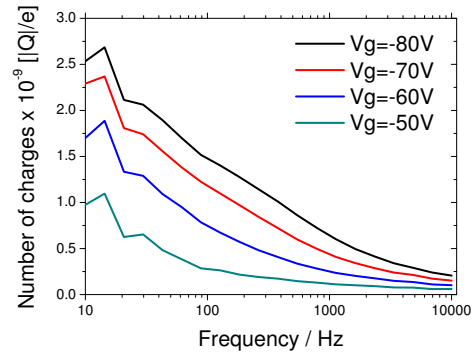
The normalised spectra obtained for hole and electron accumulation as a function of frequency are given in figures 6.6(e) and 6.6(f) respectively. Other than the increasing noise due to the reduction in signal size at high frequencies and the increased electroabsorption there does not appear to be any significant change in the spectra with frequency. Unfortunately this technique cannot go to frequencies that are low enough to study trapped charges although depending on the mechanism responsible for trapping these may not necessarily even produce a charge absorption.

6.2.5 Accuracy of technique

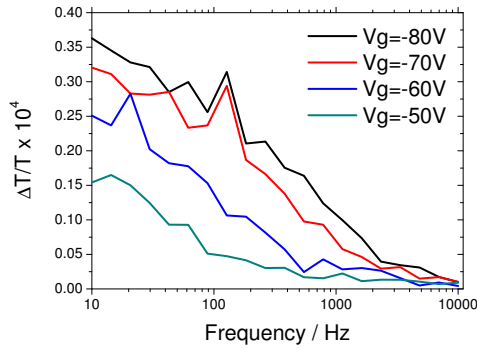
To assess the accuracy of a given measurement, a comparison of the cross section obtained on one device under different biasing conditions is shown in figures 6.7(a) and 6.7(b) for holes and electrons respectively. The upper and lower limit given by Method 1 and Method 2 bound the same region regardless of the peak to peak modulation or frequency used. As seen above, the upper and lower limits converge as the device gets further into accumulation or is operated at a lower and lower frequency. Unfortunately there is a limit to the size of the gate voltage that can be applied without causing a breakdown of the dielectric and at frequencies much below the standard 37Hz the noise of the measurement requires scan times of many hours which causes significant devices degradation. Therefore the cross section is estimated as halfway between the value given from the two techniques under the operating conditions where they are closest together.



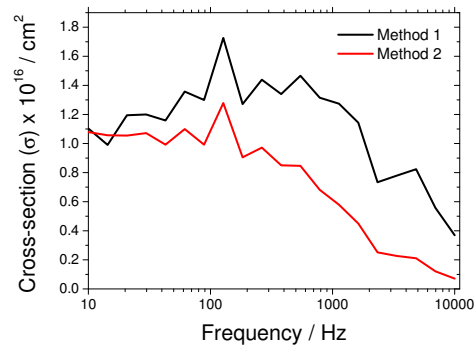
(a) Capacitance (from $Im(\mathbf{Y}/\omega)$) measured at various gate voltages.



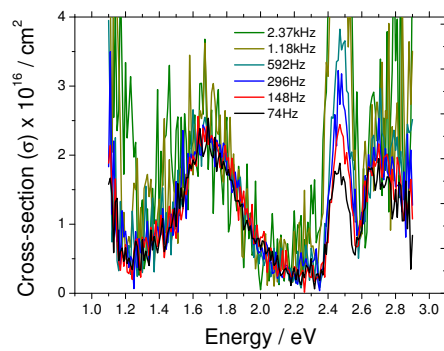
(b) Number of charges (absolute value) compared to depletion corresponding to data in figure 6.6(a).



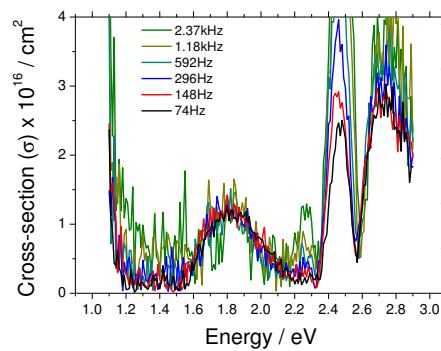
(c) $\Delta T/T$ at 477nm (2.6eV) measured simultaneously with 6.6(a).



(d) Cross section as a function of frequency at 477nm.

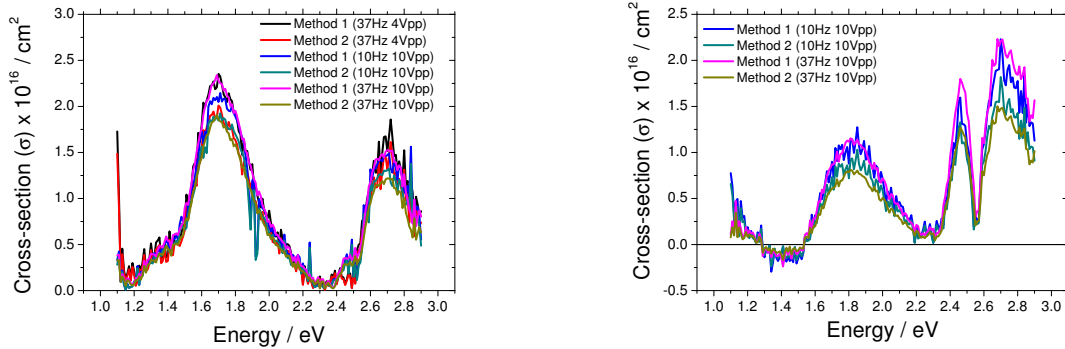


(e) Cross section spectra using Method 1 for hole accumulation at various frequencies ($V_g = -80V$ during scan).



(f) As figure 6.6(e) but for electron accumulation ($V_g = +80V$ during scan).

Figure 6.6: Analysis of the frequency response of F8BT device B24-d1a (5.27(a)) using $V_{pp}=10V$. Note the reduction in cross section above 1kHz is due to the frequency response of the detector shown in appendix B.5.



(a) Cross section spectra of holes measured with either different frequency or modulation voltage

(b) As 6.7(a) but for electron accumulation

Figure 6.7: Illustration of versatility of normalisation technique using the simultaneous measurement of $\Delta T/T$ and the charge on the device (B24-d1a (5.27(a)))

6.2.6 Separating charge absorption from electroabsorption

As seen in all the above spectra, electroabsorption exists to some degree at all frequencies and gate voltages with the inconvenient effect of obscuring the bleaching region and the high energy end of the charge absorption. By independently calculating the cross section spectra using either the X, Y or R channel of $\Delta T/T$ through equations 4.39, 4.40 and 4.38 it can be seen in figures 6.8(a) and 6.8(b) that whilst the Y channel method is not as accurate in terms of magnitude, the spectra does not contain any of the electroabsorption which is always in phase with the applied voltage. The magnitude of the spectra is incorrect due to the high sensitivity to small differences in phase between the optical and electrical measurements. The correct spectra can therefore be found by using the Y channel to calculate the shape of the spectra and then normalising using the charge absorption peak to the more accurate value found using either the R or X channel.

6.2.7 Using a drain voltage to improve signal to noise

After fully characterising the frequency and gate voltage dependence of the cross section spectra in device B24-1a, a new device, B24-2a, was measured with the aim of measuring a complete spectra with the highest signal-to-noise possible so that the PEDOT spectra could be subtracted from the Y channel-derived spectra cleanly. It was established that applying a drain voltage during the gate modulation could significantly enhance the size of $\Delta T/T$ by lowering the contact resistance. A method for trying to calculate the cross

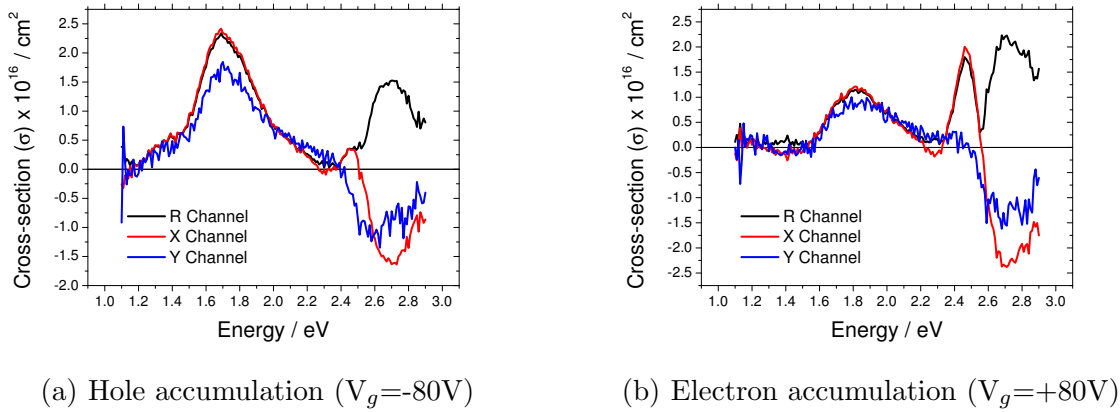
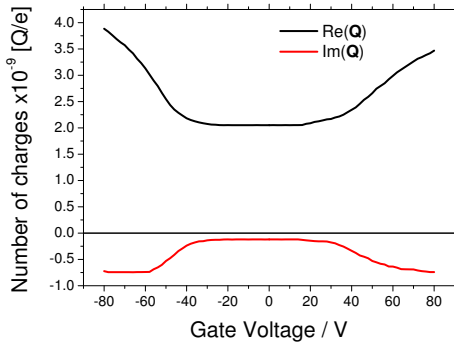


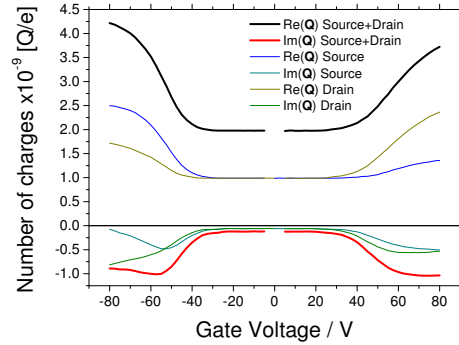
Figure 6.8: Cross section spectra of charges measured using either just the X, Y or R channel of $\Delta T/T$ and the corresponding electrical measurement. Cross sections calculated using Method 1 and measured at 37Hz with $V_{pp}=10V$ on device B24-1a (5.27(a))

section using electrical measurements taken when a drain voltage is applied was developed by choosing two sets of drain and gate biases such that the relative voltages are identical but the drain current is being measured in one case and the source in the other. The drain voltage technique is described in more detail in section 4.4.5.

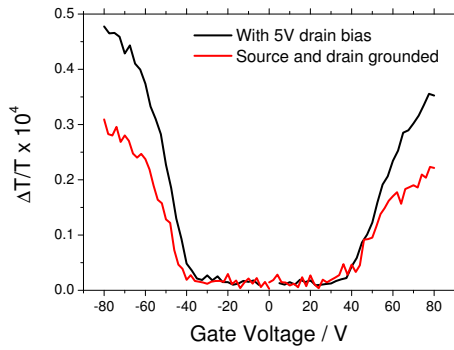
Figure 6.9(a) shows the standard measurement of charge on device B24-2a as a function of gate voltage when the source and drain are both grounded and the gate is modulated at 37Hz with $10V_{pp}$. In figure 6.9(b) the charge on the device, as measured independently from the source and drain, is shown when a drain voltage is applied but otherwise all other conditions are the same as before. By adding the charge from the source and drain together, the modulated charge that flows from source to drain cancels out leaving only the modulated charge density on the device behind. By comparing the two figures it can be seen that this suggests a larger charge density is being modulated on the device owing to the drain voltage as shown more clearly in figure 6.9(d). Looking at the size of $\Delta T/T$ in figure 6.9(c) reveals an enhancement of around 50% which is more than the enhancement in measured charge density. If the same equations are used to calculate the cross section, it therefore comes out larger when a drain bias is being used as shown by comparing figures 6.9(e) and 6.9(f). The most likely reason for this discrepancy is that the area in which the charge density is being modulated is probably different when a drain voltage is applied as charges are more likely to drift in the drain field than to spread out evenly over the gate area. In fact, comparing the values for Method 2 it would appear that charges spread over an area about 50% less than when no drain voltage is



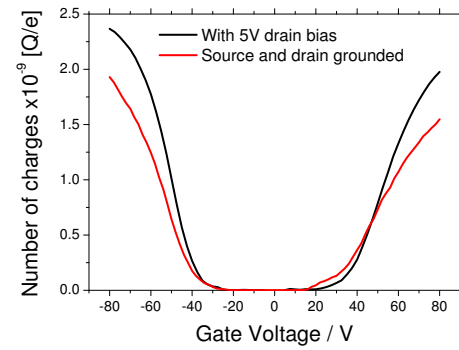
(a) Real and imaginary parts of charge with no drain bias.



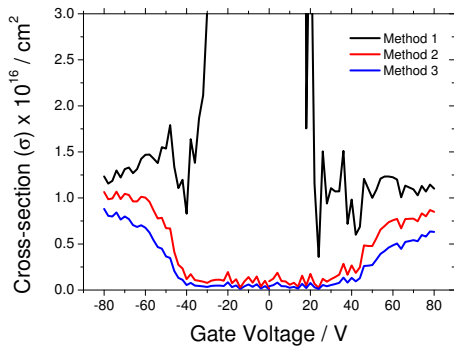
(b) Method for reconstructing magnitude and phase of charge on device with a drain bias of +5V ($V_g > 0$) or -5V ($V_g < 0$).



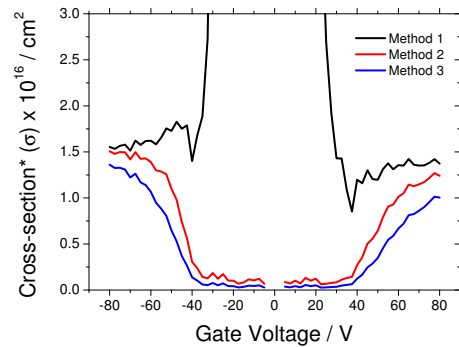
(c) $-\Delta T/T$ at 477nm (2.6eV) with and without drain bias applied.



(d) Total amount of extra charge accumulated with and without drain bias.



(e) Cross section calculated at 477nm (2.6eV) with no drain bias.



(f) As 6.9(e) but with $\pm 5V$ drain bias.

Figure 6.9: Analysis of the effect of a small drain bias on the calculated cross section using F8BT device B24-d1a (5.27(a)) with $V_{pp}=10V$ at 37Hz.

applied. With no way of determining this area accurately and whether it depends on the drain current, cross sections calculated with this method cannot be relied upon and an asterisk is shown on the axis label to point this out. However, if the cross section can be determined accurately in the case where no drain bias is applied then the spectra obtained with a drain bias can simply be scaled to the correct size.

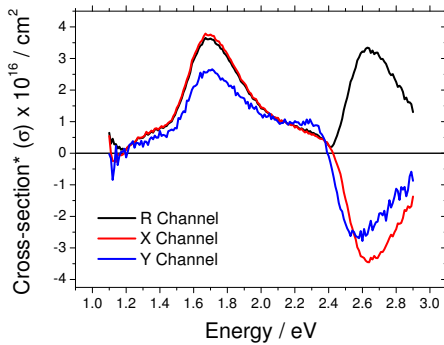
The cross section spectra calculated using the X, Y and R channels of $\Delta T/T$ when a drain bias is applied are given in figures 6.10(a) and 6.10(b) for holes and electrons respectively. Even with a drain bias applied, electroabsorption is not removed but again, the Y channel method gives a spectra containing only charge absorption and bleaching of the neutral F8BT absorption. The Y channel spectra are normalised, using the main charge absorption peak, to the cross sections obtained with device B24-1a when no drain bias was applied. The corrected spectra are given in figure 6.10(c) along with the PEDOT spectra obtained at the end of the previous chapter. It had not been possible to get the exact size of the PEDOT spectra due to the aligned F8BT transistors being far from ideal for that type of measurement however the shape is correct. The PEDOT spectra was subtracted from the F8BT hole spectra and added to the F8BT electron spectra in equal amounts. The size of the PEDOT spectra was determined by adjusting it until the shape of the modified hole and electron spectra matched those found in the aligned transistors figure 5.30(a). The spectra from the aligned transistors is believed to be accurate in its shape but the cross section could not be determined accurately enough and the spectra was noisy. Whilst this technique to obtain the final spectra may seem convoluted, we can be confident that both the shape and the size of the resulting spectra are correct and have the highest achievable signal-to-noise ratio.

6.2.8 Analysis of charge-induced spectra

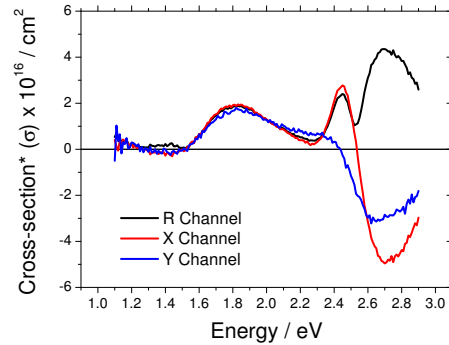
The final spectra of the F8BT radical cation and anion reveal a number of interesting features. Firstly the cation absorption has a larger peak transition strength and the total area under the charge-induced absorption is larger than in the case of the anion. The integrated area under the cross section spectra is related to the oscillator strength, f , for the transition by¹⁹⁴

$$f = \frac{2\epsilon_0 m_e c}{\pi e^2} \int_{-\infty}^{\infty} \sigma(\omega) d\omega = \frac{2\epsilon_0 m_e c}{\pi \hbar e} \int_0^{\infty} \sigma(E) dE \quad (6.1)$$

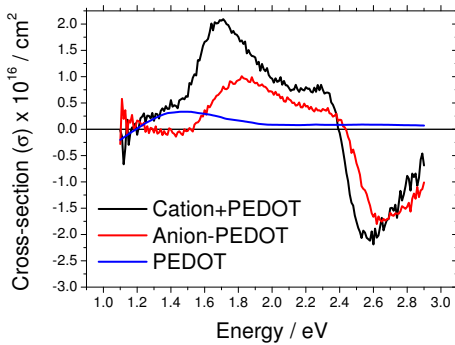
where where m_e and e are the mass and charge of an electron and the photon energy, E , is measured in eV. According to the sum rule, as applied to conjugated polymers, the sum of the oscillator strengths, f_j , for the transitions from the ground state to all j excited



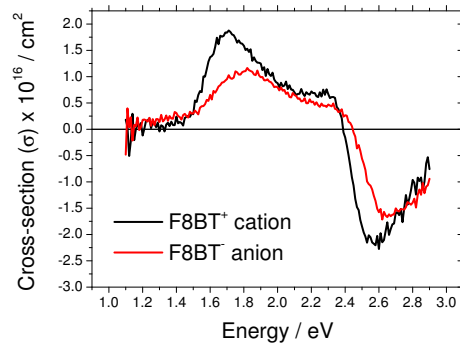
(a) Cross section spectra calculated using Method 1 applied individually to the X, Y and R channels of $\Delta T/T$ with a drain bias of $-5V$ applied in hole accumulation.



(b) As 6.10(a) but with a drain bias of $+5V$ applied in electron accumulation.



(c) Cross section spectra from the Y channel measurement with drain bias and normalised to the value calculated for device B24-1a with no drain bias. Shown also is the PEDOT cross section.



(d) Final corrected spectra for the F8BT cation and anion.

Figure 6.10: Method for calculating final spectra using fresh F8BT device B24-d2a (5.27(b)) with a drain bias applied to maximise the signal to noise ratio. The Y channel of $\Delta T/T$ is used to remove electroabsorption from the spectra and the cross section is normalised to that calculated correctly on device B24-1a. The PEDOT spectra obtained with an aligned device in figure 5.30(d) is scaled such that when the same amount is removed from the cation and anion spectra the shapes match those found with the aligned device in figure 5.30(a).

states satisfies

$$\sum_j f_j = N_e \quad (6.2)$$

where N_e is the number of π electrons in the polymer¹⁹⁰. This can be intuitively understood in terms of the amount of absorption scaling with the number of repeat units. In the case of a polaron which is self-localised to a few repeat units, the neutral absorption of the polymer is partly bleached, with the amount of bleaching corresponding to the number of π electrons in this region. Equally the total amount of absorption from the polaron will be equal to the same amount as the bleach apart from a difference of one π electron meaning that the integral of $\Delta T/T$ over the entire spectral range should be approximately zero. Whilst the entire energy spectrum is not available here, the integral shown in figure 6.11 shows how the smaller neutral bleach in the anion case compensates the smaller sub-gap absorption with the two integrals ending up at a fairly similar value. There may also be an absorption for the anion that overlaps with the bleaching which could explain why the peak is blue shifted and smaller. Figure 6.11 also has a second scale indicating the cumulative transition strength which peaks at around 0.88 for the cation and 0.65 for the anion, although as the incident light is unpolarised, these figures should be doubled to 1.76 and 1.30 to reflect the oscillator strength parallel to the transition. These values are as close as it is possible to get to the transition oscillator strengths for the higher energy sub gap absorptions given the ambiguity introduced by the possible overlap with the bleach. The similar size of the bleach for both the electron and hole indicate that the delocalisation of the electron is not that much smaller than the hole which is in agreement with the quantum chemical calculations above.

It was not possible to fit the spectra with a sensible number of Gaussian functions indicating that the shape of the spectra is not just due to energetic broadening but the presence of a range of conjugation lengths with different optical transition energies.

In order to understand the nature of the measured transitions, the absorption spectra of 5-unit and 9-unit F8BT oligomers were calculated by Dr Vincent Lemaury with quantum chemical calculations. These were performed at the MNDO level coupled to a single configuration interaction technique involving electron transitions from the highest 10 (5) occupied levels to the lowest 10 (5) unoccupied levels for the 9-unit (5-unit) oligomer. The predicted transition energies and relative weights of the absorptions are given in figure 6.12 and table 6.1. The energies of all transitions including the neutral oligomer are higher in energy than observed experimentally in films due to the calculation being carried out in the gas phase. As expected from the sum rule, the oscillator strength for the

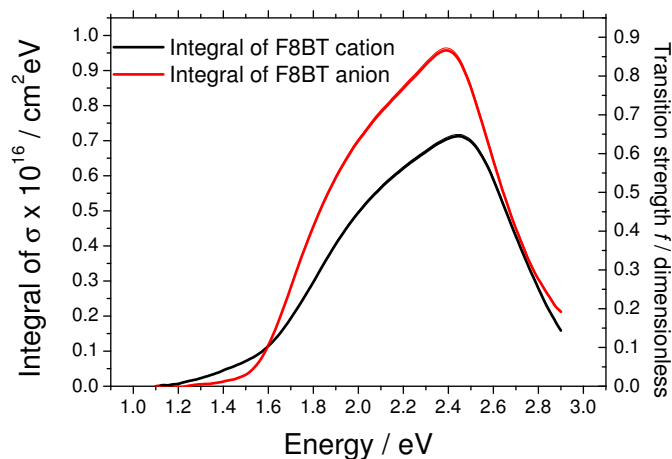


Figure 6.11: The integral of the charge absorption cross section spectra for F8BT cations and anions, also scaled to the transition oscillator strength.

9-unit oligomer for the neutral absorption is about twice that of the 5-unit oligomer. The predicted spectra for both the two different length oligomers show significant differences between the cation and anion absorptions with a common feature in both cases being a dominant cation absorption and a number of weaker similar strength anion absorptions. This contrasts with previous calculations for polythiophenes where only two transitions are predicted, or three when neighbouring molecules interact¹⁸⁸ and is a consequence of the donor-acceptor nature of F8BT. The transition strengths show very good agreement with the experimentally determined values. This represents a qualitative agreement with what was observed experimentally but the expected range of conjugation lengths in the disordered F8BT film make it impossible to correlate it to a calculation performed on a single oligomer.

6.2.9 Comparison with chemical doping

The absorption spectra of F8BT radical cations has been obtained independently through the chemical doping of F8BT films with nitrosonium tetrafluoroborate (NSTB) by Ford¹⁹³ and is compared to that obtained through CMS in figure 6.13. There are two main differences between these types of measurements. Firstly, in the doping case, all charges are measured instead of just mobile ones as in the CMS experiment. Secondly the dopant molecules can induce a larger degree of energetic disorder due to electrostatic interactions.¹⁹⁵ It may be a combination of these factors that cause the broadening and slight blue-shift of the spectra in the case of the doped film. The doped film also still contains

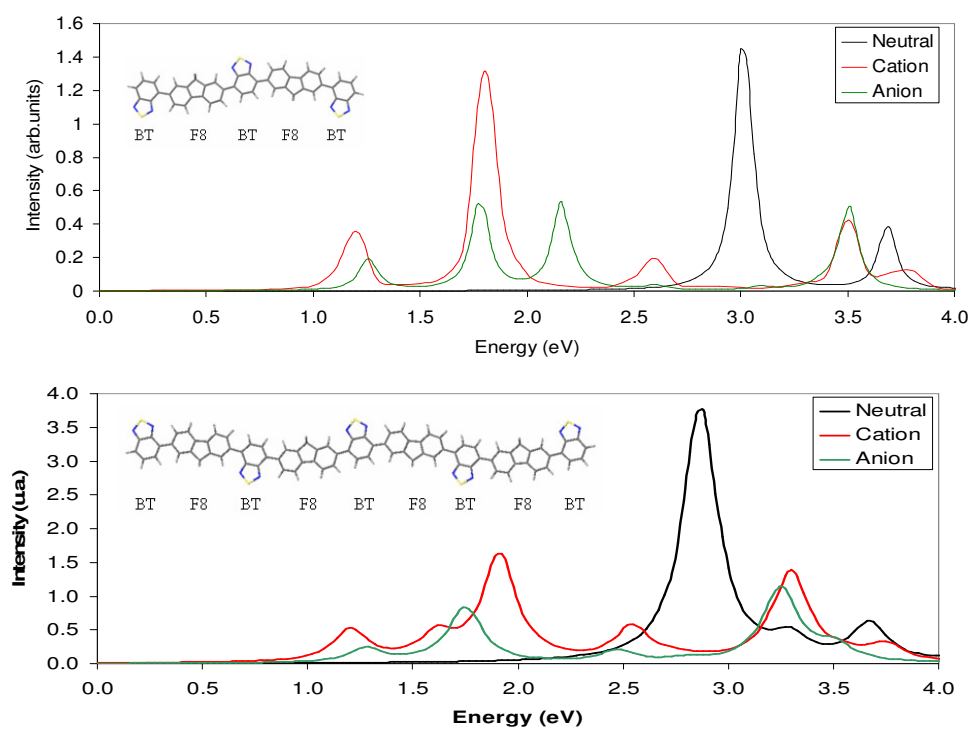


Figure 6.12: Predicted optical absorptions using quantum chemical calculations of 5 and 9 repeat unit F8BT oligomers (calculated by Dr. Vincent Lemaur).

Species	Excited state	Energy / eV	Configurations	Oscillator Strength
5-unit oligomer				
Neutral	ES1	3.01	70% H \rightarrow L	1.93
Cation	ES1	1.18	71% H \rightarrow P1 15% P1 \rightarrow P2	0.50
	ES2	1.72	78% P1 \rightarrow P2	0.01
	ES3	1.81	73% P1 \rightarrow P2 13% H \rightarrow P1	1.76
Anion	ES1	1.26	71% P2 \rightarrow L	0.22
	ES2	1.30	70% P2 \rightarrow L+1	0.02
	ES3	1.78	80% P1 \rightarrow P2	0.67
9-unit oligomer				
Neutral	ES1	2.87	42% H \rightarrow L 20% H-1 \rightarrow L+1	3.80
Cation	ES1	1.20	32% H-2 \rightarrow P1 28% H \rightarrow P1 13% P1 \rightarrow P2	0.47
	ES2	1.45	68% H-1 \rightarrow P1	0.00
	ES3	1.61	44% P1 \rightarrow P2 38% H \rightarrow P1	0.36
	ES4	1.91	33% P1 \rightarrow P2 30% H-2 \rightarrow P1	1.57
Anion	ES1	1.28	66% P2 \rightarrow L+2	0.19
	ES2	1.30	62% P2 \rightarrow L+3	0.02
	ES3	1.75	87% P1 \rightarrow P2	0.82

Table 6.1: Table with the details of the optical transitions to the various excited states of the F8BT cation and anion for both the 5 and 9-unit oligomers (calculated by Dr. Vincent Lemaire). The optimised excited states are formed by various configurations of electrons going between various levels as calculated in the ground states. P1 and P2 are the two charge-induced states in the band gap with H and L labelling the HOMO and LUMO states and those below and above.

a large number of neutral F8BT units with an absorption tail that could be skewing the charge-absorption spectra. Despite these differences, both methods seem to indicate a relatively broad absorption in the region of 1.6-1.8eV and probable further absorption at higher energy with lower transition strength.

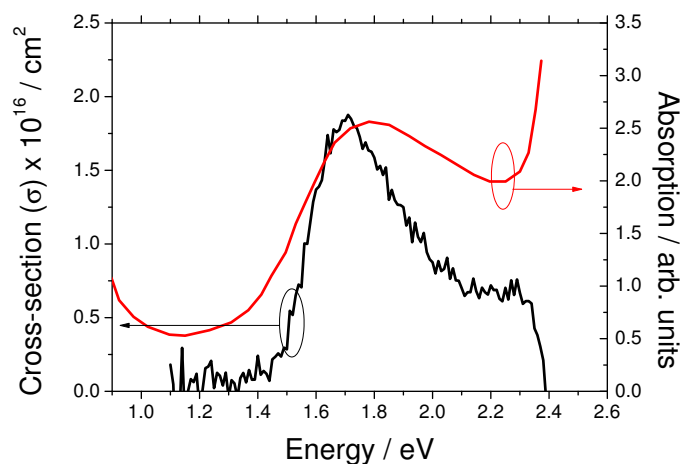


Figure 6.13: A comparison between the F8BT cation measured with CMS and from a NSTB-doped F8BT film.¹⁹³

6.2.10 Bias stress and the effect of light

Whilst the charge modulation scan is predominantly designed to measure the absorption of mobile charges on conjugated polymers, the simultaneous electrical characterisation also gives us information about charge trapping and the way that light interacts with trapped charge. Typically during a scan, the number of charges that go on and off the device decays with time, or equivalently the threshold for accumulation shifts to higher gate voltages. In the case of F8BT, we see that for both electron accumulation and hole accumulation the capacitance can recover when energy gap light is shone on the device as seen in figure 6.14.

There are a number of possible causes for this increase in capacitance including the direct generation of charges following light absorption, the detrapping of charges that had been previously been trapped or light-assisted injection into the semiconductor from the metal. Direct detrapping of charges can be ruled out as the effect occurs following energy gap absorption rather sub-gap absorption of the polaron. The increase in capacitance with energy gap appeared to be particularly pronounced in device B25-d6b, as shown in figure

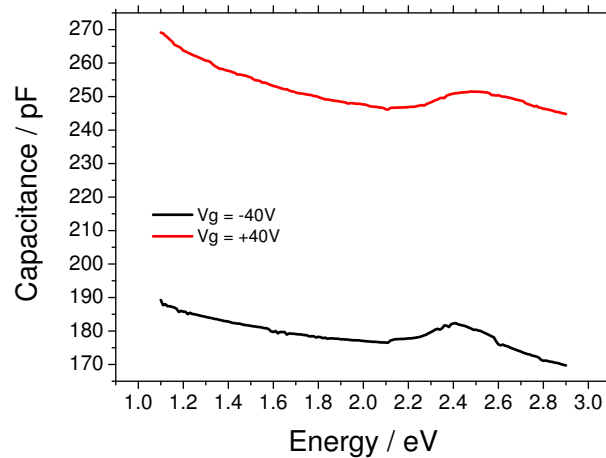
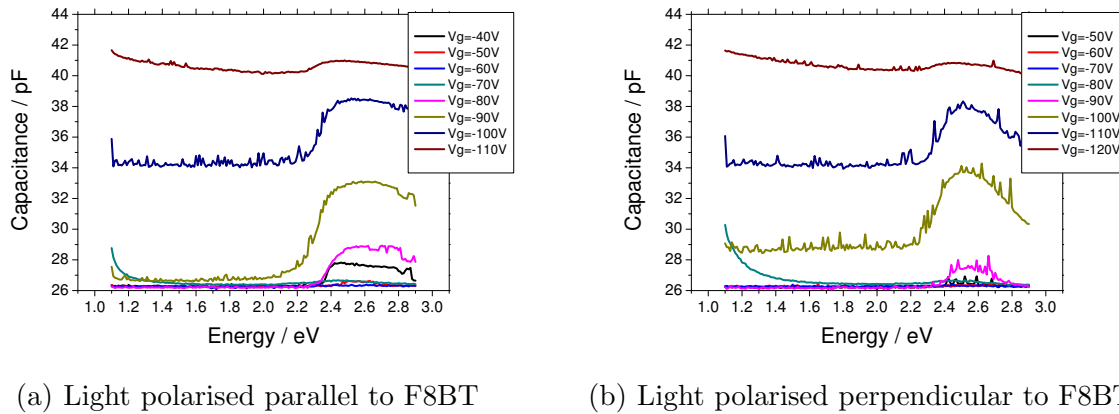


Figure 6.14: Capacitance (from $Im(\mathbf{Y}/\omega)$) of F8BT transistor B17-d7b (7nm Au source-drain electrodes/20nm F8BT/170nm PMMA/Al gate) measured during a CMS scan in both hole and electron accumulation. Scan runs from low to high energy indicating that device stresses during operation but recovers partially with energy gap light.

5.28(b), in which the semiconductor layer was made thicker than usual to allow alignment of the polymer. The CMS behaviour indicated a large contact resistance and transfer characteristics showed significant hysteresis that is thought to be related to injection rather than trapping at the dielectric interface as the same device structure with thinner F8BT shows good transistor performance. Figures 6.15(a) and 6.15(b) show the capacitance as measured during CMS scans at various gate voltages during hole accumulation when the incident light was polarised parallel or perpendicular to the F8BT alignment direction. The striking similarity between the two sets of data, even though the aligned F8BT in the channel does not absorb perpendicularly polarised light, gives irrefutable proof that the unaligned F8BT on the contacts is where this effect is occurring.

To further investigate the origin of light-induced recovery in capacitance, time-resolved capacitance measurements were performed where the device would be illuminated for a period of time during an electrical measurement with a particular gate voltage and modulation. This was done to get an idea of time response and reduce the possibility of threshold shifts being caused by prolonged gate bias stressing during the full capacitance versus gate voltage scans. In figure 6.16(a) it can be seen that upon illumination at 10.5 seconds (± 1 second) the capacitance measured on device B25-3b (see figure 5.28(a)) rises rapidly for a range of gate voltages. With the lock-in amplifier time constant of 300ms, we can expect the lag in the lock-in to limit the apparent time response to between 1.5 and



(a) Light polarised parallel to F8BT

(b) Light polarised perpendicular to F8BT

Figure 6.15: The effect of light on the capacitance (from $Im(\mathbf{Y}/\omega)$) of aligned F8BT device B25-d6b (5.28(b)) during CMS scans showing identical behaviour regardless of the polarisation of the light relative to the F8BT alignment. The fact that alignment only occurs in the channel and not on the electrodes indicates that the region above the electrodes is where light is having the effect.

3 seconds. Whilst measuring a time response with a low frequency modulation technique cannot give accurate response times we can see qualitatively that the response is faster at higher gate voltages and faster for holes than electrons; in fact the light exposure time was increased to 20 seconds for electrons to ensure that the current was fully saturated as seen in figure 6.16(b). The fact that the capacitance takes a significant time to decay to pre-exposure levels indicates that the effect is not caused by the generation of free charges enabling the accumulation layer to respond to driving gate voltage or by the assisted injection from the metal to the semiconductor. The remaining explanation is the detrapping of charges which then slowly become trapped again. It is therefore logical that trapping in the thick F8BT layer above the contacts is responsible for the observed hysteresis in this device.

By taking snapshots of the capacitance before, during and after light exposure we can see that for holes the light causes a rigid shift in the capacitance versus gate voltage plot to less negative gate voltages. In this device, electron injection was very poor as seen by the shallow slope of capacitance against gate voltage in the dark. Upon exposure to energy gap light, the shape of the CV plot changes and becomes very similar to that of holes. By plotting the recovery in terms of the shift of the threshold for hole accumulation in figure 6.16(b) the time constant for the re-trapping of charges can be seen to be approximately 15 seconds.

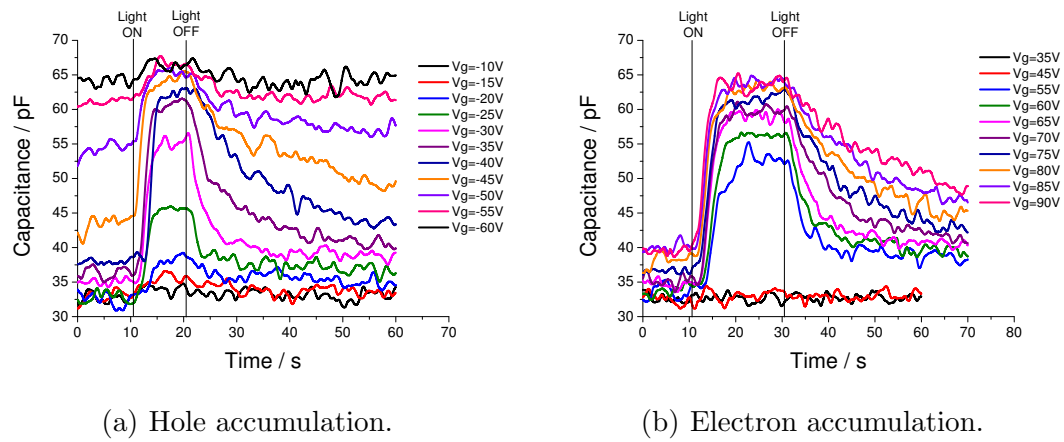


Figure 6.16: Increase and decay of capacitance for hole and electron accumulation in F8BT device B24-2a (5.27(b)) as a function of time upon illumination with 477nm energy gap light for a period of 10 seconds and 20 seconds respectively. The time constant of the lock-in was 300ms and 5-10 time constants are typically required to respond to changes.

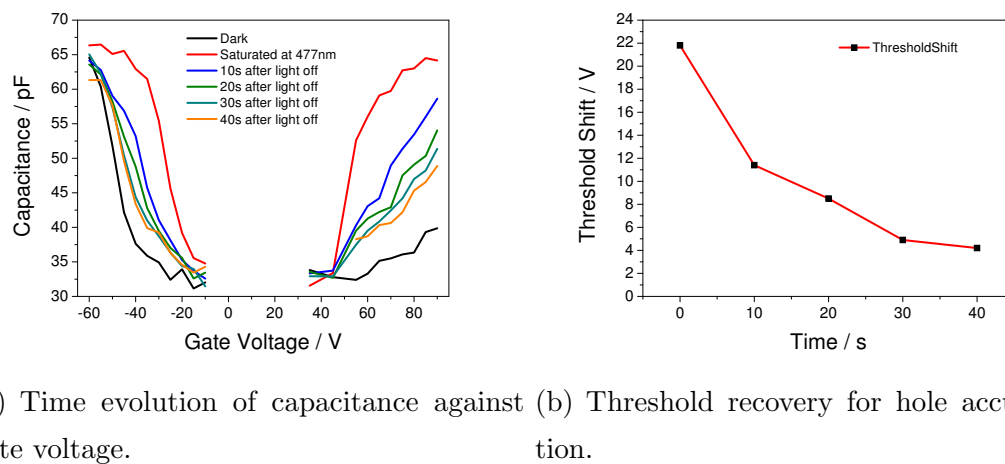
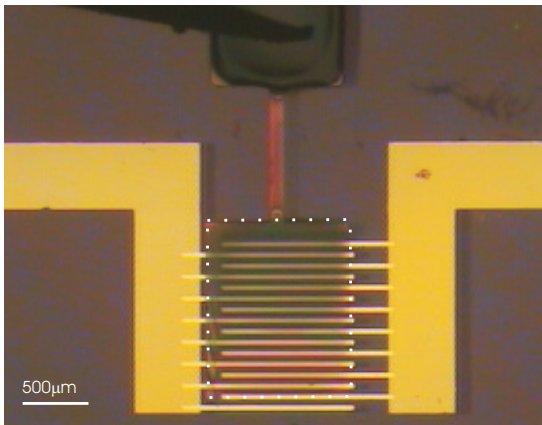


Figure 6.17: Analysis of data from figure 6.2.10 to illustrate the change in shape of the capacitance against gate voltage under illumination and the evolution of the decay when the light is turned off.

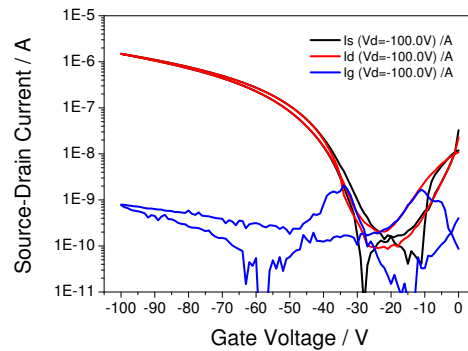
The change in the shape of the electron accumulation in figure 6.17(a) indicates that the light may not just be removing a trapped charge density which would produce a rigid shift in the capacitance. The increase in the slope of the capacitance with gate voltage under illumination could suggest that the light is increasing the mobility of the electrons in the bulk of F8BT. This concept of energy transfer from excitons to charges in low mobility states to have the effect of increasing mobility has been investigated by Reynaert et al.¹⁹⁶ and would be closely correlated with a reduction in the photo-luminescence efficiency in the presence of charges. Indeed, quenching of the luminescence by charges was observed in some devices and is explored together with photocurrent in the next chapter.

6.3 F8 CMS

With the methods for measuring CMS spectra with PEDOT:PSS-gated devices established in the case of F8BT transistors, an identical device was made with F8 as the semiconductor as shown in figure 6.18(a). The thickness of the PEDOT:PSS on the gate is difficult to control precisely and this device has a particularly thin layer. The transfer characteristics are shown in figure 6.18(b) and reveal very little hysteresis although has severely limited electron injection.



(a) Device B24-5a: Au(80nm) / F8BT(20nm) / PMMA(500nm) / PEDOT:PSS. $W=1.36\text{cm}$, $L=40\mu\text{m}$, $A_{\text{gate}} = 1.36 \times 10^{-2}\text{cm}^2$, $A_{\text{electrodes}} = 5.9 \times 10^{-3}\text{cm}^2$.



(b) Device B24-5a $\mu_h = 3.1 \times 10^{-4} \pm 1 \times 10^{-5}\text{cm}^2/\text{Vs}$.

Figure 6.18: F8 device used for CMS.

It should be noted that the solvent, n-butyl acetate, used for depositing the dielectric layer, PMMA, is known to induce a change in the properties of F8 films. When F8 is spun

from xylene, it is predominantly in the disordered glassy α phase however, if spun from other solvents¹⁹⁷, exposed to certain solvent vapour¹⁹⁸ or experiences heat treatment¹⁹⁹, the β phase can be induced. The β phase can be characterised by a “planar zig-zag” or 2_1 helix conformation²⁰⁰ with a longer conjugation length and increased interchain interactions.¹⁹⁷ A red shifted photo-luminescence spectra with well resolved vibronic structure is characteristic of the formation of the β phase although studies show that this is an intrachain ordering effect rather than interchain.²⁰⁰ The photo-luminescence spectrum shows significant changes when β phase is present due to exciton transfer to these regions²⁰¹ whereas the absorption spectrum only shows a small low energy peak or shoulder.²⁰² Such features were observed in figure 6.19 in control films of F8 in this work that were either measured as-spun, following annealing over the melting temperature and following the subsequent spinning of PMMA from n-butyl acetate. The CMS measurements on F8 in this work are therefore on films with a degree of β phase present.

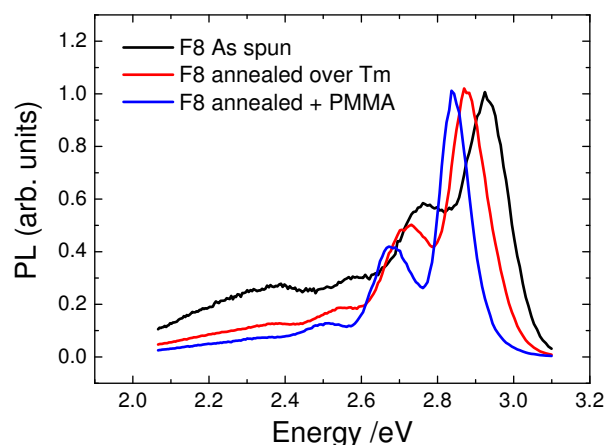
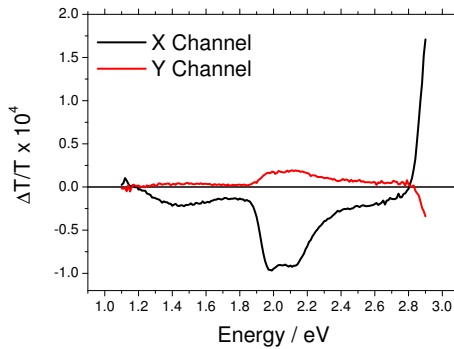
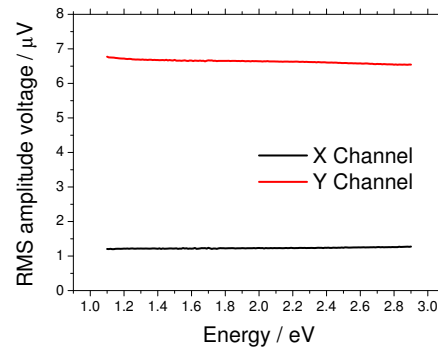


Figure 6.19: Photoluminescence spectra for F8 films after various stages involved in processing the equivalent transistor.

The typical raw data from a CMS measurement on an F8 device is shown in figure 6.20. The onset of bleaching of the neutral absorption is observed but the main feature is out of the range of this experiment due to the large energy gap in F8. There is a single prominent charge absorption in the region of 2.0-2.2eV and a feature at lower energy that is predominantly from PEDOT.

The electrical measurement during the scan shows that for hole accumulation the device is very stable with little sign of trapping occurring. Trapping during electron accumulation is so severe that only a few scans can be performed on any given device

(a) $\Delta T/T$ in hole accumulation.

(b) Lock-in measurement used to determine number of charges being modulated on device.

Figure 6.20: Raw measurements of $\Delta T/T$ and the voltage across the 130 resistor between the (shorted) source and drain contacts and ground. Scans performed with $V_{pp}=10V$, $V_g=-60V$ and at 37Hz on F8 device B24-d5a (6.18(a)).

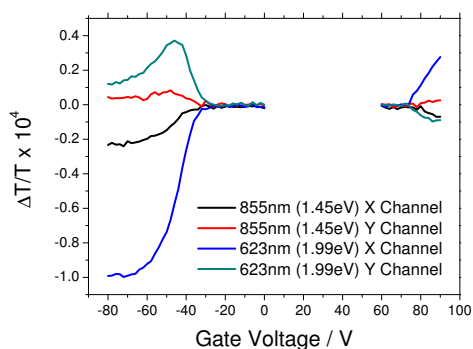
before electron accumulation is unobtainable.

6.3.1 Gate voltage dependence of charge-induced absorptions

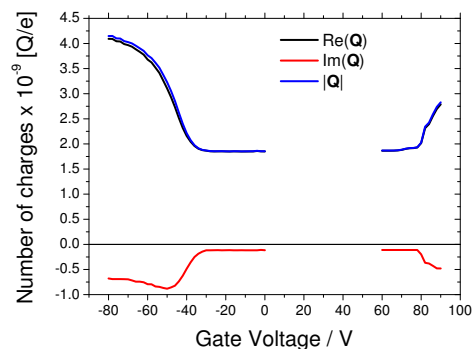
To confirm the origin of the sub-energy gap features seen in figure 6.20(a) CMS measurements were taken at 855nm (1.45eV) and 623nm (1.99eV) as a function of gate voltage. Figure 6.21(a) shows $\Delta T/T$ at both of the wavelengths used showing that full accumulation is reached for holes. In contrast, only a small amount of accumulation is observed for electrons. The fact that the phase of $\Delta T/T$ measured at 855nm is the same for both hole and electron accumulation confirm that this low energy feature is from PEDOT. The conversion of the electrical measurements into the number of charges being modulated on the device is shown in figure 6.21(b) and is used to calculate the cross section spectra using all three methods at 855nm and 623nm as shown in figures 6.21(c) and 6.21(d) respectively.

The fact that all three methods converge on exactly the same value for hole accumulation validates the theory behind the methods. However, in electron accumulation the cross sections do not converge although Method 1 gives a constant value whilst the other two continue to rise with gate voltage.

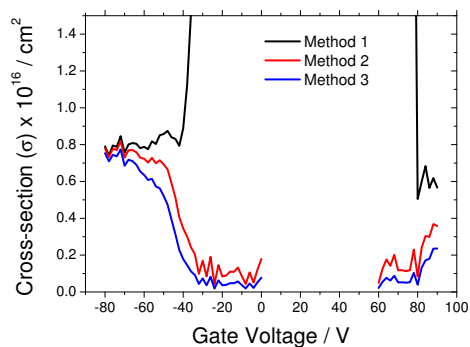
An interesting feature of the F8 cation spectrum is the double peak that makes up the only charge-induced absorption. The gate voltage dependence of this feature was



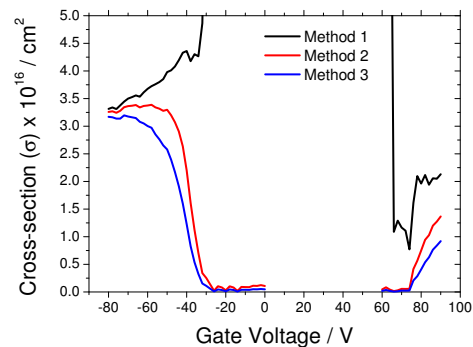
(a) $\Delta T/T$ at 855nm (1.45eV - PEDOT) and 623nm (1.99eV - F8 polaron).



(b) Number of charges on the device as a function of gate voltage.



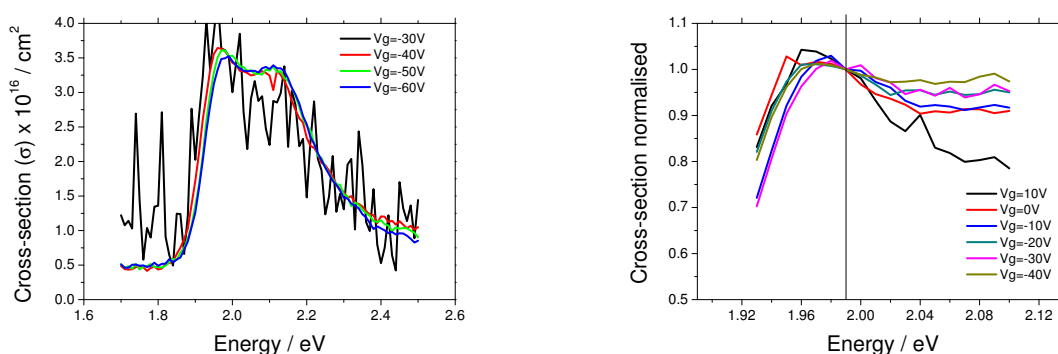
(c) Calculated cross section at 855nm (1.45eV) where the PEDOT feature dominates.



(d) Calculated cross section at 623nm (1.99eV) where the F8 polaron absorption dominates.

Figure 6.21: Analysis of the evolution of the features in the F8 cation spectrum at 855nm (1.45eV) and 623nm (1.99eV) as a function of gate voltage measured on device B24-d5a (6.18(a)). Good hole injection shows that all three methods for calculating the cross section converge.

investigated in figure 6.22(a). The peaks were normalised to the value at 1.99eV and show that as the gate voltage reduces, the size of the higher energy peak reduces relative to the lower energy one. This experiment was repeated in a narrow energy range around the lower energy peak at a later time and again showed the flat top of the two peaks gradually lowering on the high energy side at lower gate voltages. It is expected that the double peak feature is an indication of a charge residing in the ordered β phase which suggests that the proportion of charges in the α and β phases is dependent on charge density.



(a) Evolution of the entire absorption.

(b) Close look in the vicinity of the lower energy peak.

Figure 6.22: A close look at the evolution of the F8 cation absorption with gate voltage in device B24-d5a (6.18(a)). Both plots are normalised to the peak at 1.99eV in full accumulation.

6.3.2 Frequency response

The frequency dependence of the F8 cation absorption was investigated and is shown in figure 6.23 after being normalised to the peak at 1.99eV. As with F8BT there does not appear to be any clear trend with frequency. The spectrum that was collected at 37Hz was taken at a slightly different time and further into accumulation which explains why the higher energy peak is larger in that case as observed in the previous section.

6.3.3 Obtaining corrected spectra

To correct the F8 cation spectrum for the PEDOT feature a different magnitude of the cross section was required compared to the F8BT devices made at the same time. As

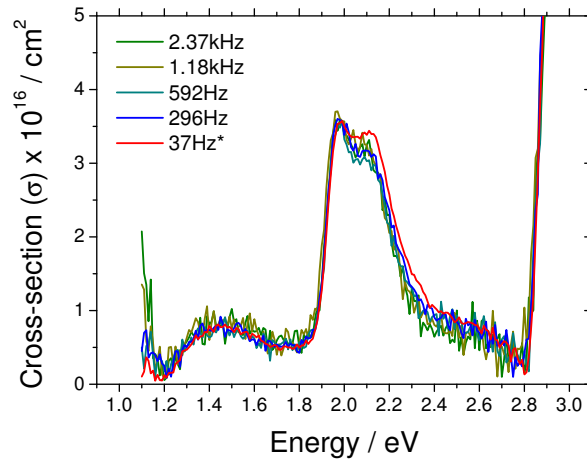
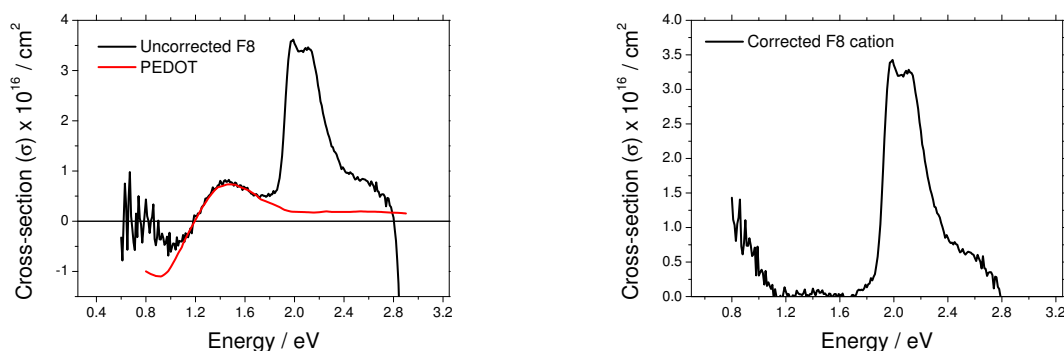


Figure 6.23: Evolution of the charge-induced absorption in F8 device B24-d5a (6.18(a)) with frequency measured with $V_{pp}=10V$. *The 37Hz trace was performed at a higher gate voltage and may reflect the gate voltage dependence rather than frequency dependence.

shown in figure 6.24(a), the PEDOT could neither have been more or less than the value given to it without resulting in a negative F8 charge absorption at some point. This indicates that there is no absorption from F8 in this region at all and it is purely the PEDOT that was being measured. The difference in the size of the PEDOT feature compared the the other two devices is possibly due to the fact that the PEDOT layer was a lot thinner which may affect the levels of doping at the interface as water can dedope PEDOT and could diffuse into the layer when the sample is mounted. The thinner PEDOT layer also explains why it was possible to extend the spectra further into the IR region which is normally too noisy due to strong absorption from the PEDOT. The PEDOT spectrum was extended into this range based on analysis of a PEDOT spectrum obtained from electrochemical doping.²⁰³

The corrected F8 cation cross section spectrum is shown in figure 6.24(b) which remains largely unchanged in the region of interest but shows the beginning of the lower energy peak that is expected with polaron absorptions.

Obtaining the F8 anion spectrum was made difficult by the combination of large contact resistance and rapid charge trapping. Figure 6.25(a) shows the noisy $\Delta T/T$ spectrum in electron accumulation. By comparing the $\Delta T/T$ spectrum with the phase of the charge (relative to depletion) on the device it can be seen that at the start of the scan the charges show up in the X channel of $\Delta T/T$ and real part of \mathbf{Q} before rotating into the Y channel of $\Delta T/T$ and the imaginary part of \mathbf{Q} in the region of the F8 anion



(a) F8 cross section spectrum with PEDOT spectrum.

(b) Corrected F8 spectrum.

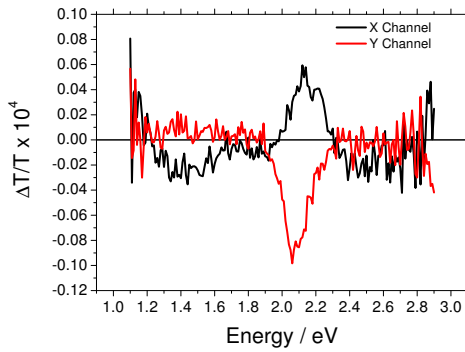
Figure 6.24: Method to remove the PEDOT feature from the F8 cation absorption. The PEDOT feature was found experimentally (see figure 5.30(b)) and extrapolated to lower energy using electrochemical data²⁰³. The PEDOT spectrum was scaled to the only possible size that leaves behind F8 absorptions of the correct sign.

absorption before rotating back again. In principle, the method of calculating the cross section should allow for this but with such small signals the spectra can become distorted and noisy. The cross section spectra for the F8 anion calculated using Method 1 is given in figure 6.25(b) with the PEDOT spectrum that was used for correcting the F8 cation. The corrected F8 anion spectrum is given in figure 6.25(d).

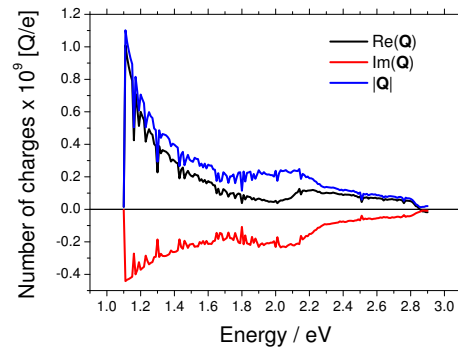
In order to get a better quality spectrum, the experiment was repeated just in the region of the charge absorption and performed with a drain bias of 5V applied. The spectra was then normalised to the point at 1.99eV as measured in figure 6.21(d) using Method 1 before having the PEDOT spectrum removed. Figure 6.25(e) shows the increased charge on the device using this method although even in this short range significant decay is observed. The final corrected spectra is given in figure 6.25(f) which shows a single peak centred at 2.07eV. It was not possible to extend the anion spectra into the IR due to the very small signal from the small number of charges that could be accumulated.

6.3.4 Analysis of charge-induced spectra

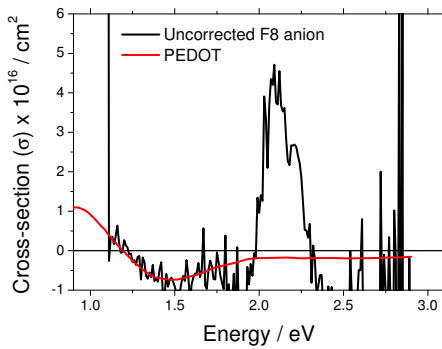
Comparing the F8 cation and anion spectra in figure 6.26 shows that both have a single absorption with a very similar energy and width indicating the similarity between the wavefunctions. The size of the peak is around 75% larger than the peak observed in F8BT although it is also much narrower. In terms of overall oscillator strength, the



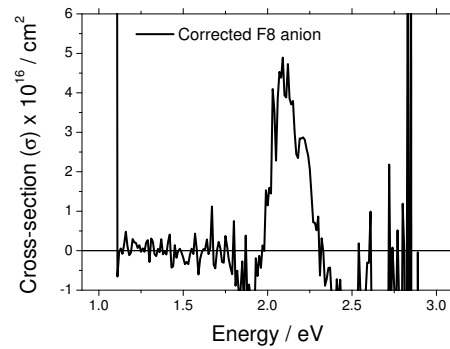
(a) $\Delta T/T$ in electron accumulation ($V_g=70V$, $V_{pp}=10V$, $f=37Hz$).



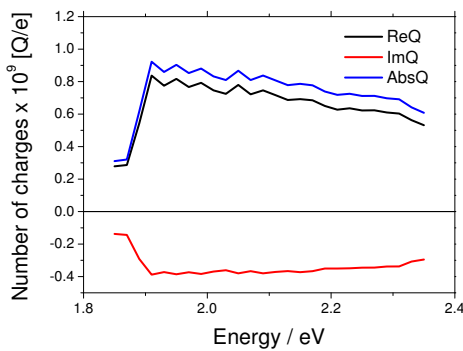
(b) Number of charges on device during CMS scan.



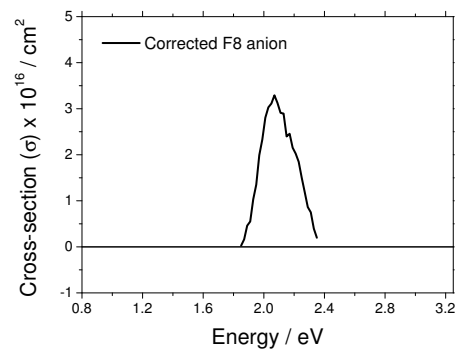
(c) F8 anion cross section and PEDOT spectrum calculated using Method 1.



(d) Corrected F8 anion cross section spectrum.



(e) Electrical measurement of number of charges on device when operated with a drain voltage of +5V and gate voltage of 100V.



(f) Cross section calculated in narrow energy range with drain voltage of +5V applied during scan. Cross section was normalised using figure 6.21(d) and then the PEDOT feature was subtracted.

Figure 6.25: Techniques used to obtain the F8 anion spectrum using device B24-d5a (6.18(a)). Taking a full scan of the entire range resulted in a noisy spectrum due to rapid electron trapping. The gate voltage was increased further, the wavelength range reduced and a drain voltage used to obtain a clean absorption peak.

integral of the F8 cation spectra above 1.2eV, given in figure 6.27, reveals an oscillator strength of 1.32 which becomes 2.64 when taking account of the fact that unpolarised light was used. The ability to resolve the double peak in the cation spectra may indicate that all the charged species being measured have electronic states of similar energy leading to the conclusion that the charges are in an ordered region where the polaron wavefunction is not limited by twists and kinks which would change the energy of the optical transition. The physical origin of the double peak could be from the coupling of the electronic state to vibronic modes, the splitting of a single peak due to intermolecular electronic coupling or simply a feature of the electronic state itself. An apparent double peak seen in a chemical doping experiment¹⁶⁶ would appear to discount intermolecular effects as the origin of the double peak in this case. The two peaks are located at 1.98eV and 2.11eV giving a spacing of 130meV which would correspond to 1048cm^{-1} in wavenumber as the spacing of vibronic levels of the cation. As a comparison, the spacing of the peaks in the photo-luminescence spectrum from the neutral excited F8 is 170meV or 1371cm^{-1} which is close enough to make the vibronic argument plausible.

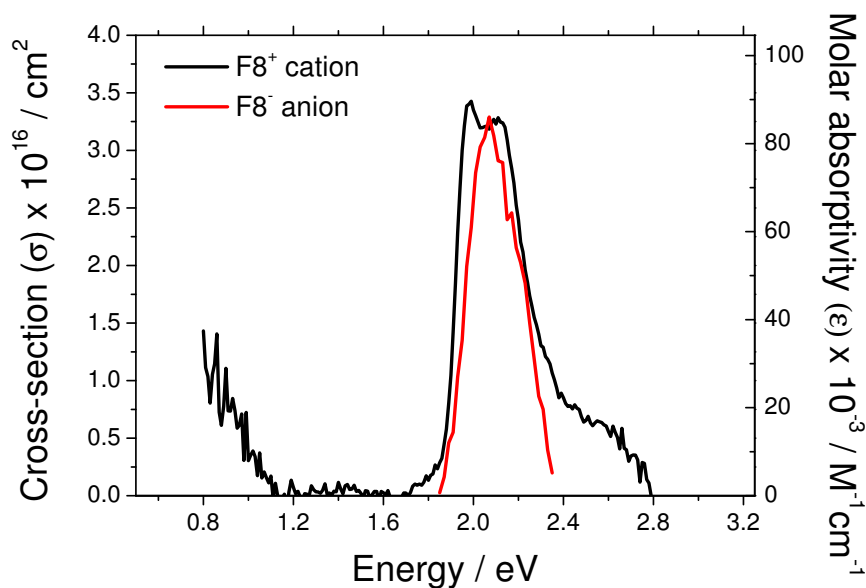


Figure 6.26: Final corrected F8 cation and anion absorption spectra from device B24-d5a (6.18(a)).

The lack of the double peak in the anion spectra could be due to the fact that the spectrum was taken when the device was barely into accumulation. As was seen with the cation spectrum, when the device is barely in accumulation, the high energy peak reduces

relative to the lower energy one. There is a slight shoulder to the anion peak which could be the early stages of a higher energy peak. It is reasonable to assume that in both cases charges first go into disordered regions at low charge densities. In more ordered regions, conjugation lengths are expected to be longer and therefore the energy of the polaronic levels are expected to be deeper into the band gap. The fact that the first charges seem to go into disordered regions may therefore require an alternative explanation and could be due to charges spending on average more time in low mobility disordered regions.

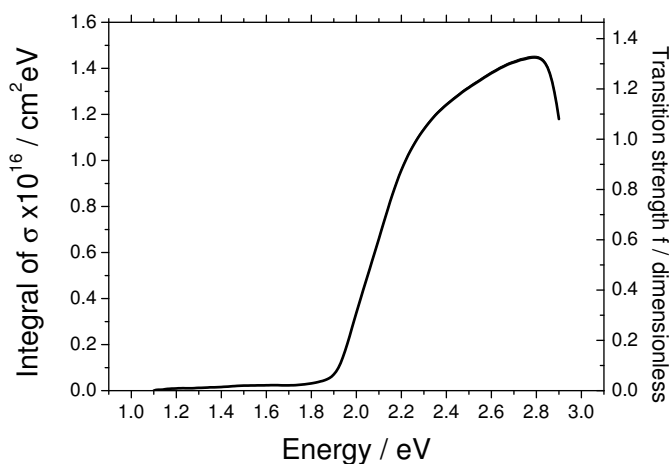


Figure 6.27: Integral of the F8 cation spectra also scaled to the transition oscillator strength.

The optical transitions of the F8 cation and anion as predicted from quantum chemical calculations are given in figure 6.28 with details in table 6.2. As expected theoretically, the quantum chemical calculations predict almost identical optical transitions both in oscillator strength and energy for the anion and cation. Whilst the energies are higher due to being calculated in the gas phase, there is very good agreement with the measured spectrum in terms of the number of transitions and the relative energies.

6.3.5 Comparison with charge-induced absorptions from pulse radiolysis

The anion and cation absorption spectrum in F8 has been measured using pulse radiolysis where high energy electrons ionise solvent molecules leading to charge transfer to F8 in solution.¹⁶⁶ The main absorption peaks appear to be slightly higher in energy relative to the CMS case which is most likely due to the experiment being performed in solution

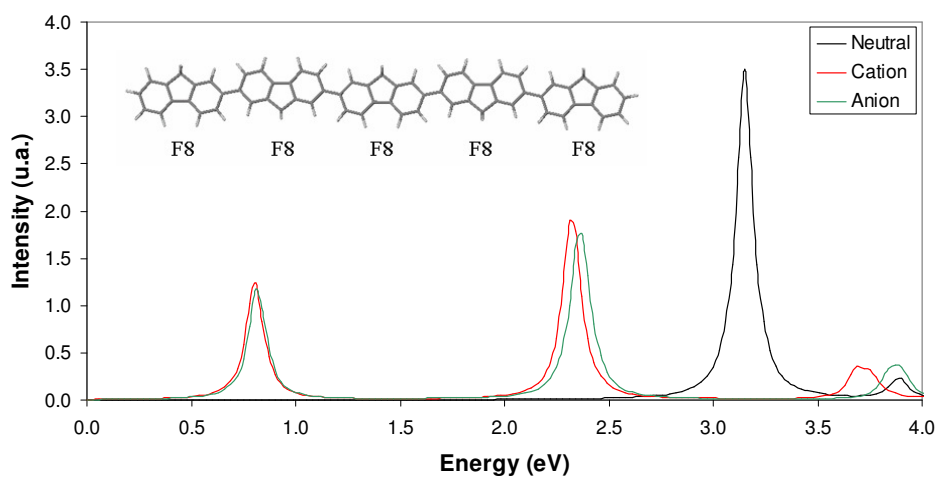


Figure 6.28: Predicted optical absorptions using quantum chemical calculations of a 5 repeat unit F8 oligomer.

Species	Excited state	Energy / eV	Configurations	Oscillator Strength
Neutral	ES1	3.15	52% H \rightarrow L 22% H-1 \rightarrow L+1	2.50
Cation	ES1	0.84	67% H \rightarrow P1 23% H-2 \rightarrow P1	1.26
	ES4	2.32	72% P1 \rightarrow P2	1.96
	ES5	2.39	91% H-3 \rightarrow P1	0.09
Anion	ES1	0.82	64% P2 \rightarrow L 27% P2 \rightarrow L+2	1.19
	ES5	2.35	64% P1 \rightarrow P2 12% P2 \rightarrow L+4 10% P2 \rightarrow L+2	1.55
	ES6	2.40	80% P2 \rightarrow L+4	0.48

Table 6.2: Table with the details of the optical transitions to the various excited states of the F8 cation and anion of the 9-unit oligomer. The optimised excited states are formed by various configurations of electrons going between various levels as calculated in the ground states. P1 and P2 are the two charge-induced states in the band gap with H and L labelling the HOMO and LUMO states and those below and above.

rather than in a thin film. The size of the peaks is also smaller in the solution case which could be explained by the F8 units being randomly orientated in three dimensions compared to being confined to a two dimensional film in the case of CMS experiments. Such geometric arguments would lead to the cross section in solution being two thirds that in a film which is close to what is observed here.

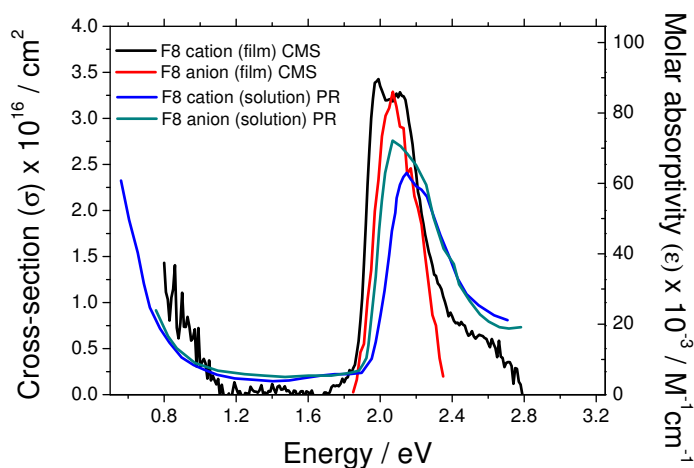


Figure 6.29: A comparison between the F8 cation and anion spectra as measured in this work with CMS and those measured using pulse radiolysis in solution. ¹⁶⁶

6.3.6 Bias stress and the effect of light

The F8 devices showed interesting behaviour during bias stress under illumination which was best illustrated in a device with both gold and aluminium electrodes shown in figure 6.30(a). Whilst this device had an unpatterned metal gate and so did not give a correct CMS spectra, the aluminium electrodes enabled significant injection of electrons making it easier to track the behaviour. The frequency response of the capacitance is given in figure 6.30(b) which demonstrates the ability for the electrode configuration to inject both holes and electrons. Figure 6.30(c) reveals that during electron accumulation the capacitance rapidly decays when the device is illuminated with light in the wavelength range where either the polaron or the neutral polymer absorb. In contrast, in hole accumulation the capacitance just decays gradually and is independent of the illumination wavelength. The reduction in capacitance during a CMS scan is the result of a shift in the threshold for accumulation due to charge trapping. Figure 6.30(d) shows the capacitance as a function of gate voltage before and after CMS scans for hole accumulation and electron

accumulation revealing a significant threshold shift associated with electron accumulation. Regardless of what gate voltage was used, the device would be in depletion by the end of the scan.

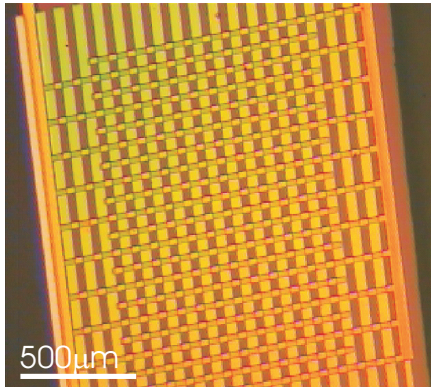
With a smaller electron affinity as compared to F8BT, F8 is already very unstable with respect to electron accumulation although when processed in inert conditions and measured in vacuum electron transport is possible. It seems that the excited charged state is unstable even in vacuum when under illumination with wavelengths less than 620nm which includes the yellow light in most testing rooms. This could also lead to electron trapping when running an F8 device in light-emitting mode where the electroluminescence could enhance the trapping. This behaviour of F8 is significantly different to that of F8BT where it is only energy gap light that causes any effect and that this effect is the detrapping of charges of both species.

6.4 Summary

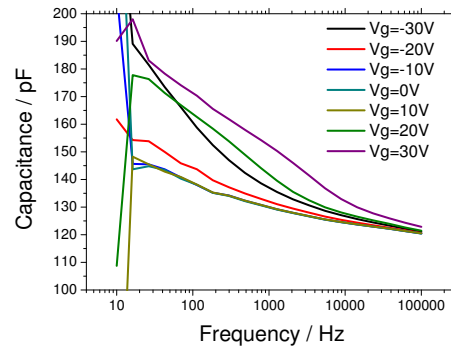
The anion and cation absorption cross sections have been measured for both F8 and F8BT. In F8BT a broad absorption was seen for both the cation and anion which could not be characterised with two or three Gaussian line shapes. The strong dependence of the predicted spectra on the number of repeat units offers an explanation into the broadened spectra that were observed indicating significant disorder in the film. There were significant differences between two charged species with the oscillator strength of the cation absorption being larger than that of the anion and peaking at a lower energy in good agreement with the calculated absorptions. There was a difference in the bleaching of the neutral absorption for the cation and anion although not enough to point to a significant difference in size of the charge species.

In the case of F8 the cation absorption was narrower in energy and made up of two well defined peaks indicating that the polarons resided in an ordered region of the film. It is known that the β phase exists in these films and it is suggested that this planar, long conjugation length phase is responsible for the cation spectra at high gate voltages. At lower gate voltages the higher energy peak begins to disappear which suggests that charges reside in different regions of the polymers at different charge densities. The anion spectra was obtained when the device was only just into accumulation which could explain the lack of the double peak feature although the energy, width and magnitude of the absorption were very similar to that of the cation.

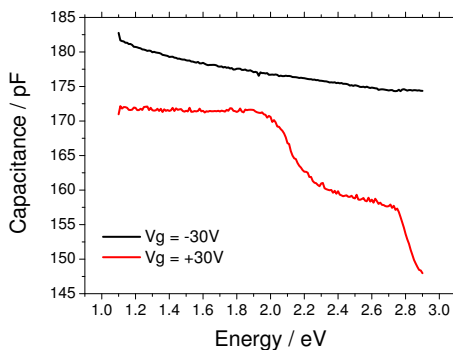
The comparison of the anion and cation absorptions in F8 and F8BT confirm the picture of symmetry breaking due to the presence of heteroatoms in conjugated polymers.



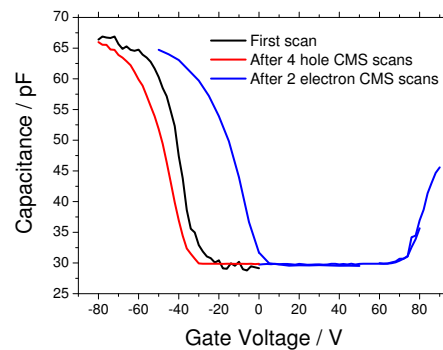
(a) Device B18-d12a Au(40nm) / Al(20nm) / F8BT(20nm) / PMMA(260nm) / Al(8nm). Au electrodes fabricated with photolithography and Al electrodes evaporated with TEM grid.



(b) Capacitance as a function of frequency for various gate voltages on device B18-d12a.



(c) Capacitance measured during CMS scan for device B18-d12a in both hole and electron accumulation.



(d) Capacitance as a function of gate voltage measured on device B24-d5a before and after CMS scans.

Figure 6.30: Examples of the effect of continuous bias stress on F8 devices under illumination. Devices stress rapidly in electron accumulation with wavelengths where both the charged and neutral F8 absorb.

This is the first time that this type of measurement has been performed and will serve as a useful tool in understanding differences the nature of charge transport for electrons and holes in polymers with broken particle-hole symmetry.

Energy gap light was found to detrap charges of both signs above the contact region in F8BT transistors leading to a temporary reduction in the threshold for accumulation which decays again in the dark as trapping resumes. This interaction of excitons and charges will be investigate further in the following chapter. For F8, interesting differences were observed between the cation and anion in the way that they reacted in the presence of light with the excited anion being highly susceptible to charge trapping.

Chapter 7

Exciton-polaron interactions in polyfluorenes

7.1 Introduction

In the previous two chapters two interesting observations were made regarding the interactions between excitons and charges in F8BT. Firstly, the highly efficient photoluminescence from F8BT is believed to be quenched in the presence of charges and secondly the bulk conductivity can be increased with energy gap light with this conductivity decaying slowly after the light is turned off. In this chapter, the photocurrent and photoluminescence quenching are studied in more detail. The effect of alignment, annealing temperature and atmosphere on the photocurrent is investigated with the findings used to investigate the concept of a lateral bilayer photovoltaic device. The inspiration for this concept comes from the reduced bimolecular recombination rates observed in aligned light emitting transistors. The origin of the photoluminescence quenching is confirmed and exploited to image transistor device operation in real time shedding light on charge trapping and the obstacles for electrically pumped lasers. The remainder of this introduction summarises the extensive literature and models involved in photocurrent and luminescence quenching.

Photovoltaic devices are characterised by the ability to transfer light energy to an electron in a semiconductor and then enable that electron to exit from the semiconductor to supply a voltage to an external circuit. Upon losing potential in the external circuit the electron returns to the semiconductor on the other side. This is equivalent to saying an electron and hole are generated upon absorption of a photon and must exit the semiconductor through the opposite contacts. In order for the electron and hole to leave the device, a built-in field is required within the semiconductor although they may also diffuse out. The built-in field can arise between n- and p-doped semiconductor regions or when the semiconductor is sandwiched between electrodes with differing workfunctions. In inorganic crystalline semiconductors at room temperature, free charges are the primary species generated from absorption whilst in organic semiconductors tightly bound excitons are the primary excitation and typically a heterojunction with another semiconductor is needed to separate them in order to achieve a significant yield of free charges. The external quantum efficiency (EQE) is defined as the ratio of extracted charges to incident photons. If a device was made that did not have rectifying contacts to produce the internal field but had sufficient large injection barriers for both charge carriers then applying an external voltage would extract the electrons and holes producing a current that would saturate at the rate of charge generation. This type of device would not be able to drive an external circuit but would enable the EQE to be measured.

The situation becomes more complex in a semiconductor with ohmic contacts but

where free carriers are still generated by optical excitation. A gain effect can be seen whereby the current through the device at a given voltage can exceed that predicted by assuming you are simply sweeping out photo-generated carriers. This effect is a result of the ability to inject charge into a material which has a constant charge carrier concentration, n , maintained by a constant photogeneration rate, G , which competes with the charge carrier recombination lifetime of τ . The generation rate can be defined in terms of incident photon power, P_{opt} , if all photons are absorbed in a device of thickness D , width W and length L where a fraction η of free charges are generated.⁴³

$$G = \frac{n}{\tau} = \frac{\eta(P_{opt}/h\nu)}{WLD} \quad (7.1)$$

The resulting current can be derived from the usual current density expression, $qn\mu E$, which is the product of the charge on an electron, q , the mobility, μ and the field E . The current can be expressed in a useful form using equation 7.1

$$I_p = (q\mu n E)WD = q \left(\eta \frac{P_{opt}}{h\nu} \right) \left(\frac{\mu\tau E}{L} \right) \quad (7.2)$$

This photocurrent only differs from the primary photocurrent, I_{ph} , by the last term in brackets meaning that the photoconductive gain can be defined as

$$\text{Gain} = \frac{I_p}{I_{ph}} = \frac{\mu\tau E}{L} = \frac{\tau}{t_r} \quad (7.3)$$

which can exceed unity if the carrier lifetime exceeds the transit time through the device, t_r . This effect might not be expected in organic semiconductors due the difficulty in making ohmic contact and the fact that strongly bound excitons, not free charges, are the primary optically-excited species. Nevertheless, limited charge generation in organic semiconductors is possible with high intensity illumination due to exciton-exciton annihilation,⁵⁴ high energy illumination of the order 1eV above the energy gap,²⁰⁴⁻²⁰⁶ dissociation at metal interfaces or defects²⁰⁷ and field induced charge separation ($E > 10^6 \text{V/cm}$).⁵⁰ Injection can also be possible even despite large theoretical energy barriers from metal contacts.³² There are however other ways to explain photocurrent in organic materials without using this tractional photoconductivity mechanism.

EQEs exceeding 100% which can take seconds to decay following illumination have been observed in many single component organic devices^{208,209} indicating that photoconductive gain can be observed. Two models with slight variants have emerged to explain these effects which have been noted in co-facial, planar, transistor and capacitor structures. The first model which shows up in various forms and will be referred to as the trapping gain model. The common theme is that upon illumination some excitons end

up as mobile charges of one sign and trapped or significantly lower mobility charges of the other sign. This effect was used by Ginger et al.²¹⁰ to explain the behaviour in CdSe metal-semiconductor-metal structures where hole trapping was proposed as the cause of an increase in the number of mobile electrons in the SCLC regime upon illumination. Whether this mechanism requires the production of free carriers as an intermediate step is difficult to prove but importantly it may not require a significant efficiency of generation of free charges if trapping is strong.

Equally, in transistors with electron trapping illumination can result in a shift of the turn on for hole accumulation to positive gate voltages and a change in the shape of the subthreshold region. A number of authors divide this into a photovoltaic (TFT ON state) and photoconductive (TFT OFF state) effect. The ‘photovoltaic effect’ seems to originate from a model for GaAs and appears to be used without physical justification but the logarithmic dependence of current on illumination intensity that the model predicts looks similar to the experimentally observed dependence. Wang et al.²¹¹ also noted that the non-linear dependence of current on light intensity in the ON state can simply be modelled as a threshold shift due to reduced contact resistance. This reduced threshold due to reduced contact resistance is consistent with the behaviour found in this work in figure 6.15. In the OFF state the increase of current is simply put down to the photoconductive effect, as given in equation 7.2, which can be enhanced at higher gate voltages due to electric field assisted dissociation. Taylor et al.¹⁴⁸ goes further to propose the creation of an inversion layer of electrons due to the generation rate exceeding the trapping rate.

A mechanism that may also be significant in some cases and does not require the trapping of photo-generated charges was proposed by Arkhipov.²¹² This model will be referred to as energy transfer gain and describes the Förster Resonance Energy Transfer (FRET) from excitons to polarons that are lying in deep states. The polaron gains energy and as a result of disorder, some time passes for it to equilibrate back to the dark DOS occupancy. During this time, more mobile charges can be injected resulting in a net gain in current. FRET depends on the overlap between the PL emission and polaron absorption which is common in most polymers.

Related to this energy transfer gain model is the process of charge-induced photoluminescence (PL) quenching which has to exist if energy transfer is occurring. Quenching of PL by charges has been observed in unipolar transistors²¹³, MIM diodes,^{214–216} MIS diodes with^{217,218} and without^{219–221} scanning near field optical microscopy techniques, blends,²²² doped²²³ and electro-chemically doped films.²²⁴ The dependence on charge or more generally acceptor density is fitted with a Stern-Volmer type function.^{213,217} This equation starts by considering the rate constants for non-radiative, k_{nr} , radiative, k_r , and

charge-induced, k_{p-ex} , decay of excitons and their relationship to the PL intensity.

$$\text{PL (no charges)} \propto \frac{k_r}{k_r + k_{nr}} \quad (7.4)$$

$$\text{PL (charges)} \propto \frac{k_r}{k_r + k_{nr} + k_{p-ex}} \quad (7.5)$$

The solution to the rate of quenching for the FRET process comes from an unusual analogous problem of the coalescence of particles in a colloidal suspension where particles move with Brownian motion and coalesce if they come within a radius R_0 . The solution comes from considering the flux through a spherical surface and is referred to as the Smoluchowski relation²²⁵ given here as applied to the current problem.

$$k_{p-ex} = 4\pi n_p (D_p + D_{ex}) R_0 \left(1 + \frac{R_0}{[\pi(D_p + D_{ex})t]^{\frac{1}{2}}} \right) \quad (7.6)$$

Here, D_p and D_{ex} are the diffusion constants of the polarons and excitons respectively and R_0 is the capture radius which in this case is the FRET radius given in 2.16. The time depended part of this can be dropped if the time intervals of interest are large enough to render that term negligible²²⁵. When applied to quenching in organic systems the second term has indeed been ignored although given that $(D_p + D_{ex}) \sim 10^{-4} - 10^{-2} \text{cm}^2 \text{s}^{-1}$ and $R_0 \sim 2 \text{nm}$, $R^2/D \sim 4-400 \text{ps}$, a value is obtained which may not be insignificant relative to the exciton lifetime of $\sim 1 \text{ns}$. This process assumes 100% capture within the radius which is fairly reasonable due to the R^{-6} dependence of the FRET rate and is thus referred to as diffusion limited. In a transistor or capacitor structure where n_p is proportional to the gate voltage the equation could take this form^{213,218,226}

$$\frac{\text{PL}(V_g)}{\text{PL}_{max}} = \frac{k_r + k_{nr}}{k_r + k_{nr} + k_{p-ex}} = \frac{1}{1 + \left(\frac{k_{p-ex}}{k_r + k_{nr}} \right)} = \frac{1}{1 + \tau_0 k' (V_g - V_t)} \quad (7.7)$$

where $\tau_0 = \frac{1}{k_r + k_{nr}}$ is the exciton decay constant in the absence of charges and k' relates the gate voltage to the polaron quenching rate constant, k_{p-ex} . For clarity, equation 7.7 has been formulated here in terms of PL_{max} to allow for doping of the transistor where $\text{PL}_{max} > \text{PL}(V_g = 0)$. In the case of doping or trapping where charges do not start entering the device at exactly $(V_g = 0)$,²¹³ the extra term for threshold voltage, V_t is also added here. Without these two modifications the equation cannot be sensibly used to fit typical experimental data. Despite the documented use of this equation it should be used with care as k_{nr} can depend on other extrinsic factors such as proximity to metal electrodes or the intensity of illumination so using literature values for τ_0 may be inappropriate in some situations and introduce errors in k' .

Equation 7.7 also neglects the fact that in transistors or capacitors the charges are only at the insulator interface so does not take account of the unmodulated PL in the bulk of the device. This will be addressed later in the chapter.

The dependence of the charge density, n_p , on applied voltage may have other forms such as for space charge limited current

$$n(x) = \frac{3}{4} \frac{\epsilon_0 \epsilon}{e} \frac{V}{L^2} \sqrt{\frac{L}{x}} \quad (7.8)$$

which varies with position, x through a device of thickness, L . This becomes more complex due to the fact that illumination often modifies this current. If there is doping or photo-generation of charges to the extent that SCLC is not significant, the carrier density can be given by

$$n = \frac{J}{e\mu V/d} \quad (7.9)$$

however this equation implies a constant carrier density which is independent of voltage so perhaps should be not be applied to photodiodes where the photocurrent is non-linear with voltage.²¹⁴ This could be valid if field-dependent photo-generation alone was responsible for the increase in current upon illumination but the slowly decaying transient observed precludes this. If the non-linear behaviour was due a constant photo-generated charge density, but with non-ohmic contact resistance, equation 7.9 would also not be valid.

Perhaps a more realistic model to calculate the quenching of excitons in disordered organic semiconductors was derived by Reynaert¹⁹⁶ by considering the nature of exciton diffusion driven by spectral relaxation in an electronic density of states (EDOS) due to different conjugation lengths. In this model, exciton diffusion occurs via FRET to either other chromophores or energy acceptors at lower energy although this could equally be applied in the case of energy transfer to polarons. The density of excitons on intrinsic sites, $p_i(t)$, which reflects the unquenched exciton density at time t is given by

$$p_i(t) = \exp\left(-\frac{t}{\tau}\right) p_0(t) + \exp\left(-\frac{t}{\tau}\right) [1 - p_0(t)] \times \left(1 + \frac{4\pi}{3} r_d^3 N_d \left(\frac{t}{\tau}\right)^{1/2} \exp\left[\frac{4\pi}{3} r_d^3 N_d \left(\frac{t}{\tau}\right)^{1/2}\right] \left\{1 - \exp\left[-\frac{4\pi}{3} r_i^3 N_t \left(\frac{t}{\tau}\right)^{1/2}\right]\right\}^{-1}\right)^{-1} \quad (7.10)$$

where τ is the exciton lifetime, r_i and r_d are the FRET radii for energy transfer within the host polymer and to an energy acceptor, and N_d and N_t are the density of energy acceptor sites and the energy-integrated density of intrinsic sites respectively. Numerical integration of this function over time can lead to the quenching ratio as a function of acceptor density.

Zaupunidi⁵¹ later reformulated the derivation in a convenient steady state form with only two fitting parameters

$$B^2 = \frac{4\pi r_i^6 n}{3r_{min}^3} Q + 1, \quad C = \frac{4\pi r_d^3}{3} \sqrt{Q} \quad (7.11)$$

where r_i and r_d have the same meaning, r_{min} and n are the distance between and density of conjugated segments respectively and Q is the photoluminescence efficiency of the host polymer. The expression that can be used to fit to data as a function of acceptor density, n_q is

$$\frac{PL(n_q)}{PL_{max}} = \frac{1}{B^2 - 1} \left(\frac{B^2 + (Cn_q)^2}{1 + (Cn_q)^2} \exp \left\{ Cn_q \pi \left(\frac{1}{B} - 1 \right) \right. \right. \\ \left. \left. + 2Cn_q \left[\arctan(Cn_q) - \frac{\arctan(Cn_q/B)}{B} \right] \right\} - 1 \right) \quad (7.12)$$

This equation is perhaps more relevant to diffusion processes in conjugated polymers where the disorder can enhance the quenching by up to 60% due to spectral relaxation in the EDOS. However these models do not allow for motion of the energy acceptors in their current form as would be the case for polaron quenching. One might also expect that the energy transferred to the polaron during the quenching process will have an effect on the polaron diffusion constant as implied by the energy transfer gain model thus a complete description of the process does not yet exist.

This chapter begins by investigating the photocurrent effects in F8BT and other polyfluorenes before moving on to the associated effect of energy transfer from excitons to polarons resulting in photo-luminescence quenching.

7.2 Photocurrent in aligned polyfluorenes

To investigate photocurrent in polyfluorenes, planar diode structures were made with gold electrodes forming a 10 μ m long channel deposited on a polyimide-coated glass substrate. After electrode deposition, the polyimide was either rubbed parallel or perpendicular to the channel and semiconductor spun on top. To investigate both the effect of alignment and the effect of the annealing temperature, the devices were tested after various 20 minute annealing steps. The added benefit to this method is to check whether the mechanical rubbing process could cause significant differences between the two alignments owing to metal being rubbed into the channel. All testing and annealing steps were performed without exposing the devices to atmosphere. A microscope light was used to provide

the light for the ‘light’ measurements and all lights including the yellow room light and computer monitors were turned off for the ‘dark’ measurement. A voltage of -100V was applied to one electrode and the other electrode was swept from -100V to 100V and back to enable the maximum fields to be applied given the ± 100 V limit of the testing equipment.

Figure 7.1(a) shows both the light and dark currents measured on an F8BT device with the rubbing direction running parallel to the field between the contacts. Interestingly, in the as-spun film there is a significant light current which reduces as the device is annealed with the dark current following the same trend. As the annealing temperature increases further and the F8BT starts to become aligned, both the light current and dark current start to recover although with a different power dependence as shown in figure 7.1(c). The initial power dependence is 2.76 for the as-spun case, and increases to 5.76 for the film after being annealed at 290°C.

In contrast, for the case when the alignment is perpendicular to the field direction, the current does not recover at the higher annealing temperatures as the polymer becomes aligned as shown in figure 7.1(b).

Figure 7.1(d) shows a summary of the light and dark current at the peak voltage for the two cases as well as a control experiment where the F8BT was on an unrubbed polyimide layer. The level of the noise at this voltage means that currents under 50pA cannot be measured however this still sets a lower limit for the ratio of photocurrent between parallel and perpendicular case of 500 which is at least a factor of 50 greater than the ratio of mobilities.²²⁷ The unaligned case shows that there is some recovery in the current at higher annealing temperatures with a recovery to around 3% of this initial current.

The fact that the dark and light current both follow the same trend suggests that the light has a multiplying effect on the existing injected current so even though the apparent photocurrent varies, the gain is approximately constant. However, a contribution to the light current from extracted photo-generated charges cannot be completely ruled out. The reduction in photocurrent between the as-spun films and those annealed at 120°C cannot be explained by morphological changes¹⁷⁴ and so can only be due in some way to the removal of residual solvent or moisture in the film. For a comparison, the behaviour of mobility with annealing temperature for F8BT transistors has been measured elsewhere. F8BT transistors show an increase in the saturation mobility of holes by approximately 20%, and a similar reduction in the electron mobility when annealing to 150°C.^{36,227} Also in top gate transistors, there is a reduction in hysteresis when annealing over the melting temperature which has been attributed to either the removal of residual solvent

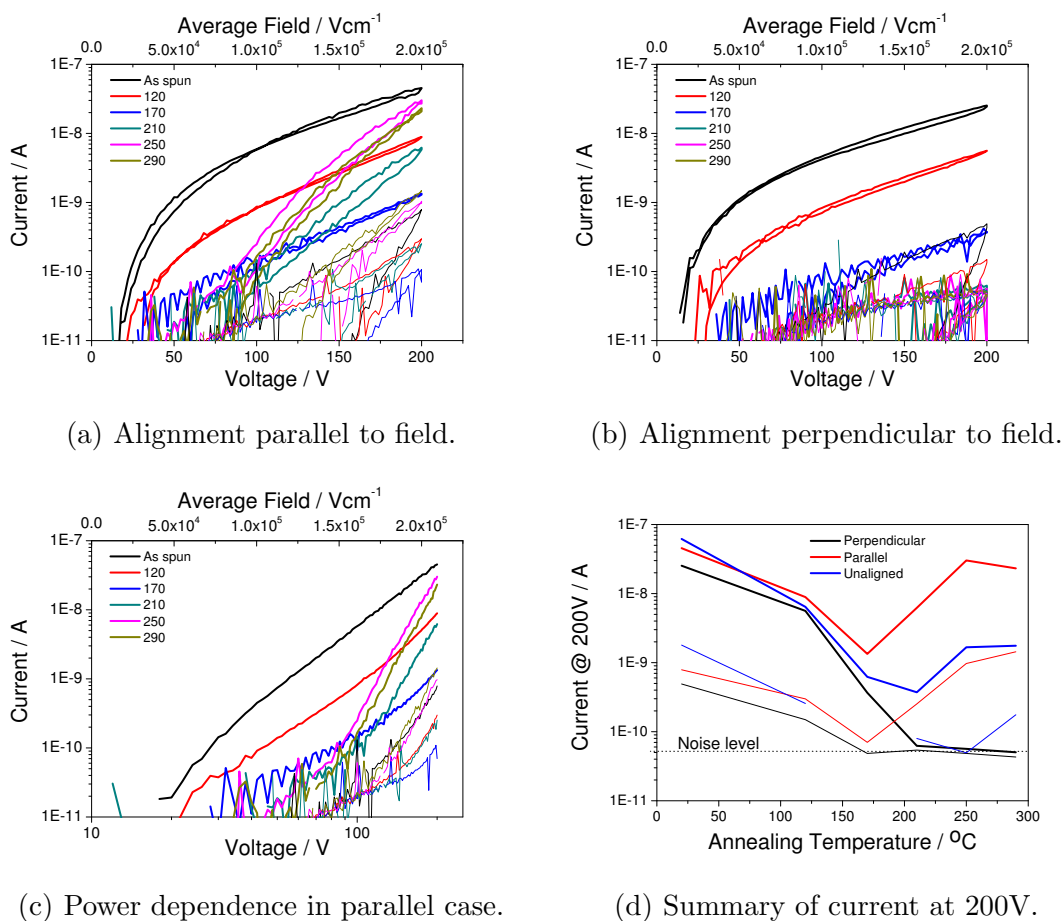


Figure 7.1: Measurements of the currents in F8BT planar diode devices in the light (thick lines) and dark (thin lines) as a function of applied voltage across a $10\mu\text{m}$ channel with gold contacts. The F8BT was spun on a polyimide alignment layer that was either parallel or perpendicular to the field direction and the measurements were taken on the same devices after sequential annealing steps.

and moisture or could be related to contact resistance via the thickness of the F8BT on the surface of the electrodes.¹⁷³ The transistor results are inconsistent with these diode devices where there is a dramatic drop in current by an order of magnitude upon annealing to 120°C. The difference in the two situations is the charge density, the field at the contacts and the contact area for injection with the transistor being ahead in all of these categories. If oxygen or moisture in the film caused a small amount of doping or enhanced injection then this would have little effect on the transistor mobility as it would be manifest in the threshold voltage. The current in a diode however would be very sensitive to doping or enhanced injection due to the low charge concentration and low field at the contacts. The recovery of the current at higher annealing temperatures with a different voltage dependence could be due to a better contact with the electrodes and in the case of the parallel alignment due to higher mobility. The ratio of current in the parallel and perpendicular alignment cases is larger than the ratio of mobilities measured in equivalent transistors

The same experiment was repeated with F8 and F8T2 diodes whose relative hole mobilities can be visualised in figure 5.14(b). The current as a function of voltage in the dark and light for the parallel and perpendicular alignment cases for F8T2 and F8 are given in figure 7.2. Larger light and dark currents were observed in F8T2 devices as compared to F8BT which cannot be simply due to higher mobility but must also be due to lower contact resistance which would be consistent with the better matching of the F8T2 HOMO level with the work function of gold. Similar behaviour was observed for the various annealing temperatures with the current reducing at first and then recovering as the polymer becomes aligned. There was a dramatic reduction in current for the F8T2 device annealed at 290°C due to the polymer dewetting the polyimide. The hysteresis in all the plots equates to a lower current as the voltage returns to zero from its maximum value.

The current measured at 200V is used to summarise the behaviour of the devices from figure 7.2 and is shown in figure 7.3. Despite absorbing light at the same energy, the gain in the F8T2 device is around an order of magnitude smaller than in the F8BT device, however due to the larger dark current in the F8T2 device the *increase* in current with light is around 1000-3000 times larger. The gain in the F8 device is even smaller than the F8T2 device due to the wide energy gap in F8 resulting less absorption.

To quantify the amount of extra current for a given amount of light, the external quantum efficiency (EQE) was measured for an aligned F8BT device with the polymer chains aligned in the direction of the field (figure 7.4(a)). The increase in current with illumination has been shown elsewhere to follow the absorption spectra of the F8BT²²⁸.

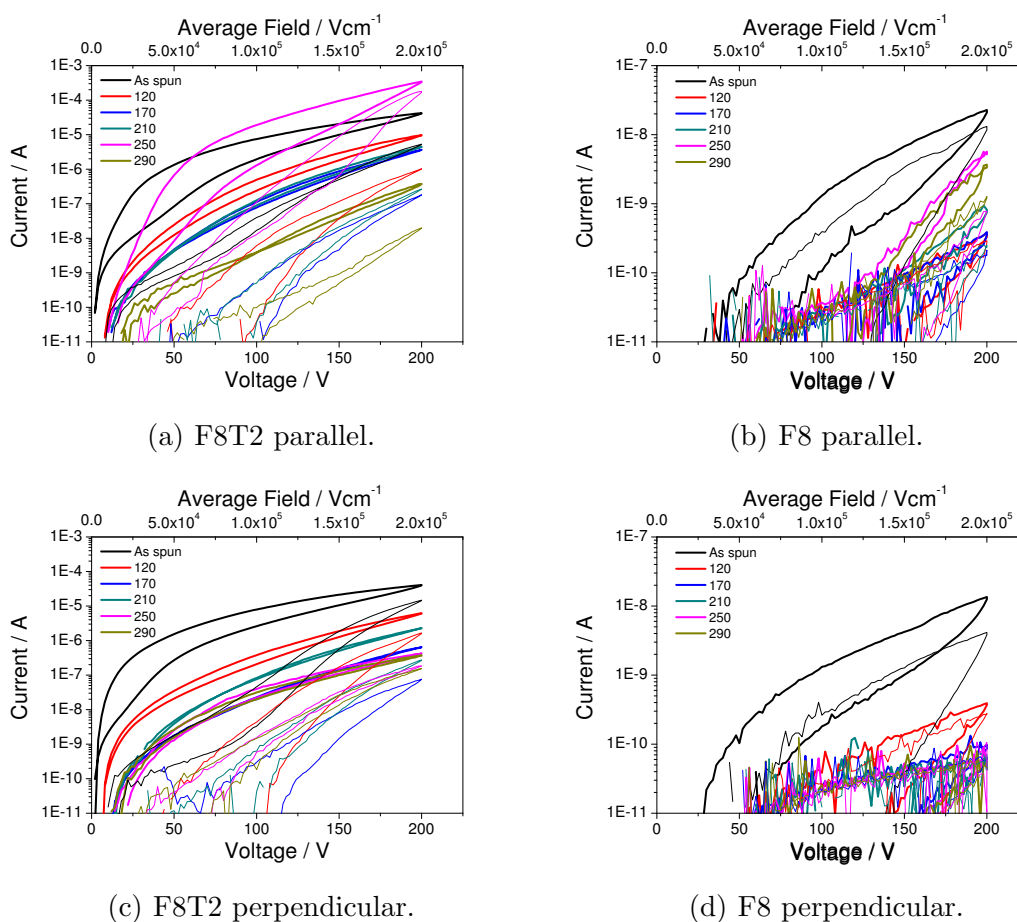


Figure 7.2: IV characteristics of F8 and F8T2 photodiodes for parallel and perpendicular alignments with respect to the field in the dark and light.

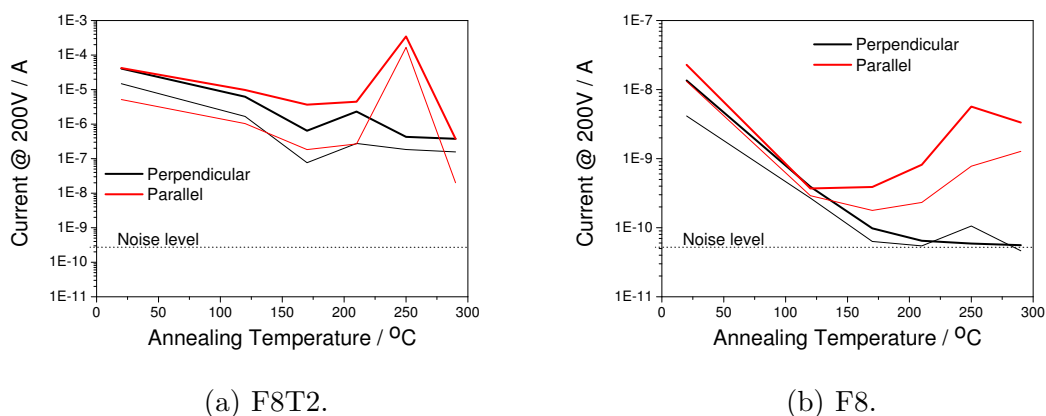
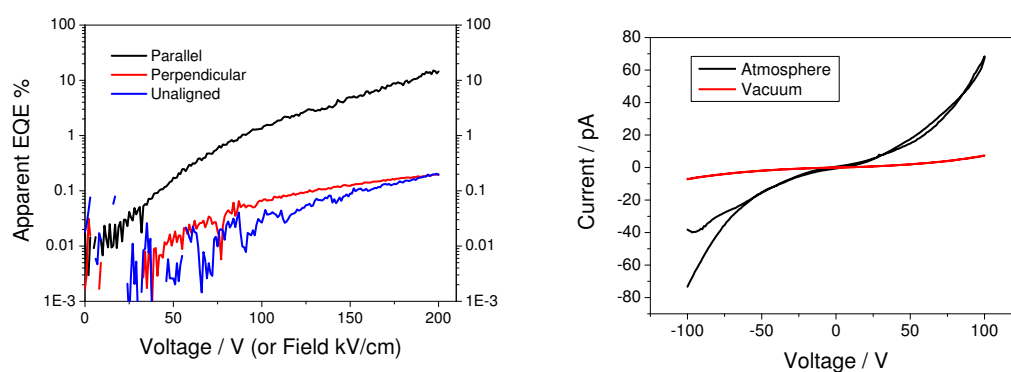


Figure 7.3: Evolution of photocurrent in F8T2 and F8 at maximum field as a function of anneal temperature.

Here, the EQE measurement at 477nm was performed both with illumination either from the top of the device or from the back of the device and yielded very similar results. Taking account of the fact that absorption in the channel region was predominantly causing the increase in current, the EQE was determined to have reached 18% before the voltage limit of the supply was reached. Given that the increase in current in the F8T2 device was orders of magnitude bigger than in the F8BT device this represents a second piece of evidence supporting the model of photo-induced gain rather than the extraction of photo-generated carriers.

The EQE measurement had been performed in air so to assess the effect of air on the measurement, an aligned F8BT device was tested both in air and under vacuum. The current measured in air was an order of magnitude larger than that measured in vacuum as shown in figure 7.4(b). This result adds further weight to the argument that the initial high currents in as-spun films relates to moisture in the film that is removed upon annealing.



(a) EQE

(b) Comparison of measurement in air with vacuum

Figure 7.4: External quantum efficiency measurement taken on planar diode structure glass/PI/Al(10 μ m channel, interdigitated)/F8BT in air. Illumination from glass side so EQE adjusted by factor of three for area of polymer not blocked by the electrodes

7.3 Electric field and photocurrent

It appears from the previous section that the dominant mechanism for increasing current with energy-gap illumination in F8BT is not from the extraction of photo-generated charges and hence could not be used to supply a current to an external circuit. Frohne et

al.²²⁹ have also noted the importance of distinguishing between the increase in injected current and the generation of charges upon illumination in conjugated polymer-fullerene blend photovoltaic devices. However, there still remains the possibility that aligning polymers in the direction of the field may enhance field-assisted exciton dissociation or offer other advantages in photovoltaic cell design.

If an exciton could be separated without the need for a heterojunction which causes energy loss then photovoltaic cells could have higher efficiencies. It is conventionally believed that fields of 10^6V/cm are required to separate excitons into free charges in conjugated polymers which is an order of magnitude larger than the built-in field in photovoltaic devices rendering blends or bilayers mandatory. However, the donor-acceptor nature of F8BT causes the electron and hole wavefunctions of the exciton to be somewhat separated which coupled with the ability to align F8BT along the field might enhance field-assisted exciton dissociation.

The alignment of F8BT could also prove advantageous in conventional two-component photovoltaic cells. The motivation for this idea comes from the recombination zone in aligned F8BT ambipolar transistors. It was noticed by Zaumseil¹⁹² that the spatial profile of the light emission from the recombination zone in aligned F8BT ambipolar transistors was highly dependent on the alignment direction. With F8BT aligned parallel to the charge transport direction, the emission profile was broad ($10\mu\text{m}$) and asymmetric with a sharp onset on the hole accumulation side and a gradual decay into the electron accumulation side. When aligned parallel to the charge transport direction, the emission profile is much narrower and at most $2\mu\text{m}$ wide. The wider recombination zone was far too wide by a factor of 100 for a Langevin recombination model suggesting that non-germinate recombination was occurring at a lower rate than expected in the aligned case. Monte-Carlo techniques were employed to take account of the asymmetry in mobility parallel to and perpendicular to the polymer alignment direction. These results showed that indeed the charges were less likely to deviate to recombine relative to continuing along in the high mobility direction and suggested that the microscopic mobility anisotropy is more like a factor of 100 rather than the FET mobility anisotropy of around 10.

Here, aligned F8T2 was also used to demonstrate the recombination zone in aligned polymers. F8BT turns out to be an ideal polymer for this measurement because after annealing to above the melting temperature there is very little hysteresis and both the holes and electrons can be injected almost equally well from photolithographically-defined electrodes which have very straight edges ensuring a uniform source-drain field. On the other hand F8T2 and F8 are less stable under ambipolar operation due to the lower electron affinity¹¹⁶ and the edges of electrodes that are formed from shadow mask evaporation,

as required with metals needed for good electron injection, are not smooth. This makes imaging of the recombination zone a lot more difficult but figure 7.5 shows that it is possible although the alignment exaggerates the effect of the rough edges of the electrodes. It can be seen that again, the recombination zone is wider when charges are moving along the alignment direction however it is not possible to say whether the asymmetry noted for F8BT is evident here.

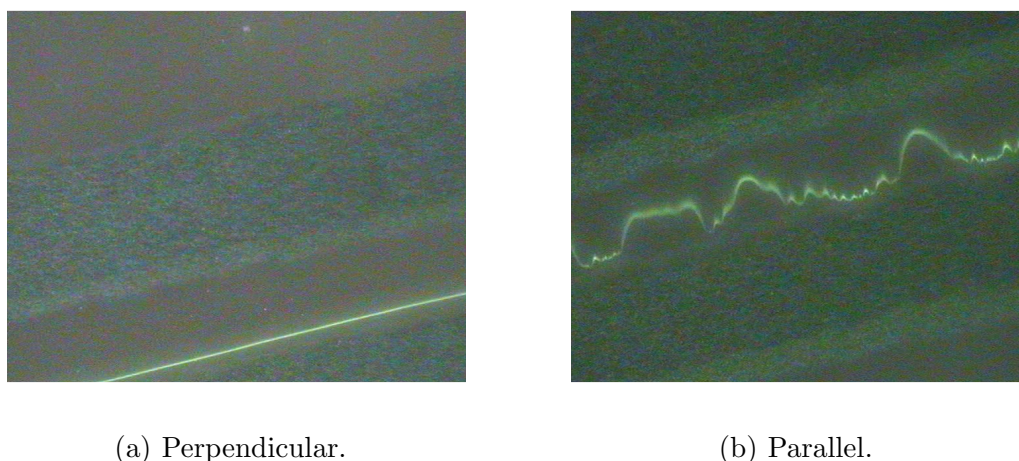


Figure 7.5: F8T2 recombination zone when the polymer is aligned either parallel to or perpendicular to the source-drain field direction.

This result of the wider recombination zone may have uses in the field of photovoltaics where for F8BT:PFB blends²³⁰ it is believed that the efficiency is limited due to separated charge pairs staying at the interface and with 75% eventually forming triplet states which cannot then generate free charges²³¹. Westenhoff concluded that strategies to direct charges away from this interface would overcome the triplet problem. By considering a lateral bilayer structure one might expect that the enhanced mobility in the field direction may enable these interfacial charge pairs to separate. Once separated, the reduced probability of recombination seen in aligned transistors might also prevent non-geminate recombination following separation in a bilayer photovoltaic structure.

To first see if alignment can have benefits for photovoltaic devices by reducing the field required to separate excitons in F8BT, the field in the channel was measured and the effect of the field on the exciton lifetime was measured. The feasibility of making lateral bilayer photovoltaic cells with PFB and aligned F8BT using rectifying contacts was then investigated.

7.3.1 Electric field in planar diodes

Natali et al.²³² suggested that in the planar diode configuration, large fields can exist at the edges of the electrodes which could be large enough to separate bound electron hole pairs in a homopolymer. In order to understand the field distribution in the actual devices used in this work scanning kelvin probe microscopy (SKPM) was performed with the help of Dr Toby Hallam on an aligned F8BT device on gold contacts with a 10 micron channel length. SKPM provides a measurement of the potential in the channel from which the field can be derived. Due to the limitations of the hardware, voltages were kept below 60V to avoid artifacts appearing in the topology traces. Figure 7.6(a) shows that there is no large field at the edges of the electrodes as the potential is fairly flat in this region. Even if there theoretically should be a large field due to the geometry, the ability to inject charge into the polymer would reduce this field as space charge builds up in the polymer. The field in channel is nearly uniform although the curvature of the potential near the electrodes indicates a concentration of holes at the hole injecting electrode and electrons at the electron injecting electrode.

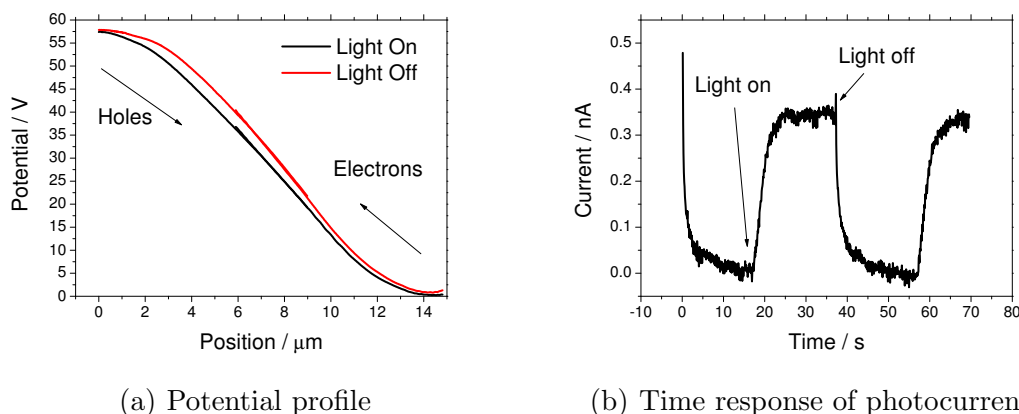


Figure 7.6: Potential in channel with 60V applied between two gold contacts with F8BT aligned in the direction of the field. Channel length appears longer than $10\mu\text{m}$ due to device being at small angle to scan direction

Upon illumination with white light, the field at the hole injecting contact increases slightly. Some models for photo-induced gain that are not due to the generation of free carriers assume ohmic contact with a space-charge limited current and the effect of light being to transfer charges in shallow traps to higher lying states.¹⁹⁶ If detrapping charges is simply to say that the mobility is effectively increased then a change in the potential might not be expected when light is shone on the device. However, combined with a

non-ohmic contact resistance, the change that would be expected in the potential profile is not easy to solve analytically.

Alternative models for gain involve the generation of charges of which one gets trapped or has lower mobility thus supporting a mobile charge density of the opposite sign.²¹⁰ Such a mechanism does not produce any space charge but could modify the potential by preventing the build up of injected charge. In the limit of a highly doped film, the potential would simply drop linearly between source and drain, so some degree of neutral charge carriers could push the potential profile towards this form although an analytical models for such a regime is not possible.²³³

A few further facts arose from the SKPM studies to help to distinguish between light-induced trapping and light-induced detrapping. Firstly, when the device is run in the dark and the voltage removed a positive charge was found to remain in the channel which was removed within a few seconds upon illumination. Secondly, the time response of the photocurrent shown in figure 7.6(b) is also consistent with a mechanism involving trapping or detrapping due to the slow rise and fall times. However, neither of these facts rule out either of the models with the rise and fall times being either the time to detrapp and retrapp holes or trap and detrapp electrons. The fact that holes are left behind when run in the dark and are detrapped quickly with light intuitively favours the hole detrapping gain mechanism. To eliminate the electron trapping gain mechanism completely, the device was measured in the dark but either after a period of darkness or illumination. If the light causes electron trapping then when measuring in the dark following illumination, a transient would be expected corresponding to the time for the electrons to detrapp. If light does not trap electrons but detraps holes there would be no difference between running the device following illumination or following darkness. The similarity between both cases as shown in figure 7.7 indicates that electrons are not trapped by illumination in vacuum. This provides strong evidence that when the aligned devices are measured in vacuum with injecting electrodes, it is the hole detrapping gain mechanism which operates.

7.3.2 Exciton lifetime measurements under applied fields

With the knowledge of the field distribution in the device, the possibility of exciton splitting under an applied field was investigated which would be manifest as a reduction in photo-luminescence. A device was fabricated with the aim of applying a field across the aligned polymer without injecting current. Aluminium which has been left in ambient conditions to form an oxide was used as the contacts with a channel length of $10\mu\text{m}$ and width of 4cm . A field of up to $2 \times 10^5 \text{V/cm}$ was applied whilst the photoluminescence was

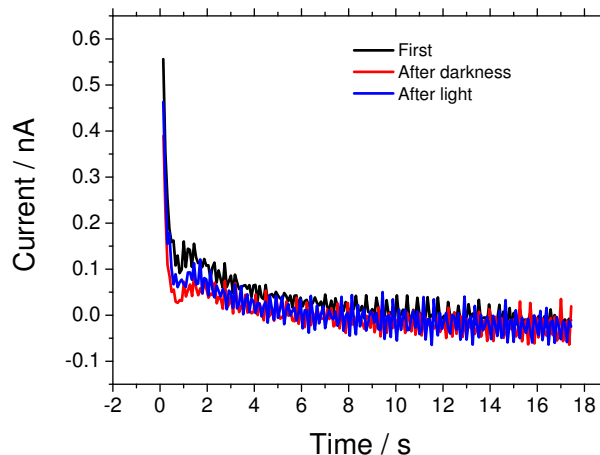


Figure 7.7: The current measured in the dark with 100V applied in an aligned (parallel to field direction) F8BT diode device after either exposure to light or darkness.

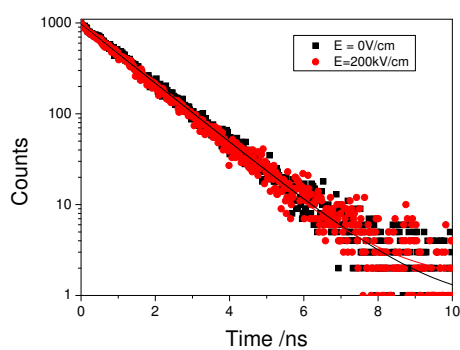
observed with a fluorescence microscope (figure 3.13) but no visible change in intensity was observed.

For a more sensitive probe, the device was tested using Time Correlated Single Photon Counting (TCSPC) with the help of Dr Ian Howard and Sebastian Albert-Seifried. In this experiment, the decay of photoluminescence after a laser pulse is monitored by counting the number of photons emitted from the sample as a function of time, averaging over many pulses. If a non-radiative exciton decay pathway rate, k_{nr} , is enhanced, the lifetime, τ of the exciton decay will be reduced as shown by

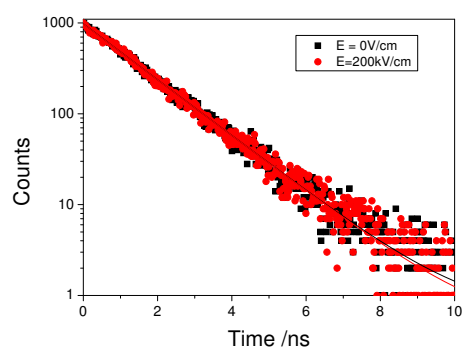
$$\tau = \frac{1}{k_r + \sum k_{nr}} \quad (7.13)$$

where k_r would be the radiative decay rate in the absence of other decay pathways.

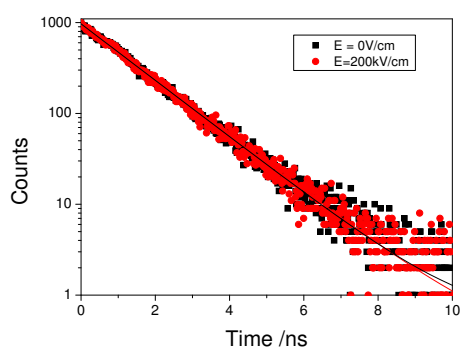
As figure 7.8 shows, excitons in the F8BT devices decayed with a time constant of ~ 1.3 ns. Even at the highest fields, there is at most a change in lifetime of $\sim 3\%$ which corresponds to a rate constant of $2.3 \times 10^7 s^{-1}$. It was however noted during this experiment that there was an increase in current when the light was on the device despite the aluminium electrodes which should not inject holes. As a result, the very small change in lifetime cannot be definitively assigned to exciton splitting and maybe due to charges in the device. Even if the change in lifetime were due to field-induced exciton dissociation along the aligned polymer chain, the size of the effect does not point to this being an material to use for single component photovoltaics.



(a) Parallel.



(b) Perpendicular.



(c) Unaligned.

Polymer alignment with field	% Change in lifetime	Uncertainty
Parallel	2.9	0.2
Perpendicular	0.0	0.3
Unaligned	1.8	0.3

(d) Summary.

Figure 7.8: TCSPC results on an F8BT planar diode with aluminium electrodes and a 10 micron channel length measured in air for various alignments of the F8BT with respect to the field between the contacts.

7.3.3 Gold/Chromium single layer devices

To investigate the feasibility of aligned F8BT forming part of a bilayer photovoltaic, planar diode device with asymmetric workfunction electrodes were fabricated. Preventing charge injection and the associated gain upon illumination is necessary to detect the photovoltaic effect in F8BT devices which otherwise swamps any measurement when using gold electrodes.²²⁸

Firstly pre-made devices photolithographically defined with gold/gold, gold/chromium and chromium/chromium electrodes with various channel lengths were used. As these were pre-patterned on glass, the F8BT could not be aligned so this was only suitable for analysing the as-spun effect. Figure 7.9 shows the photocurrent as a function of bias for the three cases with 6 micron channel lengths ($W=1\text{mm}$) when testing in nitrogen atmosphere. There is a clear asymmetry in the characteristics in both the dark and light currents indicating preferential injection of holes from the gold.

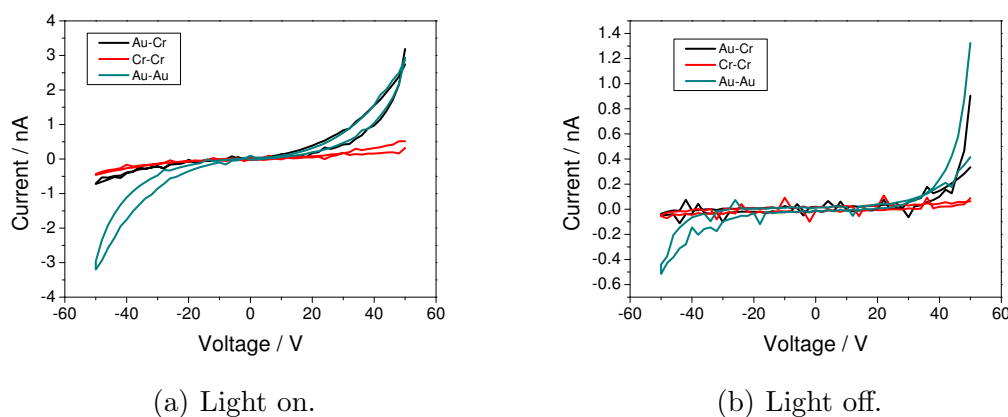
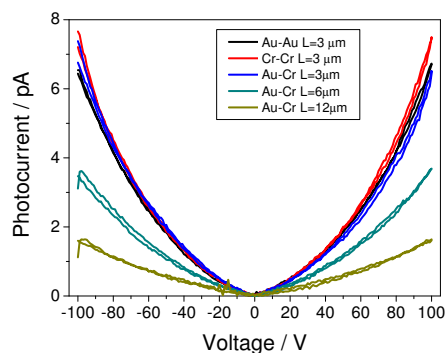


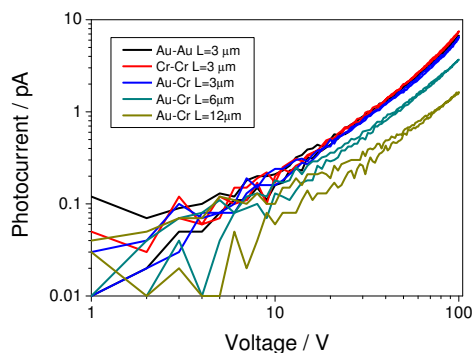
Figure 7.9: Unaligned, as spun F8BT planar diode devices with various combinations of gold and chromium electrodes measured in a nitrogen glovebox with or without illumination from a microscope lamp.

When measured in vacuum however, the devices behaved differently and whilst the light intensities cannot be compared quantitatively, the currents were three orders smaller and independent of the electrode metal as shown in figure 7.10(a). The dark current was also below the noise of the system which in this case was around 0.5pA at 200V and this can be compared to the dark current in the glovebox which was around 1nA at 50V . The most likely explanation for this is that under vacuum, the impurities from the film were removed much like annealing to 150°C had done. This small current that was independent of the electrode is believed to be from the collection of photo-generated charges. The

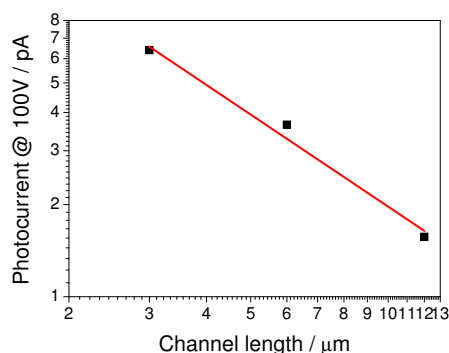
mechanism for the charge generation cannot be determined from this measurement but the current follows a power law dependence on voltage with an exponent of between 1.8 and 2.2 as shown in figure 7.10(b). It was not however possible to detect an open circuit voltage despite the different workfunctions of the contacts.



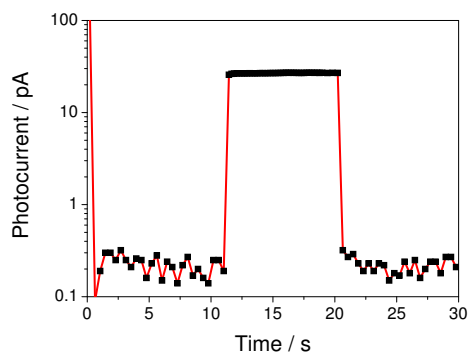
(a) Photocurrent vs voltage for a range of channel lengths and electrode types.



(b) Log-log plot of figure 7.10(a).



(c) Channel length dependence of photocurrent Au-Cr devices.



(d) Time response of photocurrent from 3μ Cr device.

Figure 7.10: Unaligned, as spun F8BT planar diode devices with various combinations of gold and chromium electrodes measured in vacuum.

Figure 7.10(c) shows the channel length dependence of the photocurrent with a power exponent of -1 fitted to the data points indicating a reciprocal relationship between channel length and photocurrent. Given that the voltage dependence was quadratic, the length dependence indicates that the photocurrent could be proportional to the square of the electric field multiplied by the channel area.

The time response of the photocurrent shown in figure 7.10(d) shows a very rapid (<500ms) increase and reduction when the light source is uncovered and covered again

which again indicates that trapping mechanisms are not responsible for this current.

7.3.4 Gold/Aluminium single layer and bilayer devices

With the method established for measuring photocurrent in as-spun films with bottom contacts that is believed to show just photo-generated charges, devices were fabricated to do a similar measurement on aligned films to see if alignment in the field direction might assist charge separation. In order to investigate the photocurrent in aligned F8BT with different work function metals it was necessary to evaporate them on top of the pre-aligned F8BT to avoid exposure of the electrodes to air as the polyimide would have to have been rubbed after the electrode deposition. Two masks of slightly different spacing electrodes were used to sequentially evaporate gold and aluminium. The different spacing means that each channel differs by 10 microns with the smallest, labelled S , being <10microns as shown in figure 7.11(a).



(a) Aligned F8BT film with Au/Al electrodes (line width=1.5mm).

(b) Photo-luminescence image of F8BT with PFB layer on top.

Figure 7.11: Aligned F8BT film with aluminium and gold electrodes evaporated on top. PFB was later laminated on top of the devices.

To the authors knowledge, this is the first realisation of such short channel asymmetric top electrode planar photovoltaic devices with previous methods having longer 1.37-2mm channel lengths¹⁴⁶ or bottom contacts defined with photolithography.^{144,234} This new method enables the contacts to be formed without exposing the electrodes to air and can allow the electrodes to be in contact with both the top and bottom layer of a bilayer device. The patterning technique can also be applied to ambipolar transistors, as seen in appendix figure A.2, to make two completely different electrodes rather than

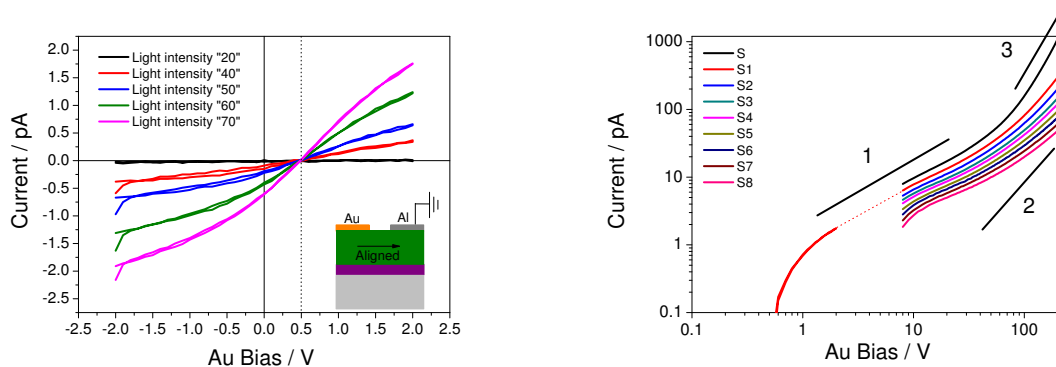
using the angle technique which leaves some ambiguity as to where the charge is being injected from.

The devices were first measured in vacuum before having a layer of PFB, obtained with the float-off technique using distilled water, laminated on top of the F8BT and then annealed at 120° for 20 minutes in the glovebox to remove moisture. When measured in the dark, only the very shortest devices showed any sign of a dark current which showed an exponential dependence on voltage and only becoming significant at around 200V where it reaches 10% of the photocurrent. This may be due to the diffusive nature of the edges of shadow evaporated electrodes.

With this device structure it was possible to measure an open circuit voltage of 0.5V under illumination in vacuum which is shown in figure 7.12(a) for an aligned F8BT device with the chains in the direction of the field. The generation of charges at such small fields and the linear increase with voltage implies that the light is generating a charge density which is swept out by the field rather than being generated by the field. When calibrated for the intensity of the light, the increase in current with light intensity is linear as shown in appendix A.3(b). Just like with the Au/Cr devices, the current curves lie on top of each other when plotted with field on the x-axis and the current is normalised for the channel area indicating that charges are generated uniformly in the channel. At higher fields that are comparable to those in the Au/Cr devices, the current starts to increase super-linearly indicating that the field might be either aiding charge generation or reducing bimolecular recombination.

The photocurrent was measured for a range of devices with the F8BT either aligned parallel or perpendicular to the field direction, annealed over the melting temperature without alignment or as-spun. The photocurrent for the shortest ($\sim 5\mu\text{m}$) and second shortest ($\sim 15\mu\text{m}$) channels are shown in figures 7.13(a) and 7.13(b) respectively. As noted above, there was only measurable dark current in the shortest channel devices so the second shortest channel provides the cleanest measure of photocurrent. When measuring up to fields in the region of 10^5V/cm the photocurrent is fairly symmetric in both forward and reverse bias for all the devices. The photocurrent was largest with the alignment parallel to the field direction, followed by the unaligned but annealed, the perpendicular alignment and the as-spun devices which is most likely to be a measure of the mobility when measured in vacuum. The as-spun devices displayed similar currents as the as-spun F8BT with Au/Cr electrodes which had a similar channel width and length and were also measured in vacuum.

When PFB was laminated onto these devices and they were retested under exactly the same illumination conditions the photocurrents were different. The largest photocurrent



(a) Evidence for built in voltage in lateral structure.

(b) Voltage dependence of photocurrent for different channel lengths (numbers indicate exponent).

Figure 7.12: Photocurrent in F8BT-only planar device with the polymer aligned along the field direction and measured in vacuum. Shortest channel, S , is $5\mu\text{m} \pm 2\mu\text{m}$ and each subsequent channel, S_n , is $S + 10n \mu\text{m}$.

was observed in the device with the unaligned yet annealed F8BT and is much larger in forward bias. The device with the F8BT aligned perpendicular to the field also showed an increase in photocurrent in forward bias with the device with the F8BT aligned parallel to the field showing even a slight reduction in photocurrent. The photocurrent for the as-spun device increased but due to the annealing step after the lamination it cannot be used as a fair comparison. The asymmetry observed in the devices where the photocurrent increased suggested that charge injection was occurring into the PFB; either holes being injected from the gold or electrons from the aluminium. This was confirmed by observing the dark current in the device where F8BT was aligned perpendicular to the field. As seen in figure 7.14, the addition of PFB results in an increase in both dark and light current in forward bias indicating that the gold and aluminium bottom contacts are rectifying for PFB. The open circuit voltage is still observed in these devices.

Even taking into account the dark current, the light current in forward bias is larger than in reverse bias suggesting that there is a gain mechanism still occurring. These gain effects seem to dominate in lateral structures where charges can be injected and are rarely mentioned in cofacial structures²²⁹ which could be due to the longer channel length. If the light can continuously detrapp injected charges then they can easily make it from one side of the device to the other, however the photo-generated charges are likely to recombine before exiting the device. Even at the high voltages where the field approaches that found in cofacial devices the charges will have similar velocity but still have to travel thousands

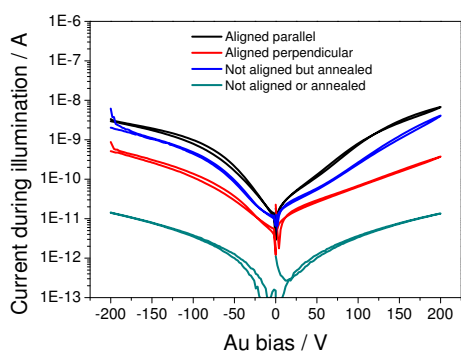
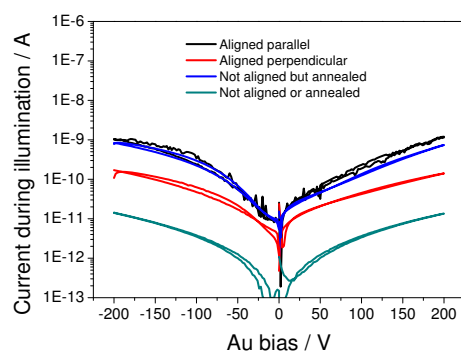
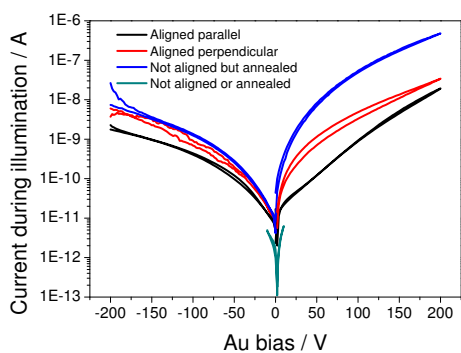
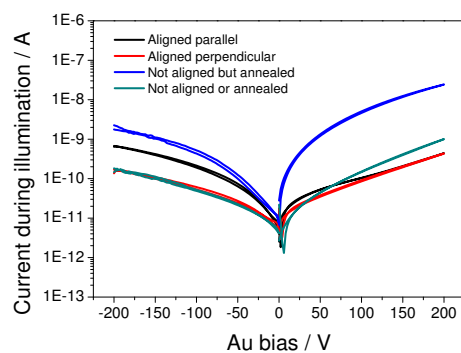
(a) $\sim 5\mu\text{m}$ channel length with F8BT only.(b) $\sim 15\mu\text{m}$ channel length with F8BT only.(c) $\sim 5\mu\text{m}$ channel length after PFB layer added.(d) $\sim 15\mu\text{m}$ channel length after PFB layer added.

Figure 7.13: Photocurrent for the $\sim 5\mu\text{m}$ and $\sim 15\mu\text{m}$ channel length F8BT devices with gold and aluminium contacts shown before and after the PFB layer was added.

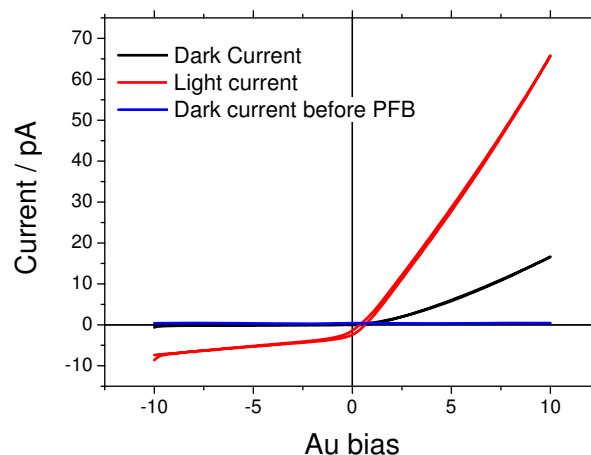


Figure 7.14: Light and dark currents under small bias for Au/Al F8BT device with chains aligned perpendicular to the field direction before and after the PFB was added on top.

rather than tens of nanometres. Comparing the reverse bias current in figures 7.13(b) and 7.13(d) reveal that the PFB has little effect on the photocurrent when injection is not taken into account. This is most likely also due to charge recombination. In order to fully understand the benefits of alignment on photovoltaic devices, lateral devices need to be made with even shorter channel lengths or with larger fields which was beyond the scope of this work.

To summarise the photocurrent effects in polyfluorenes it appears that the current increase upon illumination is highly dependent on a number of factors including the contacts, the annealing temperature of the film, the environment in which it is tested and the alignment of the polymer. The current can be attributed to two mechanisms involving either photo-induced gain of an existing dark current or the generation of charges that can be extracted with a field. As-spun polyfluorene films on gold contacts have an intrinsically large dark current and through the gain effect have a correspondingly high light current when measured in a glovebox. It is thought that impurities or moisture in the film is responsible for the high currents in the as-spun films. Annealing these films reduces both currents although the gain remains constant. When annealed at temperatures around the polymer melting temperature a recovery in the current is observed which is even larger when the polymer chains are aligned in the direction of charge transport or smaller when aligned perpendicular to this. The effect of annealing is thought to be to improve the morphology of the film either on the contacts or in the channel or both. An indication of this kind of behaviour is the observation of a dark current that is proportional to the light

current with both being dependent on the workfunction of the injecting electrode. The gain effect in the annealed films is also increased when measured in air which suggests electron trapping may enhance the current, although in vacuum the effect is thought to be simply due to the detrapping of holes. In contrast, when measured in vacuum, the as-spun devices show no dark current and a small light current that is independent of the electrode material which has been attributed to the extraction of photo-generated charges. The mechanism that produces these charges is as yet unconfirmed but cannot be due to field at the voltages applied in these experiments. A similar effect is seen in the annealed films with top contacts which do not inject charges into F8BT and the current from the extracted charges is dependent on the alignment of the polymer chains. It was found that the fields that could be applied in these devices were not sufficient to extract all of the charges before they recombine due to the large distances that the charges must travel.

7.4 Quantifying charge-induced photoluminescence quenching

The fact that excitons have been seen in the previous sections to detrapp charges and increase the current in devices should indicate that the photo-luminescence from F8BT should be reduced in the presence of charges. This exciton-polaron quenching was indeed observed during the CMS experiments and is investigated further here to quantify the process accurately.

In the CMS setup there is no monochromator after the sample so when measuring the transmission of energy gap light the detector also measures a small amount of photoluminescence (PL). Whilst this PL is significantly smaller than the transmitted intensity, as shown in figure 7.15, if it were to change significantly in the presence of charges then it could effect the CMS spectra in the bleaching region. Indeed an apparent absorption rather than bleach in the energy gap region was observed on thicker F8BT films. As the light enters the F8BT film from the surface where the charges are modulated, if the PL from this region is modulated by ΔPL , the detector will pick up this change, the size of which will be independent of the F8BT thickness. On the other hand, the transmitted intensity at the energy gap wavelength will be attenuated as the F8BT thickness increases. In the limit of an infinitely thick film, only the PL would be detected and so $\Delta T/T$ would actually be $\Delta PL/PL$. The size of $\Delta PL/PL$ depends on the thickness of the film as the charges are only modulating the PL in the accumulation layer and the rest of the PL

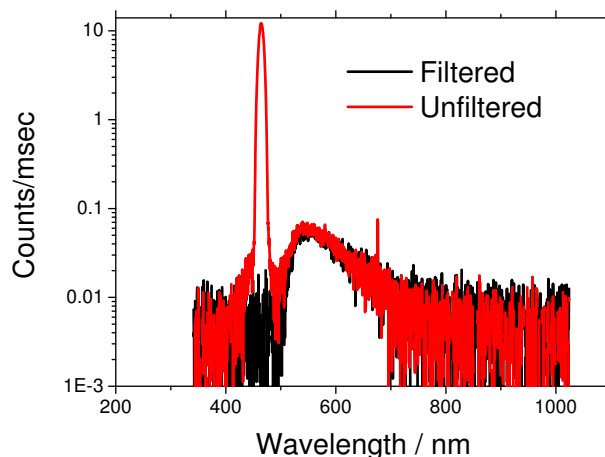
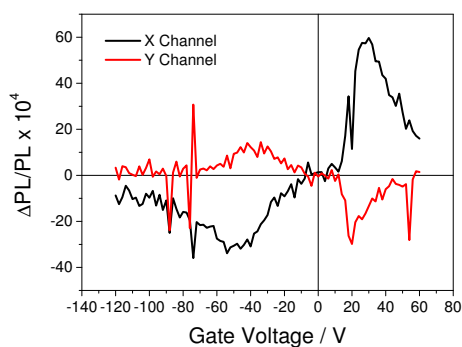


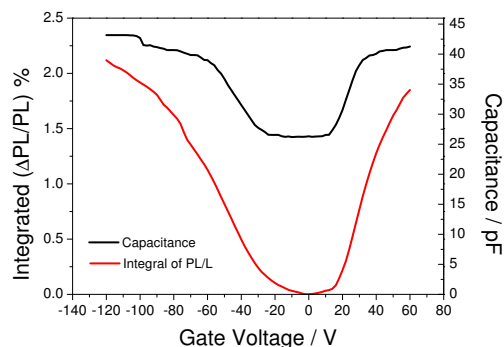
Figure 7.15: Spectra of light in CMS setup after passing through an F8BT sample with and without a 515nm filter before the detector. The filter blocks the light that originated from the monochromator but allows the photo-luminescence from the F8BT to pass through.

remains constant. To simulate an infinitely thick F8BT film, a filter that blocks light with wavelengths shorter than 515nm was inserted after the sample and $\Delta PL/PL$ was measured using 477nm illumination.

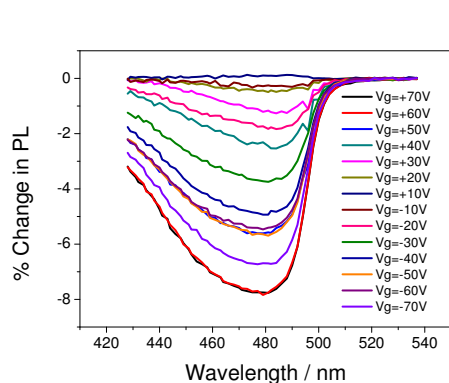
Figure 7.16(a) shows $\Delta PL/PL$ measured as a function of gate voltage. Unlike charge absorption features that increase with gate voltage and then remain constant, the PL quenching increases and then reduces again. The explanation for the behaviour of the PL quenching comes from the fact that at a certain charge density the PL in the region of the charges becomes completely quenched and therefore the addition of more charges will no longer have any effect. To visualise this saturation of the quenching, the integral of the data in figure 7.16(a) was taken and divided by the modulation voltage. As shown in figure 7.16(b) the integrated PL quenching follows the capacitance data very closely indicating that the quenching must be from the modulation of the charge density rather than the field. As it was noticed that the PL quenching was so large, the experiment was repeated without the modulation simply by locking into to the reference from a chopper wheel and measuring the intensity of the PL as a function of gate voltage and comparing it to the value at 0V. Figure 7.16(c) shows the percentage change in PL as a function of wavelength for various gate voltages showing that the feature matches the F8BT absorption spectrum. Each data point represents two averages of the difference between the PL at that gate voltage and at zero volts which means that should charge trapping occur that would shift the effective gate voltage, the PL at zero volts may reduce which would reduce the



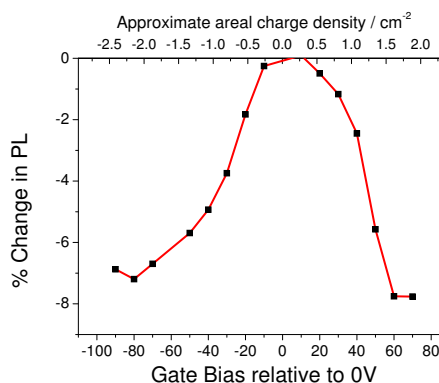
(a) X and Y channels of $\Delta PL/PL$ with $V_{pp}=10V$ under 477nm illumination.



(b) Normalised integral of 7.16(a) and capacitance.



(c) PL quenching vs wavelength with on:off scans.



(d) Peak PL at 480nm from fig 7.16(c).

Figure 7.16: Photoluminescence quenching measurements of F8BT transistor B25-6b (5.28(b)) in the CMS setup with 515nm filter before the detector to only allow only photoluminescence to be detected. The modulation spectra in figure 7.16(a) indicated the changes were large enough to be measured in an on:off method where the transmission is simply measured with the gate voltage on and off. The light is chopped during this experiment before the sample simply in order for the detector to be able to measure the transmission.

measured difference. Figure 7.16(d) shows a summary of the percentage change in PL as a function of gate voltage measured at 480nm. The change in PL is larger in this case than it was when integrating the modulated PL because this is effectively a steady state measurement where the accumulation layer has time to fill completely. The sudden flattening of the change in PL at the highest gate voltages and the asymmetry of the plot is believed to be due to the PL at zero volts changing due to threshold shifts from trapping. However, it is clear that both holes and electrons lead to the same final degree of quenching which had been a matter of debate in the literature.^{216,235–237} A change of PL by about 7.5% in an F8BT film of 65nm indicates that a 5nm thickness of the film has been completely quenched of luminescence with a charge density of around $2\text{-}3 \times 10^{12} \text{cm}^{-2}$ or one per $33\text{-}50 \text{nm}^2$. The radius of a circle including this area is around 3-4nm which is consistent with the thickness of the film that was quenched being 5nm.

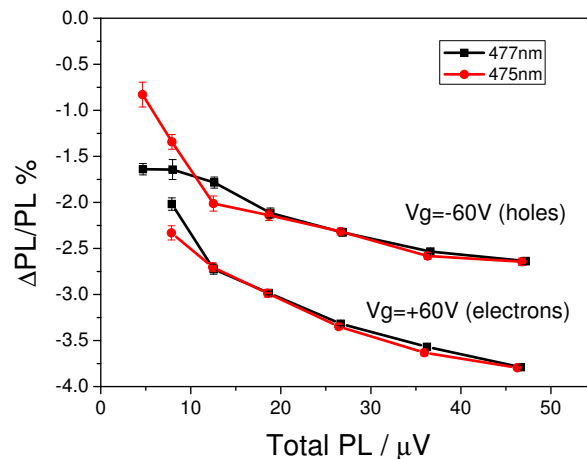


Figure 7.17: Effect of the light intensity on the PL quenching measured on aligned F8BT device B25-3b. Devices were held at the gate voltage for a few seconds before each measurement to give sufficient time to fully accumulate the channel with the aim of creating the same charge density regardless of light intensity. Total PL when there is no gate voltage applied was used as the x axis since it should be proportional to illumination intensity.

In theory, if the PL is completely quenched by the charges, then if only one exciton was created in the charge region this should also be quenched. This is to say that the quenching should be independent of the intensity of the illumination. There are a few mechanisms that might cause the PL quenching to be intensity dependent. Firstly, if the exciton is transferring energy to the polaron, it can only receive so much energy and so

might, for a brief period not be available to quench another exciton. An insufficiently rapid relaxation of the excited polaron therefore might cause a reduction in the size of $\Delta PL/PL$ with intensity. On the other hand, by transferring energy to the polaron it might gain kinetic energy which would increase the probability of finding another exciton by sampling a larger volume during the exciton lifetime. To investigate the effect of intensity on PL quenching a device was held at a large gate voltage for a number of seconds at various light intensities and the change in PL was measured as shown in figure 7.17. A large voltage and long pre-measurement wait was used to try to guarantee that the same charge density was in the device for each measurement as light is known to speed up the accumulation process from previous chapters. For both holes and electrons there is a measured increase in the PL quenching as a function of the incident light intensity which supports the theory of light adding to the kinetic energy of the polarons or equivalently increasing the mobility.

As the size of $\Delta PL/PL$ increases for thinner layers of F8BT due to the reduction in the amount of unmodulated PL, a device with a thin layer of F8BT ($< 20nm$) was used to study the mathematical form of the quenching as a function of charge density. This experiment was performed using a fluorescence microscope in order to achieve higher illumination intensities such that the intensity dependence, which appears to saturate at high intensities, does not effect the measurement. With the help of Michael Gwinner, the device was mounted within a sample holder with electrical feedthroughs in order to provide a nitrogen environment for testing. Figure 7.18 shows images of this device taken in depletion and accumulation making it clear the extent to which the charges quench the PL.

PL images were taken at various gate voltages and the average intensity of the PL was measured relative to the case with zero volts applied and plotted in figure 7.19. As can be seen in the figure, the maximum PL was not at zero volts and so the plot was scaled such that the maximum PL corresponded to 100%. The cause of this position of the maximum PL can only be due to charge trapping of holes meaning that at zero volts there are trapped holes and compensating electrons. Either the trapped hole does not quench the PL or the close proximity of a compensating electron causes the two charge species to quench only as many excitons as one charge would. The light is so intense as to completely remove the thresholds for accumulation which is achieved either by the generation of free charges or the continuous detrapping of charges.

Attempts were made to fit the Stern-Volmer and Zapunidi equations (7.7 and 7.12) to the data however these had to be modified for the fact that the accumulation layer does not extend through the entire film. The following equation was used as a container for the

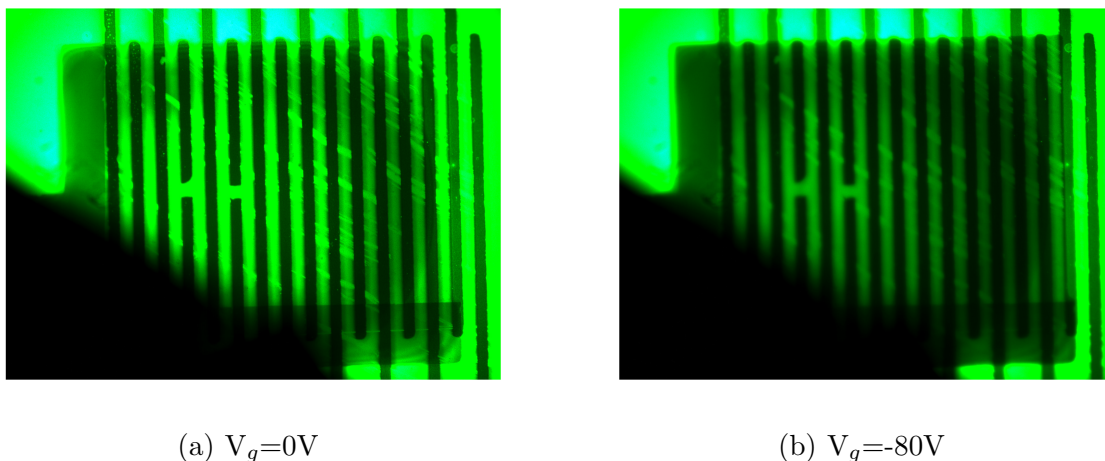


Figure 7.18: PL images in depletion and accumulation of device B24-6a: Au(80nm) / F8BT(<20nm) / PMMA(500nm) / PEDOT: PSS.

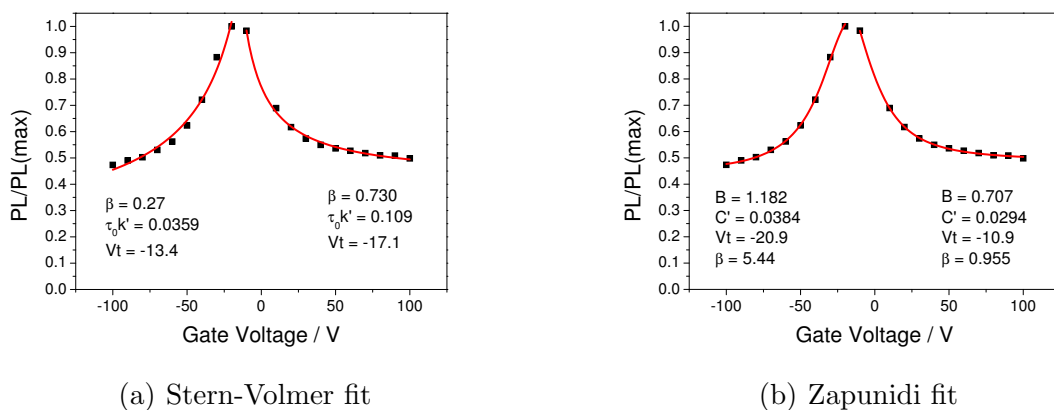


Figure 7.19: Stern-Volmer fit and Zapunidi fit to the change in PL in device B24-6a (figure 7.18) as a function of gate voltage.

fitting equations to attempt to map the measured fractional change in PL to that near the accumulation layer which the equations model.

$$\frac{PL_{meas}(V_g)}{PL_{max,meas}} = \frac{\left(\frac{PL(V_g)}{PL_{max}}\right) + \beta}{1 + \beta} \quad (7.14)$$

The quantity $\beta = (d - a)/a$ represents the ratio of the unmodified region of PL to the modified region with d being the thickness of the semiconductor and a being the thickness of the film affected by charges in the accumulation layer. β increases from zero to infinity as the film thickness increases and is equal to 1 when it is twice as thick as the region influenced by the accumulation layer. Even though the fit looks good, the Zapunidi equation is not able to produce sensible parameters with B being less than 1 for hole accumulation and β being unreasonably large in electron accumulation. The likely cause of the problem with this fitting equation is the number of variables and the limited applicability to the particular geometry of the system. The parameter C' relates to C in equation 7.12 through

$$C' = \frac{C_i}{ed_a} \frac{4\pi r_d^3}{3} \sqrt{Q} \quad (7.15)$$

where the symbols correspond to those previously defined and d_a is the thickness of the region that eventually becomes completely quenched. The Stern-Volmer fit has one less fitting parameter and in hole accumulation yields reasonable parameters where

$$k' = \frac{4\pi(D_{ex} + D_p)R_0C_i}{ed_a} \quad (7.16)$$

$$(D_{ex} + D_p) = \frac{(k'\tau_0)ed_a}{4\pi R_0C_i\tau_0} \quad (7.17)$$

The Stern-Volmer method yields a result that contains the product of the exciton lifetime in the absence of charges, the exciton and polaron diffusion constants and the Förster capture radius. From the measured cross sections and the PL spectra shown in figure 7.20 it was possible to calculate the Förster capture radius using equation 2.16 as being 1.42nm for holes and 1.35nm for electrons (using 82% PL efficiency for F8BT 114 batch from CDT data sheet). The intrinsic lifetime, τ_0 , of excitons in F8BT has already been measured in this thesis as being 1.3ns which together with the measured τ_0k' of 0.109 gives an estimate of the sum of diffusion constants ($D_{ex} + D_p$) as being between 0.012-0.12nm²/ps depending on the value for d_a . The two extremes of charge density can be estimated using the 1nm thickness of the accumulation layer or the total thickness of F8BT quenched by the charges which is estimated to be up to 10nm. The charges and excitons

together diffuse somewhere between 4-40nm during the lifetime of the exciton depending on the value of d_a . To overcome this uncertainty, a more sophisticated model considering two-dimensional charge diffusion coupled with three-dimensional exciton diffusion needs to be developed from first principles although that is beyond the scope of this work.

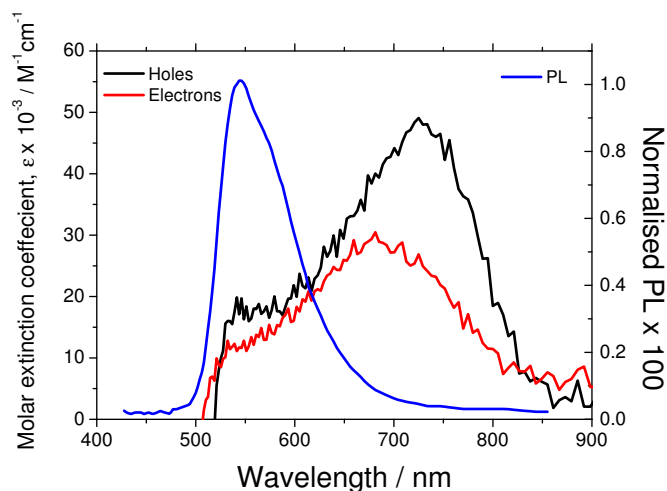
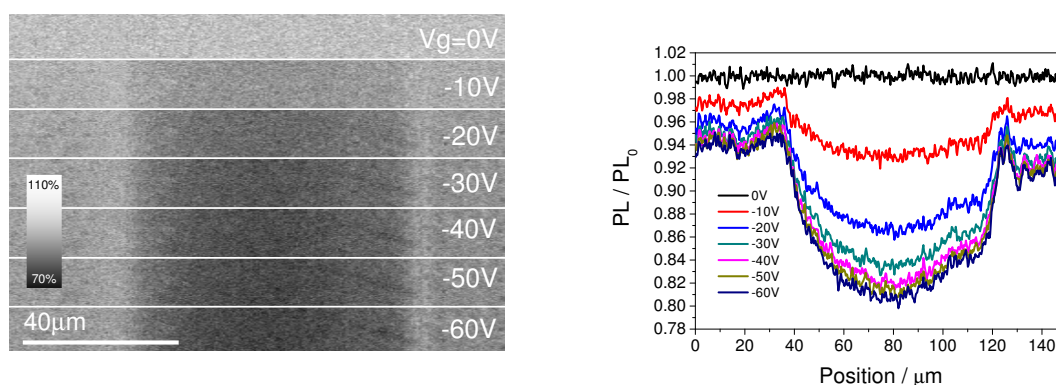


Figure 7.20: Normalised (integral=1) F8BT PL spectrum and the molar extinction coefficients for holes and electrons measured in F8BT.

7.5 Using charge-induced photoluminescence quenching to visualise device operation

An obvious application to take advantage of the high efficiency of PL quenching by charges is to image an FET device during operation. A similar technique has been used in light-emitting electrochemical cells (LECs) to track the slow progress of ionic motion which causes the doping of a polymer film under an applied bias.^{145,238–241} The goal of such a technique applied to FETs would be to map the charge density and possibly potential in an analogous way to SKPM but for devices where the channel is inaccessible due to the top gate electrode and dielectric. The obvious route to map charge density would be to take PL images of the device under various operating voltages and compare the image to one taken when the device is depleted of charges. Figure 7.19(a) could then be used to map the change in PL to a charge density. It became quickly apparent however that the change in PL, as the equations suggest, depends on the initial PL lifetime which in the vicinity of metal electrodes is significantly less. The change in PL from charge quenching

is diluted in effect by the additional non-radiative decay path near the electrodes^{49,242} as shown in figures 7.21(a) and 7.21(b) for the F8BT on the electrodes. At the high magnification used for these images of the channel, the intensity of the light becomes significantly higher which manifests itself in a reduction in the fractional change in PL as compared to when measured at lower magnifications. The cause could be though the damaging of the polymer film causing a reduction in the PL efficiency. In addition, changes to the F8BT thickness or the out-coupling of light from the accumulation layer will also have an effect on the fractional change in PL which may explain why the reduced PL quenching near the electrodes extends further into the channel than the exciton diffusion length. In order to properly convert these PL images into charge density maps, one would have to form a three dimensional lookup table generated from taking images at numerous fixed gate voltages and then performing all subsequent measurements without the device moving at all. A processor-heavy computer program would need to be written to relate all subsequent images via the lookup matrix to a charge density. For the current work, maps of the change in PL are shown without attempting to convert to charge density but these are sufficient to understand the physics of the processes involved in device operation.



(a) Image of F8BT PL changes in the channel and on the source and drain electrodes at various gate voltages.

(b) Averaged cross sections from figure 7.21(a)

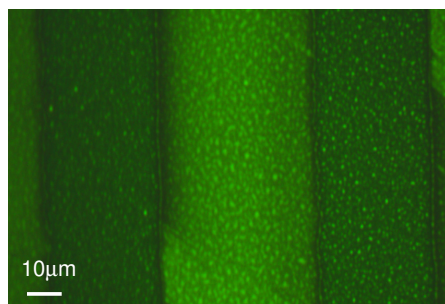
Figure 7.21: Imaging changes in PL in the channel of F8BT transistor B24-6a at various fixed gate voltages. The regions on the left and right of the image and plot are the, shorted and grounded, source and drain electrodes where the change in PL is reduced due to the shorter PL lifetime in the vicinity of the metal.

Figure 7.22 shows a sequence of images that were created by converting still frames, from a video of the PL from an F8BT device during operation, into maps of the difference

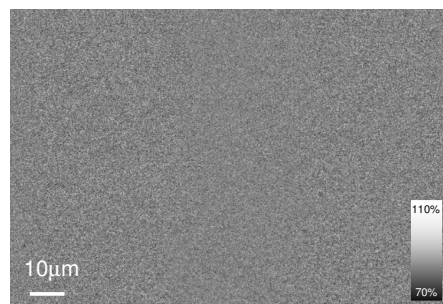
between the PL in that frame and when the device was turned off. The frame rate was approximately 10Hz which gave time to show the charging of the region above the electrodes with the charges spreading up the electrode and into the channel. The charging appeared to occur first in regions where the microscope light was brightest. Figure 7.22(d) shows the device in saturation during hole accumulation. There is no accumulation layer above the source electrode as it is at the same potential as the gate ($V_g = 0$ in all plots) however there is current flowing from source to drain with the charge density reducing as it approaches the pinch off region just before the source. When -100V is applied to what was the source electrode, electrons start accumulating above and the device enters the ambipolar regime with holes being injected from the left and electrons from the right.

The fact that the PL is quenched by the charges in the device seems to be at odds with the ability to observe light emission from ambipolar transistors however, in the recombination zone there is a lower charge density as it is effectively the meeting point of two pinch off saturation regions. The bright line observed in this regime is either light emission or the lack of PL quenching due to the lower charge density in the recombination zone or some combination of the two. When this device was run in the dark over a whole range of voltages, no light emission was observed however under illumination the current increased by 20% which corresponds to an increase of a couple of orders of magnitude when considering the region being illuminated. It is therefore possible that it is electroluminescence being observed in these figures although this would have been easier to confirm had the apparent PL exceeded the original value. We can conclude however that the fact that the PL in the recombination zone does not exceed the value when the device is off appears to suggest that there are some quenching losses in the recombination zone.

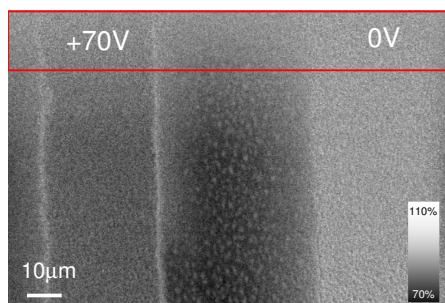
After a few seconds of operation, the recombination zone moves towards the electron-injecting electrode indicating that electron trapping was occurring and increasing the threshold voltage for electron injection. Indeed when the device was turned off again, there is still some quenching above the electron-injecting electrode indicating that trapped electrons with presumably an equal number of compensating holes remain behind. Figure 7.23 shows cross section plots that were averaged from the red regions in figure 7.22. During the device operation it can clearly be seen in figure 7.23(b) that the number of charges above the electron-injecting electrode is reducing with time which suggests that the trapped electrons do not quench the charges. This is confirmed in figure 7.23(c) where after turning the device off the amount of quenching *increases* as compared to the last plot in figure 7.23(b) as the compensating holes move in. With time this quenching starts to reduce as the electrons become detrapped. Turning the device back on again in figure 7.23(d) shows that the PL increases when electrons are being accumulated again because



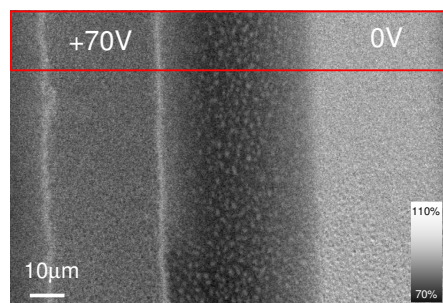
(a) PL image of transistor (darker areas are source and drain electrodes).



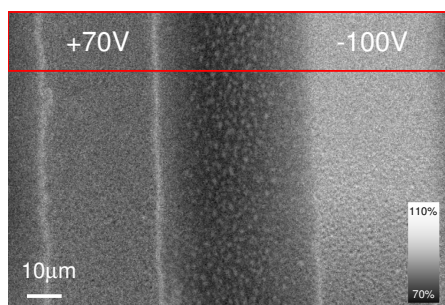
(b) Change between subsequent frames.



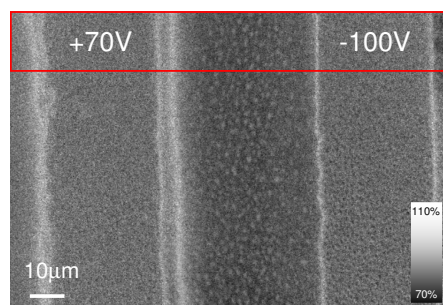
(c) Change in PL after +70V applied.



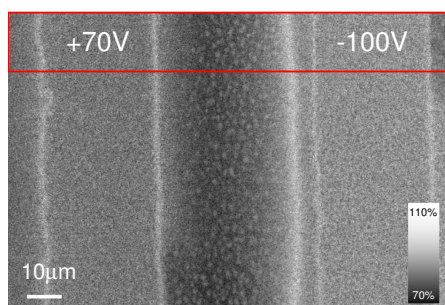
(d) ~ 0.1 s after 7.22(c).



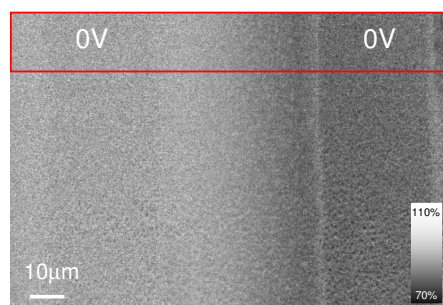
(e) Change in PL after -100V applied.



(f) ~ 0.1 s after 7.22(e).

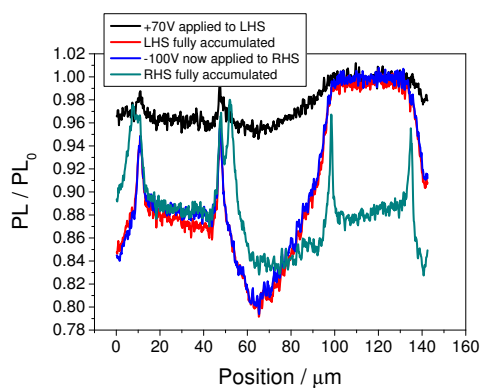


(g) After ~ 2 s of operation.

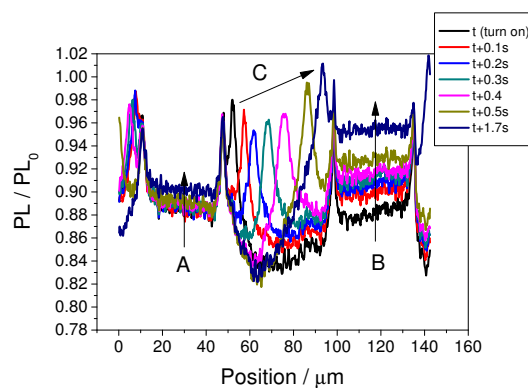


(h) Residual change after turning off.

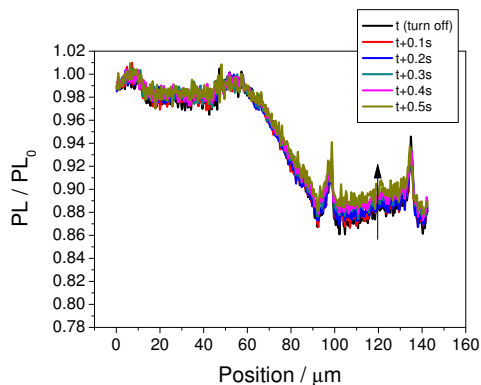
Figure 7.22: Images of PL and PL change during operation of F8BT device B24-6a.



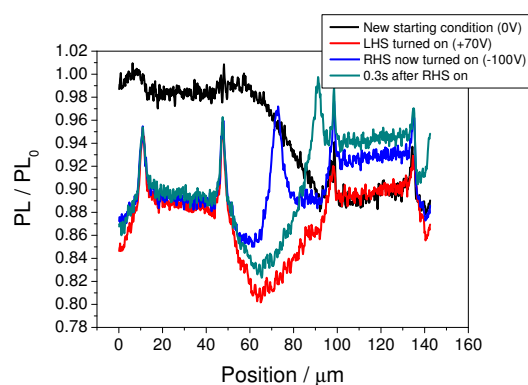
(a) Turning on electrodes as in figures 7.22(a)-7.22(d).



(b) Evolution of PL quenching under constant bias conditions including 7.22(f) and 7.22(g).



(c) Recovery after bias removed as in figure 7.22(h).



(d) Device turned on again.

Figure 7.23: Plots of vertically averaged sections marked with red rectangles in figure 7.22. Gate voltage is zero throughout.

the compensating holes are removed and mostly trapped electrons remain.

It becomes apparent that the device bias history can strongly influence the degree of PL quenching and that the light is a non-invasive method of observation. For this type of experiment to be fully optimised, a modified experimental setup and technique should be adopted. Firstly, the calibration of the PL with zero charges would need to be performed on a brand new device before any kind of bias is applied. The PL lookup table then needs to be created with as few measurements or in as short a time as possible. Finally, if enough sensitivity is possible, the images should be taken with very short flashes of energy gap light to avoid influencing the current and possibly the trapping.

7.6 Implications of charge-induced photoluminescence quenching for electrically pumped lasing

The ability for a full accumulation layer to completely quench all luminescence in F8BT begs the question how light emission is possible at all in LEFETs. Despite there being a lower charge density in the recombination zone the results of the previous chapter suggest that PL quenching does still occur in this region. Naber et al.¹³⁴ showed that when optimising the dielectric to accumulate higher charge densities and mobilities, the EQE of F8BT transistors showed a peak value before reducing at higher current densities. It was suggested that this might be due to the polaron quenching effect although no quantitative study was performed. Estimates made in calculating the out-coupling of light and the open question of singlet exciton yield during bimolecular recombination make it difficult to access the exact amount to which quenching occurs. Capelli et al.²⁴³ recently demonstrated an LEFET with a sandwich structure of a hole transporting layer, emissive layer and electron transmitting layer which demonstrated EQEs that were 10 times that reported in F8BT LEFETs²⁴⁴ and 100 times higher than the equivalent LED structure. It is suggested that this structure is so efficient because the excitons are spatially separated from the mobile charges and electrodes. Again, the degree of polaron quenching that exists or might exist at higher current densities is not known although this technique is a clear improvement. With the LEFET structure being a possible candidate for an electrically pumped organic laser, these losses at high current densities will prove to be decisive. It has been suggested that due to the long triplet lifetime electrically pumped lasing is a physical impossibility as the triplet population build-up and subsequent annihilation with singlet excitons will always reduce the emission efficiency²⁴⁵⁻²⁴⁷. Triplet quenchers have been suggested as a solution to this particular issue. Another problem with these types of

device structure is that the recombination zone tends to move around as trapping occurs and in aligned materials the width can increase thus reducing the gains in exciton density from the higher current.

Figure 7.24 shows a possible approach to solving these two issues whereby a defect in the alignment of F8T2 both pins and narrows the recombination zone for a range of gate voltages. This defect was from spin coating and just happened to be in the channel, but similar defects can be created easily using a dektak to mark a line in the polyimide as shown in figure 7.25. If the defect is narrow enough and can align the F8BT at right angles to the charge transport direction it should also reduce FRET between excitons and charges as the molecular orientation factor would go to zero. A technique like this which reduces the mobility in a narrow region and separates the integral of the emission spectra and polaron absorption spectra overlap could possibly generate the exciton density required for lasing.

7.7 Summary

The absorption of light in conjugated polymers leads predominantly to strongly bound excitons rather than free charges however significant increases in current under energy gap illumination have been observed. The diffusion length and lifetime of the exciton and the spectral overlap between its emission and the absorption by a polaron can lead to very efficient energy transfer to the polaron and occurs for both electrons and holes. The manifestation of this energy transfer is the quenching of the exciton and a kick in energy to the charge which can free it from sites where it has insufficient energy to escape or simply promote mobile charges up in the density of states leading to an increase in current in the cases where some current is already observed in the dark. This process cannot be simulated by shining sub gap light on the device as this process possibly due to the small cross section of charge absorption. There are so many neutral units that can absorb energy gap light that there will be a significant density of excitons in the vicinity of the charge making energy transfer highly likely. The radius for energy transfer has been calculated to be 1.42nm for holes and 1.35nm for electrons which leads to an estimate of the sum of diffusion constants of charges and excitons as being between 4 and 40nm. The gain when shining light on F8BT planar diode structures is fairly constant however annealing and alignment can cause changes in the dark current and, through a constant gain, can cause similar changes in the light current. It has been suggested that moisture or solvent residue in the as-spun films leads to an enhanced current in these devices which reduces upon annealing at temperatures in the region of 120°C-150°C. A slight recovery

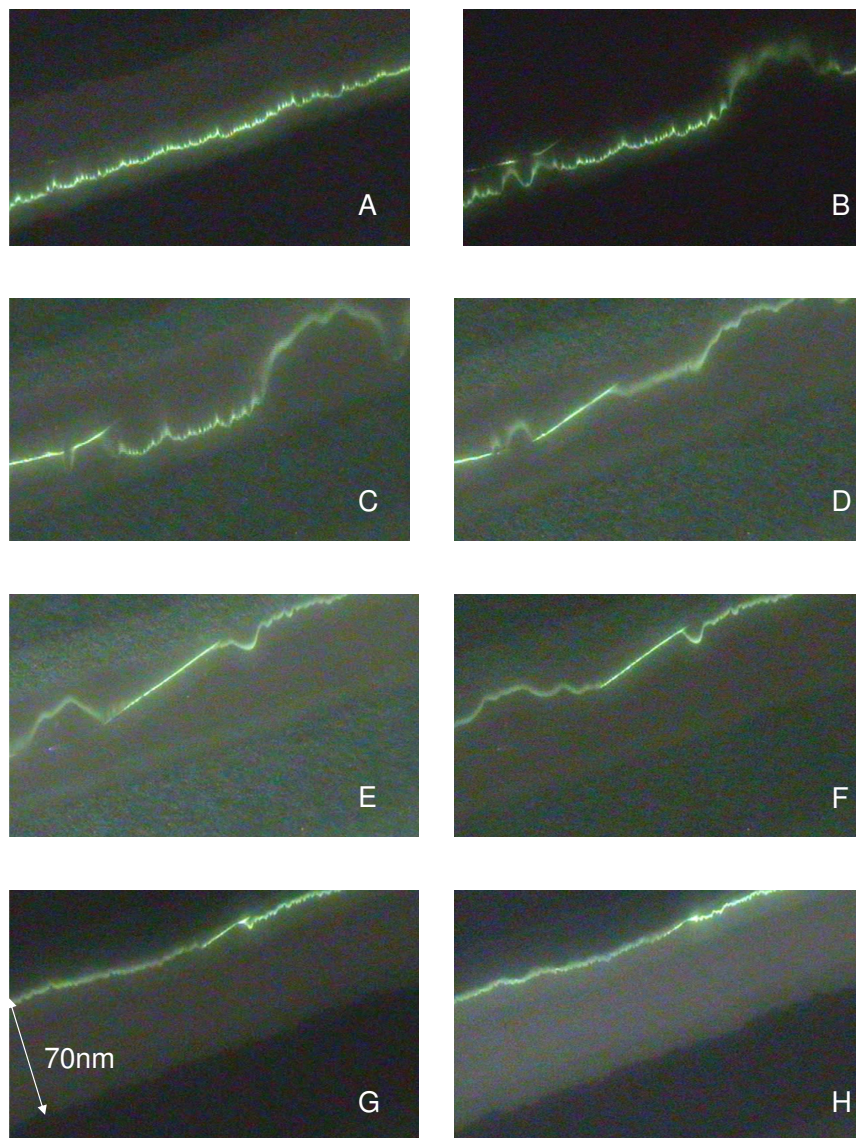


Figure 7.24: F8T2 ambipolar transistor with the polymer chains aligned in the direction of charge transport between the two electrodes (dark regions). Whilst the recombination zone is wide with this kind of alignment, a defect in the channel pins and narrows the recombination zone over a range of voltages.

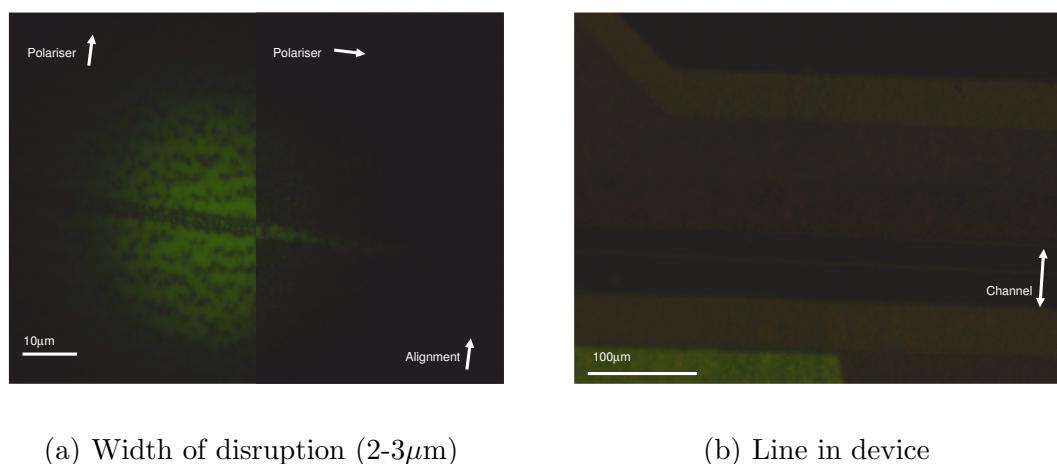


Figure 7.25: Illustration of how the alignment can be disrupted in a narrow region by scanning the dektak needle across the polyimide alignment layer following rubbing and before F8BT deposition.

is seen in the current after the film is annealed around the melting temperature which is attributed to morphological factors which are enhanced when the F8BT polymer is aligned in the direction of charge transport. The gain effect is enhanced when measured in air which may be due to the trapping of electrons leading to a higher supported density of mobile holes.

As well as the photo gain effect there is evidence that in F8BT devices measured in vacuum, with contacts that do not inject current in the dark that it is possible to measure the extraction of photo-generated charges. Again, this process is enhanced with alignment and the morphology improvements following the annealing of the film above its melting temperature. Evidence for this process comes from the measured built-in field and the symmetric photo-current even when using two different metal contacts. The addition of a PFB film to form a heterojunction for charge separation did not appear to increase the photo-current significantly apart from in forward bias where charge injection became possible again. It is proposed that it is the large distances that the charges have to travel in a relatively weak field that cause most of the photo-generated charges to recombine before exiting the device and this is observed as a linear increase in current with voltage.

The efficiency of charge-induced PL quenching has been harnessed to image the operation of a top gate FET in a way that has not been done before. The results of this study reveal information about the location and type of traps that occur in such devices albeit when illuminated with high intensity energy gap light. Indications are that the traps are mostly above the electrodes and this particular trap species does not quench

the luminescence as it may not have an absorption that overlaps with the PL spectrum. This study also concluded that there is at least some degree of exciton quenching in the recombination zone of F8BT LEFETs which explains the behaviour of the EQE at high current densities and would render electrically pumped lasing in this structure impossible. One of many possible routes to avoid exciton quenching and create a stable region of exciton density through manipulation of polymer alignment is suggested.

A number of ways in which to improve this method for imaging device operation have been proposed which should lead to the ability to map charge density in devices in a non-invasive way. It may also turn out that there are subtle effects relating to the drift velocity and the quenching which may enable further information regarding the field to be extracted. It is suggested that a new model be constructed from first principles in order to use this technique to extract the diffusion constants for excitons and polarons much more accurately.

Chapter 8

Conclusions and outlook

8.1 Conclusions and further work

One of the main aims of this work was to take advantage of recently developed ambipolar transistors in order to measure the charge-induced absorptions of both holes and electrons on the same polymer. It turned out that whilst these devices are able to demonstrate ambipolar device operation, the ability to inject charges is severely limited due to a combination of large injection barriers and low semiconductor bulk conductivity. The relatively small absorption cross sections in F8BT coupled with the larger contact resistance meant that the fields required to observe the same change in transmission were approximately 30 times larger in F8BT as compared to state-of-the-art high mobility polymers such as N2200. An artifact exists in this experiment that is due to the field-induced change in thickness of the device was identified and it became clear that a move away from even the thinnest metal gate electrodes was necessary. A conducting polymer was used as a gate electrode which reduced reflections at this interface and yielded reproducible spectra. An unfortunate consequence of this PEDOT:PSS gate electrode was that it had some small changes in charge-induced absorptions during the gate voltage modulation. By exploiting the ability to align F8BT, devices could be made where only the PEDOT absorptions and bleaching were measured enabling this artifact to be removed from all subsequent spectra. The pursuit of clear, reproducible and accurate CMS spectra that was necessary for measuring absorptions on such non-ideal devices led to a number of improvements in the understanding of the experiment. The need to pattern either the semiconductor or the gate, the effect of leakage current, methods to remove electroabsorption effects and the correct normalisation of CMS scans were all investigated and these improvements will enable better future practices for CMS even in the case of materials that are more suited to this kind of experiment.

The results of the CMS experiment on two conjugated polymers revealed interesting similarities and differences between electrons and holes. In the hydro-carbon only polymer F8, the charge absorption for both holes and electrons had the same energy and shape indicating that electron-hole symmetry is observed as expected. In the case of the polymer F8BT which has an additional moiety that tends to localise the electron wavefunction, the symmetry was broken and the shape, size and energy of the absorption differed between electrons and holes. The experimental observations were compared to quantum chemical calculations showing good agreement however it was noted that the F8BT absorptions are highly sensitive to the conjugation length which explains the broad features observed experimentally. In contrast, the F8 film appeared to have more order which was manifest by well resolved absorption features and a double peak in the cation spectra. It is believed

that the planar, β -phase of F8 which can arise following heat treatment or solvent exposure is responsible for this effect.

As well as the charge-induced absorption spectra, a number of other interesting results emerged from the CMS experiment. Firstly, the ability to monitor the capacitance during the scan revealed that in F8BT energy gap light can detrapp charges leading to improved injection which reduces the threshold for charge injection. By comparing devices where the F8BT was aligned in the channel but not on the electrodes, it was clear that this trapping which limits device performance was occurring in the region above the electrodes in the bulk of the F8BT film. In contrast, to this, with F8, energy gap light caused rapid trapping of electrons. It was also noticed that light at the energy at which the electron absorbs also caused trapping to occur indicating the instability of the excited F8 radical anion.

A second interesting observation from the CMS experiment was that the charges were capable of quenching the photo-luminescence completely from a significant thickness of the F8BT film estimated to be around 5nm. Given the thickness of the accumulation is usually estimated at 1nm this indicates the degree to which excitons are able to diffuse during their lifetime. The process for the quenching was attributed to Förster Resonance Energy Transfer from the exciton to the polaron. The measured CMS spectra could be used to estimate the capture radius for this process to be 1.42nm for holes and 1.35nm for electrons which in turn suggested that the excitons and/or charges can diffuse distances of between 4-40nm during the exciton lifetime.

A link was made between the energy transfer from excitons to polarons and the detrapping of charges. The detrapping of charges was investigated further in planar diode configurations and it turned out that when charges can be injected into F8BT, the effect of energy gap light is to multiply the current by a constant factor. The dark current itself turned out to be dependent on the injecting electrode, the annealing history of the F8BT films, the environment in which it is tested and the alignment of the polymer. It appears that some impurities in the film that can be removed with annealing actually serve to increase the current in this planar diode configuration. At annealing temperatures around the melting temperature of the F8BT, the current recovers somewhat which is attributed to improved morphology either on the contacts or in the channel. The current is larger by around 500 times when the polymer is aligned parallel to the field rather than perpendicular to it which is larger than the measured anisotropy in FET devices.

In the case where charges are not injected, which occurs in vacuum for as spun films with bottom contacts or in vacuum with top contacts for annealed films, a photocurrent was observed that was independent of the work function of the contacts and is attributed

to the sweeping out of photo-generated charges. An open circuit voltage of 0.5V was observed in these devices when gold and aluminium electrodes were used. A new patterning technique to enable this measurement to be performed on aligned F8BT devices with a free choice of electrodes yet still maintaining short channel lengths was pioneered for this experiment. Whilst again, for the F8BT only devices, the aligned F8BT in the field direction yielded the highest photocurrent, the addition of PFB to form a bilayer device did not appear to show a conclusive improvement in the device performance. Bimolecular recombination is believed to be limiting the ability to extract charges due to the low field acting over the relatively large distances in these devices.

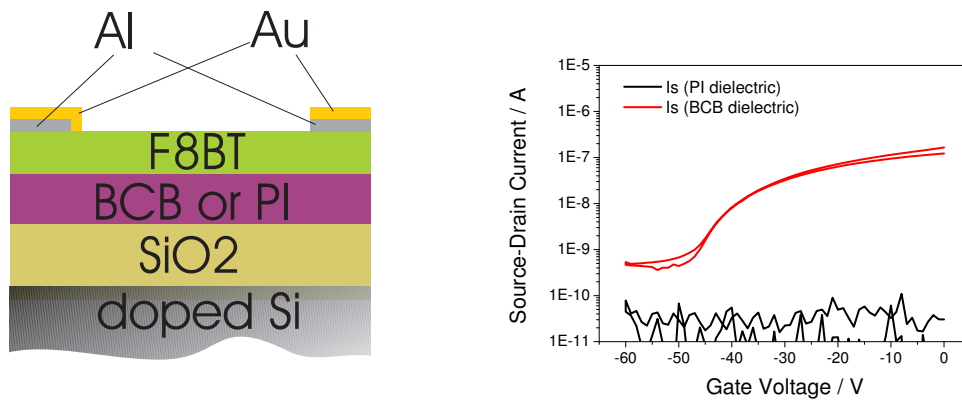
Finally, the previous observation of photo-luminescence quenching from the CMS experiment was exploited to image the device operation of an operating ambipolar F8BT FET. The results indicated that the charge density of mobile charges could be observed and that charge trapping could be mapped. A further observation regarding the degree of photo-luminescence quenching in the recombination zone indicates that polaron-exciton quenching is indeed occurring here and is limiting the efficiency of these devices. In order to get to the higher exciton densities required for lasing, new device architectures will be required to prevent this quenching and one possible method of achieving this is suggested. This technique could serve as a useful way of assessing new device structures to observe the degree of exciton quenching that is present.

It is this last result where further work may be most usefully targeted and there is a lot of work that can be done to improve the imaging technique. A number of suggestions have been made which would enable this technique to non-invasively study the charge density in operating FETs as accurately as SKPM can.

Appendix A

Supporting measurements

Evaporating source drain electrodes onto polyimide (PI) after the rubbing process yields devices where the alignment of the polymer on top of the PI is not aligned in a region around the electrodes. One attempt to avoid this involved trying to evaporate the source and drain electrodes on top of the F8BT after it had been aligned. Attempting this in a top contact/top gate structure resulted in shorted devices so top contact/bottom gate devices were attempted (figure A.1(a)). BCB was also used as a control to check that charge injection was working as electron transport is known to be impossible on bare SiO_2 for most polymers. Figure A.1(b) shows that there is no electron current when PI is used as the dielectric when compared to BCB. There was no hole transport on either devices which may be due to the narrow gold contact which is known not to be optimal for hole injection however the result shows that since there is no electron current, light emission would be impossible.



(a) Top contact, bottom contact structure.

(b) Device transfer characteristics.

Figure A.1: PI and BCB as a dielectrics in bottom gate F8BT transistors.

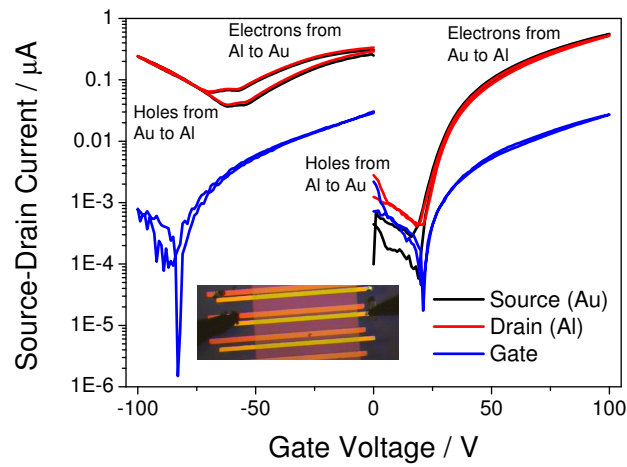
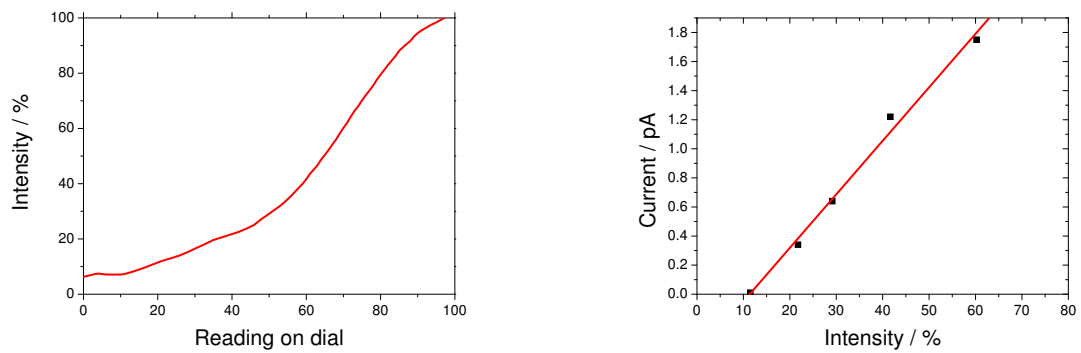


Figure A.2: Closer look at charge injection with an F8BT transistor with separate gold and aluminium electrodes.



(a) Calibration chart for low temperature rig light source¹⁶⁵.

(b) Current at 2V from figure 7.12(a) plotted against % intensity of low temperature rig light source showing linear relationship.

Figure A.3: Calibration curve and current plotted against actual light intensity rather than dial reading corresponding to plot 7.12(a).

Appendix B

Equipment characterisation

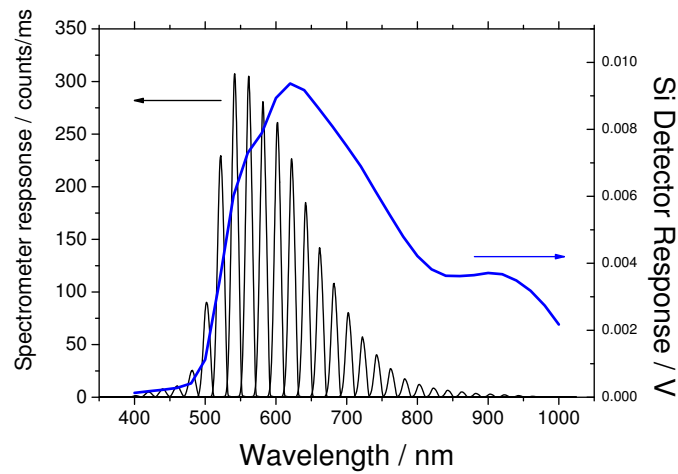


Figure B.1: Comparison of transmitted light detected after a sample in the cryostat with a spectrometer compared to the silicon detector used in CMS.

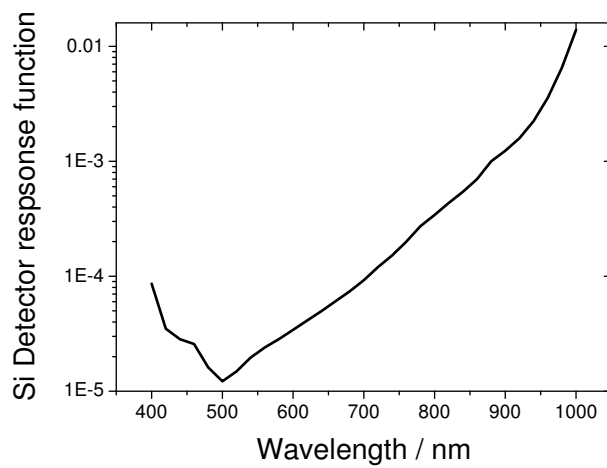


Figure B.2: Shape of the response function of the detector in arbitrary units.

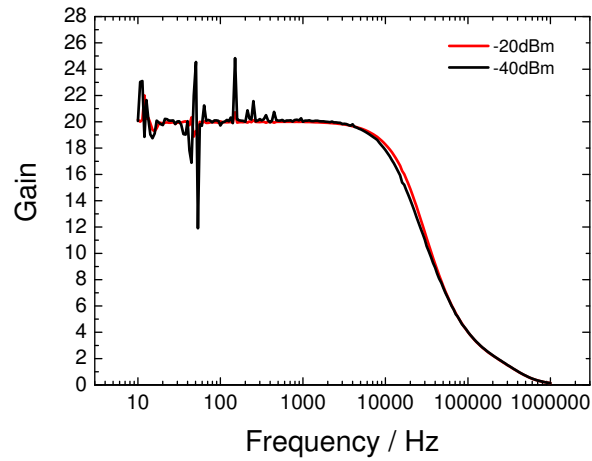


Figure B.3: Frequency response of the gain of amplifier used after the signal generator.

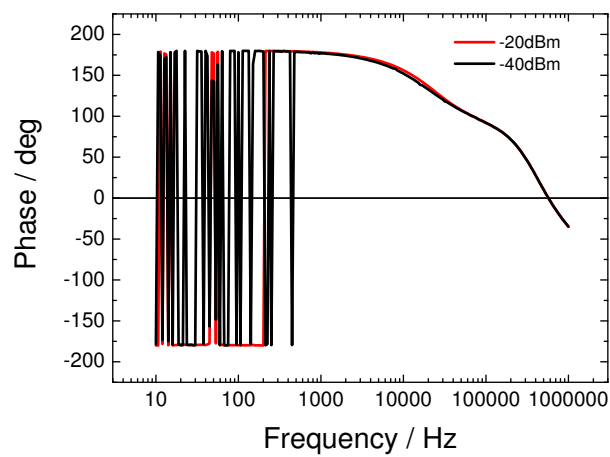


Figure B.4: Frequency response of phase of amplifier used after the signal generator which together with figure [B.3](#) shows the gain is -20.

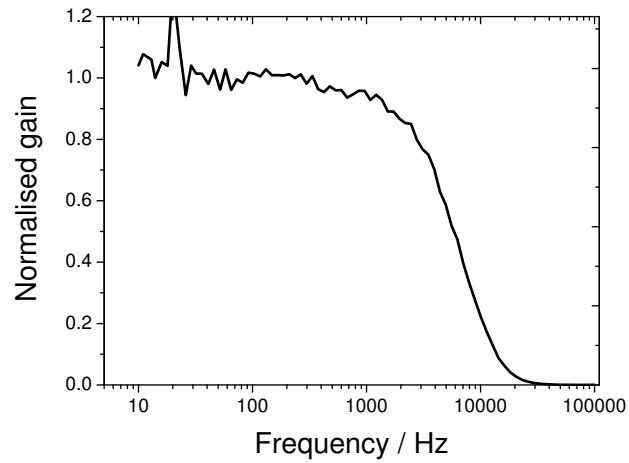


Figure B.5: Frequency response of the (normalised) gain of the detector using a spectral feature from plot 5.18(a).

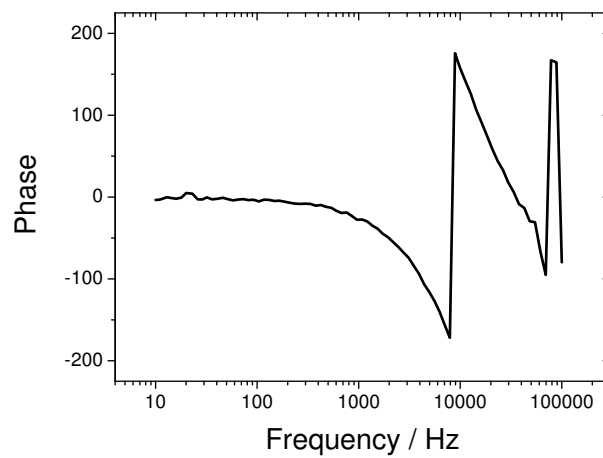


Figure B.6: Frequency response of phase of the detector which comprising of two stages of amplification.

Appendix C

Code

This is the code, to be compiled in Origin, used to solve the equations given in Chapter 4 to produce the data given in the plots.

```

#include <Origin.h>
#include <wksheet.h>
#include <stdio.h>
#include <complex.h>

////////////////////////////////////

double e=1.6e-19; // Elementary charge
double eps0=8.85e-14; // F/cm
double epsr=3.65; // rel eps
double d_ins=500.0e-7; // cm
double d_sc=50.0e-7; // cm double u=1.0e-3; // mobility
double Vg_max=100.0; //max gate voltage
double Vt=0.0; // gate voltage
double rc=1e7; // Contact resistance minimum
double A=100.0e7; //
Contact resistance constant of proportionality
double W=2.0; // Channel width
double Vpp=10.0; // Peak to peak voltage
double L=40.0e-4; // Channel length
double Ac=8.0e-3; //Contact area double
p=3.142; //Pi
double w=2*p*37.0; // Omega
double Vg; // gate voltage
double r; // Resistance per unit length
double R1,R2; // Contact resistance

complex V, Z0_it; double absV,argV,reV,imV;

double Cins=epsr*eps0*Ac/d_ins; //Capacitance of insulator in above contacts
double Csc=epsr*eps0*Ac/d_sc; //Capacitance of semiconductor above contacts
double c=epsr*eps0*W/d_ins; //Capactiance per unit length

```

```
int imax=100; int row_num; int num_rows=100; double x;

double reV_total; double imV_total; double reV_prev; double
imV_prev; double dx=L/num_rows;

void channel(void) {
    Vg=100.0;
    R1=A/(Vg-Vt)+rc;
    R2=A/(Vg-Vt)+rc;
    r=d_ins/(W*u*epsr*eps0*(Vg-Vt));

    //Calculate impedance of channel
    ZO_it=ZOiterative(r);

    int row_num;
    int num_rows=100;
    double x;

    //Create worksheet for cross section of V in device
    Worksheet section_wks;
    section_wks.Create();
    int colnum = section_wks.AddCol("Phase");
    colnum = section_wks.AddCol("RealV");
    colnum = section_wks.AddCol("ImV");

    //Create worksheet for total V in different regions
    //and all device
    Worksheet summary_wks;
    summary_wks.Create();
    colnum = summary_wks.AddCol("Phase");
    colnum = summary_wks.AddCol("RealV");
    colnum = summary_wks.AddCol("ImV");

    reV_total=0.0;
    imV_total=0.0;
```

```

reV_prev=0.0;
imV_prev=0.0;
dx=L/num_rows;

complex arg1(0,w*r*c);
complex arg2(0,w*Cins);
complex arg3(0,w*c/r);
complex arg4(0,w*Csc);

for(row_num=0;row_num<num_rows+1;row_num++){

    //Set x values
    x=L*(row_num)/num_rows;

    //Main function describing the complex V(w,x) in channel
    V=Vpp*(exp(-sqrt(arg1)*x)+exp(sqrt(arg1)*(x-L)))/
    (1+(arg2+1/(R2+1/sqrt(arg3)))/(1/R1+arg4))/(1+R2*sqrt(arg3))
    /(1+exp(-sqrt(arg1)*L)); //for Z0 with infinite L

    //V=Vpp*(exp(-sqrt(arg1)*x)+exp(sqrt(arg1)*(x-L)))/
    (1+(arg2+1/(R2+Z0_it))/(1/R1+arg4))/(1+R2/Z0_it)/
    (1+exp(-sqrt(arg1)*L)); //for Z0 with finite L

    //Get modulus, argument, real and imaginary parts of V
    absV=cabs(V);
    argV=V.GetPhase();
    reV=V.m_re;
    imV=V.m_im;

    //Write values in channel to sheet
    section_wks.SetCell(row_num+1,0,x);
    section_wks.SetCell(row_num+1,1,absV);
    section_wks.SetCell(row_num+1,2,argV);
    section_wks.SetCell(row_num+1,3,reV);
    section_wks.SetCell(row_num+1,4,imV);
}

```

```
//integrate complex V in channel
if(row_num!=0){

    reV_total=reV_total+(reV+reV_prev)*dx/2;
    imV_total=imV_total+(imV+imV_prev)*dx/2;
}

reV_prev=reV;
imV_prev=imV;
}

//Overall complex value for channel as a whole and
//contacts as a whole
complex boundary=Vpp*(exp(-sqrt(arg1)*0.0)
+exp(sqrt(arg1)*(0.0-L)))/(1+(arg2+1/(R2+1/sqrt(arg3)))
/(1/R1+arg4))/(1+R2*sqrt(arg3))/(1+exp(-sqrt(arg1)*L));
//for Z0 with infinite L

//complex boundary=Vpp*(exp(-sqrt(arg1)*0.0)
+exp(sqrt(arg1)*(0.0-L)))/(1+(arg2+1/(R2+Z0_it))
/(1/R1+arg4))/(1+R2/Z0_it)/(1+exp(-sqrt(arg1)*L));
//for Z0 with finite L

complex contacts=boundary*L;
complex channel(reV_total,imV_total);
complex device=contacts+channel;

//Compute complex boundary value of V and get modulus,
//argument, real and imaginary parts
double boundaryABS=cabs(boundary);
double boundaryARG=boundary.GetPhase();
double boundaryRe=boundary.m_re;
double boundaryIm=boundary.m_im;

//Write values at contact edges to sheet
section_wks.SetCell(0,0,-L/2);
```

```
section_wks.SetCell(num_rows+2,0,L+L/2);
section_wks.SetCell(0,1,boundaryABS);
section_wks.SetCell(num_rows+2,1,boundaryABS);
section_wks.SetCell(0,2,boundaryARG);
section_wks.SetCell(num_rows+2,2,boundaryARG);
section_wks.SetCell(0,3,boundaryRe);
section_wks.SetCell(num_rows+2,3,boundaryRe);
section_wks.SetCell(0,4,boundaryIm);
section_wks.SetCell(num_rows+2,4,boundaryIm);

//Calculate overall phase and amplitude in channel and
//total device

double channelABS=cabs(channel);
double channelARG=channel.GetPhase();
double channelRe=channel.m_re;
double channelIm=channel.m_im;

double contactsABS=cabs(contacts);
double contactsARG=contacts.GetPhase();
double contactsRe=contacts.m_re;
double contactsIm=contacts.m_im;

double deviceABS=cabs(device);
double deviceARG=device.GetPhase();
double deviceRe=device.m_re;
double deviceIm=device.m_im;

summary_wks.SetCell(0,0,"Channel");
summary_wks.SetCell(0,1,channelABS);
summary_wks.SetCell(0,2,channelARG);
summary_wks.SetCell(0,3,channelRe);
summary_wks.SetCell(0,4,channelIm);

summary_wks.SetCell(1,0,"Contacts");
summary_wks.SetCell(1,1,contactsABS);
```

```
summary_wks.SetCell(1,2,contactsARG);
summary_wks.SetCell(1,3,contactsRe);
summary_wks.SetCell(1,4,contactsIm);

summary_wks.SetCell(2,0,"Device");
summary_wks.SetCell(2,1,deviceABS);
summary_wks.SetCell(2,2,deviceARG);
summary_wks.SetCell(2,3,deviceRe);
summary_wks.SetCell(2,4,deviceIm);
}

void devchan(void) {

    //Create worksheet for total V in different regions and all device
    Worksheet summary_wks;
    summary_wks.Create();
    int colnum = summary_wks.AddCol("QdevIm");
    colnum = summary_wks.AddCol("QdevABS");
    colnum = summary_wks.AddCol("QdevPhase");
    colnum = summary_wks.AddCol("QchanRe");
    colnum = summary_wks.AddCol("QchanIm");
    colnum = summary_wks.AddCol("QchanABS");
    colnum = summary_wks.AddCol("QchanPhase");

    for(int i=0;i<imax+1;i++){

        Vg=i*Vg_max/imax;
        R1=A/(Vg-Vt)+rc;
        R2=A/(Vg-Vt)+rc;
        r=d_ins/(W*u*epsr*eps0*(Vg-Vt));
        Z0_it=Z0iterative(r);

        reV_total=0.0;
        imV_total=0.0;
        reV_prev=0.0;
        imV_prev=0.0;
    }
}
```

```

complex arg1(0,w*r*c);
complex arg2(0,w*Cins);
complex arg3(0,w*c/r);
complex arg4(0,w*Csc);
complex arg5(0,w);

for(row_num=0;row_num<num_rows+1;row_num++){

    //Set x values
    x=L*(row_num)/num_rows;

    //Main function describing the complex V(w,x) in channel
    //V=Vpp*(exp(-sqrt(arg1)*x)+exp(sqrt(arg1)*(x-L)))/
    (1+(arg2+1/(R2+1/sqrt(arg3)))/(1/R1+arg4))/(1+R2*sqrt(arg3))
    /(1+exp(-sqrt(arg1)*L)); //for infinite Z0

    V=Vpp*(exp(-sqrt(arg1)*x)+exp(sqrt(arg1)*(x-L)))/
    (1+(arg2+1/(R2+Z0_it))/(1/R1+arg4))/(1+R2/Z0_it)/
    (1+exp(-sqrt(arg1)*L)); //for finite Z0

    //Get modulus, argument, real and imaginary parts of V
    absV=cabs(V);
    argV=V.GetPhase();
    reV=V.m_re;
    imV=V.m_im;

    //integrate complex V in channel
    if(row_num!=0){

        reV_total=reV_total+(reV+reV_prev)*dx/2;
        imV_total=imV_total+(imV+imV_prev)*dx/2;
    }

    reV_prev=reV;
    imV_prev=imV;
}

```

```
}

//calculate admittance of device as a whole
//complex Zdev=1/(1/R1+arg4)+1/(arg2+1/(R2+(sqrt(1.0/arg3)))));
//for infinte Z0

complex Zdev=1/(1/R1+arg4)+1/(arg2+1/(R2+Z0_it));
//for finite Z0

complex channel(reV_total,imV_total);

//Overall complex value for channel as a whole and contacts
//as a whole

complex Qchan=channel*c/e;
complex Qdev=Vpp/Zdev/arg5/e;

//Calculate overall phase and amplitude in channel and
//total device

double channelABS=cabs(Qchan);
double channelARG=Qchan.GetPhase();
double channelRe=Qchan.m_re;
double channelIm=Qchan.m_im;

double deviceABS=cabs(Qdev);
double deviceARG=Qdev.GetPhase();
double deviceRe=Qdev.m_re;
double deviceIm=Qdev.m_im;

summary_wks.SetCell(i,0,Vg);
summary_wks.SetCell(i,1,deviceRe);
summary_wks.SetCell(i,2,deviceIm);
summary_wks.SetCell(i,3,deviceABS);
summary_wks.SetCell(i,4,deviceARG);
summary_wks.SetCell(i,5,channelRe);
```

```
        summary_wks.SetCell(i,6,channelIm);
        summary_wks.SetCell(i,7,channelABS);
        summary_wks.SetCell(i,8,channelARG);
    }

}

complex Z0iterative(double r_){

    double looptotalRe,looptotalIm,inftyZ0Re,inftyZ0Im;

    int loop_max=1000;
    double dl=L/loop_max;
    double rdl=r_*dl;
    complex total,temp;
    complex iwcdl(0,w*c*dl);
    complex inftyZ0=sqrt(rdl/iwcdl);

    for(int loop=0;loop<loop_max;loop++){
        if(loop==0){
            total=rdl+1/iwcdl;
        }
        else{
            temp=iwcdl+1/total;
            total=rdl+1/temp;
        }

        looptotalRe=total.m_re;
        looptotalIm=total.m_im;
    }

    return total;

}
```

References

1. R. McNeill, R. Siudak, J. H. Wardlaw and D. E. Weiss. Electronic conduction in polymers. i. the chemical structure of polypyrrole. *Australian Journal of Chemistry*, **16**(19), 1056 (1963). [2](#), [138](#)
2. R. McNeill, R. Siudak, J. H. Wardlaw and D. E. Weiss. Electronic conduction in polymers. ii. the electrochemical reduction of polypyrrole at controlled potential. *Australian Journal of Chemistry*, **16**(13), 1076 (1963). [2](#), [138](#)
3. R. McNeill, R. Siudak, J. H. Wardlaw and D. E. Weiss. Electronic conduction in polymers. iii. electronic properties of polypyrrole. *Australian Journal of Chemistry*, **16**(13), 1090 (1963). [2](#), [138](#)
4. C. K. Chiang, C. R. Fincher, Y. W. Park, A. J. Heeger, H. Shirakawa, E. J. Louis, S. C. Gau and A. G. MacDiarmid. Electrical conductivity in doped polyacetylene. *Phys. Rev. Lett.*, **39**(17), 1098–1101 Oct 1977. [2](#), [17](#), [138](#)
5. A. J. Heeger. Nobel lecture: Semiconducting and metallic polymers: The fourth generation of polymeric materials. *Reviews of Modern Physics*, **73**(3), 681 (2001). [2](#)
6. F. Ebisawa, T. Kurokawa and S. Nara. Electrical properties of polyacetylene/polysiloxane interface. *Journal of Applied Physics*, **54**(6), 3255–3259 (1983). [2](#)
7. A. Tsumura, H. Koezuka and T. Ando. Macromolecular electronic device: Field-effect transistor with a polythiophene thin film. *Applied Physics Letters*, **49**(18), 1210–1212 (1986). [2](#)
8. J. H. Burroughes, D. D. C. Bradley, A. R. Brown, R. N. Marks, K. Mackay, R. H. Friend, P. L. Burns and A. B. Holmes. Light-emitting diodes based on conjugated polymers. *Nature*, **347**(6293), 539–541 (1990). [2](#)

9. S. Karg, W. Riess, V. Dyakonov and M. Schwoerer. Electrical and optical characterization of poly(phenylene-vinylene) light emitting diodes. *Synthetic Metals*, **54**(1-3), 427–433 (1993). [2](#)
10. M. Granstrom, K. Petritsch, A. C. Arias, A. Lux, M. R. Andersson and R. H. Friend. Laminated fabrication of polymeric photovoltaic diodes. *Nature*, **395**(6699), 257–260 (1998). [2](#), [37](#)
11. G. Yu and A. J. Heeger. Charge separation and photovoltaic conversion in polymer composites with internal donor/acceptor heterojunctions. *Journal of Applied Physics*, **78**(7), 4510–4515 (1995). [2](#), [37](#)
12. J. J. M. Halls, C. A. Walsh, N. C. Greenham, E. A. Marseglia, R. H. Friend, S. C. Moratti and A. B. Holmes. Efficient photodiodes from interpenetrating polymer networks. *Nature*, **376**(6540), 498–500 (1995). [2](#), [37](#)
13. K. Tada, K. Hosoda, M. Hirohata, R. Hidayat, T. Kawai, M. Onoda, M. Teraguchi, T. Masuda, A. A. Zakhidov and K. Yoshino. Donor polymer (pat6) – acceptor polymer (cnppv) fractal network photocells. *Synthetic Metals*, **85**(1-3), 1305–1306 (1997). [2](#), [37](#)
14. S. Iijima and T. Ichihashi. Single-shell carbon nanotubes of 1-nm diameter. *Nature*, **363**(6430), 603–605 (1993). [2](#)
15. H. W. Kroto, J. R. Heath, S. C. O’Brien, R. F. Curl and R. E. Smalley. C60: Buckminsterfullerene. *Nature*, **318**(6042), 162–163 (1985). [2](#)
16. K. S. Novoselov, A. K. Geim, S. V. Morozov, D. Jiang, Y. Zhang, S. V. Dubonos, I. V. Grigorieva and A. A. Firsov. Electric field effect in atomically thin carbon films. *Science*, **306**(5696), 666–669 (2004). [2](#)
17. A. K. Geim and K. S. Novoselov. The rise of graphene. *Nat Mater*, **6**(3), 183–191 (2007). [2](#)
18. K. S. Kim, Y. Zhao, H. Jang, S. Y. Lee, J. M. Kim, K. S. Kim, J.-H. Ahn, P. Kim, J.-Y. Choi and B. H. Hong. Large-scale pattern growth of graphene films for stretchable transparent electrodes. *Nature*, **457**(7230), 706–710 (2009). [2](#)
19. Notable products include the first small molecule OLED television, the Sony XEL-1; the first e-reader incorporating solution-processed OFETs, the Plastic Logic QUE Reader; the first device with a PLED display, the Philips Philishave HQ8894 Sensotec

- Shaver using a Cambridge Display Technology display; the first polymer solar cell product, Neuber's Energy Sun-Bags using a Konarka panel and the Samsung Super-AMOLED which is the current high standard in OLED mobile displays. [2](#)
20. N. W. Ashcroft and D. N. Mermin. *Solid State Physics*. Brooks/Cole, (1976). [2](#)
 21. C. Kittel. *Introduction to Solid State Physics*. Wiley, (2004). [2](#)
 22. P. W. Anderson. Absence of diffusion in certain random lattices. *Physical Review*, **109**(5), 1492 (1958). [2](#), [23](#)
 23. J. Veres, S. Ogier, S. Leeming, D. Cupertino and S. M. Khaffaf. Low- ϵ insulators as the choice of dielectrics in organic field-effect transistors. *Advanced Functional Materials*, **13**(3), 199–204 (2003). [2](#), [34](#), [98](#)
 24. M. Pope and C. E. C. E. Swenberg. *Electronic Processes in Organic Crystals*. Clarendon Press, Oxford, (1955). [2](#), [16](#)
 25. M. P. De Haas and J. M. Warman. Photon-induced molecular charge separation studied by nanosecond time-resolved microwave conductivity. *Chemical Physics*, **73**(1-2), 35–53 (1982). [2](#)
 26. G. Dicker, M. P. de Haas, L. D. A. Siebbeles and J. M. Warman. Electrodeless time-resolved microwave conductivity study of charge-carrier photogeneration in regioregular poly(3-hexylthiophene) thin films. *Physical Review B*, **70**(4), 045203 (2004). [2](#)
 27. E. Hendry, J. M. Schins, L. P. Candeias, L. D. A. Siebbeles and M. Bonn. Efficiency of exciton and charge carrier photogeneration in a semiconducting polymer. *Physical Review Letters*, **92**(19), 196601 (2004). [2](#)
 28. J.-M. Zhuo, L.-H. Zhao, P.-J. Chia, W.-S. Sim, R. H. Friend and P. K. H. Ho. Direct evidence for delocalization of charge carriers at the fermi level in a doped conducting polymer. *Physical Review Letters*, **100**(18), 186601 (2008). [2](#), [127](#), [139](#), [144](#)
 29. J. T. L. Navarrete and G. Zerbi. Lattice dynamics and vibrational spectra of polythiophene. ii. effective coordinate theory, doping induced, and photoexcited spectra. *The Journal of Chemical Physics*, **94**(2), 965–970 (1991). [3](#)
 30. K. E. Ziemelis, A. T. Hussain, D. D. C. Bradley, R. H. Friend, J. Rhe and G. Wegner. Optical spectroscopy of field-induced charge in poly(3-hexyl thienylene) metal-insulator-semiconductor structures: Evidence for polarons. *Physical Review Letters*, **66**(17), 2231 (1991). [3](#), [17](#)

31. L.-L. Chua, J. Zaumseil, J.-F. Chang, E. C. W. Ou, P. K. H. Ho, H. Sirringhaus and R. H. Friend. General observation of n-type field-effect behaviour in organic semiconductors. *Nature*, **434**(7030), 194–199 (2005). 3, 32, 94
32. J. Zaumseil, C. Donley, J.-S. Kim, R. Friend and H. Sirringhaus. Efficient top-gate, ambipolar, light-emitting field-effect transistors based on a green-light-emitting polyfluorene. *Advanced Materials*, **18**(20), 2708–2712 (2006). 3, 51, 92, 141, 181
33. A. W. Grice, D. D. C. Bradley, M. T. Bernius, M. Inbasekaran, W. W. Wu and E. P. Woo. High brightness and efficiency blue light-emitting polymer diodes. *Applied Physics Letters*, **73**(5), 629–631 (1998). 3
34. M. Redecker, D. D. C. Bradley, M. Inbasekaran and E. P. Woo. Nondispersive hole transport in an electroluminescent polyfluorene. *Applied Physics Letters*, **73**(11), 1565–1567 (1998). 3, 141
35. Y. He, S. Gong, R. Hattori and J. Kanicki. High performance organic polymer light-emitting heterostructure devices. *Applied Physics Letters*, **74**(16), 2265–2267 (1999). 3
36. C. L. Donley, J. Zaumseil, J. W. Andreasen, M. M. Nielsen, H. Sirringhaus, R. H. Friend and J.-S. Kim. Effects of packing structure on the optoelectronic and charge transport properties in poly(9,9-di-n-octylfluorene-alt-benzothiadiazole). *Journal of the American Chemical Society*, **127**(37), 12890–12899 (2005). 3, 141, 186
37. J. Cornil, I. Gueli, A. Dkhissi, J. C. Sancho-Garcia, E. Hennebicq, J. P. Calbert, V. Lemaure, D. Beljonne and J. L. Bredas. Electronic and optical properties of polyfluorene and fluorene-based copolymers: A quantum-chemical characterization. *The Journal of Chemical Physics*, **118**(14), 6615–6623 (2003). 3, 139
38. <http://www.science.uwaterloo.ca/~cchieh/cact/c120/hybridcarbon.html>. 7
39. <http://www-teach.ch.cam.ac.uk/teach/A4/lect5.pdf>. 10
40. F. A. Cotton. *Chemical Applications of Group Theory (Third Edition)*. Wiley, (1990). 11
41. R. Peierls. *Quantum theory of solids*. Clarendon Press, Oxford, (1999). 11
42. J.-L. Brdas, J. Cornil, D. Beljonne, D. A. dos Santos and Z. Shuai. Excited-state electronic structure of conjugated oligomers and polymers: a quantum-chemical

- approach to optical phenomena. *Accounts of Chemical Research*, **32**(3), 267–276 (1999). [13](#)
43. Sze. *Physics of Semiconductor Devices (Second Edition)*. Wiley, (1981). [14](#), [38](#), [40](#), [42](#), [181](#)
44. W. Y. Liang. Excitons. *Physics Education*, **5**(4), 226 (1970). [14](#)
45. G. H. Wannier. The structure of electronic excitation levels in insulating crystals. *Physical Review*, **52**(3), 191 (1937). [14](#)
46. D. Veldman, S. C. J. Meskers and R. A. J. Janssen. The energy of charge-transfer states in electron donor-acceptor blends: Insight into the energy losses in organic solar cells. *Advanced Functional Materials*, **19**(12), 1939–1948 (2009). [15](#)
47. A. Abrusci. *Bulk Heterojunction Solar Cells Based on a Polyfluorene Copolymer*. PhD thesis, University of Cambridge, (2009). [16](#), [36](#)
48. A. Haugeneder, M. Neges, C. Kallinger, W. Spirkl, U. Lemmer, J. Feldmann, U. Scherf, E. Harth, U. Mühl, A. Gel and K. Henning. Exciton diffusion and dissociation in conjugated polymer/fullerene blends and heterostructures. *Physical Review B*, **59**(23), 15346 (1999). [15](#)
49. H. Becker, S. E. Burns and R. H. Friend. Effect of metal films on the photoluminescence and electroluminescence of conjugated polymers. *Physical Review B*, **56**(4), 1893 (1997). [15](#), [212](#)
50. V. I. Arkhipov and H. Bässler. Exciton dissociation and charge photogeneration in pristine and doped conjugated polymers. *physica status solidi (a)*, **201**(6), 1152–1187 (2004). [15](#), [181](#)
51. S. A. Zapunidi, Y. V. Krylova and D. Y. Paraschuk. Analytical model for photoluminescence quenching via Förster resonant energy transfer in a conjugated polymer doped by energy acceptors. *Physical Review B*, **79**(20), 205208 (2009). [15](#), [185](#)
52. H. Nakanotani, H. Sasabe and C. Adachi. Singlet-singlet and singlet-heat annihilations in fluorescence-based organic light-emitting diodes under steady-state high current density. *Applied Physics Letters*, **86**(21), 213506–3 (2005). [17](#)

53. Y. Zaushitsyn, K. G. Jespersen, L. Valkunas, V. Sundström and A. Yartsev. Ultrafast dynamics of singlet-singlet and singlet-triplet exciton annihilation in poly(3-2'-methoxy-5'-octylphenyl)thiophene films. *Physical Review B*, **75**(19), 195201 (2007). [17](#)
54. S. M. King, D. Dai, C. Rothe and A. P. Monkman. Exciton annihilation in a polyfluorene: Low threshold for singlet-singlet annihilation and the absence of singlet-triplet annihilation. *Physical Review B*, **76**(8), 085204 (2007). [17](#), [181](#)
55. U. Albrecht and H. Bässler. Langevin-type charge carrier recombination in a disordered hopping system. *physica status solidi (b)*, **191**(2), 455–459 (1995). [17](#)
56. P. W. M. Blom, M. J. M. de Jong and S. Breedijk. Temperature dependent electron-hole recombination in polymer light-emitting diodes. *Applied Physics Letters*, **71**(7), 930–932 (1997). [17](#)
57. M. Wohlgenannt, K. Tandon, S. Mazumdar, S. Ramasesha and Z. V. Vardeny. Formation cross sections of singlet and triplet excitons in [π]-conjugated polymers. *Nature*, **409**(6819), 494–497 (2001). [17](#)
58. W. P. Su, J. R. Schrieffer and A. J. Heeger. Solitons in polyacetylene. *Physical Review Letters*, **42**(25), 1698 (1979). [17](#), [138](#)
59. K. Fesser, A. R. Bishop and D. K. Campbell. Optical absorption from polarons in a model of polyacetylene. *Physical Review B*, **27**(8), 4804 (1983). [18](#), [138](#)
60. P. Brown. *Charge Modulation Spectroscopy of Poly(3-alkylthiophene)*. PhD thesis, University of Cambridge, (2000). [21](#), [93](#)
61. P. W. M. Blom, M. J. M. de Jong and M. G. van Munster. Electric-field and temperature dependence of the hole mobility in poly(p-phenylene vinylene). *Physical Review B*, **55**(2), R656 (1997). [21](#)
62. C. Tanase, E. J. Meijer, P. W. M. Blom and D. M. de Leeuw. Unification of the hole transport in polymeric field-effect transistors and light-emitting diodes. *Physical Review Letters*, **91**(21), 216601 (2003). [21](#), [27](#)
63. L. Bozano, S. A. Carter, J. C. Scott, G. G. Malliaras and P. J. Brock. Temperature- and field-dependent electron and hole mobilities in polymer light-emitting diodes. *Applied Physics Letters*, **74**(8), 1132–1134 (1999). [21](#)

64. N. Tessler, Y. Preezant, N. Rappaport and Y. Roichman. Charge transport in disordered organic materials and its relevance to thin-film devices: A tutorial review. *Advanced Materials*, **21**(27), 2741–2761 (2009). [21](#), [27](#)
65. V. Coropceanu, J. Cornil, D. A. da Silva Filho, Y. Olivier, R. Silbey and J.-L. Brdas. Charge transport in organic semiconductors. *Chemical Reviews*, **107**(4), 926–952 (2007). [21](#)
66. N. F. Mott and W. D. Twose. The theory of impurity conduction. *Advances in Physics*, **10**(38), 107 – 163 (1961). [22](#), [23](#)
67. P. G. Le Comber and W. E. Spear. Electronic transport in amorphous silicon films. *Physical Review Letters*, **25**(8), 509 (1970). [22](#)
68. N. F. Mott. On the transition to metallic conduction in semiconductors. *Canadian Journal of Physics*, **34**(12), 1356 – 1368 (1956). [23](#)
69. E. M. Conwell. Impurity band conduction in germanium and silicon. *Physical Review*, **103**(1), 51 (1956). [23](#)
70. A. Miller and E. Abrahams. Impurity conduction at low concentrations. *Physical Review*, **120**(3), 745 (1960). [23](#), [26](#)
71. R. A. Marcus. Electron transfer reactions in chemistry. theory and experiment. *Reviews of Modern Physics*, **65**(3), 599 (1993). [23](#), [25](#)
72. H. Frhlich, H. Pelzer and S. Zienau. Xx. properties of slow electrons in polar materials. *Philosophical Magazine Series 7*, **41**(314), 221 – 242 (1950). [24](#), [34](#)
73. L. Landau. *Phys. Z. Sowjet*, **3**, 664 (1933). [24](#)
74. T. Holstein. Studies of polaron motion : Part i. the molecular-crystal model. *Annals of Physics*, **8**(3), 325–342 (1959). [24](#)
75. T. Holstein. Studies of polaron motion : Part ii. the "small" polaron. *Annals of Physics*, **8**(3), 343–389 (1959). [24](#)
76. R. A. Marcus. Nonadiabatic processes involving quantum-like and classical-like coordinates with applications to nonadiabatic electron transfers. *The Journal of Chemical Physics*, **81**(10), 4494–4500 (1984). [24](#)

77. J. R. Miller, L. T. Calcaterra and G. L. Closs. Intramolecular long-distance electron transfer in radical anions. the effects of free energy and solvent on the reaction rates. *Journal of the American Chemical Society*, **106**(10), 3047–3049 (1984). 25
78. M. C. J. M. Vissenberg and M. Matters. Theory of the field-effect mobility in amorphous organic transistors. *Physical Review B*, **57**(20), 12964 (1998). 27
79. V. Ambegaokar, B. I. Halperin and J. S. Langer. Hopping conductivity in disordered systems. *Physical Review B*, **4**(8), 2612 (1971). 27
80. G. E. Pike and C. H. Seager. Percolation and conductivity: A computer study. i. *Physical Review B*, **10**(4), 1421 (1974). 27
81. E. J. Meijer, C. Tanase, P. W. M. Blom, E. van Veenendaal, B. H. Huisman, D. M. de Leeuw and T. M. Klapwijk. Switch-on voltage in disordered organic field-effect transistors. *Applied Physics Letters*, **80**(20), 3838–3840 (2002). 28
82. V. I. Arkhipov and et al. Weak-field carrier hopping in disordered organic semiconductors: the effects of deep traps and partly filled density-of-states distribution. *Journal of Physics: Condensed Matter*, **14**(42), 9899 (2002). 28
83. A. Peled, L. B. Schein and D. Glatz. Hole mobilities in films of a pyrazoline:polycarbonate molecularly doped polymer. *Physical Review B*, **41**(15), 10835 (1990). 28
84. L. B. Schein, D. Glatz and J. C. Scott. Observation of the transition from adiabatic to nonadiabatic small polaron hopping in a molecularly doped polymer. *Physical Review Letters*, **65**(4), 472 (1990). 29
85. S. V. Novikov, D. H. Dunlap, V. M. Kenkre, P. E. Parris and A. V. Vannikov. Essential role of correlations in governing charge transport in disordered organic materials. *Physical Review Letters*, **81**(20), 4472 (1998). 29
86. H. Bässler. Charge transport in disordered organic photoconductors a monte carlo simulation study. *physica status solidi (b)*, **175**(1), 15–56 (1993). 30
87. P. E. Parris, V. M. Kenkre and D. H. Dunlap. Nature of charge carriers in disordered molecular solids: Are polarons compatible with observations? *Physical Review Letters*, **87**(12), 126601 (2001). 30
88. I. I. Fishchuk, A. Kadashchuk, H. Bessler and S. Neprek. Nondispersive polaron transport in disordered organic solids. *Physical Review B*, **67**(22), 224303 (2003). 30

-
89. I. I. Fishchuk, V. I. Arkhipov, A. Kadashchuk, P. Heremans and H. Bessler. Analytic model of hopping mobility at large charge carrier concentrations in disordered organic semiconductors: Polarons versus bare charge carriers. *Physical Review B*, **76**(4), 045210 (2007). [30](#)
90. K.-i. Nakayama, M. Umehara and M. Yokoyama. Electron injection layers consisting of naphthalene tetracarboxylic dianhydride and indium in n-type organic field-effect transistors. *Japanese Journal of Applied Physics*, **45**(Copyright (C) 2006 The Japan Society of Applied Physics), 974 (2006). [30](#)
91. R. Schroeder, L. A. Majewski and M. Grell. Improving organic transistor performance with schottky contacts. *Applied Physics Letters*, **84**(6), 1004–1006 (2004). [30](#)
92. J. C. Riviere. The work function of gold. *Applied Physics Letters*, **8**(7), 172–172 (1966). [30](#)
93. R. M. Eastment and C. H. B. Mee. Work function measurements on (100), (110) and (111) surfaces of aluminium. *Journal of Physics F: Metal Physics*, **3**(9), 1738 (1973). [30](#)
94. M. Chelvayohan and C. H. B. Mee. Work function measurements on (110), (100) and (111) surfaces of silver. *Journal of Physics C: Solid State Physics*, **15**(10), 2305 (1982). [30](#)
95. A. Emelyanov. Electron work function estimated from the delay time of breakdown in vacuum. *Technical Physics Letters*, **29**(1), 39–40 (2003). [30](#)
96. L. Armand, J. L. Bouillot and L. Gaudart. Photoemission of thin and ultrathin films of calcium. *Surface Science*, **86**, 75–82 (1979). [30](#)
97. A. R. Brown, D. D. C. Bradley, J. H. Burroughes, R. H. Friend, N. C. Greenham, P. L. Burn, A. B. Holmes and A. Kraft. Poly(p-phenylenevinylene) light-emitting diodes: Enhanced electroluminescent efficiency through charge carrier confinement. *Applied Physics Letters*, **61**(23), 2793–2795 (1992). [30](#)
98. N. Koch, A. Vollmer and A. Elschner. Influence of water on the work function of conducting poly(3,4-ethylenedioxythiophene)/poly(styrenesulfonate). *Applied Physics Letters*, **90**(4), 043512–3 (2007). [30](#)

99. A. Wan, J. Hwang, F. Amy and A. Kahn. Impact of electrode contamination on the [alpha]-npd/au hole injection barrier. *Organic Electronics*, **6**(1), 47–54 (2005). [30](#)
100. L. Lindell, A. Burquel, F. L. E. Jakobsson, V. Lemaire, M. Berggren, R. Lazzaroni, J. Cornil, W. R. Salaneck and X. Crispin. Transparent, plastic, low-work-function poly(3,4-ethylenedioxythiophene) electrodes. *Chemistry of Materials*, **18**(18), 4246–4252 (2006). [30](#)
101. B. de Boer, A. Hadipour, M. Mandoc, T. van Woudenberg and P. Blom. Tuning of metal work functions with self-assembled monolayers. *Advanced Materials*, **17**(5), 621–625 (2005). [31](#)
102. B. H. Hamadani, D. A. Corley, J. W. Ciszek, J. M. Tour and D. Natelson. Controlling charge injection in organic field-effect transistors using self-assembled monolayers. *Nano Letters*, **6**(6), 1303–1306 (2006). [31](#)
103. T. Shizuo and et al. Metal oxides as a hole-injecting layer for an organic electroluminescent device. *Journal of Physics D: Applied Physics*, **29**(11), 2750 (1996). [31](#)
104. H. T. Nicolai, G. A. H. Wetzelaer, M. Kuik, A. J. Kronemeijer, B. de Boer and P. W. M. Blom. Space-charge-limited hole current in poly(9,9-dioctylfluorene) diodes. *Applied Physics Letters*, **96**(17), 172107–3 (2010). [31](#)
105. F. Rissner, G. M. Rangger, O. T. Hofmann, A. M. Track, G. Heimel and E. Zojer. Understanding the electronic structure of metal/sam/organic semiconductor heterojunctions. *ACS Nano*, **3**(11), 3513–3520 (2009). [31](#)
106. Y. Shen, A. R. Hosseini, M. H. Wong and G. G. Malliaras. How to make ohmic contacts to organic semiconductors. *ChemPhysChem*, **5**(1), 16–25 (2004). [31](#)
107. H. Ishii, K. Sugiyama, E. Ito and K. Seki. Energy level alignment and interfacial electronic structures at organic/metal and organic/organic interfaces. *Advanced Materials*, **11**(8), 605–625 (1999). [31](#)
108. A. Kahn, N. Koch and W. Gao. Electronic structure and electrical properties of interfaces between metals and π -conjugated molecular films. *Journal of Polymer Science Part B: Polymer Physics*, **41**(21), 2529–2548 (2003). [31](#)

109. T. J. Richards and H. Sirringhaus. Analysis of the contact resistance in staggered, top-gate organic field-effect transistors. *Journal of Applied Physics*, **102**(9), 094510–6 (2007). [31](#), [41](#), [104](#)
110. J. H. Kang, D. d. S. Filho, J.-L. Bredas and X. Y. Zhu. Shallow trap states in pentacene thin films from molecular sliding. *Applied Physics Letters*, **86**(15), 152115–3 (2005). [31](#)
111. M. Urien, G. Wantz, E. Cloutet, L. Hirsch, P. Tardy, L. Vignau, H. Cramail and J.-P. Parneix. Field-effect transistors based on poly(3-hexylthiophene): Effect of impurities. *Organic Electronics*, **8**(6), 727–734 (2007). [31](#)
112. A. Salleo and R. A. Street. Kinetics of bias stress and bipolaron formation in polythiophene. *Physical Review B*, **70**(23), 235324 (2004). [31](#)
113. T. N. Ng, J. A. Marohn and M. L. Chabynyc. Comparing the kinetics of bias stress in organic field-effect transistors with different dielectric interfaces. *Journal of Applied Physics*, **100**(8), 084505–6 (2006). [32](#)
114. D. B. A. Rep, A. F. Morpurgo, W. G. Sloof and T. M. Klapwijk. Mobile ionic impurities in organic semiconductors. *Journal of Applied Physics*, **93**(4), 2082–2090 (2003). [32](#)
115. H. Sirringhaus. Reliability of organic field-effect transistors. *Advanced Materials*, **21**(38-39), 3859–3873 (2009). [32](#)
116. D. M. de Leeuw, M. M. J. Simenon, A. R. Brown and R. E. F. Einerhand. Stability of n-type doped conducting polymers and consequences for polymeric microelectronic devices. *Synthetic Metals*, **87**(1), 53–59 (1997). [32](#), [191](#)
117. T. D. Anthopoulos, G. C. Anyfantis, G. C. Papavassiliou and D. M. de Leeuw. Air-stable ambipolar organic transistors. *Applied Physics Letters*, **90**(12), 122105–3 (2007). [32](#)
118. C. R. Newman, C. D. Frisbie, D. A. da Silva Filho, J.-L. Brdas, P. C. Ewbank and K. R. Mann. Introduction to organic thin film transistors and design of n-channel organic semiconductors. *Chemistry of Materials*, **16**(23), 4436–4451 (2004). [33](#), [45](#)
119. X. Cheng, M. Caironi, Y.-Y. Noh, J. Wang, C. Newman, H. Yan, A. Facchetti and H. Sirringhaus. Air stable cross-linked cytop ultrathin gate dielectric for high yield

- low-voltage top-gate organic field-effect transistors. *Chemistry of Materials*, **22**(4), 1559–1566 (2010). [33](#)
120. A. Salleo, F. Endicott and R. A. Street. Reversible and irreversible trapping at room temperature in poly(thiophene) thin-film transistors. *Applied Physics Letters*, **86**(26), 263505–3 (2005). [33](#)
121. L. Bürgi, T. Richards, M. Chiesa, R. H. Friend and H. Sirringhaus. A microscopic view of charge transport in polymer transistors. *Synthetic Metals*, **146**(3), 297–309 (2004). [33](#), [41](#)
122. A. Salleo and R. A. Street. Light-induced bias stress reversal in polyfluorene thin-film transistors. *Journal of Applied Physics*, **94**(1), 471–479 (2003). [33](#)
123. M. F. Calhoun, C. Hsieh and V. Podzorov. Effect of interfacial shallow traps on polaron transport at the surface of organic semiconductors. *Physical Review Letters*, **98**(9), 096402 (2007). [33](#)
124. C. Goldmann, D. J. Gundlach and B. Batlogg. Evidence of water-related discrete trap state formation in pentacene single-crystal field-effect transistors. *Applied Physics Letters*, **88**(6), 063501–3 (2006). [33](#)
125. K. P. Pernstich, D. Oberhoff, C. Goldmann and B. Batlogg. Modeling the water related trap state created in pentacene transistors. *Applied Physics Letters*, **89**(21), 213509–3 (2006). [33](#)
126. S. Scheinert, G. Paasch and T. Doll. The influence of bulk traps on the subthreshold characteristics of an organic field effect transistor. *Synthetic Metals*, **139**(2), 233–237 (2003). [33](#)
127. E. J. Meijer, C. Detcheverry, P. J. Baesjou, E. van Veenendaal, D. M. de Leeuw and T. M. Klapwijk. Dopant density determination in disordered organic field-effect transistors. *Journal of Applied Physics*, **93**(8), 4831–4835 (2003). [33](#)
128. S. Hoshino, M. Yoshida, S. Uemura, T. Kodzasa, N. Takada, T. Kamata and K. Yase. Influence of moisture on device characteristics of polythiophene-based field-effect transistors. *Journal of Applied Physics*, **95**(9), 5088–5093 (2004). [33](#)
129. A. Arias, F. Endicott and R. Street. Surface-induced self-encapsulation of polymer thin-film transistors. *Advanced Materials*, **18**(21), 2900–2904 (2006). [33](#)

130. C. Vterlein, B. Ziegler, W. Gebauer, H. Neureiter, M. Stoldt, M. S. Weaver, P. Buerle, M. Sokolowski, D. D. C. Bradley and E. Umbach. Electrical conductivity and oxygen doping of vapour-deposited oligothiophene films. *Synthetic Metals*, **76**(1-3), 133–136 (1996). [33](#)
131. M. S. A. Abdou, F. P. Orfino, Z. W. Xie, M. J. Deen and S. Holdcroft. Reversible charge transfer complexes between molecular oxygen and poly(3-alkylthiophene)s. *Advanced Materials*, **6**(11), 838–841 (1994). [33](#)
132. T. Richards, M. Bird and H. Sirringhaus. A quantitative analytical model for static dipolar disorder broadening of the density of states at organic heterointerfaces. *The Journal of Chemical Physics*, **128**(23), 234905–5 (2008). [34](#)
133. N. G. Martinelli, M. Savini, L. Muccioli, Y. Olivier, F. Castet, C. Zannoni, D. Beljonne and J. Cornil. Modeling polymer dielectric/pentacene interfaces: On the role of electrostatic energy disorder on charge carrier mobility. *Advanced Functional Materials*, **19**(20), 3254–3261 (2009). [34](#)
134. R. C. G. Naber, M. Bird and H. Sirringhaus. A gate dielectric that enables high ambipolar mobilities in polymer light-emitting field-effect transistors. *Applied Physics Letters*, **93**(2), 023301–3 (2008). [34](#), [216](#)
135. I. N. Hulea, S. Fratini, H. Xie, C. L. Mulder, N. N. Iossad, G. Rastelli, S. Ciuchi and A. F. Morpurgo. Tunable frohlich polarons in organic single-crystal transistors. *Nat Mater*, **5**(12), 982–986 (2006). [34](#)
136. N. Zhao, Y. Y. Noh, J. F. Chang, M. Heeney, I. McCulloch and H. Sirringhaus. Polaron localization at interfaces in high-mobility microcrystalline conjugated polymers. *Advanced Materials*, **21**(37), 3759–3763 (2009). [34](#), [144](#)
137. K. P. Pernstich, S. Haas, D. Oberhoff, C. Goldmann, D. J. Gundlach, B. Batlogg, A. N. Rashid and G. Schitter. Threshold voltage shift in organic field effect transistors by dipole monolayers on the gate insulator. *Journal of Applied Physics*, **96**(11), 6431–6438 (2004). [35](#)
138. I. McCulloch, M. Heeney, C. Bailey, K. Genevicius, I. MacDonald, M. Shkunov, D. Sparrowe, S. Tierney, R. Wagner, W. Zhang, M. L. Chabynyc, R. J. Kline, M. D. McGehee and M. F. Toney. Liquid-crystalline semiconducting polymers with high charge-carrier mobility. *Nat Mater*, **5**(4), 328–333 (2006). [35](#)

139. J. A. Geurst. Theory of space-charge-limited currents. *Physica Status Solidi (b)*, **15**, 107–118 (1966). [36](#)
140. T. Agostinelli, M. Caironi, D. Natali, M. Sampietro, P. Biagioni, M. Finazzi and L. Duo. Space charge effects on the active region of a planar organic photodetector. *Journal of Applied Physics*, **101**(11), 114504–4 (2007). [36](#), [37](#), [61](#)
141. P. N. Murgatroyd. Theory of space-charge-limited current enhanced by frenkel effect. *J. of Phys. D*, **3**, 151 (1970). [36](#)
142. C. W. Tang and S. A. VanSlyke. Organic electroluminescent diodes. *Applied Physics Letters*, **51**(12), 913–915 (1987). [37](#)
143. C. Adachi, M. A. Baldo, M. E. Thompson and S. R. Forrest. Nearly 100 percent internal phosphorescence efficiency in an organic light-emitting device. *Journal of Applied Physics*, **90**(10), 5048–5051 (2001). [37](#)
144. M. Caironi, T. Agostinelli, D. Natali, M. Sampietro, R. Cugola, M. Catellani and S. Luzzati. External quantum efficiency versus charge carriers mobility in polythiophene/methanofullerene based planar photodetectors. *Journal of Applied Physics*, **102**(2), 024503–7 (2007). [37](#), [199](#)
145. J. Gao and J. Dane. Planar polymer light-emitting electrochemical cells with extremely large interelectrode spacing. *Applied Physics Letters*, **83**(15), 3027–3029 (2003). [37](#), [211](#)
146. J. Gao, J. Hui, Y. Hou and S. Alem. Planar polymer photovoltaic cells with millimeter interelectrode spacing. *Journal of Applied Physics*, **104**(8), 084512–5 (2008). [37](#), [199](#)
147. S. Grecu, M. Bronner, A. Opitz and W. Brtting. Characterization of polymeric metal-insulator-semiconductor diodes. *Synthetic Metals*, **146**(3), 359–363 (2004). [41](#)
148. D. M. Taylor, J. A. Drysdale, I. Torres and O. Fernandez. Electron trapping and inversion layer formation in photoexcited metal-insulator-poly(3-hexylthiophene) capacitors. *Applied Physics Letters*, **89**(18), 183512–3 (2006). [41](#), [182](#)
149. O. Fernandez, D. M. Taylor, J. A. Drysdale and D. M. Ellis. Photogenerated minority carrier trapping and inversion layer formation in polymer field-effect structures. *Dielectrics and Electrical Insulation, IEEE Transactions on*, **13**(5), 1093–1100 (2006). [41](#)

150. M. Ullah, D. M. Taylor, R. Schwodiauer, H. Sitter, S. Bauer, N. S. Sariciftci and T. B. Singh. Electrical response of highly ordered organic thin film metal-insulator-semiconductor devices. *Journal of Applied Physics*, **106**(11), 114505–6 (2009). [41](#)
151. T. Miyadera, T. Minari, K. Tsukagoshi, H. Ito and Y. Aoyagi. Frequency response analysis of pentacene thin-film transistors with low impedance contact by interface molecular doping. *Applied Physics Letters*, **91**(1), 013512–3 (2007). [41](#), [81](#)
152. R. Schroeder, L. A. Majewski and M. Grell. A study of the threshold voltage in pentacene organic field-effect transistors. *Applied Physics Letters*, **83**(15), 3201–3203 (2003). [43](#)
153. C. Dimitrakopoulos and P. Malenfant. Organic thin film transistors for large area electronics. *Advanced Materials*, **14**(2), 99–117 (2002). [45](#)
154. J. Zaumseil and H. Sirringhaus. Electron and ambipolar transport in organic field-effect transistors. *Chemical Reviews*, **107**(4), 1296–1323 (2007). [45](#)
155. S. Janietz, D. D. C. Bradley, M. Grell, C. Giebeler, M. Inbasekaran and E. P. Woo. Electrochemical determination of the ionization potential and electron affinity of poly(9,9-dioctylfluorene). *Applied Physics Letters*, **73**(17), 2453–2455 (1998). [51](#)
156. J. L. Bredas, R. Silbey, D. S. Boudreaux and R. R. Chance. Chain-length dependence of electronic and electrochemical properties of conjugated systems: polyacetylene, polyphenylene, polythiophene, and polypyrrole. *Journal of the American Chemical Society*, **105**(22), 6555–6559 (1983). [51](#)
157. A. Morteani. *The Electronics and Photophysics of Polymer Heterojunctions*. PhD thesis, University of Cambridge, (2004). [51](#)
158. A. J. Campbell, D. D. C. Bradley and H. Antoniadis. Quantifying the efficiency of electrodes for positive carrier injection into poly(9,9-dioctylfluorene) and representative copolymers. *Journal of Applied Physics*, **89**(6), 3343–3351 (2001). [51](#)
159. E. R. Bittner, J. G. S. Ramon and S. Karabunarliev. Exciton dissociation dynamics in model donor-acceptor polymer heterojunctions. i. energetics and spectra. *The Journal of Chemical Physics*, **122**(21), 214719–9 (2005). [51](#)
160. J.-H. Huang, C.-P. Lee, Z.-Y. Ho, D. Kekuda, C.-W. Chu and K.-C. Ho. Enhanced spectral response in polymer bulk heterojunction solar cells by using active materials

- with complementary spectra. *Solar Energy Materials and Solar Cells*, **94**(1), 22–28 (2010). 51
161. E. Lim, B.-J. Jung and H.-K. Shim. Synthesis and characterization of a new light-emitting fluorene-thieno[3,2-b]thiophene-based conjugated copolymer. *Macromolecules*, **36**(12), 4288–4293 (2003). 51
162. T. Hamasaki, T. Morimune, H. Kajii, S. Minakata, R. Tsuruoka, T. Nagamachi and Y. Ohmori. Fabrication and characteristics of polyfluorene based organic photodetectors using fullerene derivatives. *Thin Solid Films*, **518**(2), 548–550 (2009). 51
163. V. Bodrozic, T. M. Brown, S. Mian, D. Caruana, M. Roberts, N. Phillips, J. J. Halls, I. Grizzi, J. H. Burroughes and F. Cacialli. The built-in potential in blue polyfluorene-based light-emitting diodes. *Advanced Materials*, **20**(12), 2410–2415 (2008). 51
164. P. Sreearunothai. *Time-Resolved Photoluminescence Studies of Polydioctylfluorene and its Copolymer Derivatives*. PhD thesis, University of Cambridge, (2006). 52
165. <http://www.spectraservices.com/Merchant2/pdf/Ace-Specs.pdf>. Schott Ace Halogen light source. 65, 227
166. N. Takeda, S. Asaoka and J. R. Miller. Nature and energies of electrons and holes in a conjugated polymer, polyfluorene. *Journal of the American Chemical Society*, **128**(50), 16073–16082 (2006). 76, 170, 171, 174
167. H. Matsui and T. Hasegawa. Visualization of accumulated charge density in operating organic thin-film transistors. *Applied Physics Letters*, **95**(22), 223301–3 (2009). 81, 82, 83, 120
168. R. L. Brewster. *Telecommunications Technology*. Wiley, (1986). 82
169. T. Richards. *Internal potentiometry of polymer field effect transistors*. PhD thesis, University of Cambridge, (2007). 83
170. Y. Deng. *Charge Modulation Spectroscopy of All-Polymer Transistors*. PhD thesis, University of Cambridge, (1994). 93, 109, 118, 127, 128
171. N. Zhao. *Field-Effect Transistors Based on Microcrystalline Conjugated Polymers*. PhD thesis, University of Cambridge, (2009). 93

172. C. R. McNeill, S. Westenhoff, C. Groves, R. H. Friend and N. C. Greenham. Influence of nanoscale phase separation on the charge generation dynamics and photovoltaic performance of conjugated polymer blends: balancing charge generation and separation. *The Journal of Physical Chemistry C*, **111**(51), 19153–19160 (2007). [94](#)
173. X. Cheng, Y.-Y. Noh, J. Wang, M. Tello, J. Frisch, R.-P. Blum, A. Vollmer, J. P. Rabe, N. Koch and H. Sirringhaus. Controlling electron and hole charge injection in ambipolar organic field-effect transistors by self-assembled monolayers. *Advanced Functional Materials*, **19**(15), 2407–2415 (2009). [94](#), [188](#)
174. M. C. Gwinner, S. Khodabakhsh, H. Giessen and H. Sirringhaus. Simultaneous optimization of light gain and charge transport in ambipolar light-emitting polymer field-effect transistors. *Chemistry of Materials*, **21**(19), 4425–4433 (2009). [94](#), [106](#), [186](#)
175. M.-H. Yoon, H. Yan, A. Facchetti and T. J. Marks. Low-voltage organic field-effect transistors and inverters enabled by ultrathin cross-linked polymers as gate dielectrics. *Journal of the American Chemical Society*, **127**(29), 10388–10395 (2005). [95](#)
176. L. Bürgi, T. J. Richards, R. H. Friend and H. Sirringhaus. Close look at charge carrier injection in polymer field-effect transistors. *Journal of Applied Physics*, **94**(9), 6129–6137 (2003). [98](#)
177. H. Yan, Z. Chen, Y. Zheng, C. Newman, J. R. Quinn, F. Dotz, M. Kastler and A. Facchetti. A high-mobility electron-transporting polymer for printed transistors. *Nature*, **457**(7230), 679–686 (2009). [101](#)
178. S. T. Lee, X. Y. Hou, M. G. Mason and C. W. Tang. Energy level alignment at alq/metal interfaces. *Applied Physics Letters*, **72**(13), 1593–1595 (1998). [104](#)
179. I. G. Hill, D. Milliron, J. Schwartz and A. Kahn. Organic semiconductor interfaces: electronic structure and transport properties. *Applied Surface Science*, **166**(1-4), 354–362 (2000). [104](#)
180. M. Schidleja, C. Melzer and H. von Seggern. Investigation of charge-carrier injection in ambipolar organic light-emitting field-effect transistors. *Advanced Materials*, **21**(10-11), 1172–1176 (2009). [104](#)

181. C. A. Elderling, A. Knoesen and S. T. Kowel. Use of fabry–p[e-acute]rot devices for the characterization of polymeric electro-optic films. *Journal of Applied Physics*, **69**(6), 3676–3686 (1991). [112](#)
182. A. Baba, J. Lübben, K. Tamada and W. Knoll. Optical properties of ultrathin poly(3,4-ethylenedioxythiophene) films at several doping levels studied by in situ electrochemical surface plasmon resonance spectroscopy. *Langmuir*, **19**(21), 9058–9064 (2003). [131](#), [134](#)
183. C. W. Spangler and T. J. Hall. Oxidative doping studies of ppv oligomers. *Synthetic Metals*, **44**(1), 85–93 (1991). [138](#)
184. R. Schenk, H. Gregorius and K. Mllen. Absorption spectra of charged oligo (phenylenevinylene)s: On the detection of polaronic and bipolaronic states. *Advanced Materials*, **3**(10), 492–493 (1991). [138](#)
185. M. Deussen and H. Bessler. Anion and cation absorption spectra of conjugated oligomers and polymers. *Chemical Physics*, **164**(2), 247–257 (1992). [138](#), [139](#)
186. J. Cornil, D. Beljonne and J. L. Bredas. Nature of optical transitions in conjugated oligomers. i. theoretical characterization of neutral and doped oligo(phenylenevinylene)s. *The Journal of Chemical Physics*, **103**(2), 834–841 (1995). [138](#)
187. J. Cornil, D. Beljonne and J. L. Bredas. Nature of optical transitions in conjugated oligomers. ii. theoretical characterization of neutral and doped oligothiophenes. *The Journal of Chemical Physics*, **103**(2), 842–849 (1995). [138](#)
188. D. Beljonne, J. Cornil, H. Sirringhaus, P. J. Brown, M. Shkunov, R. H. Friend and J. L. Brdas. Optical signature of delocalized polarons in conjugated polymers. *Advanced Functional Materials*, **11**(3), 229–234 (2001). [139](#), [155](#)
189. Z. Q. Li, V. Podzorov, N. Sai, M. C. Martin, M. E. Gershenson, M. Di Ventra and D. N. Basov. Light quasiparticles dominate electronic transport in molecular crystal field-effect transistors. *Physical Review Letters*, **99**(1), 016403 (2007). [139](#)
190. W. Barford. *Electronic and Optical Properties of Conjugated Polymers*. Clarendon Press, Oxford, (2005). [139](#), [154](#)

191. A. J. Campbell, D. D. C. Bradley and H. Antoniadis. Dispersive electron transport in an electroluminescent polyfluorene copolymer measured by the current integration time-of-flight method. *Applied Physics Letters*, **79**(14), 2133–2135 (2001). [141](#)
192. J. Zaumseil, C. Groves, J. M. Winfield, N. C. Greenham and H. Sirringhaus. Electron-hole recombination in uniaxially aligned semiconducting polymers. *Advanced Functional Materials*, **18**(22), 3630–3637 (2008). [141](#), [191](#)
193. T. Ford. *Long-lived excitations in conjugated polymer blend films and devices*. PhD thesis, University of Cambridge, (2005). [144](#), [155](#), [158](#)
194. R. C. Hilborn. Einstein coefficients, cross sections, f values, dipole moments, and all that. **50**(11), 982–986 (2002). [152](#)
195. V. I. Arkhipov, P. Heremans, E. V. Emelianova, auml and H. ssler. Effect of doping on the density-of-states distribution and carrier hopping in disordered organic semiconductors. *Physical Review B*, **71**(4), 045214 (2005). [155](#)
196. J. Reynaert, V. Arkhipov, P. Heremans and J. Poortmans. Photomultiplication in disordered unipolar organic materials. *Advanced Functional Materials*, **16**(6), 784–790 (2006). [162](#), [184](#), [193](#)
197. A. Hayer, A. L. T. Khan, R. H. Friend and A. Khler. Morphology dependence of the triplet excited state formation and absorption in polyfluorene. *Physical Review B*, **71**(24), 241302 (2005). [163](#)
198. M. E. Caruso and M. Anni. Real-time investigation of solvent swelling induced β - phase formation in poly(9,9-dioctylfluorene). *Phys. Rev. B*, **76**(5), 054207 Aug 2007. [163](#)
199. M. J. Winokur, J. Slinker and D. L. Huber. Structure, photophysics, and the order-disorder transition to the β phase in poly(9,9-(di-*n*, *n*-octyl)fluorene). *Phys. Rev. B*, **67**(18), 184106 May 2003. [163](#)
200. M. Grell, D. D. C. Bradley, G. Ungar, J. Hill and K. S. Whitehead. Interplay of physical structure and photophysics for a liquid crystalline polyfluorene. *Macromolecules*, **32**(18), 5810–5817 (1999). [163](#)
201. C. Wu and J. McNeill. Swelling-controlled polymer phase and fluorescence properties of polyfluorene nanoparticles. *Langmuir*, **24**(11), 5855–5861 (2008). [163](#)

202. A. L. T. Khan, M. J. Banach and A. Khler. Control of [beta]-phase formation in polyfluorene thin films via franck-condon analysis. *Synthetic Metals*, **139**(3), 905–907 (2003). 163
203. http://www.chem.ufl.edu/~reynolds/research/Electrochromic_polymers/Electrochromic_polymers.htm. 167, 168
204. J. J. M. Halls, A. C. Arias, J. D. MacKenzie, W. Wu, M. Inbasekaran, E. P. Woo and R. H. Friend. Photodiodes based on polyfluorene composites: Influence of morphology. *Advanced Materials*, **12**(7), 498–502 (2000). 181
205. A. Kohler, D. A. dos Santos, D. Beljonne, Z. Shuai, J. L. Bredas, A. B. Holmes, A. Kraus, K. Mullen and R. H. Friend. Charge separation in localized and delocalized electronic states in polymeric semiconductors. *Nature*, **392**(6679), 903–906 (1998). 181
206. D. Hertel and H. Bessler. Photoconduction in amorphous organic solids. *ChemPhysChem*, **9**(5), 666–688 (2008). 181
207. D. Kabra and K. Narayan. Direct estimate of transport length scales in semiconducting polymers. *Advanced Materials*, **19**(11), 1465–1470 (2007). 181
208. J. Gao and F. A. Hegmann. Bulk photoconductive gain in pentacene thin films. *Applied Physics Letters*, **93**(22), 223306–3 (2008). 181
209. J. Huang and Y. Yang. Origin of photomultiplication in c[sub 60] based devices. *Applied Physics Letters*, **91**(20), 203505–3 (2007). 181
210. D. S. Ginger and N. C. Greenham. Charge injection and transport in films of cdse nanocrystals. *Journal of Applied Physics*, **87**(3), 1361–1368 (2000). 182, 194
211. X. Wang, K. Wasapinyokul, W. De Tan, R. Rawcliffe, A. J. Campbell and D. D. C. Bradley. Device physics of highly sensitive thin film polyfluorene copolymer organic phototransistors. *Journal of Applied Physics*, **107**(2), 024509–10 (2010). 182
212. V. I. Arkhipov, E. V. Emelianova and H. Bessler. Quenching of excitons in doped disordered organic semiconductors. *Physical Review B*, **70**(20), 205205 (2004). 182
213. P. Dyreklev, O. Ingans, J. Paloheimo and H. Stubb. Photoluminescence quenching in a polymer thin film field effect luministor. *Synthetic Metals*, **57**(1), 4139–4144 (1993). 182, 183

214. R. Karpicz, M. Kirkus, J. Vidas Grazulevicius and V. Gulbinas. Fluorescence quenching by charge carriers in indolo[3,2-b]carbazole-based polymer. *Journal of Luminescence*, **130**(4), 722–727 (2010). [182](#), [184](#)
215. V. Gulbinas, R. Karpicz, I. Muzikante and L. Valkunas. Fluorescence quenching by trapped charge carriers in n,n-dimethylaminobenzylidene 1,3-indandione films. *Thin Solid Films*, **518**(12), 3299–3304 (2010). [182](#)
216. Y. Luo, H. Aziz, G. Xu and Z. D. Popovic. Electron-induced quenching of excitons in luminescent materials. *Chemistry of Materials*, **19**(9), 2288–2291 (2007). [182](#), [207](#)
217. J. D. McNeill, D. Y. Kim, Z. Yu, D. B. O’Conno and P. F. Barbara. Near field spectroscopic investigation of fluorescence quenching by charge carriers in pentacene-doped tetracene. *The Journal of Physical Chemistry B*, **108**(31), 11368–11374 (2004). [182](#)
218. A. J. Gesquiere, S.-J. Park and P. F. Barbara. F-v/sms: A new technique for studying the structure and dynamics of single molecules and nanoparticles. *The Journal of Physical Chemistry B*, **108**(29), 10301–10308 (2004). [182](#), [183](#)
219. J. Bolinger, K.-J. Lee, R. E. Palacios and P. F. Barbara. Detailed investigation of light induced charge injection into a single conjugated polymer chain. *The Journal of Physical Chemistry C*, **112**(47), 18608–18615 (2008). [182](#)
220. S.-J. Park, A. J. Gesquiere, J. Yu and P. F. Barbara. Charge injection and photooxidation of single conjugated polymer molecules. *Journal of the American Chemical Society*, **126**(13), 4116–4117 (2004). [182](#)
221. T. Haskins, A. Chowdhury, R. H. Young, J. R. Lenhard, A. P. Marchetti and L. J. Rothberg. Charge-induced luminescence quenching in organic light-emitting diodes. *Chemistry of Materials*, **16**(23), 4675–4680 (2004). [182](#)
222. A. J. Ferguson, N. Kopidakis, S. E. Shaheen and G. Rumbles. Quenching of excitons by holes in poly(3-hexylthiophene) films. *The Journal of Physical Chemistry C*, **112**(26), 9865–9871 (2008). [182](#)
223. S. Hayashi, K. Kaneto and K. Yoshino. Quenching of photoluminescence in poly(thiophene) films by electrochemical doping. *Solid State Communications*, **61**(4), 249–251 (1987). [182](#)

224. R. E. Palacios, F.-R. F. Fan, J. K. Grey, J. Suk, A. J. Bard and P. F. Barbara. Charging and discharging of single conjugated-polymer nanoparticles. *Nat Mater*, **6**(9), 680–685 (2007). [182](#)
225. S. Chandrasekhar. Stochastic problems in physics and astronomy. *Reviews of Modern Physics*, **15**(1), 1 (1943). [183](#)
226. P. Dyreklev, O. Inganäs, J. Paloheimo and H. Stubb. Photoluminescence quenching in a polymer thin-film field-effect luministor. *Journal of Applied Physics*, **71**(6), 2816–2820 (1992). [183](#)
227. J. Zaumseil. *N-Channel, Ambipolar and Light-Emitting Polymer Field-Effect Transistors*. PhD thesis, University of Cambridge, (2006). [186](#)
228. K. Lin. Charge generation in organic semiconductors. Master’s thesis, University of Cambridge, (2008). [188](#), [197](#)
229. H. Frohne, C. R. McNeill and P. C. Dastoor. Photoenhanced injection currents in organic solar cells. *Applied Physics Letters*, **85**(6), 1042–1044 (2004). [191](#), [201](#)
230. C. R. McNeill, H. Frohne, J. L. Holdsworth and P. C. Dastoor. Near-field scanning photocurrent measurements of polyfluorene blend devices: directly correlating morphology with current generation. *Nano Letters*, **4**(12), 2503–2507 (2004). [192](#)
231. S. Westenhoff, I. A. Howard, J. M. Hodgkiss, K. R. Kirov, H. A. Bronstein, C. K. Williams, N. C. Greenham and R. H. Friend. Charge recombination in organic photovoltaic devices with high open-circuit voltages. *Journal of the American Chemical Society*, **130**(41), 13653–13658 (2008). [192](#)
232. D. Natali, L. Fumagalli and M. Sampietro. Modeling of organic thin film transistors: Effect of contact resistances. *Journal of Applied Physics*, **101**(1), 014501–12 (2007). [193](#)
233. M. A. Lampert and P. Mark. *Current Injection in Solid*. Academic Press Inc. [194](#)
234. J. C. Ho, A. Arango and V. Bulovic. Lateral organic bilayer heterojunction photoconductors. *Applied Physics Letters*, **93**(6), 063305–3 (2008). [199](#)
235. R. H. Young, C. W. Tang and A. P. Marchetti. Current-induced fluorescence quenching in organic light-emitting diodes. *Applied Physics Letters*, **80**(5), 874–876 (2002). [207](#)

236. J. Yu, N. W. Song, J. D. McNeill and P. F. Barbara. Efficient exciton quenching by hole polarons in the conjugated polymer meh-ppv. *Israel Journal of Chemistry*, **44**(1-3), 127–132 (2004). [207](#)
237. H. Hieda, K. Tanaka, K. Naito and N. Gemma. Fluorescence quenching induced by injected carriers in organic thin films. *Thin Solid Films*, **331**(1-2), 152–157 (1998). [207](#)
238. J. Dane and J. Gao. Imaging the degradation of polymer light-emitting devices. *Applied Physics Letters*, **85**(17), 3905–3907 (2004). [211](#)
239. J. Dane, C. Tracy and J. Gao. Direct observation of a frozen junction in polymer light-emitting electrochemical cells. *Applied Physics Letters*, **86**(15), 153509–3 (2005). [211](#)
240. J. Gao and J. Dane. Visualization of electrochemical doping and light-emitting junction formation in conjugated polymer films. *Applied Physics Letters*, **84**(15), 2778–2780 (2004). [211](#)
241. J.-H. Shin, S. Xiao and L. Edman. Polymer light-emitting electrochemical cells: The formation and effects of doping-induced micro shorts. *Advanced Functional Materials*, **16**(7), 949–956 (2006). [211](#)
242. A. L. Burin and M. A. Ratner. Exciton migration and cathode quenching in organic light emitting diodes. *The Journal of Physical Chemistry A*, **104**(20), 4704–4710 (2000). [212](#)
243. R. Capelli, S. Toffanin, G. Generali, H. Usta, A. Facchetti and M. Muccini. Organic light-emitting transistors with an efficiency that outperforms the equivalent light-emitting diodes. *Nat Mater*, **9**(6), 496–503 (2010). [216](#)
244. J. Zaumseil, C. R. McNeill, M. Bird, D. L. Smith, P. P. Ruden, M. Roberts, M. J. McKiernan, R. H. Friend and H. Sirringhaus. Quantum efficiency of ambipolar light-emitting polymer field-effect transistors. *Journal of Applied Physics*, **103**(6), 064517–10 (2008). [216](#)
245. M. A. Baldo, R. J. Holmes and S. R. Forrest. Prospects for electrically pumped organic lasers. *Physical Review B*, **66**(3), 035321 (2002). [216](#)

246. N. C. Giebink and S. R. Forrest. Temporal response of optically pumped organic semiconductor lasers and its implication for reaching threshold under electrical excitation. *Physical Review B*, **79**(7), 073302 (2009). [216](#)
247. C. Gartner, C. Karnutsch, U. Lemmer and C. Pflumm. The influence of annihilation processes on the threshold current density of organic laser diodes. *Journal of Applied Physics*, **101**(2), 023107–9 (2007). [216](#)